University of Sussex

The impact of environment on galaxy evolution

Starburst and AGN activity

Rosemary Theresa Coogan

Submitted for the degree of Doctor of Philosophy

University of Sussex

June 2019

Declaration

I hereby declare that this thesis has not been and will not be submitted in whole or in part to another University for the award of any other degree.

Chapter 3 was published in Strazzullo et al. (2018), Astrophysical Journal, Volume 862, Issue 1, pages 64-75. I am the second author of Strazzullo et al. (2018), and my main contributions to this paper were in the data analysis, as well as discussion and comments on the interpretation.

Chapter 4 was published in Coogan et al. (2018), Monthly Notices of the Royal Astronomical Society, Volume 479, Issue 1, pages 703-729. I contributed to all aspects of this paper, with all coauthors also contributing comments and feedback. Some coauthors gave access to data and helped with aspects of the analysis.

Chapter 5 was published in Coogan et al. (2019), Monthly Notices of the Royal Astronomical Society, Volume 485, Issue 2, pages 2092-2105. I contributed to all aspects of this paper, and all coauthors contributed comments and advice. Some coauthors also provided access to data or helped with parts of the analysis.

Signature:

Rosemary Theresa Coogan

UNIVERSITY OF SUSSEX

Rosemary Theresa Coogan, Doctor of Philosophy

The impact of environment on galaxy evolution: Starburst and AGN activity

Summary

This thesis aims to understand the processes driving galaxy evolution across a range of environments, focusing on submillimeter-radio interferometric observations to characterise the interstellar medium (ISM) of galaxies. I investigate the formation of the first massive, passive galaxies in clusters, as a key step towards establishing the prominent environmental trends seen at low redshift. Cl J1449+0856 is an excellent case to study this - a galaxy cluster at z=2 with an already virialised atmosphere. Thanks to the significant over-density of galaxies in Cl J1449+0856, we have uncovered a diverse range of cluster members at z=2. I use multi-wavelength observations to study how dust-obscured star-formation, ISM content and Active Galactic Nuclei (AGN) are linked to environment during this crucial phase of cluster evolution. I find that the dense cluster environment significantly increases the star-formation efficiency and gas excitation of the massive galaxies, and conclude that these effects are driven by the high number of mergers, interactions and AGN in the cluster core. I then examine the sub-M* population in the cluster, probing this important and so-far poorly characterised ISM regime. I place these low-enrichment galaxies on ISM scaling relations, and find evidence for increased gas-to-dust ratios in this regime at z=2, compared with the local Universe. I quantify the effect of low metallicity on high-J CO transitions, finding that both the diffuse and denser gas phases are significantly photo-dissociated at z=2. Finally, looking towards future surveys of obscured star-formation across all environments, I start preparations for the Square Kilometer Array (SKA). I construct high-resolution mock images of an entire survey field as observed by the SKA, containing galaxies with a variety of morphologies and star-formation rates at $0 < z < 3$. This will both inform future observational strategies, and enable us to efficiently analyse the large amounts of SKA data that will soon become available.

Acknowledgements

This thesis is dedicated to my incredible Mum. Thank you, for everything.

There are so many people to whom I'm truly grateful. Thank you to my supervisor, Mark Sargent, for his careful and honest guidance over the past four years. I'm so glad to have delved into astronomy with such a patient and knowledgable mentor, and I really appreciate the enormous amount of time he invested in developing these projects with me. A huge thank you also to Emanuele Daddi, for welcoming me into his group during my time at CEA Saclay. He has continued to be encouraging and supportive far beyond what I could have hoped for, and I feel very lucky to have had the opportunity to work together. I've collaborated with so many great people over the course of my PhD, all of whom have contributed to the research presented in this thesis. I also acknowledge the financial support of STFC grant ST/N504452/1.

Working at Sussex has been a great experience, and the Astronomy corridor is full of fantastic people who are always happy to help. I've also met some wonderful friends, who have made the last few years so much fun. Thank you to all of my 4C13 officemates for endless amusement, and a sympathetic ear when things don't go to plan. Thank you Phil, Ridwan and Alberto for interesting discussions from the beginning, and Carlos, Azizah, Sunayana and Michele for pizza and scary movie nights ever since. Thank you to my inspiring radio buddy Daniel and his board game evenings, to Marion and Luke for taking me out of the Astro bubble from time to time, and to everyone on the Astronomy corridor (the list is endless!) for constant smiles and great end-of-the-week outings. Thank you also to my friends and colleagues in Saclay, to Max for always encouraging me to do more, to Anelise, Antonello, Shuowen, Jeremy, and everyone who has welcomed me back on my visits since then.

Finally, I owe the most enormous amount to my family. Thank you to Mum, Jul, Keith and Grandad, without whose love and support I could have never done a PhD, and to my adorable siblings Emrys, Rufus and Violet. I would be lost without you all.

To confine our attention to terrestrial matters would be to limit the human spirit.

STEPHEN HAWKING

Contents

List of Tables

List of Figures

Chapter 1

Introduction

There are an infinite number of avenues to explore on our journey to understanding the Universe we live in. As astronomers, we turn our attention to observations of the sky, building instruments that allow us to see far beyond anything we could have imagined with the naked eye. As we reach outside of our solar system, and even beyond the Milky Way, we find that our Galaxy is just one small piece in an endless, ever-expanding Universe.

One of the first known examples of using a telescope for astronomical purposes is Galileo Galilei's work in 1610. Remarkably, Galileo was able to deduce the existence of the four largest moons of Jupiter, using just a small optical refracting telescope to observe their orbits. In the 400 years since then, the field of observational astronomy has vastly expanded, now spanning the entirety of the electromagnetic spectrum. This enables us to explore the formation and evolution of a multitude of galaxies, from our closest neighbours in the local Universe to galaxies observed just a few hundred million years after the Big Bang. In this chapter, I discuss our current understanding of galaxies and their evolution, and highlight the outstanding questions that drive the work presented in this thesis.

1.1 Galaxies

A galaxy is a gravitationally bound collection of stellar material, gas and dust ('baryonic matter'), contained within a halo of dark matter comprising $\sim$95% of the galaxy's total mass. The majority of the galaxy population also host a supermassive black hole in their core (sometimes presenting as an Active Galactic Nucleus, AGN), for all except the least massive, 'dwarf' galaxies (e.g. Salpeter 1964; Lynden-Bell 1969; Begelman et al. 1984; Kormendy & Richstone 1995; Kormendy & Gebhardt 2001; Wang & Zhang 2003; Ferrarese & Ford 2005; van den Bosch et al. 2012; Reines et al. 2014; Marleau et al. 2017). We can observe and study galaxies at great distances - however,

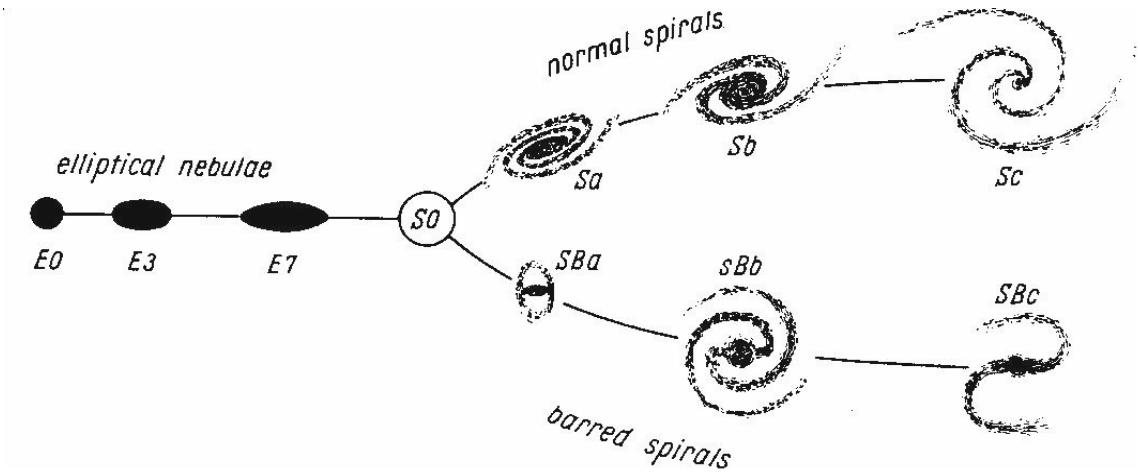

Figure 1.1: The Hubble tuning fork (Hubble, 1936), illustrating different morphological galaxy types. Observationally, we find that elliptical galaxies tend to have older stellar populations and lower SFRs than spiral galaxies, as well as different kinematic properties. This suggests that elliptical galaxies may be at a later evolutionary stage than spiral galaxies.

the Universe is continually expanding, with the rate of expansion increasing with distance from the local Universe (Hubble, 1929). The outwards expansion of the Universe causes galaxies at cosmological distances to recede from one another, thereby introducing a Doppler shift in the observed properties of a galaxy's emission. This is known as the 'redshift', z, of a galaxy from the observer. The redshift of a galaxy increases with distance, thereby enabling us to place constraints on the distance to a galaxy by measuring the frequency shift of known spectral lines from their 'rest-frame', non-redshifted positions. Hand-in-hand with these cosmological distances, the light from other galaxies takes a significant travel time to reach our telescopes at the finite speed of light. By observing distant galaxies at high redshift, we are observing light that left galaxies millions or even billions of years ago, allowing us to study these galaxies in their early evolutionary stages.

We show the 'Hubble tuning fork' in Fig. 1.1, an illustration of the different galaxy morphology classifications, as documented by Edwin Hubble in the local Universe (Hubble, 1936). This figure demonstrates some important observations and terminology that we use to describe the galaxy population. We see in Fig. 1.1 both 'elliptical' and 'spiral' galaxies, also known as 'early-type' and 'late-type' galaxies respectively (for historical reasons). Elliptical galaxies are observed to have relatively red colours compared to spiral galaxies, arising from their older, cooler stellar populations (e.g. Strateva et al. 2001; Bell et al. 2004; Baldry et al. 2004, 2006; Dekel & Birnboim 2006; Mateus et al. 2006; Gargiulo et al. 2012; Trayford et al. 2016; Nelson et al. 2018; Marian et al. 2018). Particularly in the local Universe, early-type galaxies (ETGs) also host relatively small amounts of interstellar gas and dust (see Section 1.3), resulting in low star-formation rates

(SFRs, the stellar mass per year formed within the galaxy). Conversely, disk or spiral galaxies tend to be bluer, and are still actively forming stars through consumption of their interstellar medium (ISM). The evolutionary path of galaxies therefore takes them from an active, spiral or disk-like galaxy, to an elliptical galaxy that has become passive or 'quenched'. It is thought that elliptical galaxies form as a result of either an intense burst of star-formation, through quenching via AGN feedback, or from the hierarchical build-up of galaxies through both minor and major merging activity, which could play a role in disrupting spiral morphologies and giving rise to the increased velocity dispersions found within ETGs (e.g. Navarro et al. 1996; Longhetti et al. 1999; Chiosi & Carraro 2002; van Dokkum & Ellis 2003; Springel et al. 2005b; Thomas et al. 2005; Kormendy et al. 2009; Wild et al. 2009; Yesuf et al. 2014; Carnall et al. 2018; Maltby et al. 2018; Rowlands et al. 2018). These different galaxy morphologies have been observed across a wide range of redshifts, and the relative prevalence of different morphological types as a function of environment can give revealing insights into the drivers behind galaxy evolution (see Section 1.4.1).

As with many astronomical sources, galaxies emit light across the full range of the electromagnetic spectrum. The energy emitted by a galaxy as a function of wavelength is given by the galaxy's spectral energy distribution (SED), and can be modelled to infer many physical properties of the galaxy (e.g. Oke 1971; Kinney et al. 1996; Bolzonella et al. 2000; Förster Schreiber et al. 2004; Burgarella et al. 2005; Brammer et al. 2008; Casey 2012; Wild et al. 2014; da Cunha et al. 2015; Ciesla et al. 2018). For example, the majority of a galaxy's stellar emission is emitted at rest-frame ultraviolet (UV) to optical wavelengths, and was therefore the classic tracer of galaxy emission in the early stages of observational astronomy. However, galaxies also emit a large proportion of their light at wavelengths invisible to the eye, particularly very low frequencies such as infrared (IR) - submillimeter - radio wavelengths that trace the dust-obscured star-formation within a galaxy. The balance between UV-optical and IR emission in the total extragalactic background is split approximately equally, highlighting the importance of this long wavelength emission. Throughout this thesis, I use primarily submillimeter - radio observations to study the evolution of galaxies.

1.2 Galaxy evolution

1.2.1 The cosmic star-formation history

Over the last few decades we have started to build increasingly large numbers of telescopes, from high-energy gamma- and X-ray observatories (e.g. Fermi, Chandra, XXM-Newton), all the way to the longest centimeter-radio wavelengths (e.g. the Karl G. Jansky Very Large Array (VLA) and the LOw Frequency ARray LOFAR). These instruments have enabled us to collect observations

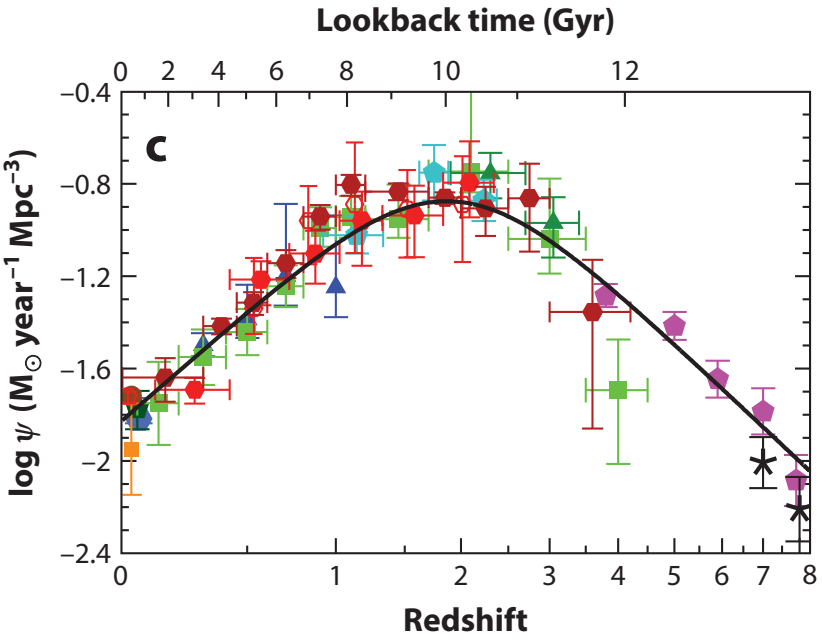

Figure 1.2: The cosmic star-formation history (Madau & Dickinson, 2014). The green, cyan, purple and blue symbols come from UV measurements; the red, dark red and orange symbols are from infrared measurements. It can be seen that the peak of the cosmic star-formation history was ∼10 billion years ago, at z∼2.

of galaxies reaching redshifts up to z=7-8 (e.g. Steidel et al. 1999; Shapley et al. 2001; Yan & Windhorst 2004; Daddi et al. 2009; McLure et al. 2010; Oesch et al. 2010; Saintonge et al. 2011; Wilkins et al. 2011; Bouwens et al. 2012a; Tacconi et al. 2013; Maiolino et al. 2015; Venemans et al. 2017), with rich multiwavelength data available over large regions of the sky. Building upon studies at lower redshift, there are now considerable efforts aiming to characterise how the number density of galaxies as a function of stellar mass (the stellar mass function) evolves at these early times (e.g. Bell et al. 2003; Conselice et al. 2005; Guo et al. 2010; Ilbert et al. 2010; Bouwens et al. 2012a; Behroozi et al. 2013; Lilly et al. 2013; Davidzon et al. 2017), for which future instruments such as the James Webb Space Telescope will enable significant progress.

Of particular interest for tracing the stellar mass build-up in galaxies are those observations tracing the rate of star-formation in galaxies (see Section 1.2.2). When we combine statistical samples of such data, we can quantify the total density of star-formation occurring in the Universe at a given epoch, and thus construct the 'cosmic star-formation history' (SFH). In Fig. 1.2, we show the cosmic star-formation rate density as compiled by Madau & Dickinson (2014). Quantifying the SFR density of the Universe as a function of redshift allows us to characterise the assembly history of the Universe, and identify the cosmic time at which galaxies were most active. We see a peak in the star-formation density at z∼2 - indicating that this redshift is a key epoch for the study of

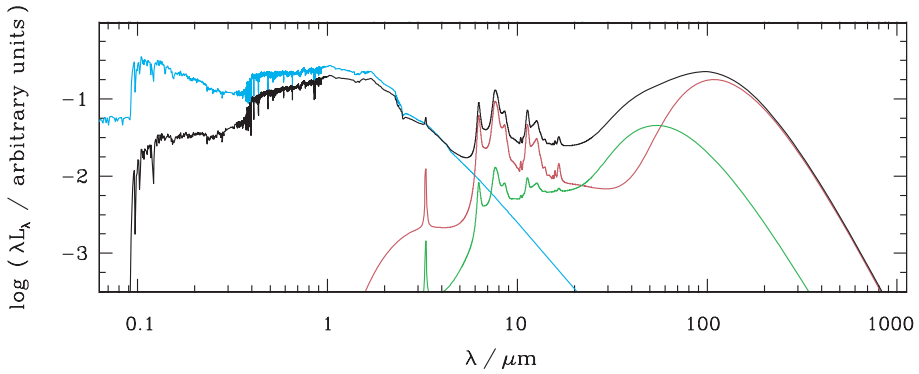

Figure 1.3: A model SED of a star-forming galaxy (da Cunha et al., 2008). The blue line shows the unattenuated stellar emission, the green line shows the emission from dust in giant molecular clouds, and the red line gives the dust re-emission in the remaining ISM. The black line shows the total SED that would be observed from the galaxy.

galaxy evolution itself. It should be noted, however, that although the volume-averaged SFR density follows the evolution shown in Fig. 1.2, individual galaxies can have a diverse range of SFHs (see e.g. Ciesla et al. 2017). Interestingly, studies tracing the cosmic history of AGN activity within galaxies have found a similar profile with redshift, also peaking at z∼2 (e.g. Boyle & Terlevich 1998; Silverman et al. 2008; Shankar 2009; Aird et al. 2010; Mullaney et al. 2012b; Delvecchio et al. 2014). This gives strong support to the notion that AGN activity and galaxy evolution are intrinsically linked, either through the regulation of star-formation via AGN feedback, a common source of fuel for both star-formation and AGN, or a delicate balance of such factors. We also note from Fig 1.2 that beyond z∼3 the measurements of the cosmic SFH come almost exclusively from UV measurements, with far fewer constraints on the obscured star-formation activity probed by the IR dust emission (see Section 1.2.2). Probing this part of the cosmic SFR density using large surveys at submillimeter wavelengths has recently become a growing area of interest (e.g. Lindner et al. 2011; Karim et al. 2013; Simpson et al. 2015; Aravena et al. 2016b; Dunlop et al. 2017; Franco et al. 2018), and will give increasingly robust constraints on the cosmic SFH at high redshift.

1.2.2 Observing star-formation in galaxies

There are several, somewhat complementary methods with which we can observe the star-formation activity within a galaxy (e.g. Donas & Deharveng 1984; Kennicutt 1998a; Kewley et al. 2002; Bell 2003; Schmitt et al. 2006; Calzetti 2008; Murphy et al. 2011; Domínguez Sánchez et al. 2012; Tabatabaei et al. 2017). As touched upon in Section 1.2.1, we often refer to ‘obscured’ and

'unobscured' star-formation. As a galaxy forms stars, it will form a certain fraction of massive, hot, short-lived stars (e.g. O- and B-type stars), as well as a fraction of less massive, cooler stars, with the relative proportions being dictated by the initial mass function (IMF, e.g. Salpeter 1955; Kroupa 2001; Chabrier 2003). These O- and B-stars are particularly luminous at the shortest wavelengths, emitting a large part of their total energy output as blue, ultraviolet radiation. In some cases, this UV emission can be observed from a galaxy directly, via UV-optical instruments such as the Hubble Space Telescope (HST). Combined with the assumed IMF, the UV luminosity can then be calibrated to give a measure of a galaxy's total unobscured star-formation rate. Similarly, nebular line emission from star-forming HII regions (e.g. the Hydrogen recombination line Hα, see Chapter 5) can also be used to give an indication of a galaxy's dust-unobscured star-formation rate.

However, galaxies often contain a significant amount of dust in their interstellar medium (alongside the gaseous content, Section 1.3) - particularly in relatively massive, actively star-forming galaxies (e.g. Mathis 1990; Charlot & Fall 2000; Draine 2003; da Cunha et al. 2010; Casey 2012; Corbelli et al. 2012; Cortese et al. 2012; Heinis et al. 2014; Santini et al. 2014; Tan et al. 2014; Pannella et al. 2015; Davies et al. 2017; Popping et al. 2017). Dust grains absorb a certain amount of the stellar and nebular radiation, where the most highly attenuated wavelengths are the short wavelengths, comparable to the size of the dust grain itself. This results in a significant amount of the UV-optical radiation emitted by young stars being absorbed by dust in the ISM. This has the effect of heating the dust to between $\sim$20-40 K, such that dust temperature can be related to the radiation intensity from young stars (Mezger et al. 1982; Calzetti et al. 2000; Draine & Li 2007; Magnelli et al. 2014; Béthermin et al. 2015; Schreiber et al. 2018). The dust re-emits the absorbed radiation in order to cool, with this blackbody emission peaking at longer, rest-frame infrared wavelengths. An example of a typical galaxy SED is shown in Fig. 1.3. We see here that the stellar emission at short wavelengths (blue line) has been attenuated in the final galaxy SED (black line). This radiation is instead re-emitted by the dust (green and red lines).

We can measure this dust emission at far-infrared (FIR) or submillimeter wavelengths, using space- or ground-based instruments such as the Herschel Space Observatory, ALMA and NOEMA. Measurement of dust-reprocessed emission can therefore be used to trace the galaxy's star-formation, that is otherwise 'obscured' at shorter wavelengths due to the dust attenuation. The most complete measure of a galaxy's total star-formation rate comes from the combination of both the obscured and unobscured star-formation rates. However, the ratio of IR- to UV- luminosity, known as the 'IR-excess', is observed to be $\gtrsim$10 in 'typical' star-forming galaxies above a stellar mass of $\sim 10^{10} M_{\odot}$ (e.g. Heinis et al. 2014; Whitaker et al. 2014; Pannella et al. 2015; Cousin

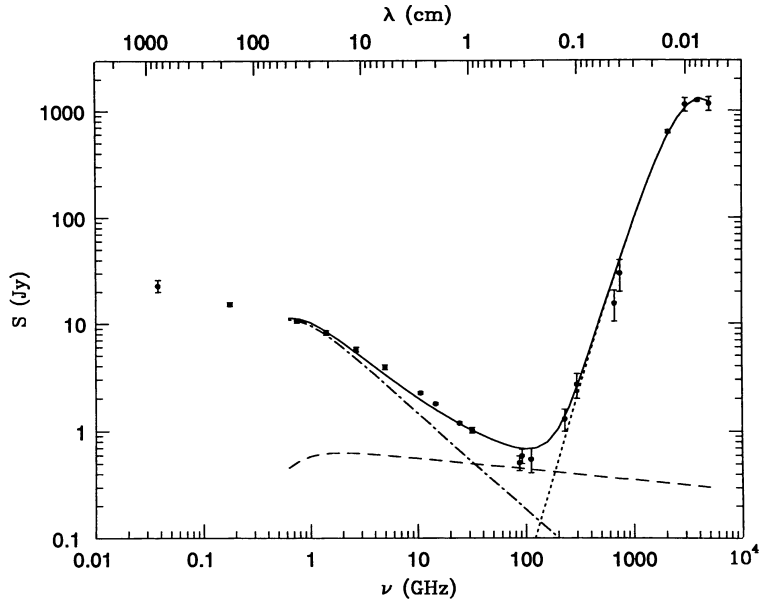

Figure 1.4: The radio-submillimeter portion of the spectral energy distribution for M82, a local star-forming galaxy (Condon, 1992). The steep dotted line shows the submillimeter contribution from dust emission in the Rayleigh-Jeans tail. The dot-dashed line shows the synchrotron emission, and the shallower dashed line is the contribution from free-free emission. The solid line shows the total flux density.

et al. 2019, see Meurer et al. 1999; Overzier et al. 2011 for discussion on more highly star-forming galaxies). This means that the obscured SFR is a good proxy for the total SFR in these galaxies. It also implies that if the UV-optical unobscured SFR is the only information available, then this must be corrected for dust attenuation (e.g. Allen 1976; Fitzpatrick 1986; Calzetti et al. 2000), as is done in Chapter 5.

Finally, another regime in which we can observe star-formation is through observations at radio wavelengths, as discussed in detail in Chapter 6. Radio continuum emission is produced by both synchrotron and free-free emission in star-forming galaxies (Condon, 1992). Synchrotron radiation is emitted when relativistic electrons are accelerated through magnetic fields, by supernova shocks of massive stars. On the other hand, free-free radiation is produced by free electrons scattering off ions in HII regions, where massive stars have ionised regions of neutral Hydrogen. In this way, radio continuum emission is also related to the star-formation activity in 'normal' galaxies (those not hosting an AGN). These contributions to the radio portion of a galaxy's SED are shown in Fig 1.4, alongside the dust contribution in the Rayleigh Jeans (RJ) tail.

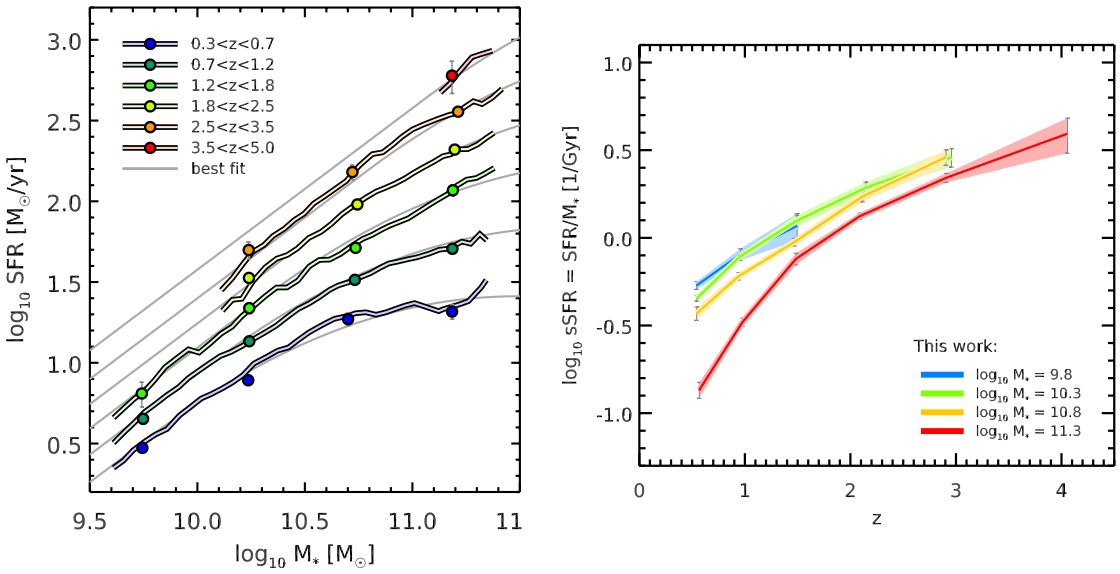

Figure 1.5: Left: The Main Sequence of star-formation, evolving as a function of redshift (Schreiber et al., 2015). It can be seen that the normalisation of the MS increases to higher SFRs with increasing redshift. Right: The evolution of sSFR as a function of both redshift and stellar mass (Schreiber et al., 2015). Evidence for a decrease in sSFR towards higher stellar masses and lower redshifts can be seen.

1.2.3 The Main Sequence of star-formation

Having gained an understanding of the global star-formation history of the Universe (and its observational tracers), we now discuss the so-called 'main sequence' (MS) of star-formation. Studies of the star-forming population have revealed a tight correlation between the current star-formation rate of a galaxy and its stellar mass (e.g. Brinchmann et al. 2004; Elbaz et al. 2007, 2011; Noeske et al. 2007; Daddi et al. 2010b; Karim et al. 2011; Rodighiero et al. 2011; Bouwens et al. 2012b; Lee et al. 2012; Whitaker et al. 2012, 2014; Speagle et al. 2014; Steinhardt et al. 2014; Schreiber et al. 2015; Tomczak et al. 2016). This relationship has been observed to prevail across several magnitudes of stellar mass, as shown in Fig 1.5. Additionally, we see in the left panel of Fig 1.5 that this relationship exists up to redshifts far beyond the peak epoch of star-formation ($z\sim2$), with the normalisation of the MS locus increasing with redshift. This means that for a fixed stellar mass, the expected SFR of a galaxy on the MS increases at earlier times. Studies have shown that the MS tends to be dominated by disk-dominated star-forming galaxies (e.g. Salmi et al. 2012; van der Wel et al. 2014; Whitaker et al. 2015; Trayford et al. 2019), which evolve along the MS locus as they build up their stellar mass.

Another parameterisation to express the galaxy MS is through the specific star-formation rate of a galaxy (sSFR), defined as the SFR per unit stellar mass (SFR/$M_\star$). This definition has, in turn,

given rise to the use of sSFR as a means of classifying galaxies as lying on the MS, or offset from it. The intrinsic scatter of the MS is ∼0.2-0.3 dex even up to z∼5-6, and may be in part a result of different galaxy selection techniques (e.g. IR-, UV- or radio-selected, Elbaz et al. 2007; Whitaker et al. 2012; Salmon et al. 2015; Schreiber et al. 2015). However, when a galaxy lies significantly above this scatter, it can be known as a 'starburst' galaxy (although note the varying definitions of starburst galaxy used in the literature). The MS-starburst divide is often adopted to be at 0.6 dex above the MS locus, equivalent to a specific SFR ∼4 times above that on the MS.

This concept of MS and starburst galaxies can be explained by the existence of two distinct modes of star-formation: a secular mode found in MS galaxies, and a significantly more rapid 'starburst' mode, resulting in the cessation of star-formation through gas depletion on short timescales (<100 Myrs, e.g. Solomon et al. 1997; Greve et al. 2005; Solomon & Vanden Bout 2005; Tacconi et al. 2008; Ivison et al. 2011). This is statistically characterised by the '2-Star Formation Mode' framework presented in Sargent et al. (2012). The fraction of starburst galaxies compared to the MS population remains approximately constant with redshift up to at least z∼4 (Rodighiero et al., 2011; Schreiber et al., 2015), and explaining this highly active population has become a significant area of research at all redshifts. In the local Universe, the population of starburst galaxies primarily consists of very bright, IR-luminous galaxies, known as Ultra Luminous InfraRed Galaxies (ULIRGs Downes & Solomon 1998, note that ULIRGs are luminosity- and therefore mass-selected, by definition). Local ULIRGs are often driven by mergers of gas-rich galaxies, which can contribute significantly to a galaxy's increase in SFR and subsequent rise above the MS (e.g. Armus et al. 1987; Sanders & Mirabel 1996; Lambas et al. 2003; Bridge et al. 2007; Ellison et al. 2013; Cao et al. 2016; Cortijo-Ferrero et al. 2017; Cibinel et al. 2019). However, the prevalence of mergers among highly star-forming galaxies at higher redshift is thought to decrease (e.g. Daddi et al. 2010a; Tacconi et al. 2010). Similarly, the effect of mergers is also predicted to have a less significant effect on increasing sSFR at higher redshift (Jogee et al., 2009; Robaina et al., 2009; Wong et al., 2011; Xu et al., 2012; Kaviraj et al., 2013; Perret et al., 2014; Fensch et al., 2017). However, there are observations supporting a link between merging activity and high SFRs in galaxies at z>1 (e.g. Dasyra et al. 2008; Kartaltepe et al. 2012; Silverman et al. 2018).

Looking below the MS, we find a population of galaxies with low SFRs for their stellar mass. These are known as 'quenched' or passive galaxies, and are believed to have reached the end stages of evolution, joining the red, 'dead' elliptical population. We note here that the exact form of the MS, particularly at the high-mass end, is a subject of continued research. Although the MS has traditionally been characterised as a power-law, there are also studies that claim evidence for significant curvature at the high-mass end of the MS, breaking away from a power-law description

(Abramson et al. 2014; Lee et al. 2015; Whitaker et al. 2015; Tomczak et al. 2016; Mancini et al. 2019; Popesso et al. 2019, also compare left and right panels in Fig. 1.5). This MS 'bending' is broadly thought to be related to the increased number of bulge-dominated galaxies at the high-mass end of the MS, whose bulge may have a relatively minor role in the star-formation activity whilst contributing significantly to the stellar mass. Another suggested explanation for this bending is the 'rejuvenation' of star-formation in quiescent galaxies below the MS, with the modest SFRs of the rejuvenated galaxies dragging down the high-mass end of the MS. This is a relatively new area of research, and is further complicated by the fact that the form of the MS at all stellar masses can be biased by selection effects (Renzini & Peng, 2015; Popesso et al., 2019).

The existence of a Main Sequence of star-formation gives evidence that star-formation in the majority of galaxies proceeds as a smooth, somewhat secular process, across a range of redshifts and stellar masses. The question that then arises is what drives this star-formation? Large statistical studies in recent years (e.g. Genzel et al. 2010; Saintonge et al. 2011; Schinnerer et al. 2016; Scoville et al. 2017; Tacconi et al. 2018) have concluded that the primary property dictating a galaxy's star-formation rate is the content of the interstellar medium - specifically the amount of molecular gas available within the galaxy. In this well-accepted framework, the scatter of galaxies above and below the MS is due to variations in the gas fractions of galaxies, with higher gas fractions giving rise to higher SFRs (see Sargent et al. 2014). It is at this point that the difference between MS and starburst galaxies becomes of interest once again. What are the molecular gas properties of starburst galaxies, compared to main sequence galaxies? What does this tell us about their star-formation activity? To further explore this, I discuss in Section 1.3 the observational tracers of the ISM in galaxies, and the fundamental relationship that exists between star-formation and the ISM for MS and starburst galaxies.

1.3 The interstellar medium

1.3.1 Observing molecular gas and dust

The interstellar medium contains a mixture of ionised, atomic and molecular gas phases, as well as grains of interstellar dust (see Ferrière 2001 for a review). Elements such as Carbon and Hydrogen are photo-ionised by the young stellar population, giving rise to the warm, ionised phases of the ISM, in addition to bubble-like structures of gas that are ionised by supernovae. Atomic gas exists at lower temperatures and higher densities than the ionised phase, where the primary emission mechanism is the 21cm recombination line. It is currently very difficult to detect 21cm emission outside of the local Universe, due to the requirement for very high sensitivities at radio wavelengths.

However, the study of cosmology and galaxy formation through this neutral gas, reaching into the first few Gyrs of the Universe, is a major science driver of the future Square Kilometer Array (Blake et al. 2004; Jarvis & Rawlings 2004; Braun et al. 2015).

Moving to the densest phase of the ISM, molecular gas (specifically molecular Hydrogen, H_2) is the fuel for star-formation itself. As such, the molecular gas content of galaxies is a crucial component for the study of galaxy evolution. Star-formation in galaxies takes place in regions known as Giant Molecular Clouds (GMCs), where the cooler, denser phases of the ISM can be found at the core (Solomon et al., 1987; Williams et al., 2000; Carilli & Walter, 2013). The formation of (proto)stars commences by the condensation of molecular Hydrogen onto dust grains in GMCs. However, although these Hydrogen molecules are of great interest, their lack of permanent dipole moment means that the lowest rotational transitions of H_2 are forbidden, in addition to requiring far higher temperatures ($\sim$500 K) than those found in GMCs. The majority of H_2 therefore does not emit readily-detectable observational signatures. In order to measure the molecular gas content of a galaxy, we must then use different components of the ISM as tracers. There are two primary methods for measuring the gas content in galaxies: (i) from the dust continuum emission (e.g. Guelin et al. 1993; Lisenfeld et al. 2000; Leroy et al. 2011; Magdis et al. 2012; Santini et al. 2014; Scoville et al. 2014, 2017; Genzel et al. 2015; Berta et al. 2016; Schinnerer et al. 2016); (ii) from spectroscopic transitions of tracer molecules (e.g. Bryant & Scoville 1999; Boselli et al. 2002; Greve et al. 2005; Daddi et al. 2010a; Saintonge et al. 2011; Aravena et al. 2016a; Riechers et al. 2019; Tacconi et al. 2018). Both of these methods are employed in Chapters 4 and 5.

The less observationally expensive method for measuring gas mass is from the dust continuum emission. As discussed in Section 1.2.2, the dust grains in the ISM emit optically-thin continuum emission at rest-frame IR wavelengths, as a result of absorbing shorter wavelength stellar emission. Measurement of this IR-submillimeter continuum emission, combined with galaxy SED models, therefore gives insight into the mass of dust present in the ISM (e.g. Dale et al. 2001; Draine & Li 2007; Compiègne et al. 2011; Béthermin et al. 2015; Kirkpatrick et al. 2017; Galliano 2018; Schreiber et al. 2018). As Hydrogen and dust coexist in the ISM, and are both core elements in the process of star-formation, it is perhaps not surprising that there is a relationship between the mass of dust in the ISM and the total mass of Hydrogen (atomic + molecular phases). We note that in Chapters 2 to 5, we are studying galaxies at z$\sim$2, where we can assume that the Hydrogen content of the galaxies is dominated by the molecular phase (Daddi et al., 2010b; Lagos et al., 2015; Tacconi et al., 2018). The conversion factor between these two quantities is known as the gas-to-dust ratio (G/D), and is strongly dependent on the metal enrichment of a galaxy, as explored

in detail in Chapter 5.

Arguably the most direct method to detect molecular gas is through tracer molecules that persist alongside Hydrogen in the gaseous ISM. Although Hydrogen is the most abundant element in the ISM, there are also several other atoms and molecules that have lower excitation requirements, and are therefore observable in the ISM through their spectral transitions (e.g. CO, C[II], CI, [OI]63μm, HCN, Boselli et al. 2002; Solomon et al. 2003; Ao et al. 2008; Aravena et al. 2010; Ivison et al. 2010; Stacey et al. 2010; Danielson et al. 2011; Walter et al. 2011; Combes et al. 2012; Coppin et al. 2012; Bournaud et al. 2015; Zanella et al. 2018). The most abundant of these tracer molecules is carbon monoxide - ^{12}CO, which is collisionally excited by H_2 itself. CO has low excitation conditions ($\sim$5-40 K, Carilli & Walter 2013), and several orders of this transition can be observed from the ground using submillimeter observatories. The ground state transition in CO, CO[1-0], traces the most diffuse phase of the gas. Interestingly, higher-order transitions such as CO[5-4] trace the denser phases of molecular Hydrogen that are currently forming stars (Daddi et al., 2015; Liu et al., 2015; Yang et al., 2017), and can therefore be used as tracers of instantaneous star-formation rate. This is discussed further in Chapters 2 to 5. However, the ground state of CO[1-0] is often of most interest for ISM studies, as it traces the total molecular gas content of the galaxy, and therefore the fuel that is available to form stars over the course of the galaxy's lifetime.

In order to calculate the total mass of molecular Hydrogen gas in a galaxy, we must convert between observed CO luminosity and molecular gas mass. This can be done in spatially resolved regions within a galaxy, thereby measuring the surface density of molecular gas, or can be integrated over the entire galaxy. In the work presented in Chapters 4 and 5, and often at high redshift, we focus on the integrated gas mass, in part due to the limited angular resolution of our observations. The conversion factor between CO luminosity and H_2 mass, $\alpha_{\rm CO}$, is defined as:

$$M_{\rm H_2} = \alpha_{\rm CO} \times L'_{\rm CO1-0} \tag{1.1}$$

where $L'_{\rm CO1-0}$ is the luminosity of the CO[1-0] line, $M_{\rm H_2}$ is the total molecular gas mass, and $\alpha_{\rm CO}$ is the conversion factor between the two. Here, $L'_{\rm CO1-0}$ is measured in K kms^{-1} pc^2, meaning $\alpha_{\rm CO}$ has units of $M_\odot$(K kms^{-1} pc^2)$^{-1}$. The traditional radio astronomy units for line intensity are K kms^{-1}, arising from the connection between intensity and brightness temperature [K] seen through the Rayleigh-Jeans approximation at low frequency[1], combined with the line velocity width [kms^{-1}]. The units of $L'_{\rm CO1-0}$ can then be reached by the addition of a [pc^2] term from the luminosity distance squared, when converting between flux and luminosity.

[1] $T_b = \frac{\lambda^2}{2k} I_\lambda$, where I_λ is specific intensity and T_b is brightness temperature. Flux density is the integral of specific intensity over solid angle Ω.

The value of $\alpha_{\rm CO}$ across different types of galaxy is a subject of active research (see Bolatto et al. 2013 for a review). Within the Milky Way, it has been possible to determine $\alpha_{\rm CO}$ using several different methods. The linewidth of emission from GMCs is observed to follow the size-linewidth relation expected for self-gravitating bodies (reflecting the cloud's velocity dispersion, Larson 1981; Solomon et al. 1987; Heyer et al. 2009). If we assume that GMCs are virialised structures with masses dominated by molecular gas, we can in turn relate the linewidth to the virial mass and thus derive the molecular gas mass. For optically thick emission where luminosity is dictated primarily by linewidth, we can then expect an almost linear relationship between virial mass (molecular gas mass) and CO luminosity. In this way, $\alpha_{\rm CO}$ can be derived by combining $L'_{\rm CO1-0}$ and molecular gas mass (equation 1.1).

Secondly, whereas CO[1-0] is optically thick, optically thin tracers could instead be used to measure the total mass of molecular Hydrogen (and therefore estimate $\alpha_{\rm CO}$), e.g. isotopologues of CO, or dust emission. For example, if one can determine the optical depth of the dust through SED modelling, then this can be related to the total gas column density. Finally, both extinction mapping and the study of diffuse γ-ray emission have also been used to estimate $\alpha_{\rm CO}$ in the Milky Way. Outside of the Milky Way, where we are limited by both sensitivity and resolution, only a subset of techniques such as the virial method, dust emission and CO isotopologue modelling are observationally feasible. In our Galaxy, and for massive galaxies that lie on the MS of star-formation more generally, the value of $\alpha_{\rm CO}$ has been measured at $\alpha_{\rm CO}\sim$4.4 (Solomon et al., 1987; Scoville et al., 1987; Strong & Mattox, 1996; Grenier et al., 2005a; Pineda et al., 2010; Planck Collaboration et al., 2011; Sandstrom et al., 2013; Schultheis et al., 2014). However, it has also been shown observationally that this value is highly dependent on the gas-phase metallicity of a galaxy. In low-metallicity environments, CO molecules are photo-dissociated, and their abundance decreases with respect to Hydrogen molecules, thus increasing $\alpha_{\rm CO}$. This topic is discussed in detail in Chapter 5, specifically outside of the local Universe.

On the other hand, studies of local luminous and ultraluminous infrared galaxies have demonstrated that the value of $\alpha_{\rm CO}$ is not universal between all galaxy types (Downes et al., 1993; Scoville et al., 1997; Downes & Solomon, 1998; Bryant & Scoville, 1999; Yao et al., 2003; Daddi et al., 2010b; Papadopoulos et al., 2012b; Sliwa et al., 2012; Kamenetzky et al., 2017). In the most luminous, starburst-like galaxies, we see that a Milky-Way-like $\alpha_{\rm CO}$ value would give rise to molecular gas masses close to, or even exceeding, the total dynamical mass of the galaxy (estimated through kinematic studies). In these cases, the assumption that the CO emission originates from virialised GMCs breaks down. In the local Universe, the population of starburst galaxies is dominated by ULIRGs, where $\alpha_{\rm CO}$ values are much smaller than in MS galaxies, at approximately $\alpha_{\rm CO}$=0.8.

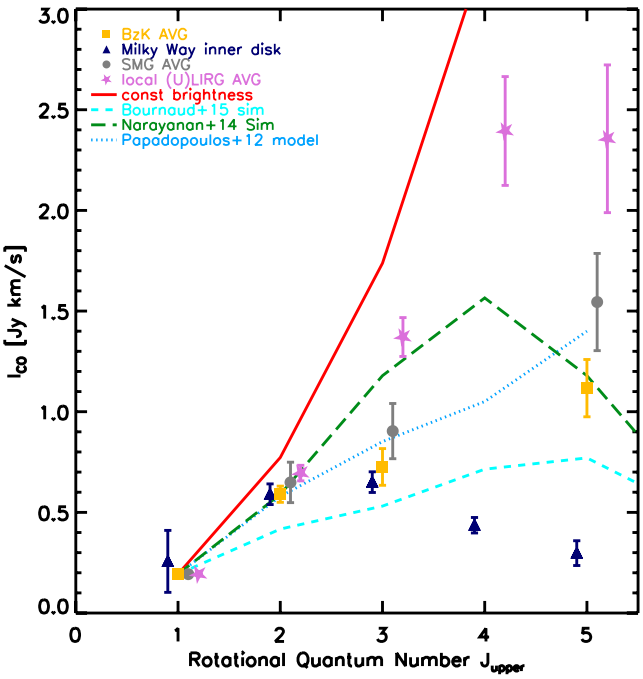

Figure 1.6: CO Spectral Line Energy Distributions for a range of galaxy types (Daddi et al., 2015). Differences can be seen between the SLEDs of MS galaxies at z$\sim$1.5 (BzK, orange squares), the Milky Way (blue triangles), submillimeter galaxies (SMGs at 1<z<4, grey circles), local ULIRGs (pink stars) and thermally excited gas (red line). The difference is most marked at higher-J transitions. For comparison, predictions from several simulations are also shown.

This is due to the change in local ISM conditions compared to MS galaxies, including warmer ISM temperatures and higher velocity dispersions of the gas (Narayanan et al., 2012; Papadopoulos et al., 2012a), such that the CO emission is less optically thick than in MS galaxies. This means that the mass of molecular Hydrogen in the ISM of local ULIRGs is a factor of $\sim$5 less than in MS galaxies, for the same CO luminosity. There is much discussion on the value of $\alpha_{\rm CO}$ in starburst galaxies, particularly outside of the local Universe, where this lower $\alpha_{\rm CO}$ is thought to prevail in high-redshift starbursts (e.g. Tacconi et al. 2008; Ivison et al. 2011; Magdis et al. 2011; Magnelli et al. 2012). Similarly, as discussed in Chapter 4, the G/D ratio in starburst galaxies is also expected to be lower in starbursts than in MS galaxies (although see e.g. Genzel et al. 2015; Scoville et al. 2016, who find a less marked variation in ISM conversion factors).

1.3.2 CO Spectral Line Energy Distributions

Having discussed $\alpha_{\rm CO}$, which relates to the luminosity of CO[1-0], I now introduce observations of the higher-order transitions of CO. The excitation of a CO transition can be described by the upper quantum level of the transition, J_{upper} (J). As we will see in Chapter 4, the flux ratio

between different CO transitions gives us insight into the state of molecular gas in a galaxy, and therefore the galaxy's star-formation activity. This is because the different transitions of CO trace physically different components of the ISM. For example, the critical density for excitation rises towards higher-J transitions, meaning that higher transitions require rapidly increasing densities and temperatures (Bolatto et al., 2013; Carilli & Walter, 2013). As star-formation occurs in relatively dense environments within GMCs, rather than in the more diffuse regions of H_2, higher-J CO transitions trace the molecular gas that is currently forming stars, rather than the total available molecular gas reservoir (seen through CO[1-0]). Indeed, as we progress towards higher J, the transitions become increasingly sensitive to the star-forming gas. At J>4, the CO luminosity correlates linearly with the FIR luminosity itself, for both MS and starburst galaxies across a range of redshifts (Daddi et al., 2015; Liu et al., 2015).

It is particularly revealing to measure the relative abundances of different CO transitions for different populations of galaxies. Fig. 1.6 shows a compilation of CO Spectral Line Energy Distributions (SLEDs) from Daddi et al. 2015. Here, we see that the ratio between high- and low-J CO transitions, i.e. the relative amount of dense gas to diffuse gas, changes between MS and starburst galaxies, and also evolves as a function of redshift (as predicted by simulations such as Lagos et al. 2012; Popping et al. 2014; Bournaud et al. 2015). This means that high-z MS galaxies contain increased amounts of excited molecular gas compared to local spirals (such as the Milky Way). Additionally, local ULIRGs and high-z submillimeter galaxies have higher gas excitations than z$\sim$0 MS galaxies and z>1 MS galaxies (BzK). By measuring the ratio of CO line fluxes, e.g. $I_{CO4-3}I_{CO1-0}$, we therefore gain information about the mode of star-formation that is occurring. The SLED of thermally excited gas is also shown in Fig. 1.6, where CO flux $\propto J^2$. Star-forming galaxies at both low- and high-redshift lie below this curve (although note that some extreme systems such as QSOs have been observed to have excitation close to thermal, or even higher in some cases, e.g. Weiß et al. 2007; Dannerbauer et al. 2019).

The physical properties that drive CO excitation have been investigated both observationally and through simulations. Several, somewhat interlinked factors have been proposed as key drivers, such as the mean radiation intensity of the starlight (and therefore the temperature of the dust in the ISM, Daddi et al. 2015), the surface density of molecular gas (Narayanan & Krumholz 2014), and the presence of dense clumps in the ISM (Bournaud et al., 2015), as well as indirect factors such as the metallicity of a galaxy. The intensity of the radiation field from young stars is expected to increase towards higher redshifts (e.g. Magdis et al. 2012; Béthermin et al. 2015), as is the hardness of the ionizing radiation field (Steidel et al., 2014), which can naturally account for the redshift evolution in CO SLEDs for MS galaxies. On the other hand, it is thought that

starburst-like galaxies such as ULIRGs contain relatively high amounts of dense molecular gas compared to MS galaxies (e.g. Daddi et al. 2010b), which is then reflected in their CO SLEDs. This increase in the amount of highly excited dense gas is likely to be linked with an increase in a galaxy's star-formation 'efficiency' (SFE, Papadopoulos et al., 2012a). To further explore the concept of star-formation efficiency, we discuss the relationship between molecular gas mass and star-formation in Section 1.3.3, for both MS and starburst galaxies.

1.3.3 The Kennicutt-Schmidt law

In Fig. 1.7, we see two correlations between the ISM of a galaxy and its SFR. In the left panel we have the observable properties - the CO[1-0] luminosity vs. the FIR luminosity (Sargent et al., 2014). This is a particularly fundamental relationship, as a single locus can be defined for MS galaxies spanning a wide range of redshifts. This is shown as the solid line in the left panel of Fig. 1.7. Offset from this relation, indicated by the dashed line in Fig. 1.7, is the trend found for starburst galaxies. As discussed above, we see that this population lies at significantly lower CO luminosities than MS galaxies, for a given IR luminosity (where IR emission is a proxy of the obscured SFR). In order to examine what is known as the Kennicutt-Schmidt (KS) law (Schmidt, 1959; Kennicutt, 1998b), we must convert these observables to physical properties of the galaxies. When we apply MS- and starburst- $\alpha_{\rm CO}$ values respectively to the x-axis, and convert $L_{\rm IR}$ to SFR (by dividing by 10^{10}, for a Chabrier 2003 IMF), we find the relationship between integrated molecular gas mass and star-formation rate shown in the right panel of Fig. 1.7. This plane illustrates an important parameter used for the study of galaxy evolution in Chapters 4 and 5. The star-formation efficiency is defined as:

$$SFE = \frac{SFR}{M_{mol}} = \frac{1}{\tau} \tag{1.2}$$

where M_{mol} is the molecular gas mass and τ is the molecular gas depletion timescale. It is clear from the Kennicutt-Schmidt plane that starburst galaxies have a higher SFE than main sequence galaxies, meaning that they have a higher SFR per unit molecular gas mass. This is a key observation, and it has been suggested that starburst galaxies are a population with distinct characteristics to Main Sequence galaxies, and are not simply the high-SFR tail of the MS distribution. As a word of caution, it should be noted that the studies from which Fig. 1.7 was compiled (full list of references can be found within Sargent et al. 2014) contained distinct starburst or MS galaxy populations by definition, and selecting samples of galaxies to fill the void between these extremes would provide useful further information. Nonetheless, even before the different $\alpha_{\rm CO}$ values are considered, we can see through the observables themselves that the starburst population separates from the MS

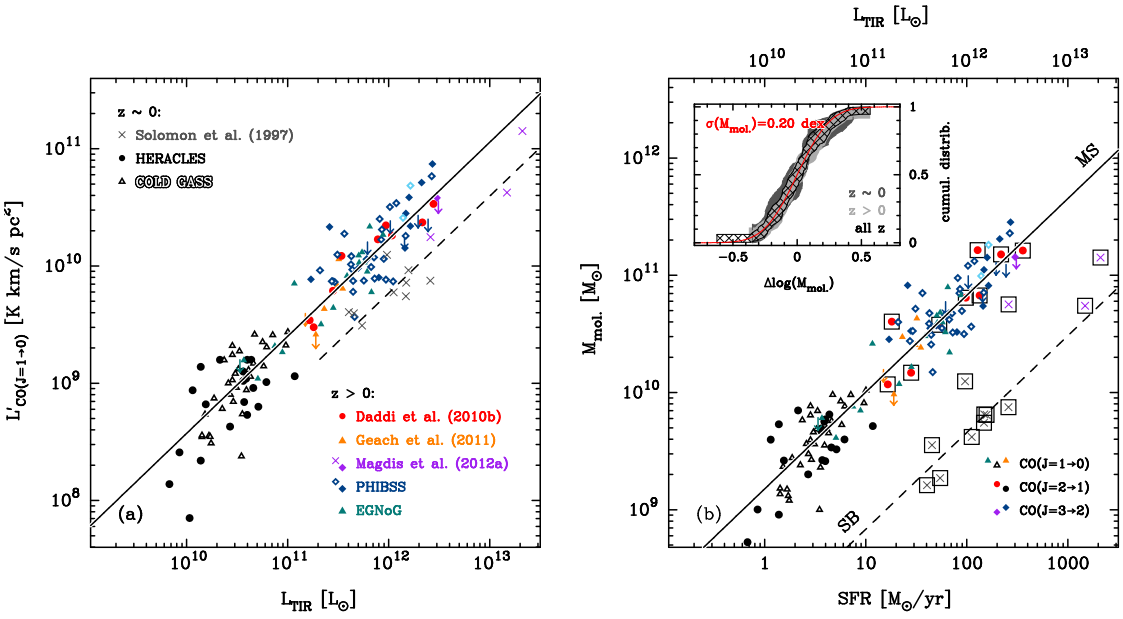

Figure 1.7: Left: CO[1-0] luminosity as a function of infrared luminosity for field galaxies at 0<z<4. Right: Molecular gas mass against star-formation rate, derived from the left panel. This is the integrated Kennicutt-Schmidt law (Kennicutt, 1998b). Both figures are from Sargent et al. (2014). In both panels, the locus on which MS galaxies lie is shown by the solid line. Starburst galaxies lie along the dashed lines, at higher SFE.

population, in the left panel of Fig. 1.7. When we take into account the different molecular gas conversion factors, the distinction between the two populations further increases in the right panel. Contrary to the secular MS, starburst galaxies are undergoing a 'burst' of violent star-formation, which will be shorter-lived than the star-formation occurring on the MS, as the gas will be converted into stars and consumed more efficiently. For this reason, starburst galaxies elevated significantly above the MS have lower molecular gas fractions than their stellar mass-matched MS counterparts (although note the dependence on the ISM conversion factor). This is in contrast to the steady increase in molecular gas fraction that drives higher sSFRs within the scatter of the MS (Tacconi et al., 2013, 2018; Sargent et al., 2014; Saintonge et al., 2016; Schinnerer et al., 2016; Elbaz et al., 2018; Freundlich et al., 2019). It's also interesting to note from the KS plane that the trend for SFR with M_{mol} is supra-linear (e.g Schmidt 1959; Kennicutt 1998b; Bouché et al. 2007; Krumholz & McKee 2005; Genzel et al. 2010; Narayanan et al. 2011; Saintonge et al. 2012; Sargent et al. 2014), indicating an increase in SFE as we move to higher SFRs (and thus higher average redshifts). I discuss the impact of environment and of low gas-phase metallicity on the position of galaxies in the KS plane in Chapters 4 and 5 respectively.

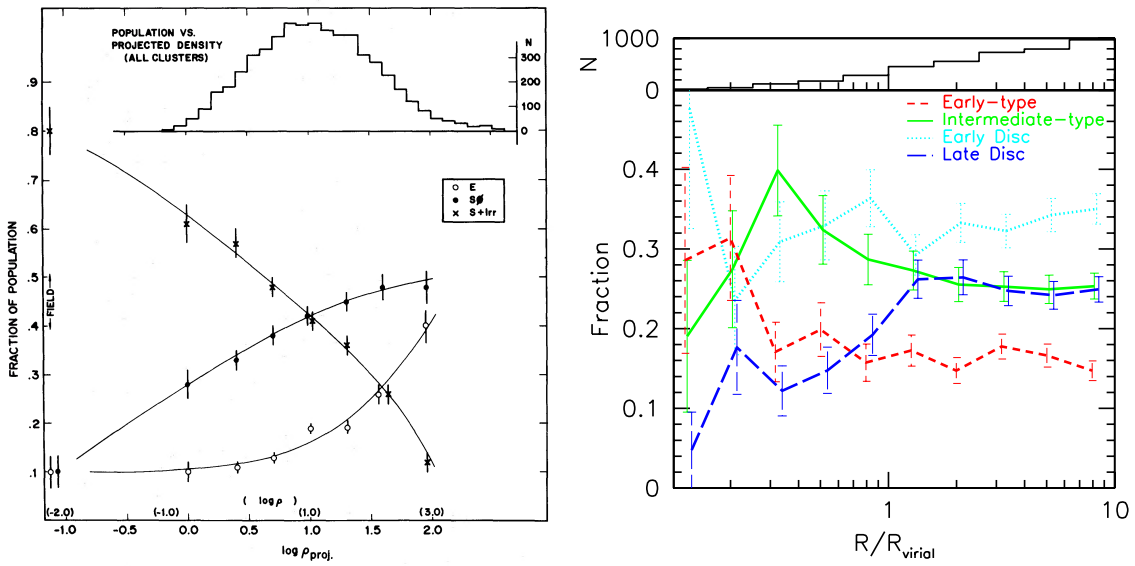

Figure 1.8: Left: The morphology-density relation in the local Universe (Dressler, 1980), showing how the fraction of the population with a given galaxy morphology changes as a function of projected density on the sky. Right: Galaxy morphology vs. cluster-centric radius to the nearest cluster, for galaxies in the Sloan Digital Sky Survey (Goto et al., 2003). In both panels, the upper histograms show the number of galaxies in each bin of cluster-centric radius.

1.4 The environmental impact on galaxy evolution

1.4.1 Galaxy evolution in overdense regions at z∼0

A key theme in this thesis is to explore the impact that a galaxy's environment has on its evolution. This is studied particularly with respect to changes in the ISM and molecular gas content, star-formation rates, and potential deviations from the global KS law. The environmental impact on galaxy evolution has been clearly motivated for a number of decades, inspired by early studies in the local Universe. Shown in the left panel of Fig. 1.8, Dressler (1980) documented what is known as the 'Morphology-Density' relation. By examining the morphological type of galaxies as a function of local density, it can be clearly seen in the local Universe that spheroid-dominated galaxies reside in the regions with the highest projected densities, such as the cores of galaxy clusters. Conversely, the fraction of disk-like galaxies drops off steeply in these environments, whereas they become more prevalent in low-density environments. In the right panel of Fig. 1.8, a more recent study by Goto et al. (2003) classified the galaxy type/morphology of Sloan Digital Sky Survey (SDSS) galaxies as a function of distance to the nearest cluster center. We should note that the quantification of 'environment' in the left and right panels is different - i.e. projected density vs. distance to a cluster, respectively. When we focus on galaxies at small $RR_{\rm virial}$, we see in the right panel of Fig. 1.8 that ETGs are significantly more prevalent than late-type disk galaxies, in the centers of

clusters. The early-type galaxies that dominate the cores of local clusters are massive, red, passive galaxies that have ceased their star-formation, having already built up a considerable stellar mass (10^{10}-10^{12}M$_{\odot}$, e.g. Padmanabhan et al. 2004; Collins et al. 2009; Hatch et al. 2009; Deason et al. 2012; Lin et al. 2013; Inagaki et al. 2015; Bellstedt et al. 2016; Ragone-Figueroa et al. 2018). The fraction of early-type galaxies in Fig. 1.8 then drops significantly as clustercentric radius increases, below the increasing fraction of late-type disks. In this way, observations in the local Universe have provided clear evidence of a link between local environment and the evolutionary history, and/or formation mechanism, of a galaxy.

These observations raise a number of questions. Does the dense, cluster environment accelerate the evolution of a galaxy? Is the quenching of these cluster galaxies related to their ISM content? At what redshifts are these environmental effects observable? In order to answer these questions, we must study cluster galaxies whilst they are in the process of actively evolving within dense environments, before they become quenched. We therefore need to observe clusters outside of the local Universe, at the epoch of active stellar mass build-up within the cluster galaxies (e.g. Butcher & Oemler 1984; Gladders & Yee 2005; Thomas et al. 2005; Hayashi et al. 2010; Alberts et al. 2016; Hayashi et al. 2016; Aravena et al. 2012; Santos et al. 2015a; Webb et al. 2015a; Wang et al. 2016; Stach et al. 2017; Coogan et al. 2018; Miller et al. 2018; Smith et al. 2019, discussed further in Chapter 4). In these high-redshift structures, there is evidence to suggest that the SFR-density relation observed in the local Universe (i.e. a suppression of star-formation in dense regions) no longer holds. In fact, a reversal in this relation has been observed, such that at z$\gtrsim$1 the average SFRs of galaxies increases with increasing local galaxy density (e.g. Elbaz et al. 2007; Cooper et al. 2008; Tran et al. 2010; Tonnesen & Cen 2014; Santos et al. 2015b; Strazzullo et al. 2018, although see e.g. Quadri et al. 2012; Ziparo et al. 2014 for alternative discussions). One such cluster that is a perfect candidate for environmental studies is Cl J1449+0856, a high-redshift cluster that has 'matured' by z=1.99. Cl J1449+0856 is the focus of Chapters 2 to 5, and is introduced in detail in Chapter 2.

1.4.2 High-redshift galaxy clusters

Although high-redshift galaxy clusters are highly informative for the study of the environmental effect on galaxy evolution, they are also rather rare objects. The build-up of structure in the Universe, for both clusters and galaxies themselves, is hierarchical (e.g. Kauffmann et al. 1993, 1999; Lacey & Cole 1993; Baugh et al. 1996; Springel et al. 2005a; Gonzalez-Perez et al. 2011; De Lucia et al. 2012; Somerville et al. 2012; Jiang et al. 2015). As clusters are the most massive, gravitationally bound structures in the Universe ($\gtrsim 10^{14}$M$_{\odot}$), it naturally follows that the assembly

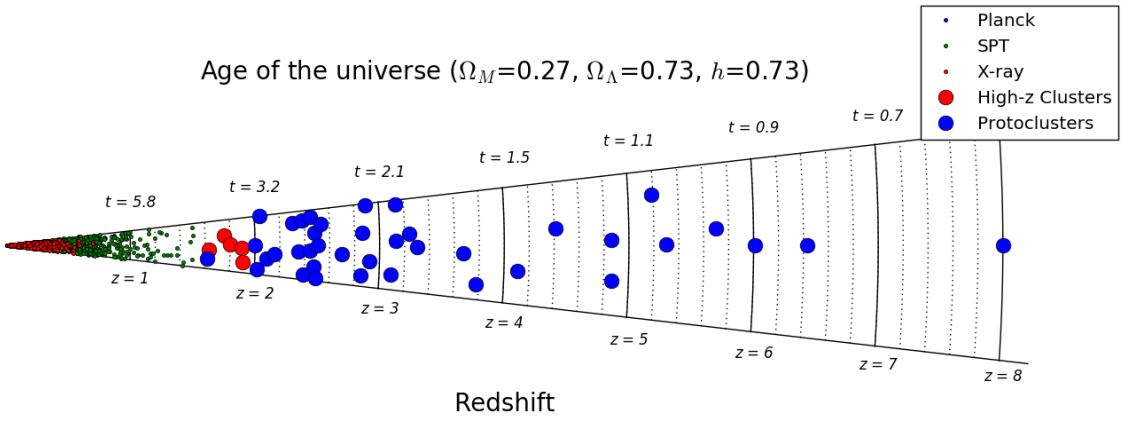

Figure 1.9: A summary of cluster and protocluster detections as a function of redshift (Overzier, 2016). High-z clusters (large red circles) are shown at z>1.6. The number of established clusters falls quickly above z∼2, giving way to protoclusters. The local clusters (small circles) were detected either in SZ surveys (by Planck or the South Pole Telescope, SPT), or through X-ray emission, as indicated. The age of the Universe in Gyrs is given on the top axis.

and virialisation of clusters occur at relatively late cosmic times. However, there are many observational efforts currently searching for these structures at high redshift (e.g. Oke et al. 1998; Kurk et al. 2000; Eisenhardt et al. 2008; Hatch et al. 2011; Castignani et al. 2014; Clements et al. 2014; Casey et al. 2015; Flores-Cacho et al. 2016; Cai et al. 2017; Noirot et al. 2018). Although I focus on galaxy evolution in this thesis, characterising the cluster population has additional important applications. In particular, we can further our constraints on the cosmology of the Universe through the identification of clusters, by comparing observations of the cluster mass function in several redshift bins with expectations from simulations using different cosmological parameters (e.g. Borgani et al. 1999; Allen et al. 2002; Battye & Weller 2003; Voit 2005; Allen et al. 2011; Planck Collaboration et al. 2014; Mantz et al. 2016). However, here I focus on the impact of galaxy clusters on the evolution of their members.

The distinction between clusters and protoclusters at high redshift is often a point of debate. As the name suggests, a protocluster is a galaxy cluster in its early stages of formation, and an important distinction between these structures is whether or not the system has yet become virialised. When a protocluster reaches a critical density, it breaks away from the Hubble flow of expansion and undergoes gravitational collapse (Lynden-Bell, 1967; Rees & Ostriker, 1977; Farouki et al., 1983; Levin et al., 2008; Mo et al., 2010). During this process, both the dark matter and baryonic components of the protocluster collapse, liberating gravitational potential energy and invoking energetic shocks in the intracluster medium (ICM) as layers of the ICM collide with one another. This energy release results in a significant heating of the ICM (to $\sim 10^6$ K), and subsequent

cooling via X-ray emission. At this point, we refer to the protocluster as a mature cluster, where the presence of a dense, hot ICM is likely to have an effect on the evolution of galaxies both already in the cluster, and on those that are accreted in the future. Galaxy evolution in both protoclusters and clusters are interesting areas of study, but it is the presence of a particularly dense, virialised environment, along with the dominance of ETGs in cluster cores, that motivates research into the quenching of galaxies in clusters.

There are several methods that can be employed to find high-redshift galaxy clusters. Above z>1, the most successful methods include identifying galaxy overdensities themselves, particularly red, quiescent galaxies (Kodama & Arimoto, 1997; Gladders et al., 1998; Kajisawa et al., 2000; Andreon et al., 2008; Lidman et al., 2008; Mei et al., 2009; Rudnick et al., 2012; Snyder et al., 2012a; Strazzullo et al., 2016). We can also search for tracers of the hot ICM, through thermal bremsstrahlung X-ray radiation from energetic electrons (Truemper, 1993; Böhringer et al., 2000, 2007; Rosati et al., 2002; Allen et al., 2004; Borgani et al., 2004; Voit, 2005; Pillepich et al., 2012; Clerc et al., 2014; Xu et al., 2018), or Sunyaev-Zel'dovich (SZ) distortion of the cosmic microwave background (Dicke et al. 1965; Sunyaev & Zeldovich 1980; Itoh et al. 1998; Motl et al. 2005; Reese et al. 2010; Kay et al. 2012; Adam et al. 2017; Mroczkowski et al. 2019; Capasso et al. 2019; Hurier et al. 2019; Gobat et al. 2019). The highest-redshift cluster discovered to date is Cl J1000+0220, at z=2.51 (Wang et al., 2016), selected as an overdensity of distant red galaxies. Similarly to Cl J1449+0856, this cluster displays signatures of X-ray emission from the hot ICM, confirming the maturity of this cluster. Cl J1000+0220 and Cl J1449+0856 are however at different evolutionary stages. Observed at an earlier time, the core of Cl J1000+0220 is dominated by highly star-forming galaxies, with very few galaxies having yet succumbed to the environment and begun quenching. Aside from Cl J1000+0220 and Cl J1449+0856, the high-redshift cluster population is relatively sparse until z<2, where the majority of environmental studies on galaxy evolution begin. Fig. 1.9 shows a summary of cluster and protocluster detections compiled from the literature (Overzier, 2016), and highlights the lack of established clusters at high redshift. An interesting observation is that both Cl J1449+0856 and Cl J1000+0220 are shown as protoclusters in Fig. 1.9. This arises from the different definitions of 'cluster' that are used across the literature. In Fig. 1.9, the author makes the division that clusters are both virialised and *already* have a total mass $M>10^{14}M_{\odot}$. This reinforces the rarity of detecting structures such as Cl J1449+0856 and Cl J1000+0220, which have become virialised at such early cosmic times (see Chapter 2).

I discuss Cl J1449+0856 in more detail in Chapter 2, and highlight some of the most interesting features for the study of the environmental effect on galaxy evolution. Galaxy evolution in clusters is a vast field, so in Chapter 4 we focus on the environmental effect on the interstellar medium of

galaxies - the gas and dust content, and the accompanying star-formation. In particular, we focus not on galaxies being accreted onto the edges of established clusters (leading to effects such as RAM-pressure stripping, starvation etc. Moore et al. 1996; Abadi et al. 1999; Quilis et al. 2000; Vollmer et al. 2001; Boselli & Gavazzi 2006; McGee et al. 2014; Marasco et al. 2016; Poggianti et al. 2017; Davies et al. 2019), but on galaxies that are actively evolving in the core regions of clusters.

1.5 Observations in the submillimetre-radio regime through interferometry

I will finish by broadly introducing the type of telescopes used to make the submillimeter-radio observations used in this thesis. As discussed in Sections 1.2.2 and 1.3.1, tracing obscured star-formation and the content of the ISM are both performed at long wavelengths, in the submillimeter-radio regime. However, one of the limitations that is encountered in low-frequency astronomy, particularly when observing high-redshift sources, is the poor angular resolution of single-dish telescopes compared to observations at shorter wavelengths. The relation that defines the diffraction-limited angular resolution of a circular aperture is:

$$\theta \propto \frac{\lambda}{D}. \tag{1.3}$$

Here θ is the angular resolution in radians (the smallest resolvable scale), λ is the wavelength and D is the diameter of the telescope aperture. Therefore, when λ is very large, the smallest resolvable angular scale is also very large. As an example, if we want to individually observe galaxies in a cluster at z$\sim$2, we need to be able to resolve scales of $\sim$0.5-1", in order to distinguish galaxies from one another in this crowded region. For a single-dish submillimeter-radio telescope, this would require an aperture of $>$200-400 m, to measure the thermal dust emission at $\sim$870 μm in individual galaxies. Building telescopes this size becomes an unfeasible engineering task, particularly when you consider the need to move and steer the aperture to the desired target. Currently, the largest fully-steerable radio telescope ever constructed is the Green Bank Telescope at 100 m in diameter, although there are a number of fixed-aperture radio telescopes that have superseded this in size.

In order to gain higher angular resolution than is possible with single-dish telescopes, the submillimeter-radio community has turned to interferometry, a technique first invented by Albert A. Michelson. An astronomical interferometer is a collection of single-dish apertures that observe a source simultaneously, and by doing so, can be treated as a single telescope. When operated in this way, the signals from each separate aperture need to be combined, or 'correlated' with one

another, so that the effective aperture of the interferometer is the distance between the apertures, rather than the individual aperture diameters. Combining signals from different apertures in this way is referred to as 'aperture synthesis'. The distance between each pair of apertures in an interferometer is known as a 'baseline', which corresponds to a certain angular scale on the sky according to equation 1.3. The cross-correlation of each aperture with every other aperture in the array allows for a number of different angular scales to be simultaneously sampled. The observed telescope response of each baseline is then a function of the integral of the intensity of the target source. In order to recover the intensity distribution on the sky, we must perform an inverse Fourier transform on the telescope response. For this reason, we refer to the raw telescope response as 'visibility data', expressed in terms of coordinates (u, v), measured in wavelength units. A discrete Fourier transform of these visibilities brings us to the celestial plane, expressed in coordinates (x, y) (Wilson et al., 2009a).

However, the incomplete sampling of the (u, v)-plane (hereafter uv-plane), due to the finite number and orientation of aperture pairs (baselines), gives rise to unwanted effects in interferometric data. The untreated image that is produced from the inverse Fourier transform of these data is called the 'dirty' image. This refers to the fact that the dirty image is a convolution of the raw visibility data with the 'dirty beam' - the finite uv-sampling of the total telescope array. The dirty image thus assumes that the response of the interferometer is zero where a baseline does not exist in the uv-plane. In order to minimise the effect of incomplete sampling in interferometers, several deconvolution methods have been proposed to remove the effects/artefacts of the dirty beam. One of the most commonly used deconvolution techniques is called `CLEAN`, which takes an iterative approach to modelling the sky intensity as a sum of point sources. `CLEAN` starts from the dirty image and attempts to deconvolve the dirty beam by instead convolving pure point sources in the intensity distribution with a 'clean', or 'synthesised' beam. This synthesised beam corresponds to the Gaussian core of the dirty beam, without the inclusion of the sidelobes (Högbom, 1974). However, in order to avoid model-dependent artefacts introduced by the choice of deconvolution method, we do not focus on deconvolution techniques in Chapters 2 to 5, and instead perform our analysis primarily in the uv-plane, as described. Deconvolution in the image plane is, on the other hand, considered for our simulated interferometric images, created in Chapter 6.

1.5.1 Current and future interferometers

Two of the most sensitive submillimeter-radio interferometers currently in operation are the Karl G. Jansky Very Large Array (Thompson et al., 1980; Perley et al., 2009), and the Atacama Millimeter/submillimeter Array (Wootten & Thompson, 2009). The VLA is an array of 27 dishes,

each with a diameter of 25 m. It covers a relatively low frequency of ∼70 MHz to 50 GHz, making it an ideal instrument for the measurement of synchrotron and free-free radiation from galaxies at z∼2, as well as the low quantum state spectral transitions of CO at these redshifts. On the other hand, ALMA operates at higher frequencies between ∼100-900 GHz, which is particularly well-suited for the observation of thermal dust emission in the RJ tail of a galaxy's SED, in addition to higher-order transitions of CO. Unlike the VLA, ALMA hosts two different types of dish - a collection of approximately fifty 12 m telescopes covering long baselines (up to several kilometers), as well as a compact array of twelve 7 m dishes. This compact array, known as the Atacama Compact Array (ACA), can be used for observing large angular scales on the sky, such as large-scale diffuse emission. It is therefore a powerful tool for the study of diffuse emission from the hot ICM of high-redshift clusters such as Cl J1449+0856, demonstrated by the detection of SZ emission by Gobat et al. (2019, see Section 2.2).

Looking towards the future of astronomical interferometers, Chapter 6 focuses on observations that will be made by the Square Kilometer Array (SKA[2], Blake et al. 2004; Jarvis & Rawlings 2004; Huynh & Lazio 2013; Braun et al. 2015). The SKA observatory is a project planned for construction over both Australia and South Africa, and will be the largest radio observatory in existence, both in terms of the number of dishes/antennae and the total collecting area. The SKA will contain a variety of different apertures, from low- and mid-frequency aperture arrays to mid-frequency dishes similar to those used by ALMA and the VLA. We focus in Chapter 6 on 'phase 1' of the SKA mid-frequency array (SKA1-MID), which will contain ∼200 dishes covering a frequency range ∼350 MHz to 14 GHz. Both the survey speed and the angular resolution of SKA1-MID (reaching a maximum baseline of 150 km) will be unprecedented by current instruments, and will enable a wide range of science goals to be explored. We focus in Chapter 6 on the use of the SKA to measure continuum fluxes and morphologically classify the star-forming regions within galaxies from $0<z<3$.

1.6 Simulations of galaxy evolution

To finish this chapter, I will briefly introduce the types of simulation that are currently used to study galaxy evolution. Although this thesis focuses on the observational side of galaxy evolution, simulations are a highly complementary tool alongside observational studies. One of the advantages of galaxy simulations is the ability to test physics that may have been inferred from observations. As an example, one of the areas of galaxy evolution that is currently proving most difficult to decipher is the influence of AGN feedback on galaxies. As mentioned in Section 1.2.1, we have

[2]https://www.skatelescope.org

observationally inferred a widespread link between AGN activity and star-formation. This is a complex topic, but one of the places where AGN feedback is thought to play a significant role is at the high-mass end of the galaxy stellar mass function. It is expected that without AGN disrupting star-formation through feedback mechanisms, many more galaxies would create more stellar mass than is observed (see e.g. Silk & Mamon (2012) for a review, and e.g. Kauffmann & Haehnelt 2000; Di Matteo et al. 2005; Hopkins et al. 2005; Somerville et al. 2008; Thacker et al. 2014; Gutcke et al. 2015; Volonteri et al. 2015; McAlpine et al. 2017 for simulations investigating the AGN-SFR connection). Modelling the correct amount (and triggering mechanism) of AGN feedback required in order to reproduce observed galaxy stellar mass functions is a current challenge, but it demonstrates one of the areas of galaxy evolution that can be probed through the combination of simulations and observations. One of the other primary uses of galaxy simulations is to make predictions about galaxy populations that we cannot easily observe, for example at very high redshift (e.g. Salvaterra et al. 2011; Bauer et al. 2015; Waters et al. 2016; Liu et al. 2017; Bhowmick et al. 2018).

There are two primary types of simulation: (i) semi-analytic models (SAMs, e.g. GALFORM (Cole et al., 2000; Lacey et al., 2016), the Munich semi-analytic model (Henriques et al., 2015)), and (ii) hydrodynamical simulations (e.g. Illustris (Vogelsberger et al., 2014), EAGLE (Schaye et al., 2015), BlueTides (Feng et al., 2016)). SAMs attempt to model the many physical processes associated with galaxy evolution using approximate, analytic techniques. They model the Universe across redshift space by tracing only the dark matter content, and then populate the simulation with baryons after the dark matter merger trees have already been created. The properties of galaxies will then be decided according to the 'sub-grid physics' applied to the baryons. The advantage of this approach is that it is much less computationally expensive than simulating the full baryon physics at all times, and the SAMs can be quickly re-run with different sub-grid physics to make comparisons between the applied analytic descriptions. On the other hand, hydrodynamical simulations model the full physics of dark matter plus baryons throughout the simulation, down to a certain resolution. This allows for potentially more realistic outputs, but is considerably more computationally expensive, and hydrodynamical simulations are therefore more volume-limited than SAMs. Due to the limited box size of these simulations, large-scale environments such as galaxy clusters are often unprobed, particularly in statistical numbers. However, projects such as the hydrodynamical Cluster-EAGLE simulation (Barnes et al., 2017) have recently started to advance this field (see also Pike et al. 2014; Rasia et al. 2015; Hahn et al. 2017; Le Brun et al. 2018 for examples of simulations of galaxy clusters).

1.7 Summary

In this chapter, I introduced the study of galaxies and galaxy evolution. I discussed the observational tracers of star-formation and the interstellar medium of galaxies, and outlined the key relationships (the Main Sequence of star-formation and the Kennicutt-Schmidt law) that are followed by the majority of star-forming galaxies. I then introduced the concept of astronomical interferometry, and finished the chapter by summarising some of the existing galaxy evolution simulations. The structure of the rest of this thesis is as follows. In Chapter 2, I introduce a mature galaxy cluster at z=1.99, Cl J1449+0856, whose galaxy population forms the basis of Chapters 3, 4 and 5. In Chapter 6, I introduce my current work simulating radio continuum observations from the SKA, which is an ideal instrument to identify larger numbers of such high-redshift star-forming overdensities.

I summarise the main findings of the thesis and outline future work in Chapter 7. The appendicies (A, B, C and D) and a publications list can be found following the bibliography.

Chapter 2

Cl J1449+0856: A mature cluster in the early Universe

2.1 A brief history of Cl J1449+0856

In this chapter I introduce Cl J1449+0856, an X-ray detected galaxy cluster at z=1.99 - one of the highest redshift mature clusters discovered to date, with the mass of a typical Coma-like progenitor (Gobat et al., 2011). Cl J1449+0856 was first discovered almost a decade ago, having been detected as a significant (20σ) overdensity of red galaxies at z>1.5, as seen in Fig. 2.1. What was truly remarkable about this discovery was the presence of diffuse X-ray emission at the core of the overdensity - indicating that the cluster has already become virialised at this early time (see Section 1.4.2). Given the unprecedented redshift for a mature cluster at the time of discovery, spectroscopic follow-up using HST grism spectroscopy was awarded for Cl J1449+0856 shortly afterwards, confirming several tens of cluster member galaxies at z$\sim$2 (Gobat et al., 2013). Detailed study of the cluster member galaxies, through SED fitting and morphological analysis (Strazzullo et al., 2013) then revealed one of the most exciting properties of Cl J1449+0856 - its diverse member population. As discussed in Section 1.4.1, the cores of mature clusters are usually dominated by massive, passive galaxies, that have undergone significant quenching since their active star-formation in earlier evolutionary stages. However, the galaxy population in the core of Cl J1449+0856 contains massive red, quenched galaxies *alongside* actively star-forming galaxies, some of which are at relatively low stellar mass (Strazzullo et al., 2013; Valentino et al., 2015). This suggests that the core of Cl J1449+0856 is in an important stage of evolution, where its members are transitioning from star-forming to passive. For those of us who wish to study the environmental impact on galaxy evolution, this is a unique opportunity to observe the ISM of the star-forming galaxies in the dense cluster core.

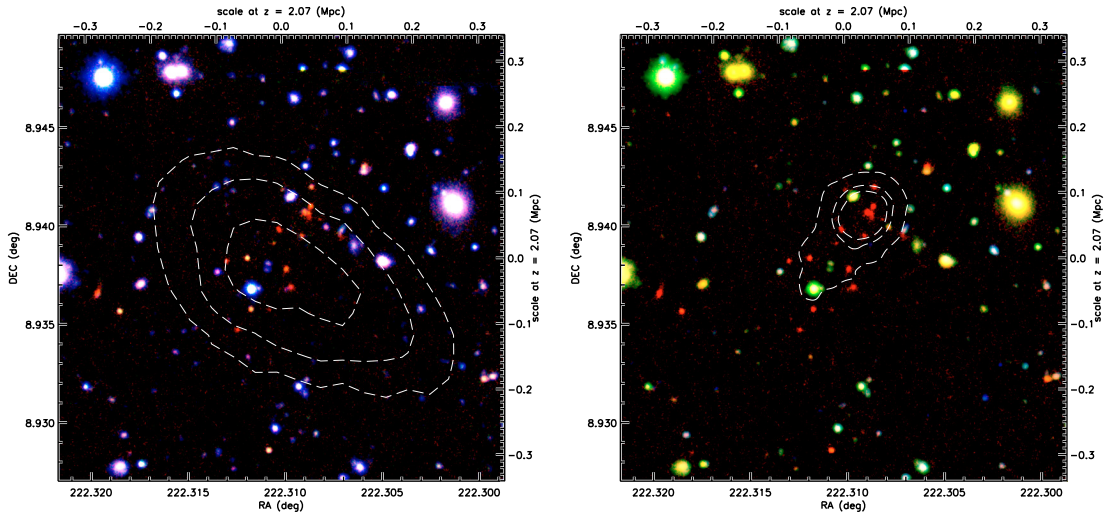

Figure 2.1: Left: K-J-z colour image of Cl J1449+0856, highlighting a very red population in the cluster core, alongside galaxies of varying colour and morphology. The white contours show the extended X-ray emission detected by XMM-Newton, indicating that the structure already has a hot intracluster medium. The contours are displayed at 1, 2 and 3σ. Right: K-B-z image of Cl J1449+0856. The contours indicate the significance of the cluster as a galaxy overdensity on the sky. The 10, 20 and 30σ contours are shown. The overdensity is defined relative to the field number density of galaxies. Both panels are taken from Gobat et al. (2011).

Since this time, a number of intriguing discoveries about Cl J1449+0856 have been made. The star-forming population in Cl J1449+0856 consists of both dusty star-forming galaxies and much bluer, lower mass galaxies. Measurement of the gas-phase metallicities of these blue galaxies by Valentino et al. (2015) led to the suggestion that the ISM in cluster galaxies may be diluted by the accretion of pristine gas onto the cluster halo. This work also directly paved the way for our study on gas-phase metallicity at high-redshift, presented in Chapter 5. Valentino et al. (2016) then went on to discover a 'giant' (>100 kpc), ionised Ly-α-emitting nebula in the core of Cl J1449+0856, potentially being replenished at a rate of $\sim$1000 $M_{\odot}$/year. This Ly-α emission gives direct evidence for energy injection into the ICM, by the two X-ray detected AGN present in the cluster core.

More recently, Smith et al. (2019) have used SCUBA-2 and Herschel submillimeter data to study the star-formation density in Cl J1449+0856. As the angular resolution of these data are not sufficient to spatially resolve the cluster members, Smith et al. (2019) use the work presented in Strazzullo et al. (2018, Chapter 3) and Coogan et al. (2018, Chapter 4), as prior information to be fed into a Bayesian inference framework. This work confirmed the high star-formation rate density found by Strazzullo et al. (2018), and the reversal in the SFR-density relation that has been suggested to occur at z>1 (e.g. Elbaz et al. 2007). In order to further explore the obscured

Publication	Topic	Location in Thesis	Primary Data
Gobat et al. (2019)	SZ emission from Cl J1449+0856	Section 2.2	ALMA 2012.1.00885 ALMA 2015.1.01335 ALMA/ACA 2016.1.01107
Strazzullo et al. (2018)	Star-formation density in the core & the BCG	Chapter 3	ALMA 2012.1.00885 ALMA 2015.1.01335 HST GO-11648 HST GO-12991
Coogan et al. (2018)	Molecular gas & dust in cluster galaxies	Chapter 4	ALMA 2012.1.00885 ALMA 2015.1.01335 VLA 12A-118
Coogan et al. (2019)	ISM content of low-metallicity cluster members	Chapter 5	ALMA 2012.1.00885 ALMA 2015.1.01335 VLA 12A-118 Subaru/MOIRCS

Table 2.1: Summary of publications on galaxy cluster Cl J1449+0856 that are included in this thesis, and their main theme. BCG here indicates the Brightest Cluster Galaxy. A comparison of the primary datasets used for each study is also shown.

star-formation in Cl J1449+0856, I present the work of Strazzullo et al. (2018) in Chapter 3.

In Table 2.1, I give an outline of the publications on Cl J1449+0856 that contribute towards this thesis, in terms of the section/chapter they correspond to, as well as the primary datasets used. In Section 2.2, I summarise the study of Gobat et al. (2019), who went in search of evidence of an SZ decrement from the cluster core (see also Section 1.4.2). Chapter 3 discusses the star-formation density in the core of Cl J1449+0856, the colour distribution of cluster members compared with the field at z=2, and gives a comparison between the optical- and submillimeter-detected members. In Chapter 4, I present a detailed study of the interstellar medium (molecular gas and dust) as well as star-formation activity in the cluster galaxies at z=2, in order to assess the environmental effect on the galaxies' ISM content. Thanks to the diverse range of galaxies residing in Cl J1449+0856, and the rich observational datasets available to us, we have also detected a population of low gas-phase metallicity galaxies in Cl J1449+0856. I therefore present work investigating the effect of low gas-phase metallicity on the ISM at z=2 - a currently sparsely-sampled regime - in Chapter 5. Table 2.2 gives a reference summary of all of the galaxies discussed in these chapters.

ID	Chapter(s)	Member	Submm. Line	Submm. Cont.	Description
H4	3	Yes	No	No	Interacting, passive
H5	3	Yes	No	No	Interacting, passive
H8	3	Yes	No	No	Passive
H9	3	Yes	No	No	Passive
H11	3	Yes	No	No	Passive
H12	3	Yes	No	No	Star-forming
A1	3, 4	Yes	Yes	Yes	Merger
A2	3, 4	Yes	Yes	Yes	Merger
13/H13	3, 4	Yes	Yes	Yes	AGN
A6/H6/6	3, 4	Yes	Yes	Yes	Prominent bulge
N7/HN7	3, 4	Yes	Yes	Yes	Interacting
B1/H1	3, 4	Yes	Yes	Yes	Merger
3/H3	3, 4	Yes	Yes	No	Passive
S7/HS7	3, 4	Yes	Tentative	No	AGN, interacting
2/H2	3, 4	Yes	No	Yes	Bulge, passive
A3	3	No	N/A	Yes	z=1.3
A4	3, 4	Undetermined	No	Yes	Bright continuum
A5/H10	3, 4	Undetermined	No	Yes	Bright continuum
V568	5	Yes	No	No	Low metallicity
V580	5	Yes	No	No	Low metallicity
V422	5	Yes	No	No	Low metallicity
V510	5	Yes	No	No	Low metallicity
V105	5	Yes	No	No	Low metallicity

Table 2.2: Summary of galaxies discussed in Chapters 3 to 5. Multiple IDs for a single galaxy arise from different naming conventions. We indicate whether or not the galaxy is a member of Cl J1449+0856, and whether we have a detection of a submillimeter spectral line at the cluster redshift, as well as continuum emission, respectively. The redshifts of cluster members in which no submillimeter lines are detected were spectroscopically determined using rest-frame optical spectroscopy (Gobat et al., 2013). 'Passive' and 'star-forming' labels are according to colour-colour criterion in Strazzullo et al. (2016).

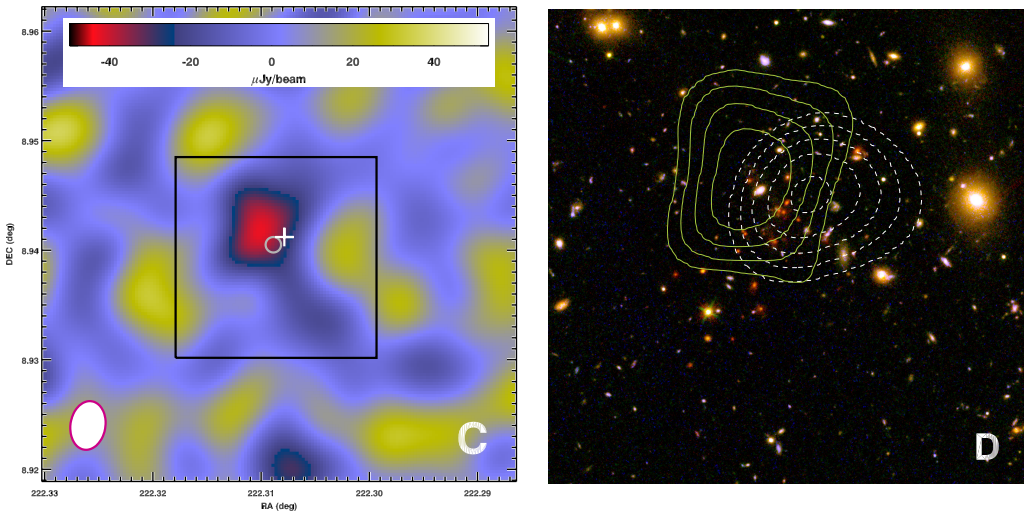

Figure 2.2: Left: combined ALMA-ACA continuum map at 92 GHz, showing the detected SZ decrement. The galaxies in the field of view have been modelled and subtracted from this image, in order to uncover the SZ decrement. The cross and the circle represent the center of X-ray emission and the Brightest Cluster Galaxy complex (see Section 3.5), respectively. The magenta filled ellipse is the average of the ALMA and ACA synthesised beams, and the black square shows the field of view of the right panel. Right: optical colour (F105W, F140W, F160W) HST image of the cluster, overlaid with white dashed Chandra X-ray contours, and solid yellow contours of the SZ decrement. Both panels are taken from Gobat et al. (2019).

2.2 Sunyaev-Zel'dovich detection of the galaxy cluster Cl J1449+0856 at z = 1.99: the pressure profile in uv-space

Recently, Gobat et al. (2019) found a significant (5σ), diffuse SZ detection from Cl J1449+0856. This is the lowest mass single SZ detection to date, and is shown in Fig. 2.2. In order to carry out this study, observations were made at 92 GHz using both ALMA and the ACA (see Section 1.5.1). As the synthesised beam of the ALMA data was 4.2" $\times$ 3.6", compared with the 16.9" $\times$ 13.0" beam of the ACA, we were able to capture both the continuum emission at 92 GHz from individual galaxies (using ALMA), as well as the large-scale structure at this frequency (using ACA). We emphasise that at 92 GHz we expect the SZ signature, arising from a shift in the CMB spectrum due to inverse Compton scattering with ICM electrons, to present as a negative flux measurement. For this reason, we refer to detection of an SZ 'decrement'. However, unlike local clusters, there is also a significant amount of positive 92 GHz continuum present in the core of Cl J1449+0856, arising from galaxy dust emission. In order to detect the diffuse SZ decrement in the cluster, it was therefore necessary to first remove the positive emission originating from the galaxies - without

disrupting the SZ signal itself. To do this, I measured the 92 GHz emission from all galaxies in the cluster field of view, using the high-resolution ALMA data. Here, the cluster members could be spatially distinguished at their known positions (Coogan et al. 2018, Chapter 4). This measured flux could then be subtracted at fixed position in the low-resolution ACA data, where the beam is too large to identify individual galaxies. Having removed all of the galaxy emission, the ALMA and ACA data were combined, enabling us to uncover the extended SZ decrement shown in the left panel of Fig. 2.2. Not only does this detection of the SZ effect give further evidence to support the fact that Cl J1449+0856 is a mature cluster, but the pressure profile of the SZ decrement as a function of spatial scale also gives constraints on both the physics of the ICM and the cluster halo mass. The total mass recovered from the pressure profile of Cl J1449+0856 was found to be consistent with the mass derived from X-ray observations (Gobat et al., 2011; Valentino et al., 2016, $\sim 6 \times 10^{13} M_{\odot}$).

Contribution

For the Gobat et al. (2019) Cl J1449+0856 Sunyaev Zel'Dovich study discussed in Section 2.2, I performed the modelling and removal of galaxy emission in the cluster field of view, in both the ACA and ALMA 92 GHz data. This was in part based on the galaxy positional and flux priors that I obtained when carrying out the work presented in Chapter 4. As described in Section 2.2 and Gobat et al. (2019), it was from these galaxy-free residual datasets that the SZ measurement was made. I also performed the initial SZ flux extraction in the uv-plane for this study, and provided feedback and discussion for the finalisation of the paper.

Chapter 3

Deciphering the Activity and Quiescence of High-redshift Cluster Environments: ALMA Observations of Cl J1449+0856 at z = 2

This chapter was published in Strazzullo et al. (2018), Astrophysical Journal, Volume 862, Issue 1, pages 64-75.

Co-authors of Strazzullo et al. (2018) are: R.T. Coogan, E. Daddi, M. Sargent, R. Gobat, F. Valentino, M. Béthermin, M. Pannella, M. Dickinson, A. Renzini, N. Arimoto, A. Cimatti, H. Dannerbauer, A. Finoguenov, D. Liu and M. Onodera. Small modifications have been made to the text for clarity in the context of this thesis.

Abstract

We present ALMA observations of the 870μm continuum and CO[4-3] line emission in the core of the galaxy cluster Cl J1449+0856 at $z = 2$, a NIR-selected, X-ray detected system in the mass range of typical progenitors of today's massive clusters. The 870μm map reveals six $F_{870\mu m} > 0.5$ mJy sources spread over an area of 0.07arcmin^2, giving an overdensity of a factor ~ 10 (6) with respect to blank field counts down to $F_{870\mu m} > 1$ mJy (> 0.5 mJy). On the other hand, deep CO[4-3] follow-up confirms membership of three of these sources, but suggests that the remaining three, including the brightest 870μm sources in the field ($F_{870\mu m} \gtrsim 2$ mJy), are likely interlopers. The measurement of 870μm continuum and CO[4-3] line fluxes at the positions of previously-known cluster members provides a deep probe of dusty star formation occurring in the core of this

high-redshift structure, adding up to a total SFR$\sim$700$\pm$100 $M_{\odot}yr^{-1}$ and yielding an integrated star-formation rate density of $\sim 10^4$ $M_{\odot}yr^{-1}Mpc^{-3}$, five orders of magnitude larger than in the field at the same epoch, due to the concentration of star-forming galaxies in the small volume of the dense cluster core. The combination of these observations with previously available HST imaging highlights the presence of a population of galaxies with already suppressed star-formation in this same volume. This diverse composition of galaxy populations in Cl J1449+0856 is especially highlighted at the very cluster center, where a complex assembly of quiescent and star-forming sources is likely forming the future Brightest Cluster Galaxy.

3.1 Introduction

Thanks to a variety of efforts devoted to the search for distant progenitors of galaxy clusters, pushing towards $z \sim 2$ and beyond (e.g. Rosati et al., 1999; Kurk et al., 2000; Mullis et al., 2005; Stanford et al., 2006; Venemans et al., 2007; Eisenhardt et al., 2008; Wilson et al., 2009b; Andreon et al., 2009; Papovich et al., 2010; Santos et al., 2011; Gobat et al., 2011; Spitler et al., 2012; Stanford et al., 2012; Muzzin et al., 2013; Wylezalek et al., 2013; Clements et al., 2014; Bleem et al., 2015; Strazzullo et al., 2015; Casey et al., 2015; Wang et al., 2016; Flores-Cacho et al., 2016; Daddi et al., 2017; Cai et al., 2017; Mantz et al., 2018), it has been possible in the last decade to significantly extend the timeline and scope of galaxy evolution studies in the densest high-redshift environments. This has eventually bridged the historically divided cluster and protocluster regimes (see recent review by Overzier, 2016), at a cosmic time which is thought - and indeed turns out - to be a transformational epoch for both clusters and their galaxies. The synergy of observations at different wavelengths, including rest-frame optical/NIR to probe stellar populations and galaxy structural properties, mid/far-IR to radio to probe star formation rates, sub-mm for gas reservoirs, as well as X-ray, mid-IR and radio for nuclear activity, has proved fundamental in exploring the many facets of cluster galaxy populations, as discussed below.

From observations of massive cluster galaxies at lower redshifts (e.g. Andreon, 2006; De Propris et al., 2007; Lidman et al., 2008; Mei et al., 2009; Strazzullo et al., 2010; Mancone et al., 2010; Wylezalek et al., 2014), we expect that the epoch around $z \sim 2$ corresponds to the transition from a regime of widespread, high levels of star-formation in dense environments, to the quiescent regime characteristic of cluster cores at $z \lesssim 1$. Direct observations at high redshifts have in fact detected increasing levels of star-formation as well as nuclear and merging activity in distant $z \gtrsim 1.5$ groups and clusters (e.g. Hilton et al., 2010; Hayashi et al., 2010, 2011; Zeimann et al., 2012; Brodwin et al., 2013; Lotz et al., 2013; Dannerbauer et al., 2014; Santos et al., 2015a; Popesso et al., 2015b; Ma et al., 2015; Tran et al., 2015; Wang et al., 2016; Alberts et al., 2016;

Hung et al., 2016; Krishnan et al., 2017; Nantais et al., 2017, and references therein). At the same time, passively evolving galaxies are often found to be over-represented, to different degrees, in the densest regions of these environments (e.g. Steidel et al., 2005; Kurk et al., 2009; Papovich et al., 2010; Gobat et al., 2013; Strazzullo et al., 2013; Tanaka et al., 2013; Snyder et al., 2012b; Spitler et al., 2012; Kubo et al., 2013; Hatch et al., 2016), and examples of (generally massive) clusters with already very strongly suppressed star-formation are also found up to $z \sim 2$ (e.g. Strazzullo et al., 2010; Andreon et al., 2014; Newman et al., 2014; Cooke et al., 2016). Cluster selection, cluster-to-cluster variation, the intrinsically transitional phase of galaxy populations at this time, and observational difficulties, have all contributed to assemble a varied, still unfinished picture that might at times still look controversial in some aspects, and sometimes difficult to reconcile with theoretical expectations (e.g. Granato et al., 2015).

Thanks to expensive - thus still limited to a relatively small number of systems - dedicated follow-up programs, a number of recent studies have started investigating in more specific detail the properties of both quiescent and star-forming galaxies in distant (proto)cluster environments. Such studies have explored a variety of aspects including: the environmental dependence of stellar ages and structure of passive populations (e.g. Gobat et al., 2013; Tanaka et al., 2013; Strazzullo et al., 2013; Newman et al., 2014; Andreon et al., 2014, 2016; Beifiori et al., 2017; Prichard et al., 2017; Lee-Brown et al., 2017; Chan et al., 2018); the environmental dependence of the specific star-formation rates, metallicities, and dust attenuation properties of star-forming galaxies (e.g. Tanaka et al., 2010; Hatch et al., 2011; Hayashi et al., 2011, 2016; Kulas et al., 2013; Koyama et al., 2013, 2014; Smail et al., 2014; Cooke et al., 2014; Tran et al., 2015; Shimakawa et al., 2015; Valentino et al., 2015; Kacprzak et al., 2015; Kewley et al., 2016; Husband et al., 2016; Shimakawa et al., 2018); and the environmental dependence of cold gas reservoirs fuelling star-formation in dense environments (e.g. Aravena et al., 2012; Emonts et al., 2013; Casasola et al., 2013; Ivison et al., 2013; Tadaki et al., 2014; Gullberg et al., 2016; Casey, 2016; Lee et al., 2017; Noble et al., 2017; Dannerbauer et al., 2017; Rudnick et al., 2017; Stach et al., 2017; Hayashi et al., 2017, 2018). Results from such investigations critically shape our understanding of galaxy population properties - and of the processes affecting galaxy evolution - in early dense environments, though the still very limited cluster galaxy samples, small number of clusters probed, and selection biases continue to preclude conclusive interpretations.

We present here new results from ALMA observations of the galaxy cluster Cl J1449+0856 (Gobat et al., 2011) at $z = 2$, complementing previous work on its galaxy populations (Gobat et al., 2013; Strazzullo et al., 2013; Valentino et al., 2015, 2016; Strazzullo et al., 2016) with a critical independent vantage point. Cl J1449+0856 was identified as an overdensity of IRAC

colour selected galaxies, and is now spectroscopically confirmed with ~ 30 spectroscopic members (Gobat et al., 2011, 2013; Valentino et al., 2015; Coogan et al., 2018). The estimated halo mass based on its extended X-ray emission and stellar mass content is $5 - 7 \times 10^{13}$ $M_{\odot}$ (Gobat et al., 2011; Valentino et al., 2016, and references therein), placing this structure in the mass range of the average progenitors of today's typical massive clusters. For what directly concerns the results presented here, previous work has highlighted the mixed galaxy population in this cluster, consisting of both quiescent and highly star-forming sources (as well as AGNs, Gobat et al., 2013; Strazzullo et al., 2013; Valentino et al., 2015, 2016). In particular, Strazzullo et al. (2016, hereafter S16) investigated the nature of the massive red population characterising the cluster core, in terms of dusty massive star-forming galaxies and sources with already suppressed star-formation, based on a purely photometric analysis at rest-frame optical/NIR wavelengths. On the other hand, in spite of the statistical validity of this approach, the ultimate confirmation of the nature of such sources, and an actual estimate of the (obscured) star-formation occurring in the cluster core, remains with star-formation rate indicators not biased by dust attenuation (although we stress that optical/NIR tracers should not be biased if dust attenuation can be correctly accounted for). Cl J1449+0856 has been previously observed with Spitzer/MIPS (24μm) and also with Herschel/PACS and SPIRE, which has indeed suggested potentially high levels of star-formation activity right in the cluster core, as already reported in the first study by Gobat et al. (2011). However, the angular resolution and depth of these data, and/or ambiguities with respect to contamination from nuclear activity, hampered the effectiveness of these observations in establishing a reliable picture of star-formation and quenching in this system.

In this work based on ALMA observations, we thus focus on three main aspects: firstly, the quantification of star-formation occurring in the core of Cl J1449+0856, for the first time using deep, high-resolution star-formation probes not biased by dust attenuation (Sections 3.3, 3.4.1). Secondly, the constraints set by these new observations on the first massive quiescent galaxies that, even as early as $z \sim 2$, are a significant feature of the core of Cl J1449+0856 (Section 3.4.2). Finally, the direct observation of the forming Brightest Cluster Galaxy (BCG, Section 3.5), that especially thanks to the combination with Hubble Space Telescope data produces a remarkably detailed picture of a critical phase in the early evolution of (proto)BCGs. Besides the scope of this paper, the ALMA observations discussed here enable the investigation of a significantly wider range of questions related to the effect of the environment on the properties and evolution of high-redshift cluster galaxies: the companion paper by Coogan et al. (2018, Chapter 4, 'C18') presents in particular the dust and gas properties of the ALMA-detected cluster members, and provides extensive descriptions of all sub-mm and radio observations of Cl J1449+0856.

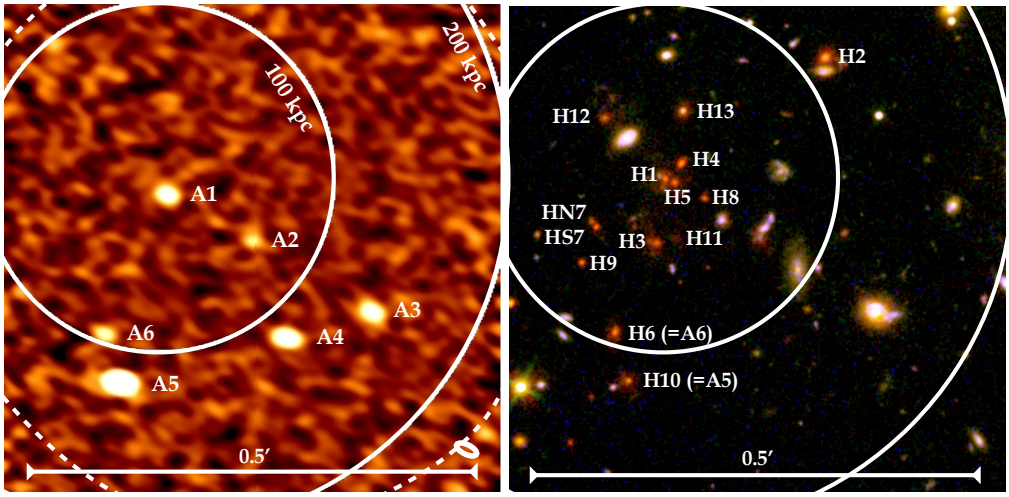

Figure 3.1: The ALMA 870μm map (left) and HST F606W-F105W-F140W pseudo-colour image (right) of the same region in the core of Cl J1449+0856. Sources discussed in this work are labelled. Note the different identifications for the ALMA/870μm sources (IDs A1 to A6) and HST/F140W sources from S16 (IDs H1 to H13, corresponding to IDs 1 to 13 in S16). The field shown is $\sim$0.56' on each side, $\sim$290 kpc (proper) at the cluster redshift. White solid circles show clustercentric distances of 100 and 200 kpc as indicated (the estimated cluster virial radius is $\sim$400 kpc). The white dashed circle shows the primary beam FWHM of the ALMA band 4 observations.

We assume a ΛCDM cosmology with Ω_M=0.3, Ω_Λ=0.7, H_0=70 km s^{-1} Mpc^{-1}. Stellar masses and star-formation rates are quoted for a Salpeter (1955) IMF in this chapter. Magnitudes and colours are quoted in the AB system.

3.2 Observations

We focus here on the constraints on star-formation activity and its suppression in the core region of Cl J1449+0856, derived from the observations of 870μm continuum and CO[4-3] line emission. We refer the reader to Chapter 4 for a full, extensive summary of the ALMA observations, and for a detailed description of the measurements of the 870μm continuum and CO[4-3] line fluxes that we use in this work. All of the analysis and results below are based on these measurements, as described in Chapter 4.

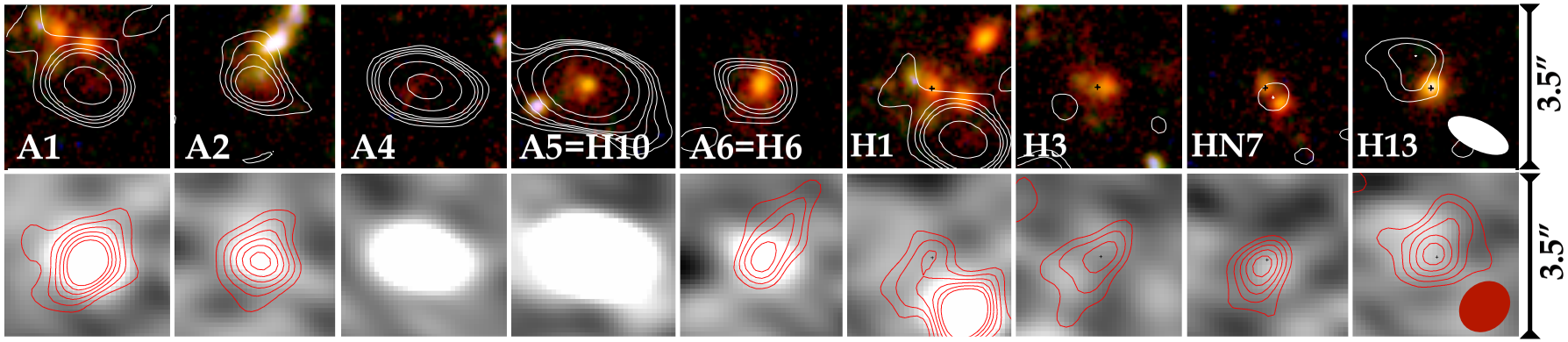

Figure 3.2: Top: HST pseudo-colour image cutouts (F606W-F105W-F140W) of sources discussed in this work (see labelling in Fig. 3.1), with overlaid (white) 870μm contours ($2, 3, 4, 5, 10, 20\sigma$). Bottom: 870μm cutouts with overlaid (red) CO[4-3] contours ($2, 3, 4, 5, 6, 7\sigma$). For IDs $H1, H3, HN7, H13$ black crosses mark the HST/F140W galaxy position. White and red ellipses in the rightmost panels show the synthesised beam of the 870μm and band 4 observations, respectively.

3.3 Overdensity of 870μm sources

The 870μm map of the core of Cl J1449+0856 reveals six continuum sources (SNR$>$ 4) with $F_{870\mu m} > 0.5$ mJy (Fig. 3.1, galaxies A1-A6), giving a projected source density in the ~ 0.3arcmin^2 survey field that is a factor ~ 6 higher than expected from blank-field counts (e.g. $\sim 1.0 \pm 0.8$ sources would be expected from Oteo et al., 2016). In fact, all six sources are concentrated within a circle of $r \sim 0.15'$. We remind the reader to refer back to Table 2.2 when necessary, in which we summarise which galaxies discussed here are currently confirmed to be members of Cl J1449+0856. Four of the six 870μm sources are brighter than 1 mJy, resulting in a projected overdensity of ~ 10 ($\sim 0.3 \pm 0.3$ sources expected to this flux limit from Oteo et al., 2016). We note that, as discussed below, the two brightest 870μm sources are likely to be background interlopers. We estimate their flux magnification due to the cluster potential, assuming a spherical NFW halo of mass 6×10^{13} M$_\odot$ and a concentration in the range $c = 1 - 5$. For the brightest, $\sim$6 mJy source (labelled A5 in Fig. 3.1), the estimated photometric redshift $z \sim 2.8$ yields a magnification factor of $\sim 12\%$ (5-18% within the 3σ range of the photometric redshift). For the other source (A4, $\sim$1.9 mJy), we estimate a magnification of about 9% to 20% (30%, 40%) for a source redshift from 2.5 to 3.5 (5, 7). Even for a source at redshift $z \sim 7$, the flux would still be brighter than 1 mJy. We thus conclude that the overdensity of mm-bright sources is not likely to be significantly affected by lensing magnification by the cluster potential.

Fig. 3.1 (left) identifies all of the ALMA-detected sources discussed in this work (labelled A1 to A6), while the right-hand panel identifies the HST-detected (F140W) sources (labelled H1 to H13, note that H6 and A6 - and H10 and A5 - correspond to the same galaxies, as indicated). Of the six 870μm sources, two have spectroscopic redshifts measured in the Gobat et al. (2013) HST grism follow-up of Cl J1449+0856: a foreground galaxy at $z \sim 1.3$ (A3, thus ignored henceforth), and the cluster member A6=H6. None of the other 870μm sources have an optical/NIR spectroscopic redshift determination. The HST counterparts to A1, A2 and A4 are very faint[1], and were thus not included in previous studies of galaxy populations in Cl J1449+0856. A5 was included in our previous work and was deemed to be likely an interloper at $z_{phot} \sim 2.8$ (Strazzullo et al. 2013, but see Sections 4.3.8 and 7.2).

On the other hand, A1 and A2 both show a highly significant detection of CO[4-3] line emission (Fig. 3.2 and Chapter 4), securely confirming their cluster membership. However, no lines are detected for the two brightest 870μm sources, A4 and A5. In fact, as discussed at length in C18,

[1]A1 and A2 are also both close to a bright neighbour, and were not extracted as individual sources in our F140W-based catalogs (e.g., Strazzullo et al., 2013) until HST/F105W-band imaging (S16) and ALMA observations pointed to these sources being separate components.

in spite of their high 870μm fluxes no lines are detected for these sources in *any* of our data sets probing CO[4-3], CO[3-2] and CO[1-0] at the cluster redshift, as well as bright mm lines ([CI](2-1), CII, CO transitions up to CO[7-6]) over a significant fraction of the $1 < z < 9$ range. Nonetheless, several redshifts remain unprobed, notably including the range around the photometric redshift of A5 (see C18, Chapter 4). Therefore we do not presently have confirmation of the redshifts of A4 and A5. We note that the likelihood of observing two such bright sources unrelated with Cl J1449+0856 in the small field probed is extremely low: as discussed in more detail in Chapter 4, these sources might in principle still be cluster members with very recently and rapidly suppressed star-formation, with the lack of CO[4-3] emission being potentially reconciled with their bright 870μm continuum by the gas and dust tracing star-formation on different timescales. Nonetheless, given their large 870μm fluxes and thus the expected very bright CO line emission compared to the depth of our observations (Fig. 3.3), we currently conclude that, at face value, the most likely explanation is that A4 and A5 are interlopers. Among the six bright 870μm sources, only A1, A2 and A6 are thus confirmed to belong to the cluster (as summarised in Table 2.2).

3.4 Activity and quiescence in Cl J1449+0856

3.4.1 Dusty star-formation in the cluster core

CO[4-3] emission is detected at $> 3\sigma$ for a total of seven cluster galaxies, including previously-known members (H1, H3, H6=A6, HN7, H13) and those newly confirmed by the detection of the CO line itself (A1, A2, Sec. 3.3, C18). All but one of these (H3) also have a $> 2.5\sigma$ 870μm detection (Figures 3.2, 3.3). Fig. 3.3 shows the infrared luminosities L_{IR} of these sources as estimated from the 870μm continuum flux ($L_{IR,870\mu m}$) or the CO[4-3] line flux[2] ($L_{IR,CO43}$).

The IR luminosity estimate $L_{IR,870\mu m}$ was derived from the measured 870μm flux using the average MS and starburst (SB) SEDs from Béthermin et al. (2012) at $z = 2$. The $L_{IR,CO43}$ estimate was derived from the measured CO[4-3] line flux by assuming the CO SLEDs (in particular, the CO[5-4]/CO[4-3] line ratio) of ULIRGs[3] (intended to represent starbursts), and star-forming BzK galaxies (intended to represent MS sources, from Papadopoulos et al., 2012a; Daddi et al., 2015, respectively), and the CO[5-4] vs. L_{IR} relation from Daddi et al. (2015). We consider the adopted

[2]We use CO[4-3] line fluxes corrected for flux boosting as detailed in C18.

[3]Given the significant uncertainties on the average CO[5-4] and CO[4-3] line fluxes adopted for ULIRGs (Daddi et al., 2015), the CO[5-4]/CO[4-3] line ratio used here is based on a weighted fit of the ULIRG SLED from CO[3-2] to CO[5-4] rather than on the actual ratio of CO[5-4] and CO[4-3] line fluxes. As discussed, this ULIRGs line ratio is shown - for comparison with the BzK line ratio - as an indication of the impact of the adopted CO SLED, and the exact value adopted does not have significant effects on the results of this work.

assumptions on the CO[5-4]/CO[4-3] line ratio as the most appropriate for galaxies in this sample, but we also show for comparison in Fig. 3.3 the effect on the $L_{IR,CO43}$ estimate of a range of different assumptions on the CO SLED, including those measured for the Milky Way (inner region, Fixsen et al., 1999), SMGs (Bothwell et al., 2013), and the Papadopoulos et al. (2012a) model (see discussion in Daddi et al., 2015, and references therein). The CO[5-4]/CO[4-3] line ratios from these different determinations are affected to different degrees by measurement uncertainties (see the original papers for details), but for what concerns this work we note that the impact of the different plausible line ratios (including their uncertainties) on our $L_{IR,CO43}$ estimate is clearly sub-dominant with respect to the scatter in the CO[5-4] vs. L_{IR} relation, as well as the typical measurement errors of CO[4-3] line fluxes in this work.

Fig. 3.3 shows these $L_{IR,870\mu m}$ and $L_{IR,CO43}$ estimates and the related uncertainties as follows. Black error bars show statistical uncertainties from flux measurement errors. The double symbol adopted for all sources highlights the systematic uncertainties in estimating IR luminosities from the 870μm continuum assuming a MS or SB SED, or from CO[4-3] line fluxes assuming the BzK or ULIRG SLED, as indicated. The thick gray error bar and shaded area along the bisector show the estimated intrinsic scatter of the adopted scaling relations, that is the scatter in SED shape (dust temperature) and in the CO[5-4] vs. L_{IR} relation (concerning $L_{IR,870\mu m}$ and $L_{IR,CO43}$, respectively). Hatched regions in the figure mark IR luminosities below a corresponding reference 3σ limit estimated by assuming: for $L_{IR,870\mu m}$, the 3σ limit of the 870μm map (Sec. 3.2) and the MS SED; for $L_{IR,CO43}$, the 3σ limit of the band 4 observations at field center (Sec. 3.2), a line width of 400 km/s, the BzK CO[5-4]/CO[4-3] line ratio, and the CO[5-4] vs. L_{IR} relation. While these are shown as an indication, the measurements, errors and upper limits shown for the individual sources account for their actual position within the band 4 primary beam Full Width Half Maximum (FWHM), and highlight the systematics due to the SED or CO SLED choice as discussed, though upper limits for $L_{IR,CO43}$ still assume a line width of 400 km/s.

As Fig. 3.3 shows, the $L_{IR,CO43}$ and $L_{IR,870\mu m}$ IR luminosity estimates are typically consistent within the estimated uncertainties. The two obvious exceptions are A4 and A5, which both have high $L_{IR,870\mu m}$ from the bright 870μm flux but no CO emission, leading to an inconsistent upper limit on $L_{IR,CO43}$ even when accounting for the estimated uncertainties. As discussed above, we therefore conclude that these sources are in fact interlopers. For all other sources, the consistency of $L_{IR,870\mu m}$ and $L_{IR,CO43}$, besides ensuring cluster membership of the 870μm detections, also confirms the reliability of the SFR estimates.

Summing the derived infrared luminosities of cluster members within the probed ~ 0.08 Mpc^2 (proper, at z=2) region yields a total $L_{IR} \sim 4.3 \pm 0.5 \times 10^{12} L_{\odot}$ (the error corresponding to the

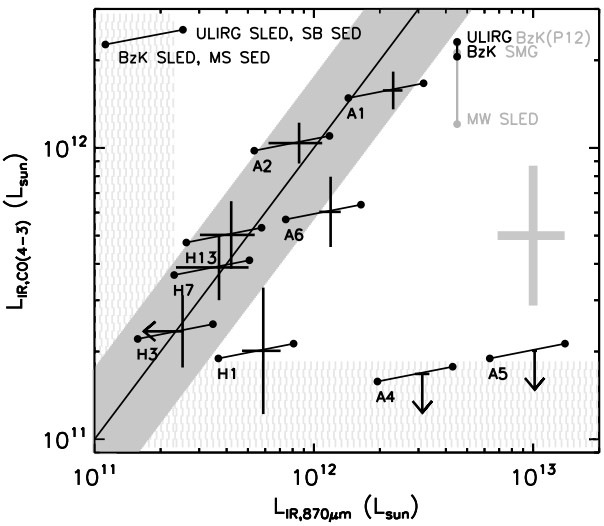

Figure 3.3: The IR luminosities of mm-detected sources as estimated from the 870μm continuum fluxes ($L_{IR,870\mu m}$) and from the CO[4-3] line emission ($L_{IR,CO43}$). The double symbol shows $L_{IR,CO43}$ as estimated assuming a BzK or ULIRG CO SLED, and $L_{IR,870\mu m}$ as estimated with a main sequence (MS) or starburst SED, as indicated. For further comparison, the systematics on $L_{IR,CO43}$ corresponding to a range of different assumptions on the CO SLED are shown in the top right corner (see text). Black error bars plotted in the middle of the two estimates show the uncertainties due to the 870μm and CO[4-3] flux measurements. The black line marks the bisector ($L_{IR,870\mu m}$ = $L_{IR,CO43}$). The thick grey band along the bisector and the grey cross both show the uncertainty derived from the (1σ) scatter in the adopted scaling relations (see text). Arrows show 2σ upper limits (see text). Hatched areas are below the 3σ limits for MS/BzK sources (see text). Note the clear outliers A4 and A5, which we therefore conclude are likely interlopers.

range obtained from $L_{IR,CO43}$ with both ULIRG and BzK SLEDs, and $L_{IR,870\mu m}$ with a MS SED[4]), corresponding to a total SFR of $\sim 700 \pm 100$ $M_\odot$/yr (adopting the Kennicutt (1998a) calibration). This yields an overall projected SFR density of $\sim 0.9 \pm 0.1 \times 10^4$ $M_\odot$ $yr^{-1}Mpc^{-2}$, and a SFR volume density $\sim 1.0 \pm 0.1 \times 10^4$ $M_\odot$ $yr^{-1}Mpc^{-3}$ within the probed region[5] (over the probed fraction of the virial volume, given the estimated cluster virial radius and assuming that the cluster is spherical). Again, these estimates assume that the two brightest 870μm sources A4 and A5 are interlopers: A5 alone would otherwise contribute a SFR of $\sim$1000 $M_\odot$/yr.

The total unobscured SFR of the ALMA-detected cluster members as estimated from the rest-frame UV luminosity L_{UV} is < 20 $M_\odot$/yr (uncorrected for dust attenuation). Given the SFR threshold reached by these observations, the high L_{IR}/L_{UV} of the resulting ALMA-detected sample further highlights how galaxy populations in this cluster core are unusually skewed towards very reddened sources (see also Fig. 3.2, further discussion in Sec. 3.4.1 and in C18). For comparison, the total unobscured SFR of all cluster galaxies within the same region is estimated to be approximately 100 ± 20 $M_\odot$/yr, having corrected for incompleteness using the field UV luminosity functions from Parsa et al. (2016); Alavi et al. (2016).

The measured SFR density is obviously orders of magnitude higher than the field average at the same redshift (e.g. Madau & Dickinson, 2014), as observed in various kinds of other high-redshift structures (e.g. Clements et al., 2014; Dannerbauer et al., 2014; Tran et al., 2015; Santos et al., 2015a; Wang et al., 2016). This is in fact largely due to the concentration of (star-forming) galaxies within the small volume of the dense cluster core, rather than to individual galaxies having particularly high SFRs. In fact, the overall specific SFR in the ALMA-probed field is sSFR$\sim 1.1 \pm 0.6$ Gyr^{-1}, compared to a field average at $z = 2$ of $\sim 1.9^{+1.9}_{-0.9}$ Gyr^{-1} (Madau & Dickinson, 2014). As shown in Fig. 3.5, and also discussed in C18, the SFRs of individual sources are generally consistent with MS levels, with the possible exception of the two brightest sources A1 and A2 having higher SFRs.

By comparison with the cluster mass $M_{halo} \sim 5 - 7 \times 10^{13}$ $M_\odot$, the estimated L_{IR}-derived SFR within the probed volume gives a lower limit (that is, not correcting for the part of the virial volume left unprobed by our ALMA observations) to the total SFR density SFR/M_{halo} of $\sim$1300$\pm$400 $M_\odot$ yr^{-1} / 10^{14} $M_\odot$, after a small correction of the total IR luminosity for the $> 3\sigma$ $L_{IR,870\mu m}$ sample down to $L_{IR} = 10^7 L_\odot$ assuming the Popesso et al. (2015a) group LF at $z \sim 1.6$, which should be the most appropriate for this system (see discussion in Popesso et al., 2015a). At

[4]Up to $\sim 8 \times 10^{12} L_\odot$ from $L_{IR,870\mu m}$ if assuming a SB SED for all sources, corresponding to a total SFR of ~ 1400 $M_\odot$/yr.

[5]Up to $\sim 1.7 \times 10^4$ $M_\odot$ $yr^{-1}Mpc^{-2}$ and $\sim 2 \times 10^4$ $M_\odot$ $yr^{-1}Mpc^{-3}$ from $L_{IR,870\mu m}$ if assuming a SB SED for all sources.

face value, this is in line with the Popesso et al. (2015b) extrapolation (from data at 0<z<1.6) to $z = 2$ for massive groups, although we remind the reader that this is a lower limit, and it is currently not possible to reliably estimate the overall contribution of the cluster outskirts (however, we note that, in the available observations, essentially all of the measured IR luminosity comes from the very central cluster region, $r \lesssim 100$ kpc, see Fig. 3.1). The derived lower limit on SFR/M_{halo} lies at the upper edge of the Alberts et al. (2016) measurements at $z \sim 1.4$ (accounting for the different IMF and marginal correction to the same L_{IR} limit), in agreement with the expected further increase out to $z = 2$, though we also note that the Alberts et al. (2016) clusters have larger estimated halo masses, in the range $2 - 5 \times 10^{14}$ $M_\odot$, and thus are expected to have lower SFR/M_{halo} (e.g. Webb et al., 2013; Popesso et al., 2015b). Indeed, the lower halo mass sample of Alberts et al. (2014) would give significantly higher SFR/M_{halo} values in the same redshift range (see discussion in Alberts et al., 2016), that are also higher than our lower limit measured here. Similarly, although our lower limit tends to be higher than measurements by e.g., Smail et al. (2014); Ma et al. (2015); Santos et al. (2015a) for clusters of very different masses (8×10^{13} $M_\odot$ to $5 \times 10^{14} M_\odot$) at $z \sim 1.5 - 1.6$ (SFR/M_{halo} overall in the range $\sim 500 - 1000$ $M_\odot$ yr^{-1} / 10^{14} $M_\odot$), it would be fully in line with these measurements for a SFR density evolution similar to that predicted by e.g. Geach et al. (2006). For comparison, the ~ 3400 $M_\odot$ yr^{-1} observed within the 80 kpc core of the similarly massive ($M_{halo} \sim 8 \times 10^{13}$ $M_\odot$) Wang et al. (2016) cluster at $z = 2.5$, results in a lower limit SFR/$M_{halo} > 4000$ $M_\odot$ yr^{-1} / 10^{14} $M_\odot$.

Colour distribution of ALMA-detected cluster galaxies

Despite the poor statistics due to the very small field probed and relatively small number of massive star-forming cluster members, the ALMA-detected sample in this region appears unusually skewed towards very red (F105W-F140W, dust-uncorrected) sources. We show in Fig. 3.4 (right panel) the colour distribution of sub-samples of the ALMA-detected sources in Cl J1449+0856 with different stellar mass and SFR thresholds, as indicated. The adopted stellar mass thresholds log(M/$M_\odot$)=10.1 and 10.5 correspond respectively to the lowest mass of the ALMA-detected cluster members, and to a mass above the mass completeness limit of the S16 sample where our formal 3σ limit on CO[4-3]-based SFR probes essentially all the 1σ range of the MS (Fig. 3.5). The adopted SFR thresholds correspond to the nominal $3, 5\sigma$ limits of the CO[4-3] observations based on the assumptions discussed in Sec. 3.4.1.

Fig. 3.4 (left panel) shows, for comparison, the colour distribution of field galaxies at $z_{phot} = 2 \pm 0.3$ with the same stellar mass and SFR limits, from a control field in GOODS-S. The control field is the same as was used in S16, and the adopted measurements are described there in more

detail (e.g. their section 2). We briefly remind the reader that we used the Guo et al. (2013) photometry, and stellar masses, photometric redshifts and model SEDs from Schreiber et al. (2015) and Pannella et al. (2015). We note that both stellar mass and SFR estimates are derived from SED fitting for the field samples, while we use the CO[4-3]-based SFRs for cluster galaxies. The selection of the field comparison samples cannot thus be considered as properly equivalent to the selection of the cluster samples, because of the initial field sample selection (Guo et al., 2013) and of the obvious biases between the different (CO[4-3] vs. SED-based) SFR estimates adopted. In this respect, we further note that for the purpose of estimating SFRs for the field sample, a constant star formation history was assumed (model SEDs synthesised with Bruzual & Charlot, 2003) for all sources, allowing for a wide dust attenuation range (A_v=0-6, assuming the Calzetti et al. (2000) attenuation law). SED-based SFRs derived from this modelling have been shown to agree with L_{IR}-based estimates within a $\sim$0.2 dex scatter (e.g. Pannella et al., 2015, for the same SED analysis as used here).

The green and blue/orange histograms in Fig. 3.4 (left panel) refer to samples including all galaxies or only galaxies classified as star-forming based on their rest-frame UVJ colours (Williams et al., 2009), respectively. While the blue/orange histograms are thus the main reference for the expected colour distribution, the green histograms are shown for comparison to account for misclassification of dusty star-forming galaxies as quiescent sources. As the bulk of UVJ-quiescent galaxies are expected to be actually quiescent, this is a conservative comparison sample in this respect, as it maximises the fraction of red sources.

We show Fig. 3.4 as an indication of our rough expectations for the colours of a mass- and SFR-selected sample of (field) galaxies at the cluster redshift. Considering 1000 realisations of galaxy samples of the same size as the cluster samples shown in Fig. 3.4, randomly drawn from the corresponding field distribution, returns a fraction of F105-F140$>$1.3 sources larger than what is measured in the cluster samples in $< 2\%$ of the realisations at worst (for the log(M/M$_\odot$)$>$10.1, SFR$>$60 M$_\odot$yr^{-1}, or generally $< 0.5\%$)[6]. In spite of the caveats outlined above originating from the non-equivalent selection of the cluster and field samples due to the different adopted SFR indicators, and of the very small number statistics of the ALMA-detected sample in the cluster, the comparison with first-order expectations from the field sample suggests at face value that very obscured sources are more prevalent in the cluster than in the field. If confirmed, this would point towards environmental effects possibly related to merger-driven star-formation episodes (see e.g. Chapter 4 and references therein) and/or differences in star-formation histories in the cluster

[6]Even considering all the UVJ-quiescent sources as misclassified dusty star-forming galaxies, the probability to observe red fractions as high as in the cluster samples in the corresponding samples drawn from the field distributions remains $< 2\%$ (or $< 7\%$ for the log(M/M$_\odot$)$>$10.1, SFR$>$60 M$_\odot$yr^{-1} sample).

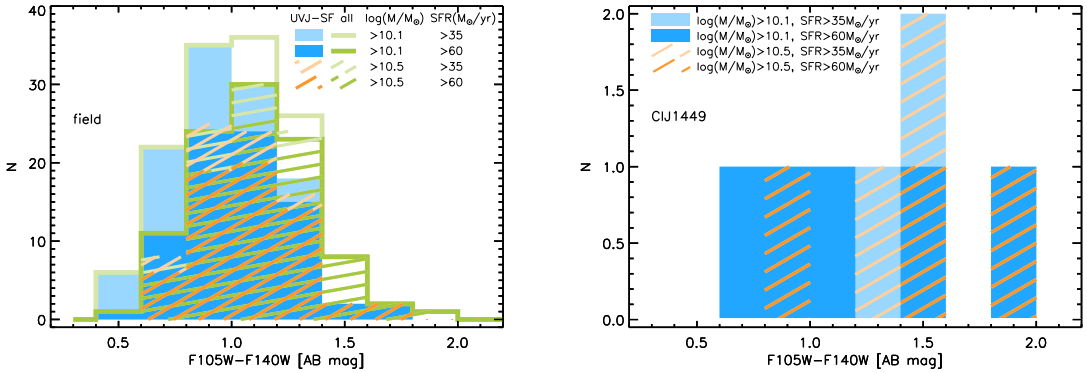

Figure 3.4: The colour distribution of stellar mass and SFR-selected samples (with different thresholds as indicated) in a control field (GOODS-S, left panel) and in the cluster field probed by ALMA observations (right panel). Note that SFRs for cluster members are based on CO[4-3] line emission, while the SFRs for the field comparison samples are derived from SED fitting. The green and blue/orange histograms in the left panel refer to field samples including all galaxies and only UVJ-star-forming sources, respectively (see text).

environment.

3.4.2 The ALMA view of the red cluster galaxy population

In S16 the authors investigated the optically red (F105-F140$\gtrsim$1) cluster galaxy population in an attempt to define its nature, thus probing quenching of star-formation and the early appearance of the red sequence in dense environments. Note that this red sample is not a *red sequence* sample (see S16), as it is not strictly limited to galaxies that fall on the red sequence. It also includes galaxies that scatter above and below the red sequence, but that are redder than the bulk of the blue star-forming cluster galaxy population. As discussed in S16, cluster galaxies with red (dust-uncorrected) optical colours (F105-F140, $\sim$U-B rest-frame) may be quiescent sources with evolved stellar populations, quenching galaxies with still relatively young stellar populations, or massive dusty star-forming galaxies. Given the characteristics of the available data, in S16 the authors adopted a star-forming vs. quiescent classification based on two broad-band colours approximately probing the rest-frame U-B and B-I (Fig. 3.5 left, see S16). Although this selection statistically allows the identification of quiescent vs. dusty star-forming galaxies, it is still likely to be affected by uncertainties and systematics on an object-by-object basis.

The ALMA observations presented here offer a fully independent view of the red population. Fig. 3.5 shows the ALMA constraints on SFR vs. stellar mass for the S16 red sample. The stellar masses shown for this sample are generally SED-based estimates from S16, with the exception

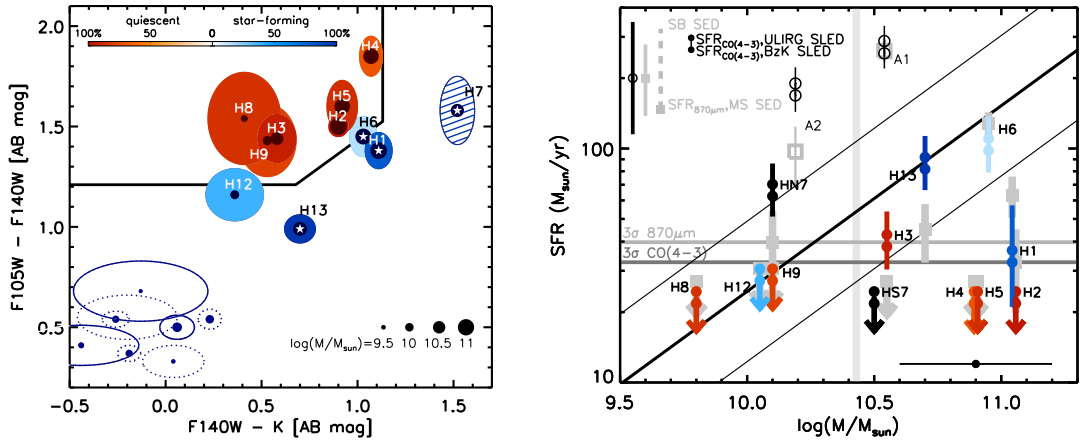

Figure 3.5: The ALMA view of red cluster galaxies. Left: the colour classification (F140W-K vs. F105W-F140W) of the red galaxy sample as defined in S16. Galaxies are shown with blue or red circles (inner circle size scales with stellar mass as indicated) according to the classification as star-forming or quiescent, respectively. The (Gaussian) probability of the given classification for each source (see colour bar) is defined from photometric uncertainties (shown as outer ellipses), and does not include uncertainties on the definition of the colour selection. Those ellipses that are filled and labelled indicate galaxies that were included in S16's red sample. H7 is filled as a dashed ellipse, as it shows the combined colours of HN7 and HS7 (see text). White stars mark 870μm-detected sources. For reference, blue spectroscopic cluster members are also shown as empty ellipses in the bottom left corner (solid or dotted for sources inside or outside the ALMA 870μm field). Right: The stellar mass vs. SFR as determined from $L_{IR,CO43}$ (circles). Colour-coding in shades of red (blue) reflects the reliability of the classification as quiescent (star-forming) according to the colour bar in left-hand panel. The SFR_{CO43} assuming both BzK and ULIRG SLEDs are shown, as in Fig. 3.3. Grey squares show (for comparison) the SFR as determined from $L_{IR,870\mu m}$ with a MS SED (the dashed line at the top left shows the effect of using a SB SED). Empty symbols show the ALMA-detected sources A1 and A2 (see text). Arrows show 2σ upper limits, as in Fig. 3.3. The black and grey error bars at the top left show the uncertainties due to the scatter in the adopted scaling relations for $L_{IR,CO43}$ and $L_{IR,870\mu m}$, respectively (see Fig. 3.3). The black error bar at the bottom right shows the typical uncertainty on stellar masses. The black thick and thin lines show the MS at the cluster redshift (parametrised as in Sargent et al., 2014) and its estimated (1σ) scatter. The horizontal lines show the 3σ limits on SFRs inferred from the 870μm and CO[4-3] line emission, as indicated (see text). The vertical line shows the mass completeness limit of the S16 sample, given the F140W magnitude threshold m_{140}=24.7, assuming a solar metallicity single stellar population with no dust attenuation formed at $z \sim 7$.

of HN7 and HS7 for which most of the photometry used in S16 is expected to be affected by contamination given their very small angular separation. We thus use here stellar mass estimates derived from just the high-resolution F105W and F140W photometry, by empirical calibration on a sample of galaxies in a similar magnitude and redshift range from the GOODS-S control field (as introduced in Sec. 3.4.1). SFR estimates are derived from the 870μm continuum and CO[4-3] line emission as discussed in Sec. 3.4.1. Fig. 3.5 shows for reference (horizontal lines) the 3σ limits on such SFRs corresponding to the limits on $L_{IR,CO43}$ and $L_{IR,870\mu m}$ discussed in Section 3.4.1, Fig. 3.3. Also here, these are shown as an indication, while the measurements, errors and upper limits for the individual sources account for the position within the band 4 primary beam, and for the systematics due to the SED or CO SLED choice (upper limits for SFR_{CO4-3} still assume a line width of 400 km/s).

Given the depth of the ALMA observations, the SFR vs. stellar mass constraints are mostly effective at high stellar masses[7], $\log(M/M_\odot)>10.5$. In this mass range, SFR upper limits suggest a confirmation of the quiescent picture for most sources colour-classified as passive, H2, H4 and H5[8]. The only exception is H3, which is colour-classified as quiescent, it is undetected at 870μm, but has a 4.8σ CO[4-3] detection. Given the estimated uncertainties and scatter in the adopted scaling relations (Figs. 3.3, 3.5) the measurements are still consistent with a MS SFR for this source. On the other hand, given the complex morphology and surroundings of this galaxy, and the limited resolution of our ALMA observations, it is possible that the "quiescent colours" and the CO[4-3] line belong to different components.

Concerning instead cluster members in this "red" sample colour-classified as star-forming, they are all (but see H7 below) detected at both 870μm and CO[4-3]. Note that the population of lower-mass ($\log(M/M_\odot)\lesssim10.3$) blue star-forming cluster galaxies (Gobat et al., 2013, S16) is not in general expected to be detected (even when falling within the probed field of view) given the SFR limits shown in Fig. 3.5. The AGN host (Gobat et al., 2013) H13 is consistent with being a MS star-forming galaxy. H1 and H6 had a particularly uncertain colour classification (see Fig. 3.5 left and S16), and indeed H6 was classified as quiescent based on previous SED (Strazzullo et al., 2013) and spectral (Gobat et al., 2013) modelling. Although we are investigating other interpretations for H6 (e.g. Gobat et al., 2018) involving a quiescent component, its SFR estimates from the observed 870μm continuum and CO[4-3] lime emission are fully consistent with each other, and in line with MS expectations, suggesting that H6 is likely a MS galaxy. On the other hand, Fig. 3.5

[7]Less massive sources, e.g. H8, H9, H12, would not be detected in our observations even if they were MS star-forming galaxies.

[8]H2 might have a tentative, low-significance 870μm detection with no associated CO[4-3] emission (see C18 and Fig. 3.5) placing it below the MS scatter.

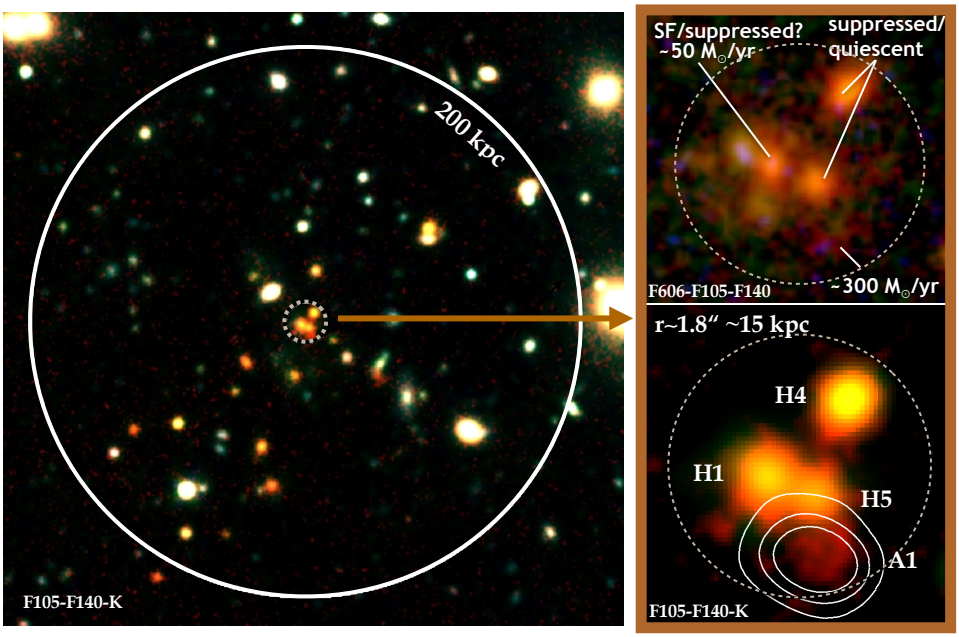

Figure 3.6: The forming BCG at the center of Cl J1449+0856. Left: A F105-F140-K (HST, Subaru) pseudo-colour image of the cluster core ($r \lesssim 200$ kpc proper). Right: F606-F105-F140 (top) and F105-F140-K (bottom, with overlaid $3, 6, 9\sigma$ 870μm contours) pseudo-colour images of the central $r \lesssim 15$ kpc. The dashed circle ($r = 1.8'' \sim 15$ kpc) encompasses three F140W-bright optically-red sources (H1, H4, H5), the brightest CO[4-3] and 870μm cluster member (A1), and several other (unmarked) faint diffuse components. The labels assigned to the four highlighted IDs in the top-right panel refer to the characteristics discussed in Secs. 3.4.1, 3.4.2, and 3.5.

suggests that the SFR of H1 might be below the MS scatter. Also note that, although we do our best in dealing with close neighbours by modeling such sources simultaneously when measuring both 870μm and CO[4-3] fluxes (see C18, Chapter 4), the continuum and line fluxes of H1 are likely affected (to different extents) by residual contamination from neighbouring sources and in particular the very bright A1 (see Fig. 3.2), which might possibly explain also the relatively large $L_{IR,870\mu m}$ vs. $L_{IR,CO43}$ offset for this source in Fig. 3.3.

Fig. 3.5 (right) also shows the two components HN7 and HS7 of a very close pair hosting an AGN (Gobat et al., 2013). In Figures 3.3 and 3.5 (left) they are shown as a single source H7 because the angular resolution does not permit deblending of the two components. Given the shape and size of the synthesised 870μm beam, the low S/N of the 870μm detection, and the angular distance between the two components, it is not possible to measure the 870μm flux of the two components

separately. On the other hand, the position of the higher-S/N CO[4-3] detection suggests that HN7 provides the dominant contribution to the observed CO emission (see HN7-related panels in Fig. 3.2). More importantly, given the redshift difference of the two components, the weak tentative detection of CO[4-3] line emission of HS7 ($\sim 2\sigma$, see C18, Chapter 4) has a relatively large separation in frequency (~ 0.7 GHz) from the much stronger detection of HN7, which allows us to separate the respective CO[4-3] contributions (see Chapter 4 for full details). Given that the total (HN7+HS7) 870μm-derived IR luminosity $L_{IR,870\mu m}$ is fully consistent with the CO[4-3]-based estimate $L_{IR,CO43}$ measured at the position and redshift of HN7 (Fig. 3.3), we conclude that HN7 provides the largest contribution to the measured 870μm flux, with the contamination from HS7 being very likely negligible. The SFR estimated for HN7 is consistent with the expected MS level (Fig. 3.5). The faintness of HS7 would suggest a SFR below the MS level (Fig. 3.5).

Given the faint optical counterparts of A1 and A2 (see discussion in Sec. 3.3), these sources were not part of the S16 red sample. Their colours (Fig. 3.2) and estimated IR luminosities (Fig. 3.3) clearly point towards these being dusty star-forming sources, likely interacting/merging with their optically-bright close neighbours (see also Chapter 4). These galaxies are shown as empty symbols in Fig. 3.5. We note that given the faintness and surroundings of both sources we could not derive reliable stellar masses from multi-band SED fitting as for the other galaxies in our sample. The stellar mass estimates shown in the figure for A1 and A2 are derived from dynamical masses inferred from the CO[4-3] resolved emission and measured line widths, under the assumptions detailed in Chapter 4. As discussed in Chapter 4, at least for A1 this estimate is consistent with a stellar mass derived empirically from the F105W-F140W colours and F140W magnitudes as described above.

Fig. 3.5 thus shows our current best picture of the massive ($\log(M/M_{\odot})>10.5$) cluster galaxy population in the central region of Cl J1449+0856, highlighting once more (and to a more significant degree than previous work, e.g. Gobat et al., 2011, 2013; Strazzullo et al., 2013, 2016) its composite nature combining very actively star-forming galaxies and sources with already suppressed star-formation.

3.5 A panchromatic snapshot of a forming Brightest Cluster Galaxy at $z = 2$

Fig. 3.6 highlights the complex of multiple, likely interacting components located close to the center of the extended X-ray emission and galaxy overdensity in Cl J1449+0856, identified as the forming cluster proto-BCG (Gobat et al., 2011), and including sources H1, H4, H5, and A1.

We note that although other cluster members (H2, H6) have stellar masses consistent with the individual masses of H1, H4, and H5 (see S16 and Fig. 3.5), the configuration of the H1, H4, H5, A1 complex discussed here below, and its location with respect to the galaxy overdensity and X-ray emission, is clearly much more suggestive, as compared to H2 or H6, of the site of main formation of the future cluster BCG. We stress for clarity that we identify this galaxy complex as a whole as the *forming proto-BCG*, and that we do not observe in Cl J1449+0856 any galaxy already exhibiting the peculiar features of BCGs.

Within a radius of $r = 1.5$" we identify the two massive quiescent sources H4 and H5, the massive star-forming galaxy H1 with potentially sub-MS star-formation activity, and the optically faint and very red, mm-brightest cluster member A1, which is forming stars at a few hundred solar masses per year (Sections 3.3, 3.4.1, 3.4.2). Indeed, Spitzer/MIPS 24μm imaging already suggested this level of star-formation associated with the proto-BCG (with obvious uncertainties related to the probed rest-frame wavelength and poor angular resolution, Gobat et al., 2011). The combination of HST colour imaging and ALMA observations prove that the bulk of the star-formation in the proto-BCG is actually occurring in the optically-faint, seemingly minor component A1, rather than in the optically-bright source H1 as originally thought (Gobat et al., 2013; Strazzullo et al., 2013). Additional faint components and tails, whose cluster membership and properties cannot be reliably determined with the current observations, are observed within $r \lesssim 1.5$" from the proto-BCG (Fig. 3.6).

These observations are strongly suggestive of an actively forming BCG still assembling its stellar mass through star-formation and merging. This is in line with results from the few first studies on distant BCGs, suggesting a strong increase in the fraction of highly star-forming systems (Webb et al., 2015b; McDonald et al., 2016; Bonaventura et al., 2017), with $L_{\rm IR} > 10^{12} {\rm L}_{\odot}$ sources likely approaching $\gtrsim 50\%$ of BCGs towards $z \sim 2$. As also discussed in previous work (Webb et al., 2015a,b; Kubo et al., 2016; Bonaventura et al., 2017) gas-rich mergers might play a significant role in this phase of BCG evolution, as suggested by our observations as well (see also the related discussion on merger-driven star-formation in Cl J1449+0856 in Coogan et al. (2018), Chapter 4). Besides the on-going star-formation activity, we stress though that a significant fraction of the stellar mass in the proto-BCG complex has already evolved to a seemingly quiescent phase. The depletion timescale estimated in Chapter 4 for the most actively star-forming component A1 is of order 100 Myr. The overall picture is qualitatively reminiscent of hierarchical models (e.g. De Lucia & Blaizot, 2007; Tonini et al., 2012), though the observations presented here alone are obviously not sufficient to constrain the details of such modelling. Given the estimated (baryonic) masses of A1, H1, H4, H5 and their relative projected distance, an approximate estimate of the

merger timescale would be of order a few hundred million years (e.g. Lotz et al., 2011, the orbital timescale giving a lower limit of ∼100 Myr), with an estimated total stellar mass of the resulting BCG of $\sim 3 \times 10^{11} M_{\odot}$.

3.6 Summary

ALMA observations of the 870μm continuum and CO[4-3] line emission in the central region of Cl J1449+0856 have significantly improved our understanding of galaxy populations in this cluster core. Crucially, CO[4-3] follow-up secured spectroscopic confirmation of optically faint, mm-bright cluster members, while questioning the membership of the two brightest 870μm sources in the field.

The 870μm continuum and CO[4-3] line emission yield a total estimated SFR within the probed $\sim$ 0.08 Mpc^2 region of $\sim$ 700 $\pm$ 100 M$_{\odot}$/yr, resulting in a projected SFR density of $\sim 0.9 \pm 0.1 \times 10^4$ M$_{\odot}$ yr^{-1}Mpc^{-2}, and a SFR volume density five orders of magnitude larger than in the field at the same redshift. The inferred lower limit (that is, not correcting for the missing SFR from the portion of the virial volume not probed by the ALMA observations) on the SFR density per halo mass is SFR/M$_{halo}$ $\gtrsim$ 1300$\pm$400 M$_{\odot}$ yr^{-1} / 10^{14}M$_{\odot}$, which at face value is consistent with extrapolations from lower redshift observations predicting high SFR densities in massive (yet sub-10^{14}M$_{\odot}$) haloes at this redshift (see discussion in Sec. 3.4.1). In spite of its relatively significant SFR density, the core of Cl J1449+0856 seems nonetheless far from the $>$ 3000 M$_{\odot}$ yr^{-1} observed within a similar (or smaller) clustercentric distance in the similarly massive Cl J1001+0220 at $z = 2.5$ (Wang et al., 2016). Three of the five most massive galaxies (H2, H4, H5, log(M/M$_{\odot}$)∼11$\pm$0.1) in the core of Cl J1449+0856 are seemingly quiescent sources remaining undetected at least 2σ below the Main Sequence (the other two being the MS star-forming galaxy H6 and the possibly suppressed H1, see Section 3.4.2, Fig. 3.5), compared to a star-forming galaxy fraction of 80% observed at $M \geq 10^{11} M_{\odot}$ in the core of Cl J1001+0220 (Wang et al., 2016).

The combination with previously available HST imaging (and grism spectroscopy) critically enhances the interpretation of these observations. Although there is generally a close correspondence between the mm- and optical/NIR-inferred pictures of most cluster galaxies discussed here, there are particular sources that can only really be understood by comparing the two. The bright ALMA sources A1 and A2 are associated with optical counterparts otherwise deemed comparatively minor components in the HST NIR imaging. Fig. 3.2 underlines that, if deep high-resolution colour imaging were not available, these ALMA detections would appear as dust and gas significantly offset from stellar emission in the nearest optical/NIR counterpart. The HST imaging reveals

instead the faint, extremely red components perfectly matching the sub-mm emission, and probably related to very recent or ongoing merging events (see further discussion in Chapter 4).

The HST and ALMA synergy also provides another striking snapshot of the early evolution of forming BCGs in this cluster (e.g. Webb et al., 2015a; Kubo et al., 2016, see Sec. 3.5), with a seemingly multiple-merger system of quiescent and highly star-forming components likely assembling the future BCG.

The results based on ALMA observations presented here extend the reach of previous studies in Cl J1449+0856, drawing quantitative details in a picture combining, right into the cluster core, star formation activity approaching a thousand solar masses per year, the first massive quiescent cluster-core galaxies, and the ongoing formation of the BCG through merging of already quiescent and still vigorously star-forming components.

Contribution

I performed the data reduction and analysis of the ALMA continuum and line observations in this chapter, as described in Section 3.2. I calculated CO[4-3] line fluxes and dust continuum fluxes, as well as star-formation rates from these submillimeter data. I also provided feedback for the interpretation of Strazzullo et al. (2018), as it is a companion paper to Coogan et al. (2018, Chapter 4). Chapter 3 is largely based on observations from ALMA programs 2012.1.00885.S and 2015.1.01355.S and HST programs GO-11648 and GO-12991.

Chapter 4

Merger-driven star formation in Cl J1449+0856 at z=1.99 as seen by ALMA and the VLA

This chapter was published in Coogan et al. (2018), Monthly Notices of the Royal Astronomical Society, Volume 479, Issue 1, pages 703-729.

Co-authors are: E. Daddi, M. T. Sargent, V. Strazzullo, F. Valentino, R. Gobat, G. Magdis, M. Bethermin, M. Pannella, M. Onodera, D. Liu, A. Cimatti, H. Dannerbauer, M. Carollo, A. Renzini and E. Tremou.

Abstract

We use ALMA and VLA observations of the galaxy cluster Cl J1449+0856 at z=1.99, in order to study how dust-obscured star-formation, ISM content and AGN activity are linked to environment and galaxy interactions during the crucial phase of high-z cluster assembly. We present detections of multiple transitions of ^{12}CO, as well as dust continuum emission detections from 11 galaxies in the core of Cl J1449+0856. We measure the gas excitation properties, star-formation rates, gas consumption timescales and gas-to-stellar mass ratios for the galaxies. We find evidence for a large fraction of galaxies with highly-excited molecular gas, contributing $>$50% to the total SFR in the cluster core. We compare these results with expectations for field galaxies, and conclude that environmental influences have strongly enhanced the fraction of excited galaxies in this cluster. We find a dearth of molecular gas in the galaxies' gas reservoirs, implying a high star-formation efficiency (SFE) in the cluster core, and find short gas depletion timescales τ_{dep} $<$0.1-0.4 Gyrs for all galaxies. Interestingly, we do not see evidence for increased specific star-formation rates

in the cluster galaxies, despite their high SFEs and gas excitations. We find evidence for a large number of mergers in the cluster core, contributing a large fraction of the core's total star-formation compared with expectations in the field. We conclude that the environmental impact on the galaxy excitations is linked to the high rate of galaxy mergers, interactions and active galactic nuclei in the cluster core.

4.1 Introduction

The evolutionary path of galaxies between the peak epoch of mass assembly (z$\sim$2) and the local Universe is complex, with many different processes influencing galaxy properties throughout cosmic time. The physical mechanisms that lead to the cessation of star-formation, so-called galaxy 'quenching', are still highly debated, and are among of the most important unsolved issues in galaxy evolution to date. Having well established that a population of early-type galaxies dominate the cores of galaxy clusters in the local Universe, the environmental effect on the evolution of galaxies has become a central aspect of current galaxy evolution studies. In order to better understand the origins and transformations of local cluster galaxies, we must trace these galaxies back in time, to the epoch of both peak galaxy and cluster assembly.

Several studies have suggested a reversal in the SFR-density relation at z$\sim$1 (e.g. Elbaz et al. 2007; Cooper et al. 2008; Tonnesen & Cen 2014), where we see the star-formation rate of galaxies start to increase with local galaxy density, contrary to what is observed in the Universe at z=0. High-z galaxy clusters are therefore a perfect laboratory for studying the environmental effects on the evolution of the galaxies that will form the most massive quenched galaxies in the local Universe. Direct observation of cluster galaxies at z$\sim$2 gives us insight into the relevance of (and link between) star-formation, active galactic nuclei activity and mergers in over-dense regions. An increase in SFRs in clusters at z$\geq$1.5 with respect to local clusters has been observed, building up the bulk of the stellar mass in these huge structures (e.g. Hilton et al. 2010, Hayashi et al. 2011, Brodwin et al. 2013, Tran et al. 2015). It has also been shown that galaxy mergers, interactions and AGN activity are enhanced in high redshift (proto)clusters (e.g. Lotz et al. 2013, Krishnan et al. 2017), and whether or not this causes a suppression or enhancement of the overall star-formation activity in these structures with respect to the coeval field is still a matter of debate.

Many processes have been invoked to explain the evolution and quenching of cluster galaxies. If galaxies in dense environments have an increased star-formation efficiency with respect to the coeval field, synonymous with rapid gas depletion, this could give rise to rapid galaxy evolution and quenching in cluster environments. Cluster-specific interactions with the intra-cluster medium

such as ram-pressure stripping, strangulation and harassment are effective at removing the atomic Hydrogen gas surrounding galaxies in clusters at z=0, and could potentially give rise to the population of quenched galaxies in the cores of local clusters if these processes are still efficient at z>0 (e.g. Gunn & Gott 1972, Aguilar & White 1985, Peng et al. 2015). However, the direct environmental effect on the fuel for star-formation, molecular gas (H_2), is not well understood, and obtaining observations of the star-forming gas in these systems becomes increasingly difficult at higher redshifts.

This study investigates the environmental effect on the cold gas reservoirs of galaxies in one of the highest redshift spectroscopically-confirmed, X-ray detected clusters discovered to date, Cl J1449+0856 at z=1.99 (Gobat et al., 2011). This is an important time for both galaxy mass assembly and cluster evolution, as it is the last epoch before star-formation must rapidly quench to form the massive, passive galaxies that dominate the cores of clusters seen at lower redshift (e.g. Gobat et al. 2008, Mancone et al. 2010, van der Wel et al. 2010). Unlike the less evolved protoclusters more commonly found at z>2, Cl J1449+0856 shows extended X-ray emission originating from hot plasma in the ICM, and already hosts a population of red, quiescent galaxies in its core alongside a number of highly star-forming galaxies. These passive galaxies are in fact starting to form a red sequence, a defining signature of dense environments, as observed in local galaxy clusters (e.g. Spitler et al. 2012, Strazzullo et al. 2016). Cl J1449+0856 also contains a diverse star-forming galaxy population, with a number of very low-metallicity, highly star-forming galaxies identified towards the edges of the cluster, possibly due to large-scale gas inflow (Valentino et al., 2015). There are also two active galactic nuclei confirmed in the cluster, thought to be powering a vast Lyman-α bubble in the core (Valentino et al., 2016). Cl J1449+0856 is a typical progenitor of present-day galaxy clusters with a mass of $\sim 6 \times 10^{13} M_{\odot}$ (Gobat et al., 2011; Valentino et al., 2016), and to date has tens of spectroscopically confirmed members (Gobat et al., 2013; Strazzullo et al., 2013). It is therefore a perfect candidate for studying the effects of a maturing cluster environment on the star-formation and evolution of galaxies at high-z.

Thanks to recent developments in the capabilities of sub-mm and radio observatories, increasing numbers of studies have started to emerge focussing on the molecular gas content of field galaxies at high redshift (e.g. Saintonge et al. 2011, Schinnerer et al. 2016, Huynh et al. 2017, Tacconi et al. 2018). Use of sub-mm and radio data allows us to measure both the dust and cold molecular gas contents of galaxies, essential to understanding the baryonic processes shaping the galaxies. The H_2 gas content of the interstellar medium is measured indirectly, based on the tracer molecule ^{12}CO (CO), via the CO-to-H_2 conversion factor $\alpha_{\rm CO}$, (see e.g. Bolatto et al. 2013).

Measurement of the extended cold gas reservoir in galaxies is estimated from the J=1-0 transition of CO, where J is the rotational quantum number of the electron state within the CO molecule. The J=1-0 transition is important in the context of galaxy evolution as it gives an indication of the total amount of fuel that is available to form stars, and therefore the time until the galaxy will quench (assuming that star-formation continues at its current rate and gas reservoirs are not replenished through accretion). Different populations of star-forming galaxies have been shown to have different relative abundances of molecular gas in different excitation states, with local ULIRGS and starburst galaxies having relatively more dense gas driving their high levels of star-formation, possibly due to mergers and interactions compacting the gas.

For the majority of field galaxies, the increase of SFR with increasing look-back time comes hand-in-hand with an increase in molecular gas fraction (and, to a lesser extent, star-formation efficiency). The interplay between these has been encapsulated in so-called 'scaling relations' in several recent studies referring to large, statistical samples (e.g. Santini et al. 2014; Sargent et al. 2014; Genzel et al. 2015; Scoville et al. 2017; Tacconi et al. 2018). Similarly, cosmological simulations and semi-analytical models have started to predict the relative importance of molecular gas as a function of redshift, and find that the role of H_2 in galaxies becomes increasingly dominant at higher redshifts (e.g. Lagos et al. 2011, 2015). However, similarly complete studies have not yet been achieved at z>1.5 in cluster environments. There is a real need for convincing detections of molecular gas in high redshift clusters, that will allow us to better characterise cluster galaxies and identify the impact of environment on the star-formation processes at these early times.

Previous studies of galaxies in clusters tend to be split between mature cluster environments at z≤1.6, and very gas-rich environments at earlier epochs. Lee et al. (2017) recently measured the gas fractions and environmental trends in a protocluster at z=2.49, finding the molecular gas masses and fractions to be on average the same as in similar field galaxies, and that the gas fraction increases with decreasing galaxy number density per unit area. Wang et al. (2016) also study the environmental effects at high redshift, in the most distant X-ray detected cluster to date at z∼2.5. This cluster is dominated by gas-rich, highly star-forming galaxies with very few quiescent galaxies yet evolved in the core. They find short gas depletion timescales (τ_{dep}) of order ∼200 Myrs, driven by a high fraction of starburst galaxies amongst the numerous star-forming galaxies. On the other hand, Dannerbauer et al. (2017) reported the first CO[1-0] detection of a normal, star-forming disk galaxy in a protocluster at z=2.15, and compiling previous CO[1-0] detections found no environmental dependence of star-formation efficiency in protocluster galaxies. Noble et al. (2017) recently studied three separate clusters at z∼1.6 containing a higher fraction of quenched galaxies. They found evidence for star-forming galaxies with higher gas fractions than in the field,

and with significantly longer gas depletion timescales, averaging τ_{dep}=1.6 Gyrs. They find that the evolution of gas fractions in cluster galaxies mimics that of the field, and suggest that dense cluster environments may encourage the formation of molecular gas compared to the field, or somehow prevent a portion of this gas from actively forming stars. Rudnick et al. (2017) were also able to obtain deep CO[1-0] data for a forming cluster at z$\sim$1.6, and find that the two detected galaxies have gas fractions and star-formation efficiencies consistent with field scaling relations.

Reaching down to z$\sim$1.46, two groups studying cluster XCS J2215 both conclude that there is a suppression of the cold molecular gas in the core, having suffered environmental gas depletion that will lead to the quenching of star-formation on short timescales (Hayashi et al., 2017; Stach et al., 2017). Stach et al. (2017) suggest that environmental processes may be stripping the more diffuse ISM, reducing the gas fractions in the galaxies and increasing their ratio of excited to diffuse gas.

The work presented here probes the molecular gas content of cluster galaxies, in a higher redshift environment than the majority of similar studies. Cl J1449+0856 provides a high-density environment for comparison with field galaxies during an important transitional phase of cluster evolution, allowing us to place better constraints on theoretical models of galaxy evolution in cluster progenitors (e.g. Saro et al. 2009). In Section 4.2, we describe the available datasets and their reduction routines. In Section 4.3, we present our results for several excitations of CO in our cluster galaxies, and derive physical galaxy properties such as star-formation rates and dust masses. In Section 4.4, we compare our findings with similar field studies and assess the environmental impact on the molecular gas properties of the cluster. We summarise our conclusions in Section 4.5. Throughout this chapter, a ΛCDM cosmology is adopted, with H_0=70kms^{-1}Mpc^{-1}, Ω_M=0.3 and Ω_Λ=0.7. We use a Chabrier initial mass function (Chabrier, 2003).

4.2 Observations and data reduction

Cl J1449+0856 was observed over a wide range of radio and submillimetre frequencies, presented below. This allowed us to measure the line fluxes of three separate CO transitions and the continuum underneath these lines, in order to study the molecular gas content and excitations of the galaxies. The ALMA band 4 and band 3 observations covered the expected frequency of the CO[4-3] and CO[3-2] lines respectively, and the VLA Ka-band data targeted the CO[1-0] line. We also study the submillimetre-radio spectral energy distributions of the galaxies, using the continuum underneath the CO lines from the above observations, as well as ALMA band 7 and VLA 3 GHz continuum observations. These observations were used to calculate the dust contents of the galaxies.

The observing runs, data reduction and flux extraction performed on each of these datasets are outlined in the following subsections, and summarised in Table 4.1.

Telescope	Pointing	Date Completed	Ave. Freq. (GHz)	Bandwidth (GHz)	On-source time (h)	FWHM$_{syn.beam}$ (")	PA$_{syn.beam}$ (°)
ALMA	Core, mosaic	December 2014	345.0	7.5	2.3	1.41×0.62	64.5
ALMA	Core, single	May 2016	146.9	7.5	2.0	1.19×0.96	-44.8
ALMA	Outskirts, single	May 2016	146.9	7.5	0.4	1.17×0.97	-34.1
ALMA	Core, single	June 2015	107.9	7.5	2.0	1.36×1.31	-5.8
VLA	Core, single	March 2012	38.2	2.0	15.5	0.70×0.64	-20.2
VLA	Core, single	November 2012	3.0	2.0	12.5	0.50×0.44	-9.61

Table 4.1: Summary of the observations discussed in this chapter. The telescope, pointing target (Cl J1449+0856 core/outskirts) and mode (pointing/mosaic), date, average frequency, bandwidth, on-source time, FWHM and position angle of the synthesised beam are shown. For the 3 GHz data, the synthesised beam given is for the A-configuration data. The on-source time given is the addition of the A- and C-configuration data.

4.2.1 ALMA Band 4 Observations

ALMA band 4 observations of the cluster were collected in two single pointings during Cycle 3 (Project ID: 2015.1.01355.S, PI: V. Strazzullo). One of these pointings was a deep observation of the core of Cl J1449+0856, and the other was a shallower observation of the low metallicity members in the outskirts of the cluster (Valentino et al., 2015). Observations were completed in May 2016, for a total on-source time of $\sim$2h in the core, and $\sim$30 minutes in the outskirts. The band 4 observations target the CO[4-3] line.

For both pointings, the CO[4-3] line at this redshift was contained in a spectral window (SPW) centered at 153.94 GHz, with a bandwidth of 1.875 GHz and a spectral resolution of $\sim$1953.1 kHz ($\sim$3.8 kms^{-1}). The remaining three SPWs were set up for continuum observations, centered at 152.00 GHz, 140.00 GHz and 141.70 GHz respectively, each with bandwidths of 1.875 GHz and spectral resolutions of 62.5 MHz ($\sim$123.27kms^{-1}). The FWHM of the primary beam at this frequency is $\sim$40.9". For the core pointing, quasar J1550+0527 was used for flux calibration, and the synthesised beam was 1.19"$\times$0.96" at a position angle (PA) of -44.8°. The 1σ noise for the data in the core pointing was 10 mJykms^{-1} over 100kms^{-1}. Over the entire bandwidth, the continuum root-mean-squared (RMS) noise was 7.98μJy/beam. From this, we were able to detect an equivalent star-forming population down to a 5σ detection limit at z=2 of $\sim$32M$_{\odot}$yr^{-1}, for a Main Sequence galaxy with a CO[4-3] linewidth of 400kms^{-1} (the approximate average CO[4-3] linewidth found for our sample, see Table 4.4).

For the off-center pointing of the low-metallicity galaxies, Titan was used for flux calibration. The synthesised beam was 1.17"$\times$0.97" at PA = -34.1°, with 1σ noise of 23.7mJykms^{-1} over 100kms^{-1}. The RMS over the whole continuum bandwidth was 19.1μJy/beam. From this, we were able to detect an equivalent star-forming population down to a 5σ detection limit at z=2 of $\sim$75M$_{\odot}$yr^{-1}, for a Main Sequence galaxy with a CO[4-3] linewidth of 400kms^{-1}.

4.2.2 ALMA Band 3 and 7 Observations

ALMA band 3 observations were taken in a single pointing on the cluster core in Cycle 1 (Project ID: 2012.1.00885.S, PI: V. Strazzullo). Observations were completed in June 2015 for a total on-source time of $\sim$2h. For band 3 observations, Titan was used for flux calibration. The CO[3-2] line was contained in a SPW centered at 114.93 GHz. The other SPWs were centered at 112.94 GHz, 102.90 GHz and 101.00 GHz respectively. As with the CO[4-3] observations, the line-free SPWs were used to measure continuum fluxes. Each SPW covered a bandwidth of 1.875 GHz and had a spectral resolution of 1953 kHz (5.09 - 6.00kms^{-1}). The FWHM of the primary beam was $\sim$54.8", with a synthesised beam FWHM of 1.36"$\times$1.31" at PA = -5.8°. The noise over 100kms^{-1} was

12 mJykms^{-1} and the continuum RMS was 8.36μJy/beam.

Band 7 observations were taken as part of the same project, using seven single pointings centered at 345 GHz (870µm) to cover the cluster core over an 0.3arcmin^2 area. Observations were completed in December 2014 for a total on-source time of ∼2.3h. Quasar J1337-1257 was used for flux calibration. Band 7 observations allowed us to derive continuum SFRs for the cluster galaxies, down to a 3σ SFR detection limit at z=2 of ∼21M$_\odot$yr^{-1}, for a Main Sequence galaxy. These observations also allowed us to put constraints on the normalisation of the submillimetre portion of the spectral energy distributions. All four SPWs were set up for continuum observations, covering a bandwidth of 7.5 GHz between ∼338-340 GHz and ∼350-352 GHz. The spectral resolution for these observations was lower, at 31.25 MHz (26.6 - 27.7kms^{-1}). The RMS noise was 67.5μJy/beam, with a FWHM resolution of the synthesised beam of 1.41"×0.62" at PA = 64.5°.

4.2.3 VLA Ka-band Observations

Deep high frequency data of Cl J1449+0856 was taken using the Karl G. Jansky Very Large Array, in order to measure the CO[1-0] lines in the cluster galaxies (project code: 12A-188, PI: V. Strazzullo). These observations were completed in March 2012, for a total on-source time of ∼15.5h in configuration C. Quasar J1331+3030 was used for flux calibration. A total bandwidth of 2.048 GHz centered at 38.15 GHz was observed over 16 SPWs in a single pointing, with a spectral resolution of 4000 kHz (29.2 - 32.3kms^{-1}). The CO[1-0] line falls in either SPW 10 or 11 or is split across both depending on the redshift, with the rest of the SPWs being used for continuum observations. The FWHM of the primary beam was ∼79.1", with a synthesised beam of 0.70"×0.64" at PA = -20.2°. The 1σ spectral noise over a 100kms^{-1} width was 4 mJykms^{-1} with a continuum RMS of 3.30μJy/beam. The depth of these observations also allowed for the 5σ detection of CO[1-0] emission from Main Sequence star-forming galaxies with SFR∼33M$_\odot$yr^{-1} assuming a CO[1-0] linewidth of 400kms^{-1}.

4.2.4 VLA S-band Observations

Continuum observations centered at 3 GHz were also obtained for the cluster using the VLA (project code: 12A-188, PI: V. Strazzullo). These observations were carried out between February and November 2012, for a total on-source time of ∼1.1h in configuration C and ∼11.4h in configuration A. Quasar J1331+3030 was used for flux calibration. These observations were used to model the radio frequencies of the galaxies' SEDs, and calculate SFRs from the radio luminosities. The primary beam FWHM of the 3 GHz observations was 15', and the FWHM of the synthesised beam at this wavelength was ∼0.50"×0.44" at PA = -9.61° for the A-configuration data, with an

RMS noise of 1.6μJy/beam. In the C-configuration, the synthesised beam was $\sim$7.0"$\times$6.1" at PA = -16.47°, with an RMS noise of 8.8μJy/beam.

The ALMA band 4, band 3, band 7, and VLA Ka-band data were calibrated using the standard reduction pipeline in Common Astronomy Software Applications (CASA, McMullin et al. 2007). For the band 3 and 7 observations, CASA version 4.2.2 was used for reduction. For band 4, version 4.5.3 was used. For the VLA K-band data, version 4.4.0 was used. For the VLA S-band data, the standard reduction pipeline was used to calibrate the A-configuration data, and manual calibration using CASA 4.6.0 was performed for the shorter configuration-C scheduling blocks.

4.2.5 Spectral flux extraction

The spectral line fluxes for all three CO transitions (CO[4-3], CO[3-2] and CO[1-0]) were extracted using the Gildas[1] tool `uvfit` directly on the uv-visibility data. The line-free continuum fluxes underneath the CO lines were also extracted from the uv-visibilities.

We see in Figs 4.1 and 4.2 (see also galaxy IDs) that for spectroscopically confirmed cluster members with HST/WFC3 counterparts, the signals in the submillimetre maps are consistent with the rest-frame optical positions, and no systematic offset is suggested by the data. Spectral extractions initially searching for the CO[4-3] line were therefore made at fixed rest-frame optical position of spectroscopically confirmed cluster members, and also at the positions of ALMA continuum detections (SNR$>$3). Once these spectra had been extracted, a line-searching algorithm was run over each 1D spectrum. The algorithm returned both the signal-to-noise (S/N, SNR) of the brightest line found in the spectrum, and the optimum velocity range to be considered as the linewidth, in order to maximise the S/N.

Having identified the galaxies with detected CO[4-3] lines in this way, the size and flux of the CO[4-3] emission in each galaxy was measured using the collapsed observational data across the optimised CO[4-3] linewidth. As stated, the flux extraction over this collapsed data was performed using `uvfit` directly on the uv-visibilities. In all cases except A1 and A2, the CO[4-3] line fluxes of the galaxies were measured at fixed rest-frame optical position in the collapsed line data. In the case of strong band 4 continuum detections with faint optical counterparts (A1 and A2, see Figs 4.1 and 4.2), the position of the emission was free to be optimised by the uv-fitting on the collapsed data. Sources that were not resolved in CO[4-3] were extracted as point-spread-functions (PSFs). Similarly, if the emission could be significantly resolved by `uvfit` (SNR$>$3 for the measured size in uv-space), the shape of the emission was fit as a 2D Gaussian with freely varying amplitude,

[1] http://www.iram.fr/IRAMFR/GILDAS

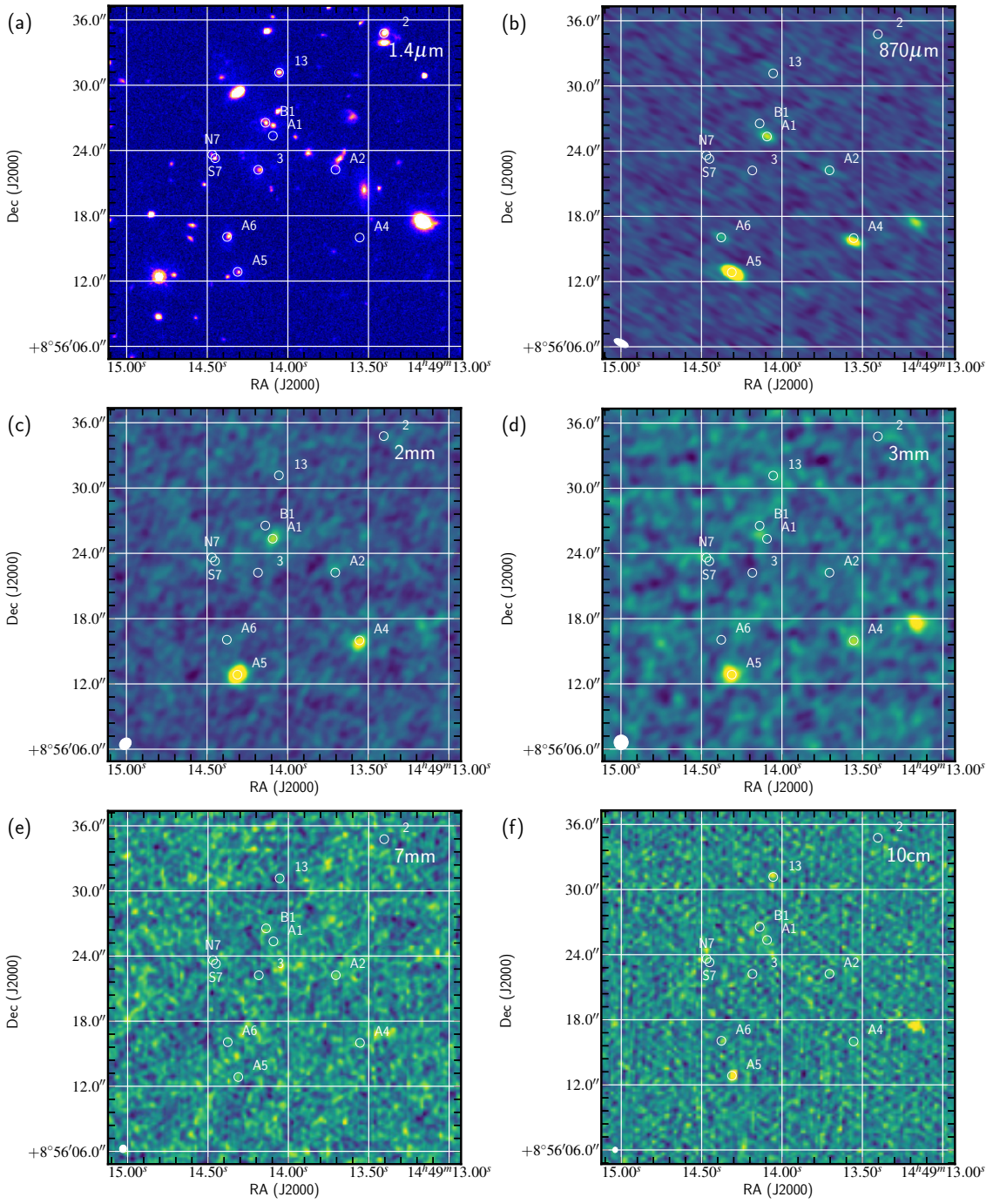

Figure 4.1: Continuum images of Cl J1449+0856: (a) near infra-red 1.4μm (HST/WFC3), (b) 870μm (ALMA), (c)-(d) 2mm and 3mm (ALMA), (e)-(f) 7mm and 10cm (VLA). Any line emission present has not been removed from the images. The signal-to-noise of the galaxies can be seen to decrease towards the longer wavelengths. In the 10cm image, only the deep, high-resolution A-configuration data is shown, without the C-configuration. The images have not been corrected for the primary beam attenuation of the instruments. The galaxies indicated show the positions of the galaxies for which we find CO[4-3] detections, with the exception of A4 and A5, which are discussed in Section 4.3.8, and ID 2, which is only detected at 870μm. A bright foreground galaxy can be seen to the West of A4, which has been spectroscopically confirmed at z=1.3, and will therefore not be discussed in this chapter.

shape and position angle. `uvfit` measures the sizes of sources by inspecting the relation between measured flux and uv-distance.

Given the crowded nature of the field, it is important to ensure that all fluxes are extracted without contamination from neighbouring sources. The `uvfit` tool allows simultaneous modelling of up to four sources at any time. We therefore first extracted the spectra of the brightest sources in the field of view simultaneously, and then subtracted these bright sources from the data. We then modelled the next brightest sources simultaneously in the data, with the first four sources already removed. This process was repeated iteratively until all of the sources had been modelled and then removed from the data. In this way, we ensured that flux from bright sources did not contaminate the extracted fluxes of fainter galaxies. We also verify that the order in which the sources were modelled does not significantly affect our results, as the power contained in the side-lobes of the known ALMA beam contain only a fraction of the power of the beam core. As our detections are not extremely bright, the side-lobes of the PSF do not carry significant amounts of flux. Additionally, the small redshift variations between the cluster galaxies result in the spectral lines being offset in frequency. However, in the case of A1 and B1, line fluxes were extracted for both sources simultaneously in each collapsed dataset, to prevent any contamination between the two, due to their very small redshift separation. No other line or continuum sources were identified in our maps other than those modelled in this way.

In order to remove the continuum contributions to the measured line fluxes, the line-free spectral channels were collapsed and averaged, and an average continuum flux was measured by `uvfit` at the same position and size as was done for the line flux. The frequency of the measured continuum was therefore close to the frequency mid-point of the total bandwidth. In order to find the continuum contribution under the line flux, we used a two-component model, $y = a\nu^b$, to model the continuum, where y is continuum flux and ν is frequency. We calculated the normalisation factor, a, from our average continuum flux and frequency, and extrapolated to the frequency under the line using a fixed spectral slope $b = 3.5$. This was then subtracted from the measured line flux.

Once the flux, position and size of the line emission had been measured from the collapsed data in this way, the full 1D spectra were re-extracted at fixed position and size in each spectral channel, binned into velocity slices of 30kms^{-1}. These 1D spectra were used to model the shapes of the line profiles, but the line fluxes used for analysis are from the collapsed data only.

For the CO[3-2] and CO[1-0] lines, line fluxes were extracted over the same linewidth as was used for the CO[4-3] lines, centered at the expected frequency of the relevant transition based on the CO redshift derived from the CO[4-3] line. This was again done in the collapsed data by `uvfit`. The fluxes were extracted at the same positions as the CO[4-3] lines, and over the same

size. The continuum contributions to the line fluxes were treated as for the CO[4-3] line. All measured fluxes were then corrected for primary beam attenuation. In this way, all line fluxes were extracted consistently. If the different CO excitations were to have different underlying linewidths, they would be physically distinct components. By studying the emission properties over the same sizes and velocity ranges, we are ensuring a self-consistent, physically meaningful extraction of the CO spectral line energy distributions.

It is useful to note here that previous studies claim evidence for extended CO[1-0] reservoirs in certain galaxies, compared to their CO[4-3] emission (e.g. Stach et al. 2017). If the sources were meaningfully resolved by our smaller beams (e.g. the CO[1-0] dataset) but not resolved in our CO[4-3] dataset where we determine emission sizes, this could introduce a small source of bias. However, both the measured sizes of the cold CO[1-0] gas for our resolved galaxies, as well as the cold dust at 870µm, are consistent with the galaxy CO[4-3] sizes, verifying that our method does not exclude significant CO[1-0] emission. A comparison of these sizes can be seen in Table 4.2, where sizes are only shown if the flux itself has SNR$>$5. In order to measure sizes in CO[3-2], CO[1-0], 2mm and 3mm for this comparison, we fixed the position of the source at the position of the CO[4-3] emission, and left the shape of the emission to be fit as a circular Gaussian whose size was left free to vary. This was done in the uv-plane. For the 870µm sizes, those sources that were fit over an extended shape in the flux extraction, with free position, were also left free to fit as a circular Gaussian for comparison here, using the software GALFIT (Peng, 2010, see Section 4.2.6). It is important to note that these circular Gaussian sizes are presented for comparison only, they do not give the flux extraction sizes. As can be seen in Table 4.2, all of the constrained emission sizes are consistent within 2σ.

ID	FWHM$_{870\mu m}$	FWHM$_{150GHz}$	FWHM$_{108GHz}$	FWHM$_{CO4-3}$	FWHM$_{CO3-2}$	FWHM$_{CO1-0}$
A2	-	-	-	0.58±0.11	<0.66	0.43±0.14
A1	0.52±0.14	0.72±0.16	-	0.51±0.08	-	-
13	-	-	-	<0.31	-	-
6	<0.28	-	-	<0.33	-	-
N7	-	-	-	<0.32	-	-
B1	<0.54	-	-	-	-	-
3	-	-	-	-	-	-
S7	-	-	-	-	-	-
A5	0.40±0.03	0.33±0.06	0.65±0.17	N	N	N
A4	0.35±0.10	0.62±0.09	<0.65	N	N	N

Table 4.2: Continuum and line-emission sizes for the 8 galaxies with gas detections discussed in this chapter, plus two additional bright continuum sources in the cluster field of view. We present continuum emission sizes at 870µm, 150 GHz and 108 GHz, and sizes for the CO[4-3], CO[3-2] and CO[1-0] emission lines. The CO[4-3] sizes have been used for the uv-plane analysis in this chapter; the rest are shown for comparison to demonstrate consistency. The 870µm emission sizes have been circularised for comparison, where more extended sources were used for the flux extraction itself. It can be seen that in all cases, the sizes at the different continuum wavelengths and different excitation transitions of CO are consistent within 2σ. We do not see evidence for extended cold gas reservoirs that would be missed using the CO[4-3] emission sizes. Where the CO[4-3] emission is resolved, flux was measured over the resolved CO[4-3] shape for all CO transitions and associated continuum. Flux was extracted over the same shape at both 870µm and 3 GHz within GALFIT. Errors on the 870µm size have here been calculated using Equation 4.1, assuming the normalisation factor to be the average between that for the 150 GHz and 108 GHz continua. 2σ upper limits are shown on the emission sizes for those sources that aren't resolved here, but have a flux SNR>5. The upper limits on the size of unresolved sources have also been derived from Equation 4.1, having calculated the normalisation using the resolved galaxies in the same dataset. Those entries marked with an 'N' highlight galaxies for which we detect no lines, to distinguish them from those in which the line emission is unresolved.

Overlays of the HST, 870μm data and CO[4-3] data are also shown in Fig. 3.2, suggesting that there is no evidence of substantial cold gas reservoirs at scales much larger than the beams that we are using. This is reasonable, as we are observing with resolutions that are larger than the typical size of our CO detections, and those sizes determined by HST imaging (Gobat et al., 2013; Strazzullo et al., 2013, 2016). By measuring the emission over the same size for each transition we are taking measurements on the same physical scales. If we were in fact missing components in CO[1-0] at wider scales, our measurements and the ratios between the different CO transitions would still be self-consistent. Although we do not see any evidence for this in our galaxies, if the CO[1-0] was more extended than the CO[4-3] gas, much of the gas in the outskirts would be at broader velocities than the CO[4-3] transition, and to use this high velocity CO[1-0] flux for our excitation analysis would result in a mixing of different physical components. By measuring line fluxes for the different CO transitions using the CO[4-3] emission sizes, we are primarily characterising the properties of the CO gas in the region where the galaxies are forming stars, and are able to draw conclusions on the gas excitations in the same region. This approach was also taken by Daddi et al. (2015). A risk of bias would arise if the CO[1-0] was much more compact than the CO[4-3] emission, in which case using extended extractions would overestimate the CO[1-0] line flux. This is however physically unlikely to be the case, as CO[1-0] is emitted by lower density gas.

As a final test of any differences in emission sizes, we perform additional CO[1-0] flux extraction using a fixed, Gaussian size, with FWHM equal to the 2σ upper limit on the CO[4-3] sizes presented in Table 4.2. This was done for those galaxies that were not resolved in CO[4-3]. We verify that this does not significantly increase our measured CO[1-0] fluxes, nor does it affect our conclusions on gas excitation.

4.2.6 Continuum flux extraction

In order to image all datasets (ALMA band 7, band 3, band 4, VLA Ka-band, S-band), the CASA routine `CLEAN` was used. This was performed for continuum mode='mfs' with natural weighting to maximise sensitivity, except for the 3 GHz data for which Briggs robust=0.0 weighting was used, as it gave the best balance between the resolution and sensitivity for the cluster field at this wavelength. This allowed us to derive primary-beam corrections and dirty-beam patterns for the instruments. With the exception of the 3 GHz map, the clean images were not used for data analysis, but are shown for visualisation in Fig. 4.1. The measurements for continuum fluxes at 150 GHz, 108 GHz and 38 GHz were taken from the ALMA band 4, band 3 and VLA Ka-band observations respectively. These were extracted in the uv-plane, using the collapsed line-free spectral windows, and extrapolating to the desired frequency. The procedure for this is described in Section 4.2.5.

Although we favour the method of flux extraction in the uv-plane, as it does not have the disadvantage of correlated noise introduced by the imaging process, it is not always possible. It was necessary to measure continuum fluxes in the image plane for the 870µm data, as the constructed mosaic could not be easily transported into the correct format for `uvfit`. Similarly, the large size of the 3 GHz dataset made conversion and analysis in the GILDAS format impractical.

In order to measure the 870µm continuum fluxes of the galaxies, GALFIT was used on the dirty, calibrated image. For those readers familiar with classical tools, GALFIT is an image plane flux-extraction software, similar in purpose to the `IMFIT` procedure in CASA, for example. We choose to use GALFIT on the images without first applying `CLEAN`, as we have full knowledge of the shape of the dirty beam with associated PSF side-lobes, derived directly from the known antenna positions and baselines. In this way, our simultaneous modelling of all sources in the field of view using GALFIT was not subject to contamination between sources or side-lobes. We do however test the consistency between these two potential image plane flux extraction techniques: using `IMFIT` in CASA on `CLEAN`ed data (shown in Fig. 4.1), and using GALFIT with the dirty beam on dirty data. To do this, we perform continuum flux extraction on the same cluster sources using each of these techniques for the 870µm data. We recover statistically indistinguishable fluxes between the two image plane methods, and present our GALFIT-measured continuum fluxes for the analysis in this chapter, for both the 870µm and 3 GHz data.

Having quantified that `CLEAN` + `IMFIT` and GALFIT reproduce consistent fluxes in our image plane data, we perform a small simulation to compare the fluxes measured by GALFIT with those measured by `uvfit`. In doing this, we aimed to evaluate any systematic differences that might arise from extracting flux in the uv-plane vs. the image plane. We simulated sources in our 2mm continuum data, with sizes between a PSF and a circular Gaussian with FWHM=2". We chose these sizes as they cover the representative range of the sizes measured for the resolved cluster galaxies, as shown in Table 4.2. For each method (GALFIT or `uvfit`), we insert an input source of fixed size and flux into the data, and then re-extracted the flux as a measurement. This was repeated 1000 times per size. We find that both GALFIT and `uvfit` return flux distributions centered on the correct input flux, with dispersions reflecting the RMS noise of the data. Further details can be found in Appendix A. Finally, a comparison of continuum fluxes extracted for our cluster galaxies using both `uvfit` and GALFIT in our other datasets was made, verifying that the two methods again give consistent results.

Continuum fluxes were extracted at the fixed positions of HST/WFC3 rest-frame optical cluster members (e.g. Gobat et al. 2011, Valentino et al. 2015, Strazzullo et al. 2016) and at the positions of additional ALMA continuum detections (SNR>3). The positions of the strong 870µm sources

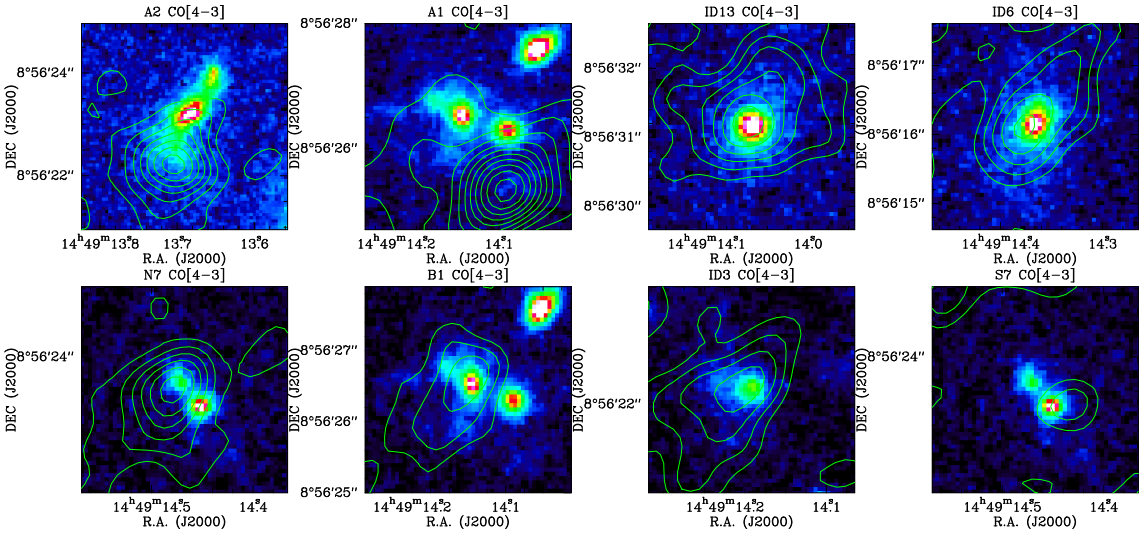

Figure 4.2: Rest-frame optical HST/WFC3 images of the galaxies in Cl J1449+0856 with CO[4-3] detections, overlaid with the CO[4-3] line contours in increments of 1σ. All contours start at 1σ. A large offset can be seen between bright optical counterparts and the dense CO[4-3] gas in A1 and A2.

seen in Fig. 4.1 were free to be optimised by GALFIT. If the emission could be resolved, i.e. when sizes could be measured with SNR$>$3, the size of the emission was left free to be fit by GALFIT. If the emission was not resolved, the galaxies were modelled as PSFs. Having run GALFIT, PSF-fitting was performed on the absolute values of the residual 870µm map, at the positions of all of the detected galaxies. We found all of the residuals to be of the order 1σ or less, with the exception of the very bright galaxy A5, for which 2σ residuals remained ($\sim$5% of the measured flux of A5). We do not expect these levels of residuals to affect our results. For the 3 GHz flux extraction, the A-configuration and C-configuration images were both `CLEAN`ed before using GALFIT with the synthesised beam as the PSF, as the wide field of view of the VLA means that several extremely bright radio galaxies were present in our 3 GHz image, for which the strong side-lobes needed to be first removed. The emission positions and sizes were fixed to those of the 870µm emission. Fluxes were measured separately in the A- and C- configuration data, and then combined for each galaxy, taking into account the weight of the flux based on the image RMS. The C-configuration data do not therefore significantly contribute to the 3 GHz flux measurements.

It is recognised that the flux uncertainties returned by GALFIT are often underestimated, which we also find to be the case for our measurements. Following standard practice, we therefore give the primary-beam corrected RMS value of the 870µm and 3 GHz maps for the point-source flux uncertainties in Table 4.3. For the resolved sources, we give twice the RMS value for the flux uncertainty. It is important to note here that the uncertainties on the quantities derived from

these data ($SFR_{870\mu m}$, M_d, $SFR_{1.4GHz}$ respectively) are much larger than those on the measured flux. The errors on these properties are dominated by factors such as the uncertainty on the dust temperature. These systematics are discussed in Section 4.3.

For the majority of the galaxies presented at 870µm in this chapter (8/11), we do not perform detection in the 870µm map, only flux measurement. Detection for these eight galaxies is done using the CO[4-3] line, as previously discussed. However, we also consider galaxies without a CO[4-3] line detection as a detection at 870µm, if the source has an 870µm continuum flux with SNR>5 (using the flux uncertainty values given in Table 4.3), or an SNR>2.5 for those sources where flux was measured at fixed position on top of an optical counterpart. In order to quantify the number of spurious sources we might detect at fixed position with SNR>2.5, we perform blind continuum extraction in the inverse-870µm map, for 500 randomly selected positions. This was done at fixed position, for a PSF shape. We find an expected number of ∼0.15 spurious sources in our data at SNR=2.5, based on the ∼25 sources for which we measure 870µm flux.

4.3 Results

4.3.1 Molecular gas detections

Images of Cl J1449+0856 in the rest-frame optical and in all five of our submillimetre-radio datasets are shown in Fig. 4.1. Prominent sources can be seen at 870µm, 2mm and 3mm. In order to investigate the molecular gas properties of our galaxies we first focus on our ALMA band 4 (2mm) data containing the CO[4-3] emission of the cluster galaxies, as this dataset is expected to have the highest signal-to-noise (thermally excited CO emission has flux $\propto J^2$, Daddi et al. 2015). Detecting galaxies in this way is closely equivalent to selecting galaxies in SFR, with the depth of our CO[4-3] data in the core pointing corresponding to a 5σ SFR detection limit of $\sim 32 M_{\odot} yr^{-1}$. Having extracted spectra at the positions of optical cluster members and prominent sub-mm detections, we find secure CO[4-3] line detections in seven galaxies, and a further tentative detection (S7), in the core of Cl J1449+0856. Galaxies 13, N7, B1, 3, 6 and S7 were extracted at fixed position corresponding to the rest-frame optical HST counterpart, increasing the reliability and robustness of these detections. By extracting spectra at fixed rest-frame optical position, we are removing the positional degree of freedom. This significantly reduces the likelihood of artificial flux boosting from the CO[4-3] data, and allows us to have more robust detections at lower signal-to-noise.

ID	$F_{870\mu m}$ (μJy)	F_{150GHz} (μJy)	F_{108GHz} (μJy)	F_{38GHz} (μJy)	F_{3GHz} (μJy)	Description
A2	515±135	29±9	<14	<9	<6	Merger
A1	1370±140	87±9	<15	<9	7±3	Merger
13	248±69	<16	19±7	<6	6±2	AGN
6	709±75	<18	<15	7±3	5±2	Prominent bulge
N7	217±79	<17	28±7	<6	5±2	Interacting
B1	346±69	<15	<11	<6	4±2	Merger
3	<141	<15	<13	<6	<3	Passive
S7	<150	<17	<15	<6	<3	AGN, interacting
A5	6047±150	359±15	96±8	<8	27±3	-
A4	1863±140	150±10	50±8	<9	<6	-
2	184±73	<18	<16	<6	<3	Prominent bulge

Table 4.3: Line-free continuum fluxes for the 8 galaxies with molecular gas detections, and two additional bright continuum sources in the cluster field of view. We also include a cluster member with a detection in 870μm, but no CO detections (ID 2). 2σ upper limits are shown. The final column gives a summary of the likely environment/state of each galaxy. Galaxy ID 3 was previously classified as 'passive' based on colour-colour criteria (Strazzullo et al., 2016).

We consider different detection thresholds for those line fluxes measured at fixed optical position, and for those for which the CO[4-3] position was fit by `uvfit`. For the galaxies for which spectra were extracted at fixed optical position, we consider two factors: both the signal-to-noise of the line flux, and the consistency of the line with the previously derived optical redshift. At these fixed positions, we impose a limit of SNR>3.5 on the extracted CO[4-3] line fluxes. When we include the effect of flux boosting by noise (see Section 4.3.1), this limit corresponds to a probability of ∼0.009 of the lines being pure noise, having accounted for de-boosting. In addition, at fixed position we also include the likelihood of the redshift of the detected line being consistent with the optical redshift, if it were a serendipitous detection. For those galaxies with the largest errors on their optical redshifts, ∼0.02-0.03, this corresponds to a likelihood of $\sim \frac{2.5}{7.5}$=0.3, from the uncertainty on the redshift in GHz, divided by the total bandwidth of the observations. When we combine the probabilities from the SNR and the redshift, our overall detection threshold gives a probability of <0.0029 of our detected lines being due to noise for single-parameter, pure Gaussian-like statistics. Galaxies 13, N7, B1, 3, and 6 are all above this detection threshold, and we find no CO[4-3] emission from other galaxies at fixed optical position under this criterion. We use this probability to calculate the expected number of spurious detections above our threshold, given the number of galaxies for which we extract CO[4-3] spectra. We find a value of only ∼0.1 spurious detections expected from our dataset.

In the cases of galaxies for which the CO[4-3] lines were free to be spatially optimised, we instead report only detections with SNR>5 (after accounting for flux de-boosting, see Section 3.2.1). A1 and A2 both lie on top of very faint, red, rest-frame optical counterparts and were left free to vary. We find no evidence for other lines at generic positions in the map that exceed our detection threshold.

We report galaxy S7 for interest, despite the fact that it does not formally satisfy our detection criterion, on the basis that we find the line at fixed spatial position on the sky, and the CO redshift derived overlaps with the previously measured optical redshift (see Fig. 4.3). We do however consider this line to be tentative, and we therefore do not include galaxy S7 when deriving physical properties of galaxies from these data.

In order to further quantify the number of spurious detections we might expect in the CO[4-3] data, we also performed blind spectral extraction in the ALMA band 4 data. We randomly selected 600 positions within the CO[4-3] dataset FWHM field of view, having removed all known sources from the map, and extracted a point-source spectrum at each fixed position. We subtracted the median continuum flux value, and applied our line-search algorithm over the spectral data. We find that for our lowest significance detection, B1, the number of spurious detections suggested by

these simulations at this SNR is ∼0.3 based on the ∼25 galaxies for which we originally extracted spectra, if we consider the full 1.8 GHz sideband. This is similar, but slightly higher, than the previous estimate. However, we notice that the redshift of this source is very close (to within 0.001) to the systemic redshift of this multiple-galaxy system. In fact, if we limit our simulation search even to just $1.98 < z < 2.0$, conservatively, we would only expect ∼0.04 spurious sources. This further confirms the robustness of our detections down to the level of B1.

We find no significant detections in any of our datasets for the low-metallicity galaxies towards the outskirts of the cluster (Valentino et al., 2015), and therefore return to further analysis of these galaxies in a future study. As discussed in Section 4.2, these galaxies were observed with a shallower pointing at 2mm than the core of the cluster.

We detect CO[4-3] emission in all of the cluster members that we see in the 870µm emission map, with the exception of galaxy ID 2 shown in Fig. 4.1. We inspect all of our datasets for evidence of additional strong spectral lines or continuum sources, to ensure that we are not missing galaxies that are not seen in CO[4-3]. We do not find any such source, and - due to the high sensitivity of the CO[4-3] data - a galaxy displaying bright CO[1-0] but not CO[4-3] emission would arguably have highly unusual excitation properties. However, as discussed, our CO[4-3] selection technique is biased, in that it is very similar to a SFR selection method. We therefore fully account for this when interpreting our results. Our key comparisons with previous studies, made in Section 4.4.2, are made with the same SFR selection limits in place.

Rest-frame optical images of the eight detected galaxies, overlaid with CO[4-3] line contours, can be seen in Fig. 4.2. We verify that the astrometry is consistent between our different datasets, using bright sources that appear in more than one image, including galaxies that are not cluster members. We find small offsets between the peak fluxes, with average $\Delta\mathrm{RA}_{peak} \sim 6.6 \times 10^{-3}$" and $\Delta\mathrm{Dec}_{peak} \sim 3.4 \times 10^{-2}$", much smaller than the positional accuracy. The CO detections in galaxies A1 and A2 are both clearly offset from the optical core of a massive galaxy nearby, separated by ∼0.95" and ∼1" respectively. It appears that although both galaxies A1 and A2 have strong CO emission, they are heavily dust-obscured. The bright optical neighbours of both galaxies are also spectroscopically confirmed cluster members, indicating that both galaxies are most likely part of gas- and dust-rich merging systems. The bright optical core near to galaxy A2 is one of the highly star-forming, low-metallicity galaxies presented in Valentino et al. (2015). Conversely, we see that for the other systems in which we detect CO-emission, the CO[4-3] and the optical counterparts for the galaxies peak on top of one another, such as for IDs 13 and 6. Small offsets between the CO[4-3] and optical emission are most likely driven by noise fluctuations. For all galaxies except for A1 and A2, the offset between the peak CO[4-3] and optical counterparts reaches only

$\lesssim$0.16", approximately one tenth of the size of the synthesised beam (with the exception of our tentative detection S7, $\sim$0.3"). These offsets are typically at $<2\sigma_{pos}$ significance with respect to the uncertainty on the CO[4-3] position returned by `uvfit` when left free to vary. This positional uncertainty was verified through simulations of injected point sources[2]. As stated above, we therefore choose to extract the spectra and line flux at fixed rest-frame optical position for all galaxies apart from A1 and A2, in order to minimize the effects of noise fluctuations. If we were to instead extract fluxes at the CO[4-3] peak position, the increase in flux would be $<1\sigma$ in all cases.

Galaxy characteristics

As can be seen in Fig. 4.2, we are detecting star-forming gas in several different types of galaxy. Two detected galaxies are part of the interacting system currently forming the future brightest cluster galaxy (A1 and B1), and it can be seen that the emission from B1 in this system is somewhat broad and potentially diffuse. It should be noted that B1 corresponds to galaxy H1 in Strazzullo et al. (2016) and Strazzullo et al. (2018, Chapter 3, see also Table 2.2). As discussed above, we also detect gas in another probable merger with a nearby low-metallicity optical component (A2), galaxies with prominent compact bulge components (galaxies 6 and 3), active galactic nuclei (galaxies 13 and S7), and an additional star-forming galaxy (N7) that is interacting with galaxy S7 at close projected separation. These characteristics are also summarised in Table 4.3.

Due to the dense environment of the cluster core, we must consider not only the projected separations of our merging sources, but also the velocity distances between them, to ensure that they are not simply projection superpositions. We compare the CO redshifts of our merging sources with the optical redshifts of their close companions, and find that the velocity offsets are also consistent with real merging or interacting systems. We find velocity offsets of $\sim$15kms^{-1} between A1 and its companion, and $\sim$15kms^{-1} between B1 and the same companion, confirming that A1 and B1 are indeed part of the merging system assembling the future BCG. We find a velocity distance of $\sim$590kms^{-1} between A2 and its bright companion, again confirming the merging nature of this galaxy pair. Finally, we find the velocity separation between the very close pair N7 and S7 to be $\sim$1380kms^{-1}, consistent with an interacting pair of galaxies at a projected separation of $<$0.5". We note that galaxies are regarded as members of Cl J1449+0856 if they lie within $\sim$2500kms^{-1} of the cluster systemic velocity, according to Gobat et al. (2013). We can therefore assert that the large number of merging galaxies that we detect is not biased by projection effects.

[2]Representative, S/N-dependent positional uncertainty values $\sigma_{\rm pos}$ were derived by injecting and re-extracting simulated point sources.

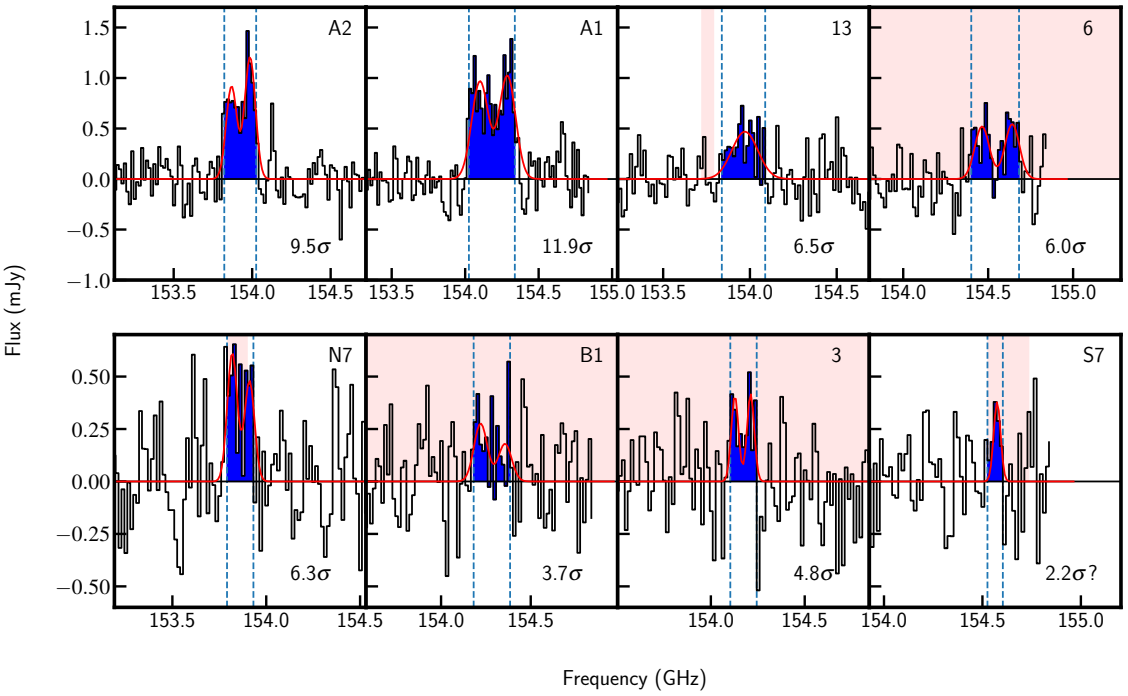

Figure 4.3: CO[4-3] line detections for eight galaxies in Cl J1449+0856. The blue shaded regions highlight the flux over the linewidth of the CO[4-3] emission, and the blue dashed lines delimit the linewidths, as discussed in the text. The red curves show the Gaussian line profiles that were fit to the data. The red shaded regions show the 1σ limits of the measured optical redshift, where available. The significances of the lines, shown in the bottom-right corner of each panel, were measured from the data collapsed over the linewidth indicated by the dashed lines. A1, A2, B1, N7 and S7 are all part of merging or interacting systems. IDs 13 and S7 are both AGN, ID 6 is a galaxy with a prominent compact bulge component, potentially transitioning from star-forming to quiescent, and ID 3 has previously been classified as a passive galaxy (Strazzullo et al., 2016).

CO line fluxes

The 1D spectra of these line detections are shown in Fig. 4.3. The spectra for the CO[3-2] lines and CO[1-0] lines are given in Appendix B. Line detection was not performed for the CO[3-2] and CO[1-0] lines, we simply highlight the velocity range over which the CO[3-2] and CO[1-0] line fluxes were extracted, corresponding to the CO[4-3] redshift and velocity width. From the line spectra in Fig. 4.3, CO redshifts were determined from the flux-weighted line centers over the channels contained in the linewidth, and are shown in Table 4.5. We show in Fig. 4.3 that the CO redshifts are in good agreement with the redshifts derived from optical/NIR spectroscopy for 6/8 of the galaxies, with offsets between $\sim$20-400kms^{-1}(Gobat et al., 2013; Valentino et al., 2015). However, A1 and A2 both appear to be heavily dust-obscured and have fainter, redder optical counterparts (Fig. 4.2). They therefore do not have an optically-derived redshift, but the redshift values calculated using the CO[4-3] lines are consistent with the redshift of Cl J1449+0856.

The line-free continuum fluxes for each galaxy are given in Table 4.3, including two strong continuum sources without CO detections (A4 and A5), which are discussed in Section 4.3.8. The integrated CO[4-3] line fluxes are tabulated in Table 4.4, measured directly from the collapsed data over the linewidths, as well as the CO[4-3] emission sizes used for flux extraction.

In the case of A1 and A2, the CO[4-3] emission is resolved, and the sizes (and associated errors) given in Table 4.4 are the FWHM of the circular Gaussians measured by Gildas in the uv-plane. To demonstrate this, we show the flux amplitude against uv-distance profiles of A1 and A2 in Fig. 4.4, binned due to the large number of individual visibilities. If these galaxies were point sources in the image plane, they would show a constant amplitude profile in the uv-plane. Conversely, decreasing amplitude with uv-distance demonstrates that the galaxies are indeed resolved, which is clearly the case for these galaxies. To quantify this, we calculate the best-fitting constant amplitude profile for both galaxies using a least-squares approach, which are shown by the dashed lines in Fig. 4.4. The χ^2 values between these fits and the binned data are 22.5 and 13.5 for A1 and A2 respectively, for 3 degrees of freedom. These give probabilities of these galaxies being unresolved of $<5.1\times10^{-5}$ and $<3.7\times10^{-3}$.

We also use these data to measure an alternative detection significance of A1 and A2, which is independent of their resolved sizes. To do this, we add in quadrature the SNR of each binned amplitude in Fig. 4.4, defined as the amplitude divided by the error on the amplitude. This gives us SNRs of 18.1σ and 13.4σ for A1 and A2 respectively - even higher than those found using the flux measurements within their Gaussian sizes.

ID	I_{CO43} (mJykms^{-1})	$I_{CO43,de-boost}$ (mJykms^{-1})	I_{CO32} (mJykms^{-1})	I_{CO10} (mJykms^{-1})	FWZI (kms^{-1})	FWHM (kms^{-1})	CO[4-3]$_{FWHM}$ size (")
A2	338 ± 36	307 ± 54	340 ± 55	72 ± 12	426	387 ± 89	0.58 ± 0.11
A1	509 ± 43	474 ± 67	401 ± 115	<28	639	619 ± 111	0.51 ± 0.08
13*	172 ± 27	148 ± 38	146 ± 56	<18	517	343 ± 93	<0.31
6*	210 ± 35	178 ± 50	-	30 ± 9	578	541 ± 162	<0.33
N7*	135 ± 21	116 ± 31	112 ± 43	<14	304	302 ± 115	<0.32
B1*	83 ± 22	62 ± 28	113 ± 56	18 ± 8	426	533 ± 213	-
3*	86 ± 18	70 ± 24	<89	<13	304	252 ± 83	-
S7*	41 ± 19	-	-	<11	183	80 ± 75	-

Table 4.4: Measured CO line fluxes and linewidths of the 8 cluster galaxies discussed in this chapter. 2σ upper limits on the line fluxes are shown. The CO[4-3] emission sizes are the source sizes used for flux extraction, as described in Section 4.2. 2σ upper limits on the sizes are shown for those sources extracted as PSFs, based on the beam size and the S/N of the detection. For A1 and A2, we show the FWHM of the circular Gaussian used for flux extraction. No CO[3-2] flux is given for S7 or galaxy 6, as the spectral setup did not cover the appropriate frequency range at the redshift of S7, and only covered a small fraction of the CO[3-2] linewidth in ID 6. The fluxes for the sources with IDs marked by a star were extracted at fixed rest-frame optical position, for all CO transitions. The FWZI values are the linewidths used to calculate I_{CO}, the linewidth corresponding to the flux highlighted in blue in Fig. 4.3. The FWHM values are from the Gaussian line fitting, also shown in Fig. 4.3. For those sources modelled as a double Gaussian, this is the sum of the FWHM of a single Gaussian, plus the separation between the two Gaussians.

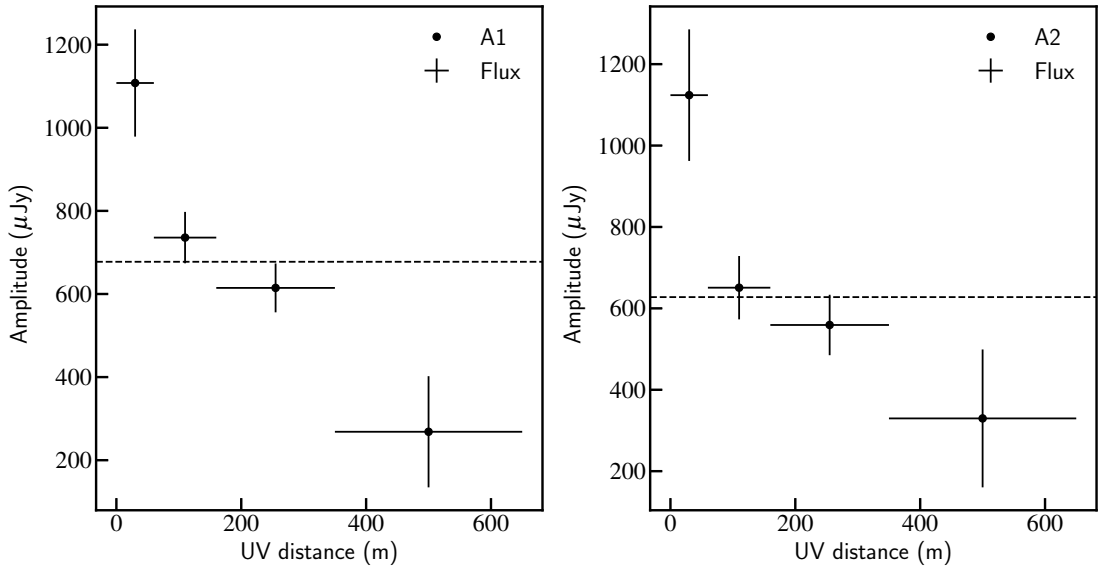

Figure 4.4: Binned flux amplitude vs. uv-distance for galaxies A1 and A2. The dashed horizontal line shows the best-fitting constant amplitude value for each galaxy, which would be an appropriate amplitude vs. uv-profile for a point source. However, the decrease in amplitude with uv-distance is clear evidence that the galaxies are resolved.

The errors on the sizes measured using `uvfit` are well-defined. Through interferometry, the ability to resolve a source is dependent on both the beam size and the signal-to-noise of the source, meaning that bright sources can be resolved down to sizes several factors smaller than the beam. This is made possible by the well-understood beam pattern. In order to characterise the relationship between the error on the size of a galaxy and its brightness, we simulate ∼70 galaxies, by inserting sources into empty regions of our 2mm dataset at fixed circular Gaussian size with a range of input fluxes and sizes. We then measure the fluxes and sizes of the simulated sources using `uvfit`. We confirm that the size errors as given by `uvfit` are sensible. We find that the relationship between flux SNR and the error on the size follows the trend $FWHM_{err} \propto SNR^{-1}$, as might be expected based on literature studies (e.g. Condon 1997). The errors on the sizes of A1 and A2 can be described by a relationship of the form:

$$FWHM_{err} = 0.93 \times \frac{FWHM_{beam}}{SNR} \tag{4.1}$$

where $FWHM_{err}$ is the 1σ error on the FWHM Gaussian size, $FWHM_{beam}$ is the circularised FWHM of the ALMA synthesised beam, SNR is the SNR of the CO[4-3] line detection, and the factor of 0.93 was calibrated by comparing the output of Eqn. 4.1 with the size errors reported by Gildas. It is the size errors given by Gildas that are shown in Table 4.4 for A1 and A2. We cannot constrain the sizes of the lowest SNR sources, as their low SNR brings into doubt our ability to

detect them if they are resolved and diffuse. We therefore put upper limits on the sizes of the SNR>6 unresolved sources using Eqn. 4.1. We see that our CO[4-3] emission sizes are likely to be relatively compact.

For comparison with the integrated CO[4-3] line fluxes over the collapsed data, we fit Gaussian line profiles to each of the detections using least-squared minimisation, which are shown over-plotted in Fig. 4.3. For all galaxies except A1 and A2, these are simply included for guidance and are not used in further analysis. For some galaxies, a double-peaked profile appears to be an appropriate fit to the data, while for others we show a single Gaussian. For the single Gaussian fits, the normalisation, center and FWHM were free to vary. For the double Gaussians, the normalisations of the two peaks were free to vary independently. We imposed the constraint that the FWHM of the two Gaussians should be equal to one another, but this FWHM and the separation between the peaks were left as free parameters. The errors on these Gaussian FWHM are derived from the simulations described in the following section (CO[4-3] flux boosting), unless the fitting procedure returned larger errors than the simulations (this was the case for B1 and S7). The shapes of the CO[4-3] lines in galaxies A1 and A2 are clearly suited to a double-peaked profile. We use a least-squared method to asses the goodness-of-fit, and find probabilities for the single Gaussian fits to the data of 1.5×10^{-5} and 2.4×10^{-3} for A1 and A2 respectively. For the double Gaussian profiles, we find probabilities of 0.031 and 0.52 respectively. This statistically confirms that the double Gaussian profiles are more appropriate fits to the data. However, the relatively low probability of A1 being described by a double Gaussian also indicates that a more complex line profile is required to well-fit the data. For the remainder of our galaxies, we find that both single and double Gaussian profiles give reasonable fits to the data, so we show the profile with the greatest probability to guide the eye in Fig. 4.3. It is important to note here that we find the linewidths between the single and double Gaussian fits to be consistent. We also compare the line fluxes integrated under both single and double Gaussian profiles with the line fluxes from the collapsed data, and find that the different methods again give consistent results within 1σ. We therefore use the line fluxes measured directly from the collapsed data for all galaxies, over the velocity range shown in blue in Fig. 4.3 (Full Width Zero Intensity, FWZI). We do however also tabulate the Gaussian-fit linewidths in Table 4.4, as these widths are more appropriate for dynamical arguments, particularly for our brightest galaxies, A1 and A2 (see Section 4.3.5). The linewidths of our detections vary between $\sim$100kms^{-1} and $\sim$650kms^{-1}, within the range of expected values for star-forming galaxies at this redshift.

CO[4-3] flux boosting

As described in Section 4.2.5, the channels over which we extract the CO[4-3] flux, shown in Fig. 4.3, were taken as the channels that gave the highest S/N, thus constraining the line. However, although common practice, it is possible that the choice of velocity range in this way could be influenced by the channel-to-channel noise, thus artificially boosting the total measured flux over this linewidth. In order to quantify this effect, we created a simulated sample of CO[4-3] double-peaked Gaussian line profiles, with recovered SNRs between 3 and 30, given the representative noise on our measured 1D spectra. We added these simulated line profiles to simulated random noise, and then applied the same line-finding algorithm as was used for our real data. We compared the output flux (signal+noise, measured flux) recovered over the linewidth found by the algorithm, with the pure input flux (signal, real flux) over the same linewidth. This gave us a direct measure of the effect of potential noise boosting. The results of these simulations are shown in Fig. 4.5. We bin our data by SNR, and calculate the median flux correction factor, the ratio of Real Flux/Measured Flux over the optimised linewidth, in each SNR bin. We then fit this binned data with a polynomial function of the form $y = ax^b$. This was done for simulations of double Gaussian profiles with FWHM of a range of linewidths between $\sim$200kms^{-1}and $\sim$700kms^{-1}, spanning the full range of linewidths for our observed galaxies. We found the flux boosting correction to be independent of linewidth.

It can be seen from Fig. 4.5 that the effect of noise boosting is minimal at high SNR, shown by Real Flux/Measured Flux = 1. The Real Flux/Measured Flux decrease smoothly with decreasing SNR, implying an increasing effect of noise boosting. The effect ranges from a minimum of $\sim$7% ($<1\sigma$) for our brightest source (A1), up to $\sim$25% for our faintest secure source (B1). We therefore use the polynomial fit to the data to calculate appropriate flux correction factors for each of our galaxies. At S/N$<$3, it is difficult to define a robust correction factor from these simulations. We therefore do not perform flux de-boosting for S7, or derive physical parameters from the line flux, due to the tentative nature of the detection. For our other detections, this correction factor was applied to the CO[4-3] line fluxes, and is essentially a de-boosting, ensuring that our results are robust. The errors on the correction factors are derived from a polynomial fit to the error bars on the binned Real Flux/Measured Flux ratios themselves, and are added in quadrature to the errors on our I_{CO4-3} values. The de-boosted line fluxes are also given in Table 4.4. Is it these de-boosted line fluxes and errors that we use for the remainder of our analysis, to derive all physical properties of the galaxies. This correction does not need to be applied to the line fluxes at lower excitations because the velocity range of the line was optimised by the CO[4-3] flux, and the channel-to-channel noise distribution is independent in the different data sets. We therefore do

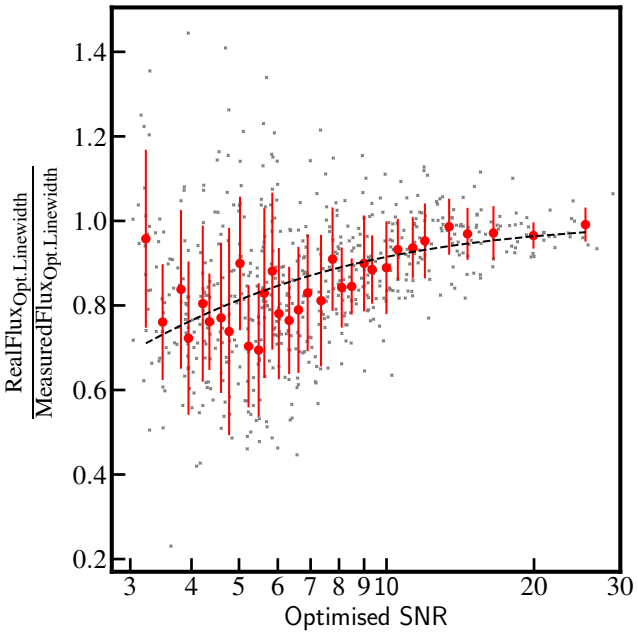

Figure 4.5: The ratio between the simulated input flux and the flux recovered by our line-search algorithm over the optimised linewidth, as a function of recovered (output) signal-to-noise for a simulation of double-Gaussian line profiles. This ratio is used to de-boost the CO[4-3] line fluxes of our galaxies. In this way, we correct for any artificial noise boosting in the spectra, arising from the optimisation of the CO[4-3] linewidth. The grey crosses are the individual data points, and the red circles are the medians of the data in bins of 20. The red error bars show the standard deviation within each bin. The black dashed line is the polynomial fit to the data, from which we have derived the flux corrections. A least-squared approach was used for this fitting.

not suffer from the same noise bias at lower J-transitions.

In addition to the flux boosting correction factors, we also use our simulations to derive diagnostics on the error on the line FWHM, as well as the potential flux loss due to 'clipping' the line in velocity space. We fit a double Gaussian to each of our simulated line profiles, before calculating the standard deviation of the output FWHM in bins of flux SNR. We find the error on the FWHM to be of the order 15-40%, depending on the SNR of the detection. The Gaussian fits to the individual line profiles in Fig. 4.3 returned smaller errors on the FWHM (except for galaxies B1 and S7), so in these cases we use the uncertainty from our simulations as a more conservative measure of the FWHM error, shown in Table 4.4.

We find the flux loss due to the linewidth optimisation to be $\sim$6%. However, this value has a certain amount of uncertainty when applied to our cluster galaxies. The flux loss due to clipping is highly dependent on the underlying profile of the CO lines of our galaxies (e.g. double or single

Gaussian, or even steeper profiles), which are not well constrained. We therefore consider the loss between the measured and intrinsic line fluxes to be 6±6%. Any potential flux loss will affect each of the CO transitions equally, assuming that the lines have the same width and profile. It therefore will not affect our results on gas excitation, and we tabulate the measured line fluxes over our defined FWZI in Table 4.4. We incorporate the effect of this possible flux loss when deriving the luminosity of the CO[1-0] transition, discussed in Section 4.3.3, and the SFRs derived from CO[4-3].

Finally, we also use our simulations to quantify the error on the redshifts derived from the CO[4-3] lines, shown in Table 4.5. We wish to compare the error on the redshift calculated from the flux-weighted central frequency of the line (as tabulated), with the intrinsic dispersion on the derived redshifts from our simulations. Our simulated lines have a known redshift, corresponding to the central redshift of the double-peaked profile, and we use the same methods to both find the lines and calculate the redshift of the simulated lines as we have used for our data. We find that the error on the redshift increases with increasing linewidth and with decreasing SNR, but that the output redshift dispersion is smaller than the formal error coming from the frequency uncertainty. The exception to this is for galaxy ID 3, at FWHM 250kms^{-1}and SNR=4.8. In this case, the two errors are the same. We therefore show only the errors from the original redshift derivation in Table 4.5.

4.3.2 CO Spectral Line Energy Distributions

In addition to the CO[4-3] emission, we also find several significant line flux measurements for both the CO[3-2] and CO[1-0] transitions in these eight galaxies, having extracted line fluxes over the velocity range corresponding to that of the CO[4-3] transition. These are shown in Table 4.4. Incorporating the integrated line flux measurements of CO[3-2] and CO[1-0] with those of CO[4-3], we are able to construct CO spectral line energy distributions for the cluster galaxies, shown in Fig. 4.6. We compare the excitation properties of the ISM gas in our eight cluster galaxies with known SLEDs: 'normal' z∼2 star-forming galaxies (BzK), ULIRG/starburst galaxies, and the Milky Way (MW) (Papadopoulos et al., 2012a; Daddi et al., 2015).

Studying the gas excitation properties of a galaxy (the ratio of the excited, high-J gas to the total gas reservoir at lower J-transitions) gives us insight into the relative physical states of the gas. Observations have shown that some populations of galaxies, such as ULIRGs and starburst galaxies, have a large amount of their molecular gas in the densest states traced by high J-transitions, compared to the more extended gas traced by lower J-transitions. The flux in the higher J-transitions is tightly correlated with the SFR of a galaxy, and these excitation properties therefore give us

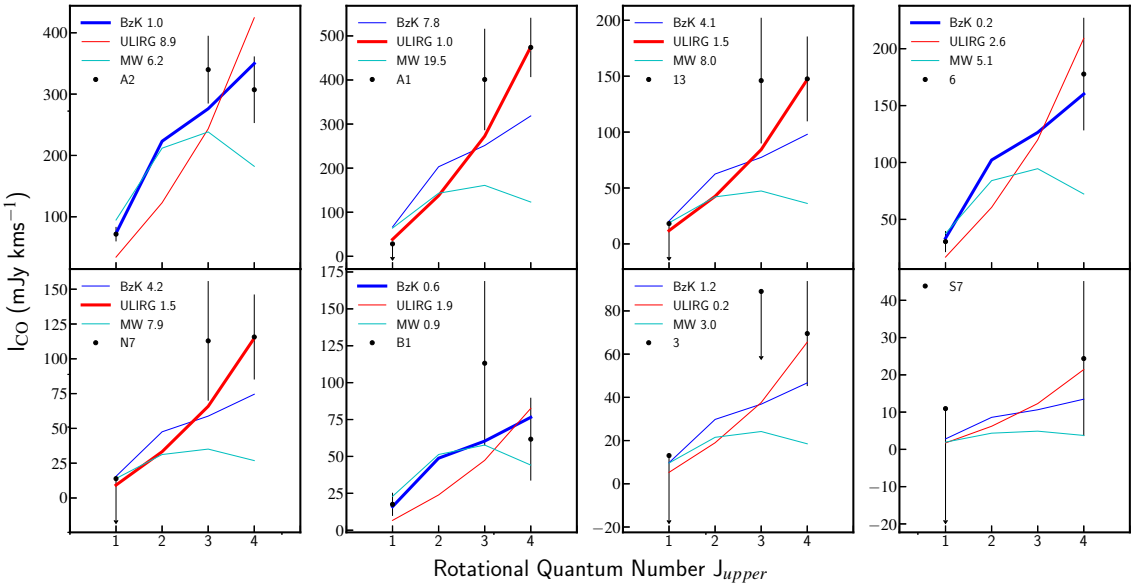

Figure 4.6: CO SLEDs of 8 cluster galaxies detected in CO[4-3]. The legends show the reduced χ^2 value for the fits of the observed galaxy CO SLED with the three excitation models: BzK, ULIRG/SB and MW. The SLEDs of some galaxies are best-fit by a BzK excitation model, and some are best-fit by a ULIRG/starburst-like model. The preferred template for each galaxy is plot with a thicker line, where possible. We do not draw any conclusions about the gas excitation of galaxies ID 3 and S7, due to the limited data available. A least-squared analysis was used for the fitting, and 2σ flux upper limits are shown.

insight into the mode of star-formation that is taking place in the galaxy (Daddi et al., 2015). ULIRG- or starburst-excited galaxies typically form stars in a violent, short-lived fashion, whilst BzK galaxies fall along the more secularly star-forming main-sequence of galaxies (Daddi et al., 2004; Elbaz et al., 2011). We do not try to find the best-fit SLED for each galaxy, but wish to characterise our galaxies with respect to the limiting cases most commonly found among star-forming galaxies. Moreover, the method of comparing our CO data with SLED templates allows us to use all three CO transitions simultaneously, and is therefore less limited by measurement upper limits than other types of excitation analysis, such as the ratios between different transitions.

From Fig. 4.6, we see that the CO excitation properties vary between galaxies in the cluster. Least-squared fitting was used to compare the data to the templates, where the normalisation of each template was allowed to vary. In the fitting process, we used the measured line flux values for each transition, not the upper limits. We are able to characterise the excitation state of the gas in six of our eight galaxies using χ^2 analysis. The reduced χ^2 values for each of the fits reveal that for 3/6 of these cluster galaxies, a starburst-like gas excitation better fits the data, with typical χ^2_{red} values between 1 and 1.5. The other three galaxies are best-fit by BzK excitation properties, with χ^2_{red}

between 0.2 and 1.0. One might expect that not having significant CO[1-0] line flux would make a galaxy more likely to show starburst-like excitation properties, and we do appear to see this trend in our data. No conclusions can be drawn with these data on the excitation properties of S7 and ID 3. For ID 3, we find that both ULIRG and BzK templates give a reasonable fit, and there were no data available for the CO[3-2] transition at the redshift of S7 with which to characterise the excitation. From Fig. 4.6, it is immediately striking that 50% of these galaxies show a starburst-like, rapid star-formation mode based on the gas excitation properties, as this is a significantly higher fraction than observed in the field (see Section 4.4.2).

ID	RA	Dec	z_{CO}	z_{opt}	SFR_{CO43}	$SFR_{870\mu m}$	$SFR_{1.4GHz}$	$\log(M_\star)$
	(deg)	(deg)	-	-	$M_\odot yr^{-1}$	$M_\odot yr^{-1}$	$M_\odot yr^{-1}$	$\log M_\odot$)
A2	222.30710	8.93951	1.9951 ± 0.0004	-	102 ± 24	85 ± 22	<157	-
A1	222.30872	8.94037	1.9902 ± 0.0005	-	128 ± 31	227 ± 22	113 ± 46	-
13	222.30856	8.94199	1.9944 ± 0.0006	1.99851 ± 0.00066	40 ± 13	38 ± 11	91 ± 24	10.46 ± 0.3
6	222.30991	8.93779	1.9832 ± 0.0007	1.98 ± 0.02	59 ± 19	118 ± 12	84 ± 24	10.71 ± 0.3
N7	222.31029	8.93989	1.9965 ± 0.0004	1.997 ± 0.001	31 ± 10	<26	70 ± 24	10.07 ± 0.3
B1	222.30891	8.94071	1.9883 ± 0.0070	1.99 ± 0.03	20 ± 10	57 ± 12	64 ± 24	10.81 ± 0.3
3	222.30910	8.93951	1.9903 ± 0.0004	2.00 ± 0.03	23 ± 9	<23	<48	10.31 ± 0.3
S7	222.31021	8.93980	~ 1.983	1.982 ± 0.002	~ 8	<26	<48	10.48 ± 0.3
A5	222.30963	8.93690	-	-	-	1004 ± 24	410 ± 46	-
A4	222.30648	8.93778	-	-	-	309 ± 22	<174	-
2	222.30586	8.94297	-	1.98 ± 0.02	-	<24	<48	10.81 ± 0.35

Table 4.5: Properties and SFRs of the 8 galaxies with CO[4-3] detections, as well as two additional bright continuum detections in the cluster field of view (A4 and A5), and a galaxy only detected at 870µm (ID 2). 2σ upper limits are shown. The SFR_{CO4-3} values were derived from the de-boosted line fluxes. The errors given on the SFRs from CO[4-3] and 870µm are displayed only with the errors corresponding to the flux measurements. These errors are smaller than the errors used for the analyses in this chapter, which also take into account the errors arising from the systematics, which are discussed in the text. The optical redshifts were calculated in previous studies using HST/WF3 grism and MOIRCS spectroscopy (Gobat et al., 2011; Valentino et al., 2015).

4.3.3 Star-formation rates

It has previously been shown that there is a tight, virtually linear correlation between the CO[5-4] line luminosity and infrared luminosity (and therefore SFR) of both MS and SB galaxies, across a range of redshifts (Daddi et al., 2015). In order to estimate an IR luminosity from the CO[4-3] line fluxes, we therefore derive CO[5-4] line fluxes for our galaxies. We adopt the preferred excitation template shown in Fig. 4.6, using the appropriate flux ratio between the two transitions (Papadopoulos et al., 2012a; Daddi et al., 2015). For those galaxies without a preferred template, we assume a BzK transition ratio. In all cases, the uncertainty introduced by the choice of SLED template is much smaller than the systematic errors on the SFRs, which are discussed below. From the CO[5-4] line flux we derive an infrared luminosity and thence a SFR for each galaxy. The SFR values derived in this way are shown in Table 4.5, $\mathrm{SFR_{CO43}}$. As discussed in Section 4.3.1, these SFRs and errors have been increased by 6%, to account for possible flux loss from clipping of the CO lines in velocity space. Alongside these, we are also able to derive other estimates of the SFR, using the 870µm and 3 GHz continuum fluxes described in Section 4.2. In the case of $\mathrm{SFR_{870}}$, the SFRs were calculated taking the average 870µm to $\mathrm{L_{IR}}$ conversion factor between the MS and SB templates in Béthermin et al. (2015) at z=2, and the systematic uncertainties introduced here are discussed below. We find several robust detections in the cluster core at 870µm (shown in Table 4.3), which allow us to derive these SFRs. For the SFRs derived from the 3 GHz data, we assume a synchrotron contribution to the radio data with a slope of $\nu^{-0.8}$, and thus map the 3 GHz fluxes to 1.4 GHz equivalent flux. We then use the templates in Béthermin et al. (2015) at z=2.0 to convert to $\mathrm{L_{IR}}$, based on the well-known $\mathrm{L_{1.4GHz}}$-$\mathrm{L_{FIR}}$ (far-IR, FIR) correlation (Condon et al., 1991; Condon, 1992). This conversion is invariant for MS and SB galaxies.

Although we cannot spatially distinguish between the 870µm and 3 GHz fluxes of N7 and S7, due to their close separation on the sky, we see in Strazzullo et al. (2018) that the infrared luminosity derived from the CO[4-3] emission of N7 is consistent with that derived from the 870µm flux emission of the combined N7-S7 system. We also see that the 3 GHz continuum flux, shown in Fig. 4.1, is much brighter at the rest-frame optical position of N7 than S7. As shown in Table 4.5, the SFR derived from CO[4-3] for S7 is very low, and we therefore believe that the continuum flux measurements at the position of this pair of sources can be associated with N7. Due to the small amount of gas measured in galaxy S7, considering N7 and S7 as a double source both contributing to the 870µm and 3 GHz continua, or considering them as separate sources and associating the continua with N7, has a negligible effect on our results. An exception to this is in the SFR-$\mathrm{M_\star}$ plane, where we are able to investigate the nature of the two galaxies separately. This is shown in Section 4.3.6. The continuum flux values underneath each of the CO lines were

measured separately for S7 and N7, given in Table 4.3.

We find that the different estimates of SFR for our sample are generally consistent. An exception to this may be the CO[4-3] vs. 870µm SFRs for galaxy A1, and a potential explanation for a discrepancy between the gas and dust properties of this galaxy is discussed in Section 4.4.3. We note that galaxy 13 contains a radio-quiet AGN, with a bolometric X-ray luminosity placing it in the quasar regime (Valentino et al., 2016). We therefore consider that the contribution from X-ray Dissociation Regions (XRDs) to the higher excitations of CO in this galaxy may not be negligible. However, the FIR regime is expected to be largely unaffected by AGN (Mullaney et al., 2012a), and so the agreement between the CO[4-3] SFR and the 870µm SFR for galaxy 13 suggests that the effect of XDR emission is not an important factor here. Additionally, we see disagreement between the $SFR_{870\mu m}$ and $SFR_{1.4GHz}$ for galaxies A4 and A5. As discussed in Section 4.3.8, we do not have redshift measurements for these galaxies, so we have assumed the cluster redshift of z=2 for the calculation of $SFR_{1.4GHz}$ (the redshift is used to map the observed radio flux to the rest-frame SED). If this redshift is incorrect, this may contribute to the inconsistency between SFRs.

As also discussed in Strazzullo et al. (2018), the CO[4-3] and 870µm SFR measurements are always consistent given the uncertainties involved in estimating L_{IR} from the 870µm continuum and CO[4-3] line fluxes. It is a useful consistency check to be able to compare these estimates of SFR, because neither CO[4-3] nor 870µm flux allows us to trace the star-formation directly. We include in our error budget ∼0.2 dex for the CO[5-4] vs. L_{IR} conversion (Daddi et al. 2015; Liu et al. 2015, E. Daddi et al. 2019, in prep.) and ∼0.15 dex for the 870µm to L_{IR} conversion. Here we are taking an average of the MS and SB conversion factors from Béthermin et al. (2015), which differ by a factor of 2. Understanding these areas of uncertainty, and finding consistent results given by both independent methods, gives us confidence that our SFR estimates are robust and not heavily biased by the assumptions made. In the remaining analyses, we therefore use the average of the SFRs from CO[4-3] and 870µm tracers as our preferred SFR. This is simply referred to as the SFR for the rest of the chapter, and all of the measurement plus systematic errors have been included in the calculation of the SFR error.

4.3.4 Star-formation efficiencies

An indirect measure of the star-formation efficiency of the cluster galaxies can be seen in Fig. 4.7, the SFR - L'_{CO1-0} relation. We define SFE as the SFR per unit molecular gas mass. We compare the SFR with the luminosity of the CO[1-0] line - a proxy of the total cold molecular H_2 reservoir. The CO[1-0] line flux (or upper limit) was measured directly using the VLA Ka-band data described in Section 4.2, not extrapolated from the best-fit SLED. Galaxy A2 is consistent with the SFR

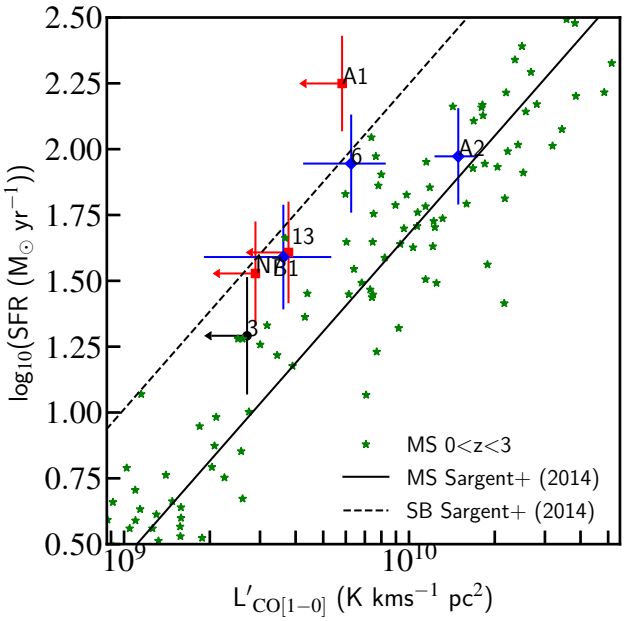

Figure 4.7: The SFR - L'_{CO1-0} relation for our cluster sample. The galaxies are coloured according to their excitation properties (red=SB, black=either, blue=BzK). SFRs are the average SFR derived from the CO[4-3] line flux and the 870μm continuum flux. Seven of the eight cluster galaxies lie at enhanced SFE, compared to the MS (Sargent et al., 2014). A sample of MS galaxies between 0<z<3 are shown by the green stars for comparison (Daddi et al., 2010b; Geach et al., 2011; Magdis et al., 2012; Bauermeister et al., 2013; Tacconi et al., 2013). The errors on the average SFRs include a 0.17 dex systematic uncertainty, as well as the measurement errors. The MS and SB relations are shown by the solid and dashed black lines respectively. 2σ upper limits are shown.

- L'_{CO1-0} relation for MS galaxies, and all of the other cluster galaxies are shifted to the left of the MS locus, indicating that they have an increased SFE with respect to MS galaxies that are selected independent of environment. The median offset of the cluster galaxies from the MS locus is 0.37 dex. This shift does not appear to depend on each galaxy's preferred excitation template. Interestingly, we don't see clear evidence for the starburst-excited galaxies (red squares) having much increased SFEs compared to the BzK-excited galaxies (blue diamonds), similar to what was recently concluded by Dannerbauer et al. (2017).

It can be seen in Fig. 4.6 that less than half of the cluster galaxies have significant CO[1-0] flux measurements in our deep Ka-band data. As can be seen in Fig. 4.7, based on the positions of these upper limits, we would have been able to measure significant CO[1-0] flux in these galaxies if they had been forming stars on the MS regime of the SFR - L'_{CO1-0} plane. This further hints that the significant star-formation of our galaxies is being fuelled by small amounts of H_2 gas.

We have not included the effect of the CO-to-H_2 conversion factor in Fig. 4.7 as we are only plotting the observed L'_{CO1-0}. Using a lower CO-to-H_2 conversion factor for galaxies A1 and A2 for example, due to their highly merging nature, would increase their SFE with respect to the MS. These conversion factors, as well as the integrated Kennicutt-Schmidt plane, are discussed in Section. 4.4.1.

4.3.5 Dynamical masses of A1 and A2

In order to discuss several properties of the cluster galaxies, we need a measure of their stellar mass. However, as can be seen from Fig. 4.2, galaxies A1 and A2 are highly dust obscured at rest-frame optical wavelengths. This means that stellar masses derived from SED modelling are potentially unreliable for these galaxies. We find that the sizes of the CO[4-3] line emission can be resolved in both A1 and A2, with 2D circular Gaussian FWHM sizes of 0.51" and 0.58" respectively. We do not significantly resolve different sizes for the major and minor axes. We can therefore derive dynamical masses for galaxies A1 and A2, using the resolved CO[4-3] emission sizes and the linewidths derived from the double Gaussian fitting of the CO[4-3] lines shown in Fig. 4.3. We use the following relation from Daddi et al. (2010a):

$$Mr < r_e = 1.3 \times \frac{r_e \times {v_{fwhm}}^2}{Gsin^2 i} \tag{4.2}$$

where v_{fwhm} is the FWHM velocity of the CO double Gaussian, r_e is the effective radius of the CO, and $Mr < r_e$ is the dynamical mass within that radius. This relation is not expected to vary significantly for mergers near coalescence. We do not have ellipticity information for A1 and A2, so we take the average inclination angle of 57$\pm$21°, from statistical averages of randomly orientated galaxies at z$\sim$2. In order to calculate the dynamical mass, we consider the minimum and maximum inclinations from the 1σ error on this average, and incorporate a correction factor on the measured r_e into Eqn. 4.2. This correction factor accounts for the fact that the circular, resolved r_e that we have measured will underestimate the intrinsic r_e, depending on the inclination angle of the galaxy. If the galaxies were at high inclination angles they would be almost edge-on, with a high b/a axis ratio. This means that the measured circular Gaussian would return an intermediate size. We therefore take a correction factor of 2 on the radius at high inclination angles. At low inclinations, the galaxies would be almost face-on, so we take a correction factor close to 1. The dynamical mass is therefore calculated taking the mid-point of the mass estimates at high and low inclination, with the error given by half of the spread between the two. The values for $M_{dyn,2r_e}$= 2$\times Mr < r_e$, the dynamical mass contained within the whole diameter of the galaxy, are shown in Table 4.6.

For the analysis in this chapter, we assume that half of the total dynamical mass of galaxies A1

ID	$\log_{10}(M_{dyn,2r_e}\ M_\odot$	$\log_{10}(\mathrm{M}_{mol,dyn}\ M_\odot$	$\log_{10}(\mathrm{M}_{*,dyn}\ M_\odot$
A1	10.58±0.3	10.28±0.3	10.28±0.3
A2	10.23±0.3	9.93±0.3	9.93±0.3

Table 4.6: The dynamical masses and the inferred molecular gas and stellar masses for galaxies A1 and A2. We have assumed that the gas and stellar masses are both equal to half of the dynamical mass of the galaxies, but the 0.3 dex errors allow for the gas mass to be between 25-100% of the dynamical mass. We have neglected the likely small contribution from dark matter.

and A2 is coming from the stellar mass, $M_{*,dyn} = \frac{M_{dyn,2r_e}}{2}$, and we assume that the other half of the dynamical mass can be attributed to the molecular gas mass (Daddi et al., 2010a; Aravena et al., 2016a). Reasonable upper and lower limits on the relative contributions from molecular gas and stellar mass, $\mathrm{M}_{mol,dyn}$:$\mathrm{M}_{*,dyn}$ between 1:3 and 3:1, are consistent with the errors on the derived masses. Comparing this assumption with the analysis in Daddi et al. (2010a), we see that the three galaxies for which Daddi et al. (2010a) derived dynamical masses had molecular gas contributions between 41% and 47% to the total dynamical mass. The galaxies in that study were star-forming isolated BzK galaxies, unlike A1 and A2, and Daddi et al. (2010a) assume a 25% contribution from dark matter. A 50% contribution from molecular gas therefore seems reasonable for our galaxies, and implies that we are observing our merging systems in an intermediate stage of the merging sequence.

We assume that the contribution from dark matter is negligible. There is evidence that the contribution from dark matter to the dynamical mass at these redshifts is small (Daddi et al., 2010a; Wuyts et al., 2016; Genzel et al., 2017), and we cannot further refine the contributions from molecular gas, stellar mass and dark matter to the dynamical mass using our data. Additionally, the empirically calibrated stellar mass estimates of A1 and A2 ((10.3±0.3) $\mathrm{M}_\odot$ and (9.6±0.3) $\mathrm{M}_\odot$ respectively, based on the HST F105W-F140W colour in a 1" aperture) are consistent with the stellar masses that we derive from the dynamical mass ($\mathrm{M}_{*,dyn}$ in Table 4.6).

Values for molecular gas mass derived from the dynamical mass are also shown in Table 4.6. Deriving the gas mass using dynamical arguments allows us to estimate values for both α_{CO} and gas-to-dust ratio, given the measured $\mathrm{L}'_{\mathrm{CO10}}$ and M_d derived from observations. This is discussed further in Section 4.3.7.

4.3.6 Specific star-formation rates

We examine the SFR-$\mathrm{M}_\star$ plane in Fig. 4.8. Multiwavelength data available for the cluster were used for SED fitting with Fitting and Assessment of Synthetic Templates (FAST, Kriek et al., 2009), in

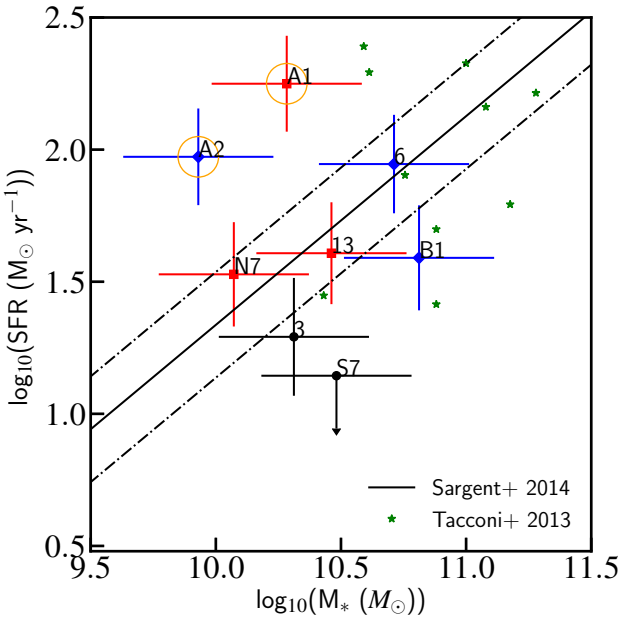

Figure 4.8: The SFR-M$_\star$ plane. The MS of star-forming galaxies at z=2 is shown by the solid black line (Sargent et al., 2014), and a sample of MS galaxies at z$\sim$2 are shown by the green stars (Tacconi et al., 2013). The dash-dotted lines represent the 0.2 dex scatter on the MS relation. The cluster galaxies do not show systematic evidence for an increased sSFR with respect to the MS. The errors on these average SFRs include a 0.17 dex systematic uncertainty, in addition to the measurement errors. The colour-coding is as in Fig. 4.7. The orange empty circles highlight galaxies that have had their stellar masses estimated from their dynamical mass, A1 and A2. 2σ upper limits are shown. For S7, the SFR has been calculated using the CO[4-3] line flux only, as we do not believe the measured 870μm flux is associated with S7.

order to derive the galaxy stellar masses shown in Table 4.5, as described in Strazzullo et al. (2016). Stellar masses for the sources S7 and N7, which are very close to each other and thus blended in all imaging besides HST, were derived from the F140W flux density and F105W-F140W colour by empirical calibration obtained from field (GOODS-S) galaxies in a similar redshift and magnitude range. We use photometry from Guo et al. (2013) and photometric redshifts, stellar mass estimates, and modelled SEDs from Schreiber et al. (2015) and Pannella et al. (2015), following the same procedure detailed in Strazzullo et al. (2016). The stellar mass estimates for A1 and A2 were derived from dynamical arguments, described in Section 4.3.5.

Interestingly, although a high fraction of these galaxies show evidence for a starburst-like star-formation mode in terms of their gas excitation, they do not appear to preferentially reside in the starburst regime on the SFR-M$_\star$ plane, shown in Fig. 4.8. Typically, dusty starburst galaxies that

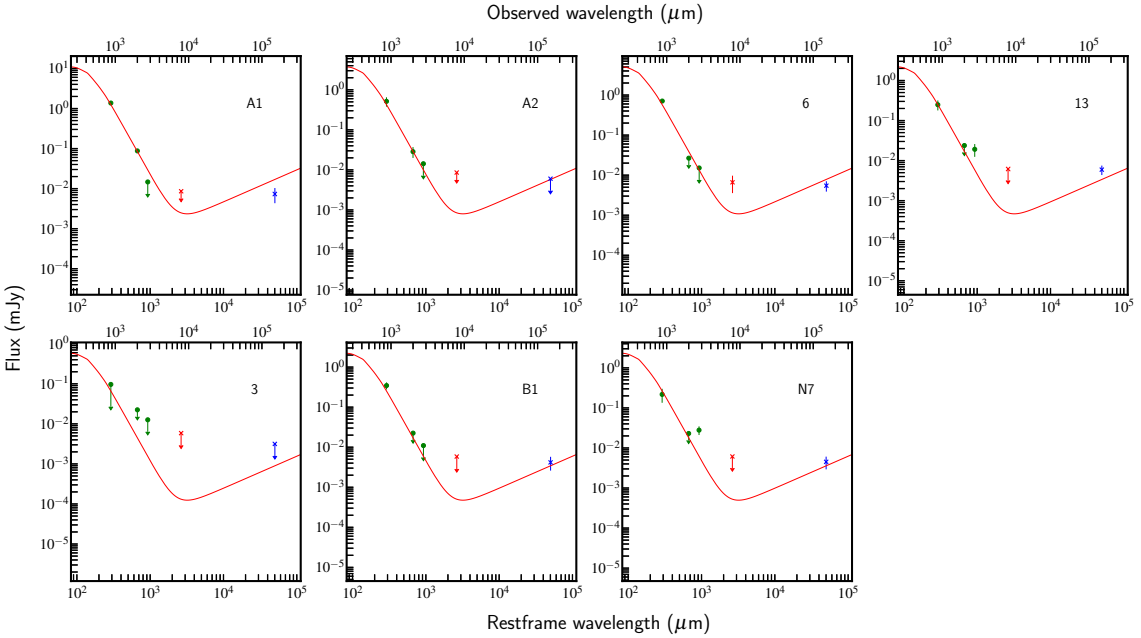

Figure 4.9: The spectral energy distributions of the line-free continuum data from 870µm to 3 GHz observed frequencies. The data primarily constraining the dust masses are shown by green dots (870µm, 2mm and 3mm observed). The observed 7mm continuum underneath the CO[1-0] line is shown by the red crosses, and the 3 GHz continuum is shown by the blue crosses. 2σ upper limits are shown. The starburst template SED from Béthermin et al. (2015) is shown by the red solid line, normalised by the green data on the RJ tail.

have a high SFE are also found to be elevated in specific star-formation rate - therefore residing above the MS of star-formation (e.g. Daddi et al. 2010b; Silverman et al. 2015; Puglisi et al. 2017). However, for our cluster galaxies, both the SB-excitation and the BzK excited galaxies scatter around the MS of star-formation at z=2, without any systematic evidence of a heightened sSFR. It can be seen in Fig. 4.8 that only galaxies A1 and A2 lie above the scatter of the MS, with some of the less highly star-forming galaxies such as IDs 3, B1 and S7 lying below the MS. It should be noted that the SFR of S7 is from CO[4-3] only, as we do not associate any 870µm continuum flux with S7, as discussed above.

It is somewhat surprising that a galaxy best fit by a BzK excitation, A2, has one of the highest sSFRs. It should be noted that A1 and A2 appear to be highly dust obscured in the optical bands, and thus the stellar masses shown here have been derived from the galaxies' dynamical masses (see Section 4.3.5). In addition, our cluster galaxies do not appear to be typical isolated star-forming disks, and therefore may not follow the expected trends of other star-forming MS and SB galaxies at z=2. This is discussed further in Section 4.4.

4.3.7 Dust and H_2 masses

Dust masses

As discussed in Section 4.3.3, in addition to the detection of molecular gas in the cluster galaxies, we also detect significant 870µm continuum flux. This is a direct detection of the galaxies' dust emission. By combining the flux measurements at 870µm, 3 GHz and continuum flux underneath the three CO lines, we are able to construct the submillimetre-to-radio portion of each of the galaxies' SEDs. These are displayed in Fig. 4.9. It can be seen that this cluster is not particularly prominent at 3 GHz, unlike the high-z cluster presented in Wang et al. (2016). It is therefore not a strong over-density of radio sources, which are expected to become more common at z>2 (Daddi et al., 2017). The slope of the Rayleigh-Jeans tail of the SED is not expected to vary significantly with dust temperature, and we choose to compare our galaxy SEDs with a warm starburst SED template in Fig. 4.9, based on the galaxy properties displayed in Figs 4.6 and 4.7. The RJ slope of the starburst template was fixed at α=-3.24, measured from the template itself, and the best-fitting normalisation of the template to the data was calculated using a least-squares fitting procedure. For this fitting, only the observational data in the RJ tail, shown by green circles in Fig. 4.9, were used. In all cases, the data themselves are used for the fitting, not the measurement upper limits. As can be seen from Fig. 4.9, the slope of this template is a good fit to the data in most cases.

Dust masses were derived using a range of templates to calculate the bolometric luminosity under the RJ tail of the galaxies' SEDs. We modelled the data using 2-component (a diffuse ISM component and a photodissociation region, PDR, component) dust models from Draine & Li (2007), and calculated the goodness-of-fit of each combination of parameters. The primary parameters that drive the dust mass are the average radiation field energy density scale factor, <U>, and the fractional contribution of the PDR dust to the model, γ. We then considered only values for dust mass, M_d, with parameter solutions in the range <U>=10-50, and γ<0.2. SED-fitting of the IR to millimeter portions of galaxy spectra has shown that typical MS-galaxies at z$\sim$2 tend to have <U> $\sim$20, and γ close to zero (Magdis et al., 2012; Béthermin et al., 2015). Highly star-forming galaxies, such as GN20, have <U> $\sim$35 and γ $\sim$0.18. We therefore choose these parameter constraints because they encompass a realistic but open range of galaxy properties. Having excluded γ $\geq$0.2, we bin the solutions of M_d as a function of <U> into bins of Δ(<U>) = 5 for each galaxy, and examine the resulting trend. This is shown in Fig. 4.10 for galaxy A1, alongside the dependence of L_{IR} over the same range of <U>. Looking within our accepted range of <U>, we find that the derived M_d varies by a factor of two, depending on the assumed <U>. We therefore take the median M_d of the data binned in this range, at <U>=28.75. We take the entire spread of the binned dust masses and their errors, between <U>=10-50, as the error on the dust mass. The

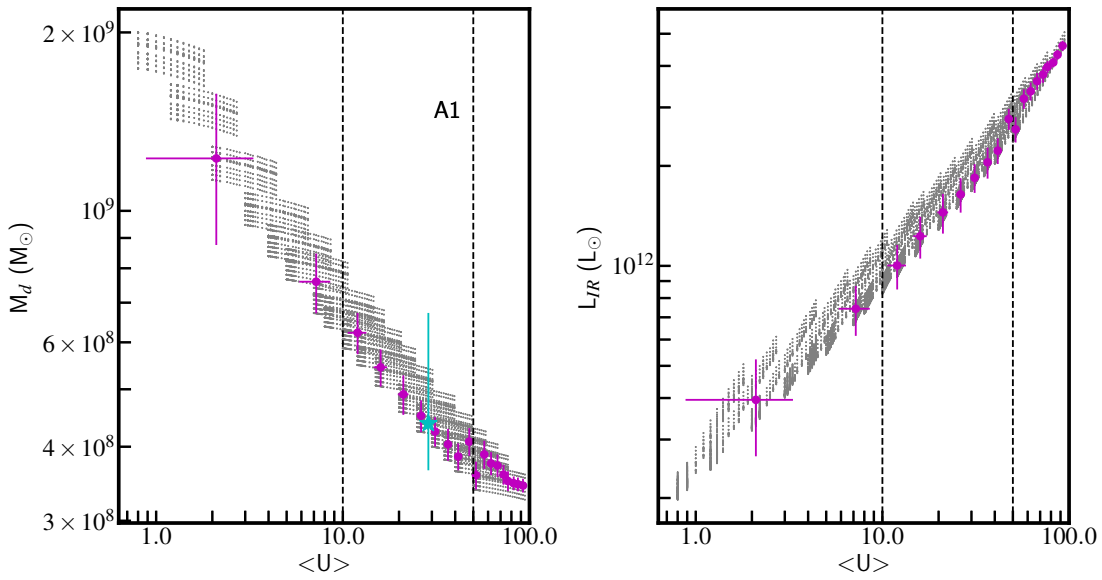

Figure 4.10: The variation of dust mass (left) and L_{IR} (right) with the average radiation field energy density, <U>, for galaxy A1. The grey crosses show all of the permutations for more minor fit parameters, and the magenta circles show the median values in bins of Δ(<U>) = 5. The error bars on the median values give the standard deviation of each quantity in the bin. For our analysis, we consider the range 10< <U> <50, which is contained within the two black dashed vertical lines. Left: the cyan star within this range is the median dust mass used for our analysis, at the median <U>=28.75. The cyan error bars show the full spread of the binned magenta data, including the error bars, within this acceptable <U> range. This is approximately a factor of two, and is taken to be the error on the derived dust mass. Right: we illustrate the dependence of L_{IR} on <U> over the same <U> range. We see a factor of 3.5 difference in the possible values of L_{IR} between 10< <U> <50.

dust masses derived in this way are shown in Table 4.7.

The galaxies N7, 6 and 13 show evidence for excess flux compared to the SED templates at longer wavelengths, shown in Fig. 4.9. However, we do not comment further on this given the relatively moderate significance of the excesses. We have recently received a deeper continuum dataset at these wavelengths (currently under analysis), and so we leave interpretation of these possible excesses for a future publication. In order to ensure that the derived dust masses were not affected by these unusual SED shapes, we calculate the average dust-to-870μm flux ratio using galaxies A1, A2 and 6, our best-constrained galaxies at 870μm. This gives an average value of $r_{d870} = 3.19 \times 10^8 M_\odot mJy^{-1}$. When we apply these dust-to-870μm ratios to the 870μm detections of galaxies 6, N7 and 13, we recover the same values for dust mass as we found using our original method. This confirms that our dust mass derivations are robust.

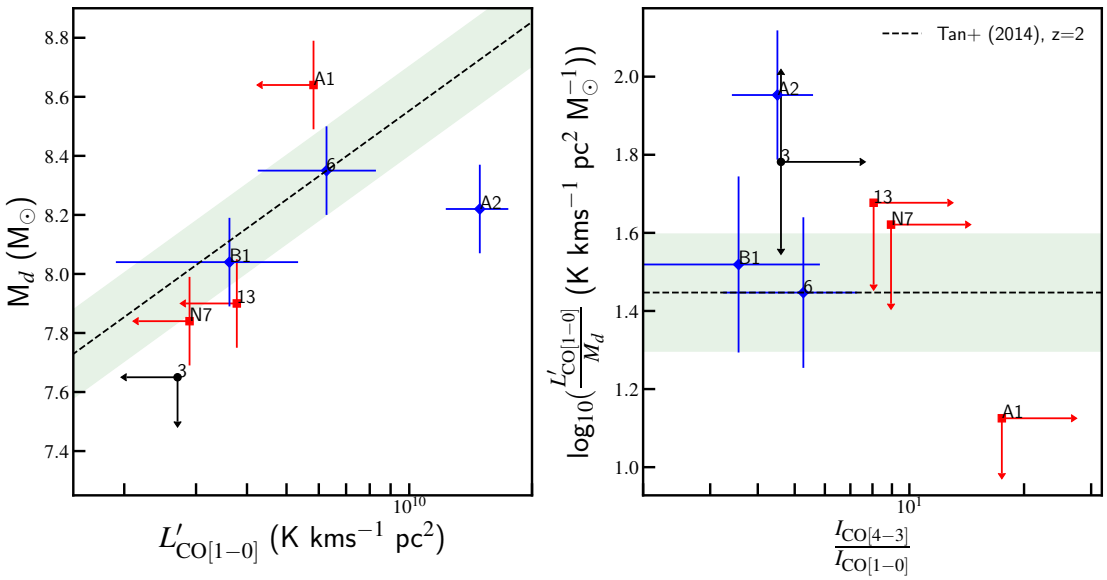

Figure 4.11: Left: Dust mass against L'_{CO1-0}. The expected MS trend from Tan et al. (2014) is shown by the black dashed line in both panels. The green bands represent the $\pm$0.15 dex scatter on the relations, from Daddi et al. (2010a). Right: $\frac{L'_{CO1-0}}{M_d}$ as a function of excitation ratio. The galaxies scatter around the expected relation, with the possible exception of A1, discussed in the text. The symbol colour-coding is as in Fig. 4.7. 2σ upper limits are shown.

Having derived dust masses for each of the galaxies, we are able to compare the dust masses with the CO[1-0] line luminosities. In Fig. 4.11, we show the relationship between these two quantities, as well as the $\frac{L'_{CO10}}{M_d}$ ratio as a function of gas excitation. As discussed in Section 4.3.1, we correct the CO[1-0] luminosities of the cluster galaxies, increasing their values (and errors) by 6%, as indicated by our simulations. Here we define the excitation as the ratio between the CO[4-3] and CO[1-0] line fluxes. As both α_{CO} and G/D vary with metallicity in the same way, we expect a constant ratio between L'_{CO1-0} and M_d in order to recover consistent molecular gas masses (Tan et al., 2014). This is shown by the dashed line at $\frac{L'_{CO1-0}}{M_d}$ $\sim$28 in both panels. Fig. 4.11 shows that the cluster galaxies scatter around the expected L'_{CO1-0} - M_d relation at z=2. Although we cannot constrain all of the $\frac{L'_{CO10}}{M_d}$ ratios due to our upper limits in CO[1-0], this confirms that our gas and dust properties are consistent with each other, and we have no reason to believe that an unusual ratio between the two is causing the heightened excitation fraction in the cluster or increased SFEs. An exception to this is galaxy A1, which appears to have a relatively large dust mass, or a relatively small L'_{CO1-0}, compared to the expected abundances. Possible interpretations of this will be discussed in Section 4.4.1.

Molecular gas masses

We now derive molecular gas masses of the galaxies using two different tracers - the dust mass and the CO[1-0] line luminosity. As previously stated (and discussed in detail in Chapter 5), the gas-to-dust ratio is dependent on metallicity, as is the CO-to-H_2 conversion factor, $\alpha_{\rm CO}$. We find no sub-mm or radio detections for the cluster galaxies that we have previously derived metallicity measurements for (Valentino et al., 2015), and we do not have gas-phase metallicity estimates for the galaxies presented here with CO[4-3] line detections. Therefore, for all of our galaxies except A1 and A2, we use the Fundamental Metallicity Relation (FMR, Mannucci et al., 2010) to derive statistical estimates of the metallicity, using the galaxy stellar masses and average SFRs. It has been suggested that the FMR is applicable for star-forming galaxies up to z$\sim$2.5, although this has proved difficult to observationally confirm and is an active area of current research (e.g. Sanders et al. 2015, Onodera et al. 2016). We then use the frameworks relating $\alpha_{\rm CO}$ and G/D to metallicity, given by Sargent et al. (2014) and Rémy-Ruyer et al. (2014) respectively, to derive $\alpha_{\rm CO}$ values and G/D ratios (see Chapter 5 for detailed discussion on this topic). The results of these calculations are shown in Table 4.7. It is important to note that these frameworks were calibrated on disk-like MS galaxies, and the galaxies in our sample are therefore likely to deviate from these relations.

For galaxies A1 and A2, we have derived the molecular gas mass from the galaxy dynamical mass, and we are therefore directly estimating values for $\alpha_{\rm CO}$ and G/D from $L'_{\rm CO1-0}$ and M_d respectively. For the rest of the galaxies, comparisons between the molecular gas masses derived using $\alpha_{\rm CO}$ and G/D are shown in Table 4.7. The gas masses derived from the G/D ratio are in fact the combination of both the molecular and the atomic Hydrogen gas in the galaxies, but we are assuming that the contribution from atomic Hydrogen in the ISM at z$\sim$2 is negligible. We do not show errors on the conversion factors in Table 4.7, as the errors are likely to be dominated by the systematic uncertainties in their derivation, due to the possibly non-standard nature of these sources. We discuss the implications of these uncertainties in Section 4.4.

ID	$\alpha_{\rm CO}$	G/D	log(M$_d$)	log(M$_{mol,dyn}$)	log(M$_{mol,CO}$)	log(M$_{mol,d}$)	μ_g	log(τ_{dep})
	$Kkms^{-1}pc^2M_\odot^{-1-1}$		$M_\odot$	$M_\odot$	$M_\odot$	$M_\odot$		(yrs)
A2	0.6*	51*	8.22 ± 0.15	9.93 ± 0.30	-	-	$1.00^{*\ +1.66}_{\ -0.62}$	7.98 ± 0.35
A1	3.6*	44*	8.64 ± 0.15	10.28 ± 0.30	-	-	$1.00^{*\ +1.66}_{\ -0.62}$	8.03 ± 0.35
13	4.5	168	7.90 ± 0.15	-	<10.25	10.12 ± 0.15	$0.46^{+0.54}_{-0.25}$	8.53 ± 0.24
6	4.2	149	8.35 ± 0.15	-	10.44 ± 0.14	10.52 ± 0.15	$0.64^{+0.75}_{-0.35}$	8.58 ± 0.24
B1	3.9	128	8.04 ± 0.15	-	10.18 ± 0.21	10.15 ± 0.15	$0.22^{+0.25}_{-0.12}$	8.56 ± 0.25
3	4.7	180	<7.65	-	<10.13	9.90 ± 0.15	$0.39^{+0.46}_{-0.21}$	8.61 ± 0.27
N7	4.2	146	7.84 ± 0.15	-	<10.10	10.00 ± 0.15	$0.86^{+1.00}_{-0.46}$	8.49 ± 0.25

Table 4.7: $\alpha_{\rm CO}$, G/D ratios, dust masses, molecular gas masses from the dynamical mass, molecular gas masses from CO, molecular gas masses from dust, gas to stellar mass ratios, μ_g, and gas depletion timescales τ_{dep}. The $\alpha_{\rm CO}$ and G/D ratios of A1 and A2, denoted by a star, have been directly derived assuming a molecular gas mass from the dynamical mass, and therefore should not be used to derive molecular gas masses. For the rest of the galaxies, $\alpha_{\rm CO}$ and G/D have been calculated using the metallicity derived from the FMR. The gas to stellar mass ratios and gas depletion timescales have been calculated using the gas mass from dust, using the G/D given. In the cases of A1 and A2, again denoted by a star, this ratio is 1 by construction from the dynamical mass calculation, as discussed in Section 4.3.5. 2σ upper limits are given.

4.3.8 Unidentified bright sources

Here we discuss the two brightest sources in our 870µm continuum images, A4 and A5, and their relationship with the cluster. A4 and A5 are shown in Fig. 4.1. Their 870µm fluxes are given in Table 4.3, at 1.8mJy and 6.0mJy respectively, implying high star-formation rates (shown in Table 4.5). In calculating these SFR estimates, we have assumed a redshift of z=2.0, and an average conversion factor between the SB and MS templates from Béthermin et al. (2015), as with the rest of the galaxies in Table 4.5. The negative K-correction of the flux at this wavelength means that our SFR estimates are not highly sensitive to the assumed redshift (Casey et al., 2014). Despite these bright sub-mm fluxes, we detect no spectral lines for either of these galaxies in any of the sub-mm/radio datasets discussed in this chapter, which were chosen to surround the expected frequencies of lines from galaxies at z$\sim$2. Additionally, we have thus far been unable to constrain the redshifts of these galaxies using optical spectroscopy, using data from the VLT and HST/WFC3. In particular, A4 has a relatively faint optical counterpart.

However, we can begin to exclude candidate redshifts for the galaxies, based on the lack of spectral lines. Using our current data, we can already exclude a large number of redshifts for these galaxies. We have created a redshift exclusion plot in Fig. 4.12, based on the non-detection of the strongest lines at submillimetre-radio frequencies that we would expect to observe in such star-forming galaxies, using existing correlations that relate line strength to the SFR (and thus L_{IR}) of a galaxy (Walter et al., 2011; Spilker et al., 2014). Based on the non-detection of each of these lines, the line rest-frame frequencies and the frequencies covered by our datasets, we show in Fig. 4.12 which redshift ranges can be excluded by each transition. We show that $\sim$80% of the redshift range 2<z<5 can already be excluded by these transitions. We would expect to detect all of the transitions given in Fig. 4.12 at S/N>8 for galaxy A5 at the redshifts shown, using the correlations with L_{IR}. For A4, we would expect to detect all transitions at S/N>5 at the given redshifts, with the exception of those transitions that are parenthesised in the left panel of Fig. 4.12. It can be seen that this does not significantly affect the excluded redshift range. These calculations were conservatively based on a ULIRG excitation template between CO transitions, and a 400kms^{-1} linewidth, based on the properties of the cluster galaxies listed in Table 4.4. It is also particularly unlikely that A4 and A5 are at z<1. The measured ratio of the 870µm to 3 GHz flux, the peak flux measured from previous SPIRE/PACS observations, as well as photo-z SED fitting all strongly exclude z<1 for A5 (Strazzullo et al., 2013). Fig. 4.12 also shows that more than 30% of redshifts at z<1 are excluded, based on the non-detection of low-J CO lines. In the right panel of Fig. 4.12, we bin candidate redshifts between z=0 and z=10 into widths of Δz=0.01, and for each redshift bin we count the number of transitions in the left panel that exclude this redshift. We see that a large

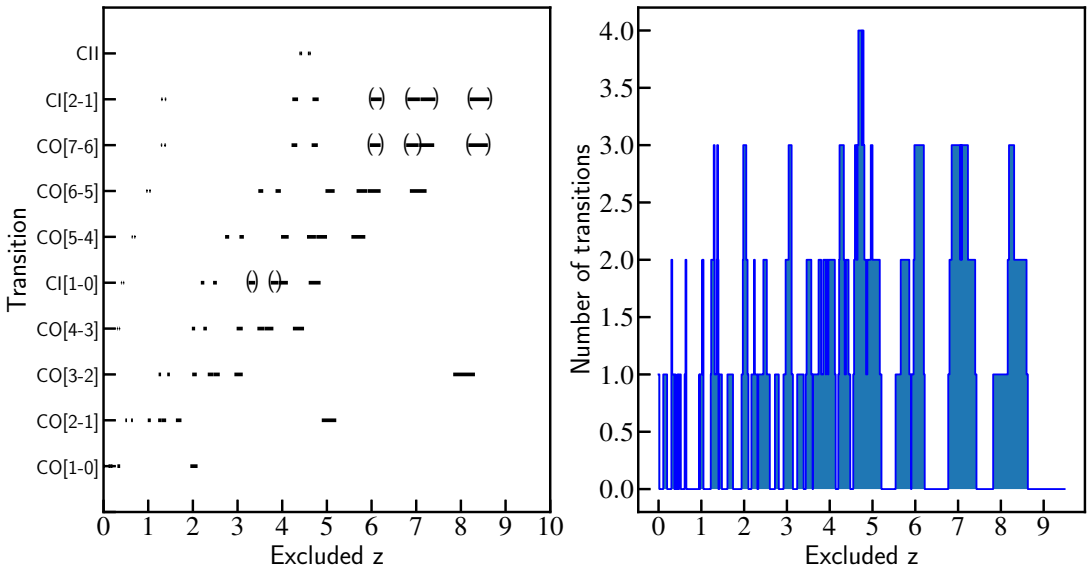

Figure 4.12: Left: Bright gas transitions at radio/submillimetre frequencies vs. redshift. For each transition that is not detected in our datasets for galaxies A4 and A5, we can exclude a range of redshifts based on the rest frequency of the line and the frequencies covered by our datasets. Different transitions therefore allow us to exclude different redshifts for each of our datasets. The parenthesised transitions would be detected at S/N<5 for the fainter galaxy, A4. Right: Histogram of the number of different transitions in the left panel that exclude each $\Delta z = 0.01$ redshift bin. The white gaps on the x-axis therefore highlight redshift ranges that have not been probed in line emission by any of our datasets.

range of redshifts are excluded using one or more non-detected transitions, including the redshift of Cl J1449+0856, z=1.99.

It is difficult to speculate whether these galaxies are likely to be cluster members. As discussed in Chapter 3, based on the non-detection of spectral lines at z$\sim$1.99, we must presently conclude that these galaxies are not cluster members. However, given observed number counts of field galaxies at 870µm (Karim et al., 2013), the probability of finding two galaxies this bright at 870µm by serendipitous detection alone, within 8" from the center of the cluster, is extremely low, $<4\times10^{-5}$. This hints at cluster membership for both galaxies. This could potentially be reconciled if the galaxies are strongly lensed, but this is unlikely to be the case based on the halo mass of the cluster (Gobat et al., 2011). We also see differences in the ratios of continuum fluxes at different wavelengths for A4 and A5, meaning that they do not have the same SED shape. This further suggests that A4 and A5 are not lensed projections of the same distant galaxy. The optical morphologies do not appear distorted in Fig. 4.1, and we don't identify suitable lensing candidates. The gravitational potential of the intra-cluster-medium of Cl J1449+0856 is not sufficient, and

there are no obvious foreground galaxy candidates.

On the other hand, we would expect to see bright accompanying CO lines in A4 and A5 based on the 870μm dust emission. For example, we would expect to see the CO[4-3] transition at S/N>100 in A5 at z=2, in our deep 2mm dataset. The measured 3σ upper limit on this line flux in A5 would therefore reveal a suppression of the CO emission by a factor >40 if A5 were in the cluster. If these bright galaxies are indeed cluster members, we would be seeing evidence of the very onset of star-formation quenching. Recent, very rapid quenching would be demonstrated by suppressed CO emission compared to the dust emission, because the gas and dust trace the star-formation on different timescales. CO is an instantaneous density tracer, whilst the dust emission traces the OB star population, and therefore takes ∼100 Myrs to decrease after the cessation of star-formation. This would indicate that the star-formation in these galaxies had fallen from hundreds of solar masses per year to zero in <100 Myrs, which would be a very extreme case. Finding galaxies in this narrow window of quenching would be extremely exciting. There are however several redshifts that are not probed by our datasets, shown in Fig. 4.12, including a small range near the photometric redshift of A5, z∼2.8. We hope that future observations targeting these yet-unprobed redshift ranges will shed more information on the nature of these extremely bright galaxies.

4.4 Discussion

4.4.1 Merger-driven enhancement in gas excitation and star-formation

We have discovered a population of cluster galaxies containing significant amounts of excited, dense molecular gas, shown by bright CO[4-3] line detections (Fig. 4.3). The SLEDs of the galaxies for which we characterise the CO excitation state reveal that 50% have starburst-like gas excitation properties. The offsets of the cluster galaxies towards the starburst SFR-L'_{CO1-0} relation shown in Fig. 4.7 also support this key conclusion. Having derived molecular gas masses for our galaxies, we can now look at their placement on the integrated Kennicutt-Schmidt plane in Fig. 4.13. The molecular gas masses derived from the CO[1-0] gas and the dust respectively, shown in Table 4.7, are found to be in good agreement, so we continue the analysis using the molecular gas mass calculated from the dust, as it is less affected by measurement upper limits than the CO[1-0] transition. The molecular gas masses for A1 and A2 are estimated from the dynamical mass. We see in Fig. 4.13 that there is a tight scatter in previous field studies around the locus of MS galaxies, and all of our cluster galaxies lie to the left of this relation, at enhanced SFEs. The median offset from the MS locus is 0.4 dex, meaning that our cluster galaxies contain on average 0.4 dex less molecular gas for their SFR compared to the MS galaxies. We see that some of our

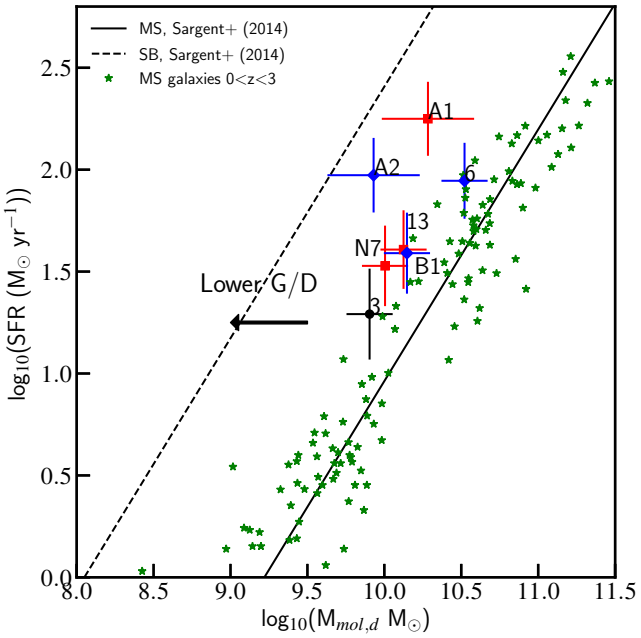

Figure 4.13: The integrated KS law. The colour-coding is as in Fig. 4.7. MS galaxies from previous studies are shown by the green stars (Daddi et al., 2010b; Geach et al., 2011; Magdis et al., 2012; Bauermeister et al., 2013; Tacconi et al., 2013), and it can be seen that the field correlation around the locus of MS galaxies is tighter here than in the SFR-L'_{CO1-0} plane, Fig. 4.7. The cluster galaxies all lie to the left of the MS relation, at enhanced star-formation efficiencies. The black arrow indicates the direction that the cluster galaxies would move if lower gas-to-dust ratios were used to derive their gas masses. This is highly relevant, as the G/D ratios derived from the FMR are currently all $>$100, and are not necessarily representative of a galaxy population containing a high fraction of mergers and AGN.

galaxies lie on the edge of the MS scatter, but it is highly plausible that the molecular gas mass has been over-estimated for these galaxies. As can be seen in Table 4.7, the G/D ratios derived from the FMR are all $>$100. It is unlikely that this is appropriate for our galaxies, especially considering their excited nature, with a high fraction of AGN and mergers/interactions in the sample. We indicate on Fig. 4.13 the direction and extent that these cluster galaxies would move if they were to have higher metallicities than derived from the FMR, and therefore G/D ratios more similar to those derived through dynamical arguments for A1 and A2. This would lead to a factor $\sim$3 lower gas mass, and even higher SFE offsets with respect to the MS relation.

As can be seen in Fig. 4.2, we find a high fraction of mergers, interactions and AGN in our star-forming cluster galaxies. Only two of our eight galaxies are isolated, non-AGN, of which one galaxy has a prominent bulge component and one was previously characterised as passive

through SED fitting and colour-colour diagnostics (Strazzullo et al., 2016). We will present further discussion on passive systems in the cluster in a future study, as this is a very exciting and expanding area of research (e.g. Sargent et al. 2015; Gobat et al. 2018).

Merging systems and AGN can naturally increase the density and excitation of the molecular gas in galaxies, and there is increasing evidence to suggest that mergers play an important part in galaxy evolution in high redshift (proto)clusters. The relative velocities of galaxies in clusters at high redshift are somewhat lower than in local clusters (e.g. $\sim$750kms^{-1}, Brodwin et al. 2011), making it more likely that galaxies will come into close contact with each other and experience either major or minor mergers. Studies of the morphologies of cluster galaxies have shown that significant numbers of cluster galaxies at z$>$1.5 have disturbed or irregular morphologies (Mei et al., 2015; Santos et al., 2015a), and mergers have also been taken to explain the larger sizes of high-redshift cluster galaxies compared to otherwise similar galaxies in the field (e.g. Delaye et al. 2014; Strazzullo et al. 2015). A recent study by Alberts et al. (2016) focussed on galaxy clusters in the range 1$<$z$<$2, and concluded that environmental interactions and an increased galaxy merger rate were triggering the heightened AGN fraction in the cores of some 11 massive clusters. Increased merger rates have also been measured in individual objects, such as the spectroscopically-confirmed protocluster Cl 0218.3-0510 at z=1.62 (Lotz et al., 2013). Here, 57% of cluster galaxies above M$_\star$ $>3\times10^{10}$M$_\odot$ were found to be in close pair/double nuclei systems compared to only 11% in the field, giving an increase in the merger rate of between 3 and 10 times above the field value. Krishnan et al. (2017) suggest that this increase in merger rate can be linked to the increase in AGN activity in this protocluster.

The high fraction of galaxy mergers and AGN in our star-forming cluster galaxies builds upon the above observations, and we suggest that increased merger and AGN activity in the cluster core is the key driver behind the high fraction of galaxies with starburst-like gas excitations, contributing a high fraction of the star-formation to the cluster core.

4.4.2 Merger driven star-formation in the core of the cluster

In order to quantify the effect of the environment on the ISM gas excitations and star-formation in the core of the cluster, we compare our primary findings with the expectations from field galaxy populations. We have discovered that 50% of our cluster galaxies have starburst-like gas excitations. This is quite a high fraction, and possibly surprising. For example, we can compare this with expectations from the 2-star-formation Mode (2-SFM) model (Sargent et al., 2014), considering the population of galaxies in this framework at stellar mass M$_\star$ $>10^{10}M_\odot$ and SFR$>30M_\odot$yr^{-1}, corresponding to the minimum stellar masses and SFRs for our galaxy sample. One might expect

that starburst galaxies in the 2-SFM model also have starburst-like excited molecular gas. In terms of the number density in the field, there are only ∼6% of starburst galaxies in the 2-SFM framework under these selection criteria at z=2 (Rodighiero et al., 2011; Sargent et al., 2012). There is a marked difference between this and the 50% of excited galaxies that we find in the cluster core.

If we now look at the star-formation rate density in the cluster, we find even more striking results. Firstly, we find that the cluster galaxies with highly excited gas contribute ∼50% of the total SFR to the cluster core. We again see a clear increase compared with the contribution of just ∼18% to the total SFR density that we would expect from starburst galaxies in the 2-SFM model, in the field at z=2. However, considering the excited galaxies in our cluster core neglects a significant fraction of the SFR driven by the large number of mergers and interactions. For example, we see that galaxy A2 contributes significantly to the total SFR, despite not having starburst-like gas excitation. If we extend our analysis and investigate the SFR contribution from mergers and interactions in the cluster core, we find that ∼75% of the total SFR in the cluster core comes from mergers and interactions alone. It is clear that the cluster environment of Cl J1449+0856 is having a significant impact on both the gas excitations and star-formation within the cluster. This is a very important result of our study, as it demonstrates and quantifies the significant impact that galaxy mergers are having on the SFR and evolution of this cluster in the early Universe.

4.4.3 Depletion timescales and gas fractions

As discussed in Section 4.4.1, the galaxies in Cl J1449+0856 with dense gas detections are not disk-like MS galaxies, nor typical isolated dusty starbursts. This makes direct comparison with the literature challenging, as we are exploring properties of galaxies that have been less widely characterised to date. In this section, we compute molecular gas depletion timescales and gas-to-stellar mass ratios for our sample of merger- and AGN-dominated cluster galaxies.

The high SFEs that we see in our galaxies imply that they have a higher SFR for their total molecular gas reservoir than MS, disk-like galaxies, and will deplete their gas supplies over relatively short timescales. Calculation of the depletion timescale is of course dependent on the conversion factors adopted between the observables (L'_{CO1-0} and M_d) and the molecular gas mass. In order to calculate gas depletion timescales, we have used the conversion factors shown in Table 4.7 for all galaxies except A1 and A2, and have assumed a constant SFR with no replenishment of the cold gas reservoir.

The values for α_{CO} and G/D for A1 and A2 were calculated directly, as stated in Section 4.3.7. It can be seen that both α_{CO} and the G/D ratio for A2 are lower than the values usually taken for solar-metallicity, MS galaxies (α_{CO}=4.4 and G/D=100). This is somewhat unsurprising, due to

the merging nature of A2. Interestingly, the G/D ratio for A1 reflects its merging nature, but the $\alpha_{\rm CO}$=3.6 is four times higher than that usually taken for typical mergers and starburst galaxies, $\alpha_{\rm CO}$=0.8. As was also seen in Fig. 4.11, there appears to be a discrepancy between the CO properties of A1 and the dust properties. A potential explanation for this is that the SFR of A1 has recently started to decrease. Dust is a longer-timescale tracer of star-formation than CO luminosity, so if the SFR of A1 recently peaked and has since started to decline, then this could be reflected in the instantaneous CO luminosity properties before it is reflected in the dust emission. The dynamical mass that we derive for A1 probes the total molecular gas content (in addition to the stellar mass, and relatively small dark matter and atomic gas contributions), and a high $\alpha_{\rm CO}$ value suggests that there is a large gas reservoir in A1 (assuming our 50:50 split between stellar mass and molecular gas is reasonable). If the SFR of A1 has recently started to decrease but there is still a large molecular gas reservoir, this could imply that it is primarily the dense, star-forming gas that has been removed, and the diffuse gas still remains. Alternatively, if the dust temperature of A1 is higher than the value that we have used, <U> = 28.75, then this would reduce the derived dust content for A1, as can be seen in Fig. 4.10. However, increasing the value of <U> would also increase the $L_{\rm IR}$ value derived from the dust, and as can be seen in Table 4.5, raising the $SFR_{870\mu m}$ in A1 would bring it further from the SFR derived from CO[4-3]. These ideas are speculation, but the fact that these conversion factors seem to suggest different physical properties raises an interesting question.

The values for molecular gas depletion timescales for all galaxies are shown in Table 4.7, again calculated using the gas masses from the dust. A typical MS galaxy, forming stars in a secular fashion, will deplete its cold gas reservoir in ∼0.5-1 Gyrs, whereas a violently starbursting galaxy can deplete its gas in <0.1 Gyrs (e.g. Saintonge et al. 2012, 2016; Leroy et al. 2013; Daddi et al. 2010b; Sargent et al. 2014; Genzel et al. 2015; Tacconi et al. 2013, 2018). We find that all of our cluster galaxies have relatively short depletion timescales, τ_{dep} <400 Myrs, with 50% of them having short timescales τ_{dep} <300 Myrs, in agreement with other recent cluster studies (Wang et al., 2016; Hayashi et al., 2017; Stach et al., 2017). Galaxies A1 and A2 have depletion timescales consistent with the short timescales observed in highly starbursting galaxies, ∼100 Myrs. We caution however that a direct comparison should not be made between our cluster galaxies and those values measured for isolated disk-like star-forming or starburst galaxies. Our galaxy sample appears heavily dominated by mergers, interactions and AGN, and is therefore not equivalent to the field samples from which these comparison values originate. Nonetheless, these short gas depletion timescales do suggest evidence for rapid star-formation quenching in this cluster environment. It is possible that this gas depletion could give rise to the massive elliptical galaxies, such as those

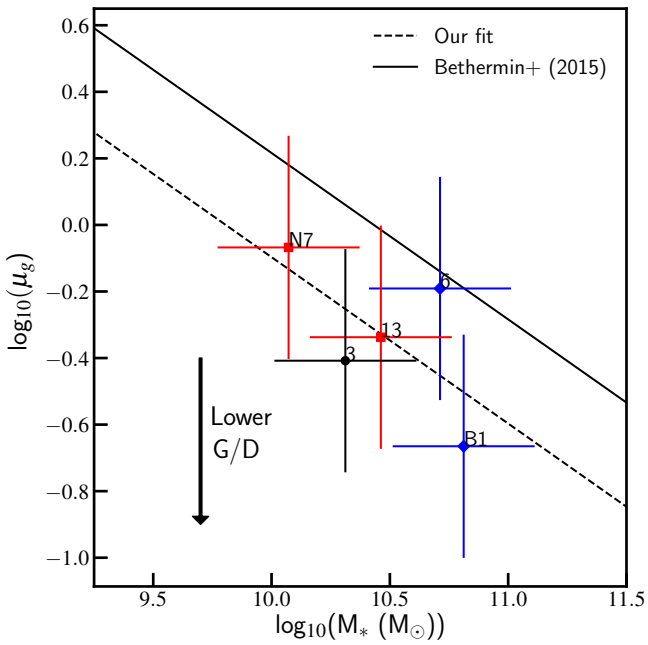

Figure 4.14: The gas-to-stellar mass ratio as a function of stellar mass. The black dashed line is the relation from Magdis et al. (2012), normalised to our data using a least-squares approach. The solid black line is the z=2 relation from Béthermin et al. (2015). The colour-coding is as in Fig. 4.7. A1 and A2 are not shown here, as their gas-to-stellar mass fractions have been set equal to 1 by construction. The normalisation of the trend for our cluster galaxies lies at lower gas-to-stellar mass ratio than for the Béthermin et al. (2015) MS relation. The black arrow indicates the direction and extent that the cluster galaxies would move if lower gas-to-dust ratios were used to derive their gas masses.

seen in local clusters, on short timescales.

We calculate gas-to-stellar mass ratios for our galaxies, μ_g, in Table 4.7, which are shown in Fig. 4.14. Here, we show the relationship between μ_g and $M_\star$ presented in Béthermin et al. (2015), $\mu_g \propto M_\star^{-0.5}$, with the normalisation calibrated for a field sample of MS star-forming disks. We fit this relationship with a fixed slope to our data, using a least squared approach, and we find that the best-fit normalisation for our galaxies is slightly lower than that of MS galaxies at z=2. This indicates that the gas-to-stellar mass ratios of our cluster member galaxies are lower than those of field MS galaxies at z=2. If our cluster galaxies were a sample of isolated, disk-like galaxies, this lower gas-to-stellar mass ratio might be expected, based on the high SFEs of the cluster galaxies that we see in Fig. 4.13. However, we cannot robustly make these direct links for our sample of cluster galaxies, which may not follow the same scaling relations as field MS disk galaxies. We believe that the lower gas-to-stellar mass ratios found for our cluster galaxies in Fig. 4.14 are driven

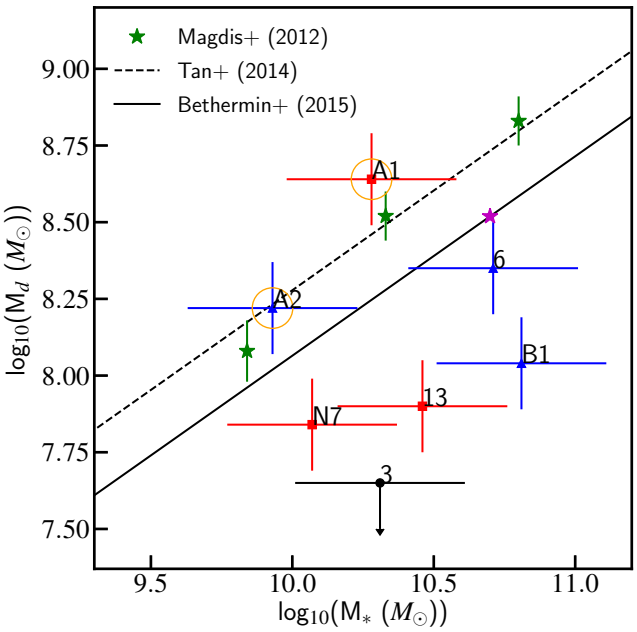

Figure 4.15: Dust mass vs. stellar mass. The colour-coding and symbols are as in Fig. 4.7. The green stars show the z∼2 MS galaxies, stacked in bins of stellar mass, from Magdis et al. (2012). The black dashed line is the relation given by Tan et al. (2014), normalised to the green data points. The black solid line is the normalisation given by the MS galaxies in Béthermin et al. (2015), with the same slope as in Tan et al. (2014). The purple star is the mean mass of the Béthermin et al. (2015) sample, used for normalisation. Several of the cluster galaxies show evidence for low dust-to-stellar mass fractions compared to these relations. 2σ upper limits are shown.

by the different physical natures of the galaxies in the cluster compared with MS disk galaxies in the field at z=2, an important outcome of this study.

As discussed in Section 4.3.7, the conversion factors and therefore gas masses derived for our cluster galaxies are based on the framework of normal MS galaxies, with the exception of A1 and A2. As can be seen in Table 4.7, we derive high $\alpha_{\rm CO}$ and G/D ratios from the FMR that do not seem to reflect the true nature of the galaxies. We might expect our active, interacting galaxies to have lower conversion factors, such as those derived directly for galaxy A2. In the case of lower conversion factors, the molecular gas masses would decrease, leading to lower gas-to-stellar mass ratios (shown on Fig. 4.14 by the black arrow), and even shorter gas depletion timescales for our galaxies. This would increase the tension between the gas-to-stellar mass ratios of our galaxies and the field galaxies shown in Fig. 4.14, and potentially imply star-formation quenching on even shorter timescales in the cluster environment. There is currently not a great deal of literature on the gas contents of such complex merging and active systems in clusters to compare our results with,

but we hope future studies on similar systems at high redshift will provide samples for comparison.

We compare the dust-to-stellar mass ratios of the cluster galaxies with previous studies in Fig. 4.15. Here, we see that approximately half of the cluster galaxies show evidence for low dust-to-stellar mass fractions compared with the MS field relations. This is not entirely unexpected, as we have seen in Figs 4.8 and 4.13 that the SFR in the cluster is being driven by relatively small amounts of molecular gas, for SFRs broadly consistent with the MS of star-formation. Fig. 4.14 illustrates this low molecular gas content per stellar mass, and we have shown in Fig. 4.11 that the dust and gas properties are consistent with one another (with the possible exception of A1). We do however caution that some cluster galaxies, such as IDs 6 and 3, are bulge-dominated, and may contain a significant passive stellar population, and we do not currently have the short-wavelength data to directly probe the dust temperatures of these galaxies. As is shown in Fig. 4.10, if we were to assume a dust temperature <U> less than 10, such as for the field elliptical galaxies studied in Gobat et al. (2018), this could in turn affect our derivations of properties for these galaxies (e.g. higher dust masses). We will return to this interesting possible effect in a future work.

4.5 Conclusions

We have presented deep observations from VLA and ALMA, in order to characterise the gas content of galaxies in a maturing cluster at z=1.99, Cl J1449+0856. In doing this, we are able to study how dust-obscured star-formation and ISM gas content are linked to the environment and galaxy interactions, during this crucial phase of high-z cluster assembly. We detect molecular gas in eight cluster galaxies, and find that these galaxies are dominated by mergers, interactions and AGN, rather than isolated disk-like star-forming galaxies. We present 870μm continuum measurements of the galaxies as well as multiple transitions of ^{12}CO: the CO[4-3] transition tracing the dense, star-forming gas, the CO[3-2] transition, and the CO[1-0] transition as a tracer of the total molecular gas reservoir. From these line fluxes, we are able to construct CO SLEDs for the galaxies, and find a highly increased fraction of galaxies with starburst-like gas excitations, $\sim$8 times greater than in the equivalent field population. We also find an enhanced contribution from the starburst-excited galaxies to the total SFR in the cluster core, $\sim$3-4 times greater than the starburst galaxy contributions to SFR in the field.

We calculate SFRs for the cluster galaxies from the CO data, and compare these with estimates from other SFR tracers such as our ALMA 870μm continuum observations. We find the tracers to be consistent, and use these SFRs to investigate the star-formation efficiencies of the galaxies, which are shown to be globally increased with respect to non-environment-selected samples. We do not however see a trend of increased sSFR. We derive dynamical masses for our two brightest,

resolved galaxies in CO[4-3], and directly calculate values for $\alpha_{\rm CO}$ and G/D based on their inferred molecular gas masses. For the rest of our galaxies, we calculate estimates of gas-phase metallicity using the FMR, and subsequently values for $\alpha_{\rm CO}$ and G/D.

We use ALMA continuum flux measurements to construct the submillimetre-radio portion of the galaxies' SEDs. We model the RJ tail of the SEDs, and in this way derive dust masses for each of the cluster galaxies. We compare molecular gas masses calculated from the galaxies' dust with gas masses and limits from the CO[1-0] line luminosities, and find the results to be in good agreement. We use the molecular gas masses derived from the dust mass for the analysis in this chapter.

We do not measure significant CO[1-0] flux for 5/8 galaxies despite our deep VLA data, further indicating that the star-formation in these galaxies is being fuelled by small amount of molecular gas. We calculate gas depletion timescales using the galaxies' SFRs and molecular gas contents, and find that the gas will be depleted on short timescales, between $\sim$100-400 Myrs. The gas-to-stellar mass ratios of the cluster galaxies appear to be lower than disk-like MS galaxies at z=2, but we caution against direct comparison with field samples due to the merging and active nature of the cluster galaxies.

Our results suggest that environmental effects in this dense cluster core have given rise to a galaxy population with a high fraction of excited, starburst-like galaxies, that will deplete their star-forming gas on short timescales. We conclude that the high gas excitations and star-formation activity are primarily driven by mergers and interactions in the core of Cl J1449+0856. We hope that increasing amounts of data will become available to facilitate further studies of the relationships between galaxy properties in clusters, continuing to build a more complete picture of the gas content and star-formation drivers of galaxies in dense environments. Future near-IR wide field surveys from space (e.g. Euclid; Laureijs et al. (2011), and WFIRST) will detect a large number of galaxy clusters at z$>$1.5-2. This will allow their synergistic study with ALMA, in order to investigate with unprecedented statistics the evolution of gas and galaxies in the most dense environments during the 'cosmic noon' epoch.

Contributions

Veronica Strazzullo provided the stellar masses and optical redshifts for the galaxies given in Table 4.5. Georgios Magdis performed the SED modelling to calculate the possible range of dust masses and radiation field intensities, described in Section 4.3.7. Mark Sargent provided the statistics from the 2-SFM model, for comparison with field galaxies in Section 4.4.2, and calculated the ISM conversion factors from the MZR given in Table 4.7. All co-authors contributed comments

and advice.

This chapter makes use of the following ALMA data: ADS/JAO.ALMA#2012.1.00885.S and ADS/JAO.ALMA#2015.1.01355.S. ALMA is a partnership of ESO (representing its member states), NSF (USA) and NINS (Japan), together with NRC (Canada), MOST and ASIAA (Taiwan), and KASI (Republic of Korea), in cooperation with the Republic of Chile. The Joint ALMA Observatory is operated by ESO, AUI/NRAO and NAOJ.

This chapter also makes use of VLA program 12A-188. The National Radio Astronomy Observatory is a facility of the National Science Foundation operated under cooperative agreement by Associated Universities, Inc.

Chapter 5

Suppressed CO emission and high G/D ratios in z=2 galaxies with sub-solar gas-phase metallicity

As a result of the significant overdensity of galaxies in Cl J1449+0856 discussed in Section 2.1, we have been able to uncover a diverse range of cluster members - from a massive assembling BCG to populations of low gas-phase metallicity and early-type galaxies at z=2. This enables us to investigate so-far poorly probed ISM regimes, and the related physical processes. This chapter therefore leads us to focus on a very important area of galaxy evolution - the low stellar mass population at z$\sim$2. Here, we take advantage of the deep multiwavelength datasets targeting Cl J1449+0856 to study both the ISM and tracers of obscured SFR in this low-enrichment subset of the population.

This chapter was published in Coogan et al. (2019), Monthly Notices of the Royal Astronomical Society, Volume 485, Issue 2, pages 2092-2105. A number of small additions have been made for this thesis.

Co-authors are: M. T. Sargent, E. Daddi, F. Valentino, V. Strazzullo, M. Béthermin, R. Gobat, D. Liu and G. Magdis.

Abstract

We study a population of significantly sub-solar enrichment galaxies at z=1.99, to investigate how molecular gas, dust and star-formation relate in low-metallicity galaxies at the peak epoch of star-formation. We target our sample with several deep ALMA and VLA datasets, and find no individual detections of CO[4-3], CO[1-0] or dust, in stark contrast to the >60% detection rate expected for

solar-enrichment galaxies with these MS Hα SFRs. We find that both low and high density molecular gas (traced by CO[1-0] and CO[4-3] respectively) are affected by the low enrichment, showing sample average (stacked) luminosity deficits >0.5-0.7 dex below expectations. This is particularly pertinent for the use of high-J CO emission as a proxy of instantaneous star-formation rate. Our individual galaxy data and stacked constraints point to a strong inverse dependence $\propto Z^{\gamma}$ of gas-to-dust ratios and CO-to-H_2 conversion factors $\alpha_{\rm CO}$ on metallicity at z$\sim$2, with $\gamma_{\rm GD}$ <-2.2 and $\gamma_{\alpha_{\rm CO}}$ <-0.8, respectively. We quantify the importance of comparing G/D and $\alpha_{\rm CO}$ vs. metallicity trends from the literature on a common, suitably normalised metallicity scale. When accounting for systematic offsets between different metallicity scales, our z$\sim$2 constraints on these scaling relations are consistent with the corresponding relations for local galaxies. However, among those local relations, we favour those with a steep/double power-law dependence of G/D on metallicity. Finally, we discuss the implications of these findings for (a) gas mass measurements for sub-M* galaxies, and (b) efforts to identify the characteristic galaxy mass scale contributing most to the comoving molecular gas density at z=2.

5.1 Introduction

Our current understanding of galaxy properties at the peak epoch of star-formation (z$\sim$2), in particular the interstellar medium, is primarily driven by observations of the brightest, most massive galaxies. The interplay between gas, dust and star-formation for the 'normal' galaxy population with $M_\star$ $\sim10^{10}$-$10^{11}M_\odot$ and approximately solar enrichment at z=2 is now reasonably well characterised (e.g. Aravena et al. 2010; Daddi et al. 2010a,b; Genzel et al. 2010; Magdis et al. 2012; Tacconi et al. 2013, 2018; Santini et al. 2014; Sargent et al. 2014; Scoville et al. 2014, 2017; Tan et al. 2014; Decarli et al. 2016). However, the ISM properties of lower mass galaxies at this redshift are much less well-understood, despite the fact that they are far more numerous than higher mass systems. This gap in our knowledge is a consequence of sub-M* galaxies being much more difficult to observe, in part due to their relative faintness. It is however important to push down to these systems to improve our understanding of the gas cycle and consumption across a broad range of halo and stellar masses.

A compounding difficulty in ISM observations is due to the low gas-phase metal abundance in these systems, as described by the 'mass-metallicity relation' (MZR), both in the local Universe and at higher redshifts (e.g. Tremonti et al. 2004, Zahid et al. 2014). The low enrichment of these galaxies affects quantities commonly used to estimate ISM content from observational data, such as the gas-to-dust ratio and CO-to-H_2 conversion factor $\alpha_{\rm CO}$. Molecular gas masses can be estimated from observations through CO spectroscopy, using $\alpha_{\rm CO}$ to convert between CO

luminosity and molecular gas mass. However, at low oxygen abundance, increasing proportions of star-formation in a galaxy are predicted to occur in 'CO-dark' molecular Hydrogen gas (e.g. Israel 1997; Grenier et al. 2005b; Wolfire et al. 2010). At low metallicity, the shielding of CO molecules by dust molecules is reduced, leading to higher photo-dissociation of CO molecules by ultra-violet radiation and a lower CO emission per unit molecular gas mass, thus increasing the value of $\alpha_{\rm CO}$.

In addition to this intrinsic lack of CO, the low-J CO transitions become observationally too faint with increasing redshift, and many low-J transitions fall out of suitable observing windows. It is therefore more practical to use sensitive instruments such as the Atacama Large Millimeter/submillimeter Array to detect emission from the higher order transitions of CO. An excitation correction is then applied, thereby adding further assumptions to the task of measuring molecular gas masses. Alternatively, gas masses can be inferred through cold dust continuum observations. This is done by relating the dust emission to the total gas mass through the G/D ratio (e.g. Guelin et al. 1993; Corbelli et al. 2012; Eales et al. 2012; Magdis et al. 2012; Bourne et al. 2013, Scoville et al. 2014; Groves et al. 2015), which is again closely linked to the metallicity of a galaxy.

Previous studies have therefore largely focussed on characterising the relationship between gas, dust and metallicity of the ISM in local galaxies (e.g. Burstein & Heiles 1982, Issa et al. 1990, Draine et al. 2007, Leroy et al. 2011, Magdis et al. 2012, Sandstrom et al. 2013, Tan et al. 2014; Rémy-Ruyer et al. 2014; Belfiore et al. 2015, Amorín et al. 2016). These works have illustrated a clear inverse dependence of G/D and $\alpha_{\rm CO}$ on metallicity. However, observations of the high redshift, low-metallicity regime are now required, in order to investigate whether similar relations as observed at low redshift also hold for galaxies in the peak epoch of galaxy formation. With the lack of equivalent information at high redshift, we are currently forced to either assume no metallicity dependence when deriving gas content from continuum or line observations at high redshift, or to assume that the scaling relations calibrated locally are valid at higher redshift. Some early attempts have been made to constrain these scaling relations at high redshift, such as those by Genzel et al. (2012) and Saintonge et al. (2013). Genzel et al. (2012) used the CO[3-2] and CO[2-1] transitions to perform a study of normal star-forming galaxies between z$\sim$1-2, with stellar mass $M_\star \gtrsim 10^{10} M_\odot$ and oxygen abundance on the Denicoló et al. (2002, D02) scale of 8.4-8.9. They found a strong inverse dependence of $\alpha_{\rm CO}$ on metallicity in star-forming galaxies at z$>$1, similar to what is observed at z$\sim$0. Saintonge et al. (2013) study the relationship between G/D and metallicity using $\sim 10^{10} M_\odot$ z$>$2 lensed galaxies over a similar metallicity range, and find an increase in the normalisation of the G/D ratio a factor 1.7 above the relation found for z=0 galaxies, suggesting an evolution of the G/D ratio with redshift as well as metallicity. By constraining these

scaling relations at lower metallicities, we will be able to more accurately use observations to characterise the properties of these galaxies, such as their star-formation efficiencies and molecular gas content.

In this chapter, we study the relationship between metallicity, gas, star-formation and dust content, in a sample of sub-solar metallicity galaxies in the cluster Cl J1449+0856 at z=1.99 (Gobat et al., 2011). Despite residing in a cluster environment, these galaxies are consistent with the MZR at z=2 (as discussed in Section 5.3.1) as well as the upper half of the main sequence (MS) of star-formation (Section 5.2.3), and are in this sense representative of the 'normal' population of galaxies for the purposes of this work. The study of these galaxies therefore allows us rare insight into the physics of the numerous sub-solar enrichment galaxies at this redshift, at masses lower than the characteristic mass of the stellar mass function at z=2 ($\log_{10}(M^*/M_\odot)\sim10.4$, Davidzon et al. 2017; see also Ilbert et al. 2010, 2013; Tomczak et al. 2014). We target the CO[4-3] and CO[1-0] transitions in our galaxies, in addition to the dust continuum emission at 870μm and 2mm. We describe our observations and data reduction in Section 5.2, and present our stacked gas and dust constraints in Section 5.3. We discuss the implications of our results in the context of star-formation rate L'_{CO}-SFR correlations, as well as scaling relations between α_{CO} and G/D with metallicity in Section 5.4. We summarise in Section 5.5. Throughout this chapter we use a ΛCDM cosmology with H_0=70kms^{-1}Mpc^{-1}, Ω_M=0.3 and Ω_Λ=0.7. We adopt a Chabrier initial mass function (IMF, Chabrier 2003).

5.2 Sample Selection and Main Data Sets

The spectroscopically-confirmed galaxy population of Cl J1449+0856 has been studied at many different wavelengths to date, spanning X-ray to radio observations (Gobat et al., 2011, 2013; Strazzullo et al., 2013, 2016, 2018; Valentino et al., 2015, 2016; Coogan et al., 2018). A subset of the $\sim$30 confirmed cluster members were selected for Subaru/Multi-object InfraRed Camera and Spectrograph (MOIRCS) near-infrared follow-up in Valentino et al. (2015, V15), based on their spectroscopic WFC3 redshifts (Gobat et al., 2013), and their star-forming *UVJ* colours (Strazzullo et al., 2013). Seven of these targeted star-forming members were detected by MOIRCS, as were two galaxies known to host X-ray AGN (Gobat et al., 2013). We exclude these AGN from our analyses, as the ionising radiation from the AGN is known to alter line ratios compared to pure star-forming galaxies (as demonstrated by e.g. the BPT diagram, Kewley et al. 2013), rendering metallicity estimates unreliable. Here, we discuss the five of these seven star-forming galaxies for which we also have follow-up ALMA and VLA observations, allowing us to probe their ISM properties.

A colour image of the cluster is shown in Fig. 5.1, alongside cutouts of the cluster members discussed here. As shown in V15, these galaxies extend from the core of the cluster towards the outskirts, reaching $\sim R_{200}$ of Cl J1449+0856 at a physical radius of $\sim$0.4 Mpc. The cores of these galaxies do not appear highly dust obscured at rest-frame optical wavelengths, demonstrated by their blue colours in Fig. 5.1, implying ongoing star-formation activity.

To study the dust and molecular gas content of our targets, we use the ALMA and VLA data described in Coogan et al. (2018), Chapter 4: CO[4-3] line and 2mm continuum fluxes were derived from ALMA band 4 data, CO[1-0] line fluxes from VLA Ka-band observations and 870μm continuum measurements from ALMA band 7 images.

5.2.1 MOIRCS observations

Our five star-forming galaxies were selected as part of a MOIRCS near-IR spectroscopic follow-up, for which the observations and data reduction are described in detail in V15. Each galaxy was observed through a HK500 grism slit of width 0.7", and the data was reduced using the MCSMDP pipeline (Yoshikawa et al., 2010). These observations primarily measured the [NII]6548, [NII]6583, [OIII]5007 and Hα emission lines, in order to derive metallicities, precise spectroscopic redshifts, and Hα SFRs. For galaxy V105, not presented in V15 but discussed in this chapter, the same approach as in V15 was taken for deriving these quantities. The results of these measurements are listed in Tables 5.1 and 5.2.

5.2.2 CO spectroscopy and dust continuum measurements

The ALMA band 4 data used to measure CO[4-3] fluxes contain a deeper, core observation (continuum RMS noise 8μJy/beam), and a shallower pointing (continuum RMS 24μJy/beam) of the outskirts of the cluster. The VLA Ka-band data used to measure CO[1-0] emission in the galaxies is a single pointing with continuum RMS 3μJy/beam.

We extracted CO spectra at fixed positions, corresponding to the rest-frame optical positions of the galaxies shown in Fig. 5.1. Line fluxes were measured directly in the uv-visibility plane with the GILDAS[1] task `uv_fit`. Visibilities were collapsed over the expected CO linewidth, chosen to correspond to the velocity range containing 90% of the Hα line flux, using the individual Hα linewidths listed in Table 5.2. It should be noted that these listed 90%-flux linewidths, $W_{90\%}$, are Full Width Zero Intensity widths, whereas the Hα linewidths are Gaussian Full Width Half Maxima. The choice of line profile is not expected to have a significant effect on our line flux measurements, as the fluxes are measured directly in the collapsed visibility data over the given

[1] http://www.iram.fr/IRAMFR/GILDAS

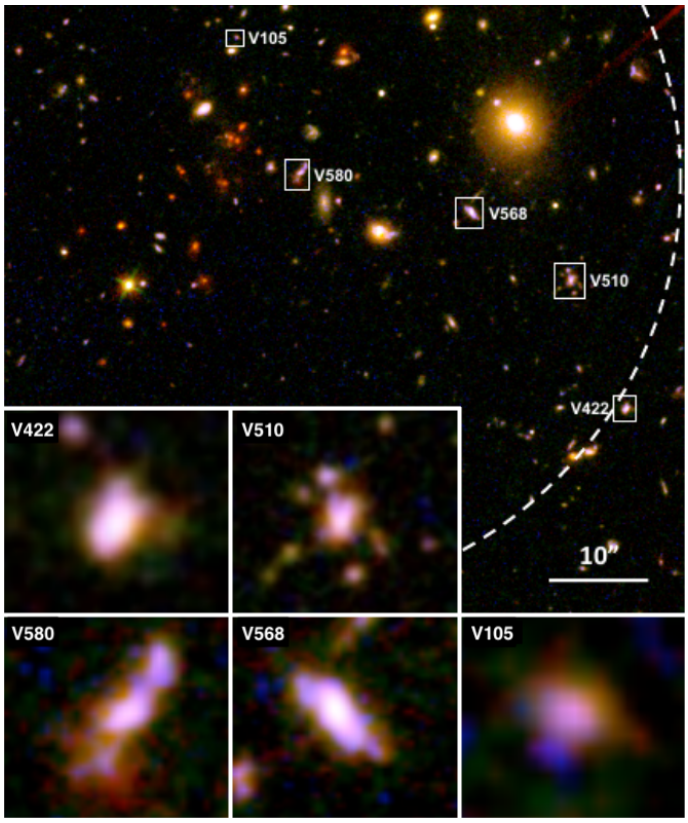

Figure 5.1: Colour image of the galaxy cluster Cl J1449+0856, using HST/WFC3 filters F606W, F105W and F140W. The five low gas-phase metallicity galaxies discussed in this chapter are indicated by white rectangles, and labelled with their IDs. The scale at the bottom right corner gives the angular scale of the main image, the cut-outs are zoomed versions of the individual galaxies as indicated. The white dashed circle shows the cluster R_{200} $\sim$0.4 Mpc physical radius (Gobat et al., 2013).

velocity width. Additionally, the line FWHM for detected CO[4-3] transitions of other members of Cl J1449+0856 were found to be consistent between a double and a single Gaussian profile in Coogan et al. (2018), Chapter 4. Due to the small optical sizes of the galaxies (see Fig. 5.1) compared with the size of the beams for the CO datasets (1.19"$\times$0.96" and 0.70"$\times$0.64" for CO[4-3] and CO[1-0] respectively), as well as the low SNR achieved by the individual CO spectra, all spectra were extracted assuming a point spread function (PSF) response (1σ spectral noise over a 100kms^{-1} width was 10 mJykms^{-1} and 4 mJykms^{-1} for the CO[4-3] core pointing and CO[1-0] respectively). In order to avoid contamination from other galaxies, particularly in the cluster core, neighbouring galaxies were iteratively modelled with GILDAS and removed from the data, before measuring the properties of the low-metallicity galaxy population. The exception to this was galaxy V580, which was modelled simultaneously with its dusty companion (galaxy ID A2 in Chapter 4).

ID	RA	Dec	z_{opt}	12 + log(O/H)	$\log_{10}(M_\star)$	δ_{MZR}	δ_{MS}	$SFR_{H\alpha}$	SFR_{UV}	$E(B-V)_{neb}$
	deg	deg	-	N2 PP04	$\log_{10} M_\odot$)	dex	dex	$M_\odot yr^{-1}$	$M_\odot yr^{-1}$	mag
V568	222.30242	8.93874	1.987±0.001	<8.26	9.66±0.30	<-0.03	0.52	39±5	41±8	0.15
V580	222.30702	8.93978	2.001±0.001	<8.48	10.06±0.30	<0.06	0.34	53±10	31±8	0.20
V422	222.29823	8.93351	1.988±0.001	8.14±0.12	9.76±0.30	-0.18	1.1	170±23	71±13	0.37
V510	222.29972	8.93691	1.988±0.001	<8.34	9.86±0.30	<-0.01	0.49	52±8	57±10	0.35
V105	222.30873	8.94340	1.988±0.001	<8.59	9.16±0.30	<0.42	0.08	6±2	<19	0.37
Sample Ave.	-	-	1.9904	8.34±0.13	9.79±0.13	0.01	0.49	52^{+19}_{-11}	41±9	-

Table 5.1: Physical properties of the five low-metallicity cluster galaxies, and their average properties. MOIRCS rest-frame optical spectroscopic redshifts are from V15. [NII] was individually undetected in all galaxies except V422, so 2σ upper limits on the oxygen abundance are shown, based on the N2 = $\log_{10}$([NII]/Hα) diagnostic and the PP04 calibration. The characteristic metallicity of the sample was derived from a weighted stack, see Section 5.3.1 for details. δ_{MS} and δ_{MZR} are the logarithmic offsets from the MS of star-formation (Sargent et al., 2014) and the MZR (Zahid et al., 2014), respectively (a negative value indicates an offset below the relations). The characteristic mass of the sample is the average of the five individual stellar mass estimates. Hα SFRs, UV SFRs, and the nebular reddening values (used to derive the dust-corrected Hα SFRs given) are also reported. The UV SFRs were calculated using continuum reddening. 3σ upper limits on UV SFR are shown. The characteristic Hα and UV SFR values of the sample are the medians of the individual SFRs.

ID	$\log_{10}(M_{mol}$, KS)	$\log_{10}(L'_{CO1-0})$	α_{CO}	$\log_{10}(M_d)$	G/D	$\sigma_{H\alpha}$	$W_{90\%}$
	$\log_{10} M_\odot$	$\log_{10}$(K kms^{-1} pc^2	$M_\odot$K kms^{-1} pc^2)$^{-1}$	$\log_{10} M_\odot$	-	kms^{-1}	kms^{-1}
V568	$10.50^{+0.08}_{-0.10}$	<9.88	>4.3	<8.26	>176	224±14	734±45
V580	$10.62^{+0.10}_{-0.13}$	<9.88	>5.5	<8.04	>375	202±27	779±29
V422	$11.03^{+0.08}_{-0.10}$	<10.19	>6.9	<8.76	>183	237±9	663±89
V510	$10.61^{+0.09}_{-0.11}$	<10.05	>3.6	<8.77	>69	233±20	763±66
V105	$9.84^{+0.16}_{-0.25}$	<9.78	>1.1	<7.98	>51	169±40	554±130
Sample Ave.	$10.61^{+0.14}_{-0.20}$	<9.58	>10.61	<7.92	>478	-	753±22

Table 5.2: ISM properties of individual galaxies in our sample, and of a stack of all 5 objects. $\log_{10}(M_{mol}$, KS) is the molecular gas mass inferred from $SFR_{H\alpha}$ via the integrated Kennicutt-Schmidt relation for main-sequence galaxies (Sargent et al., 2014). CO[1-0] line luminosities, derived α_{CO} conversion factors, dust masses, total G/D ratios, Hα linewidths from V15 and the expected CO 90%-flux widths ($W_{90\%}$) derived from these Hα lines are also listed. Upper limits on dust mass include the systematic errors discussed in the text. All upper/lower limits are placed at 3σ.

2mm continuum fluxes were measured in the uv-plane, after collapsing the data over the line-free spectral windows. The 870µm map is a mosaic formed of 7 single pointings, with a total area of 0.3 arcmin^2 centered on the cluster core. This therefore only covers the positions of galaxies V105, V580 and V568. However, we include this dataset in the analysis for these three galaxies (as well as the stacked sample) as it leads to a significant improvement in sensitivity of the dust emission maps ($\times$2 compared to the 2mm continuum). Continuum fluxes in the 870µm map were extracted using the software GALFIT (Peng, 2010), using the full dirty beam on the dirty, calibrated images, as the mosaic format made the transportation into GILDAS format impractical. We have previously verified that continuum fluxes measured with Common Astronomy Software Applications (McMullin et al., 2007), GILDAS and GALFIT for the dusty star-forming galaxies in this cluster are consistent (Coogan et al., 2018, Chapter 4). All galaxies in our sample were again modelled as PSFs in the continuum (beams of 1.19"$\times$0.96" and 1.41"$\times$0.62" for 2mm and 870µm respectively).

5.2.3 SED fitting and star-formation rates

We take stellar masses and SFRs for our sample as derived by Strazzullo et al. (2016), using Fitting and Assessment of Synthetic Templates (FAST; Kriek et al., 2009) spectral energy distribution modelling. Continuum reddening values were calculated assuming a truncated (i.e. constant) star-formation history before correction to the higher nebular extinction, as is appropriate for the Hα-derived SFRs (e.g. Calzetti et al. 2000, Kashino et al. 2013, Pannella et al. 2013, V15). The updated reddening values from Strazzullo et al. (2016) resulted in reductions of the galaxy stellar masses and Hα SFRs by $\sim$0.4 dex and $\sim$0.2 dex respectively, compared with V15. The nebular E(B-V) values and Hα SFRs are presented in Table 5.1. These galaxies have $\delta_{\rm MS}$ = SFR$_{\rm H\alpha}$/SFR$_{\rm MS}$ values between 0.08 and 1.1 dex, as shown in Table 5.1. The median offset of our galaxies from the MS is 1.6σ, where all but one of the galaxies (V422) lie below the frequently adopted 'cut-off' between the starburst and MS regimes, at 0.6 dex (Rodighiero et al., 2011; Sargent et al., 2012).

5.3 Results

In this section we describe our metallicity measurements, CO[1-0] and CO[4-3] line fluxes, dust continuum measurements and estimates for the molecular gas masses of our targets. CO fluxes are used to examine the relationship between CO luminosity and SFR in the low-metallicity regime. The combination of gas mass and L$'_{\rm CO1-0}$ allows us to put constraints on the $\alpha_{\rm CO}$ conversion factor, and similarly, we can use the dust continuum measurements to constrain G/D ratios.

ID	Hα $\times10^{-16}$	Hβ $\times10^{-17}$	[NII]6583 $\times10^{-17}$	[OIII]5007 $\times10^{-16}$	12 + log(O/H) N2 PP04	12 + log(O/H) O3N2 PP04
V568	1.87 ± 0.10	<2.92	<1.39	1.55 ± 0.08	<8.26	>8.14
V580	2.16 ± 0.25	7.38 ± 2.00	<3.96	1.49 ± 0.18	<8.48	>8.40
V422	4.19 ± 0.13	8.54 ± 1.53	1.96 ± 0.96	5.52 ± 0.08	8.14 ± 0.12	8.05 ± 0.07
V510	1.35 ± 0.10	4.84 ± 1.43	<1.41	0.96 ± 0.07	<8.34	>8.32
V105	0.14 ± 0.03	0.85 ± 0.41	<0.40	0.17 ± 0.02	<8.59	>8.46

Table 5.3: Line flux measurements from MOIRCS and corresponding metallicities. The units of Hα, Hβ, [NII]6583 and [OIII]5007 are erg cm^{-2} s^{-1} (also note the given scaling factors). Metallicities derived using these data for both the N2 and O3N2 PP04 calibrations are given. 2σ upper/lower limits are shown.

5.3.1 Gas phase metallicity measurements

We derive oxygen abundances with the N2 = $\log_{10}$([NII]6583/Hα) diagnostic and the Pettini & Pagel (2004, PP04) calibration using the MOIRCS spectra of our targets. Significant (SNR>5) Hα line detections were found for all five galaxies, but [NII] remained undetected with the exception of V422 where we find a weak detection (2.0σ). We therefore derived upper limits on the metallicities of the [NII]-undetected galaxies, using the upper limits on the [NII] fluxes. Known disadvantages of the N2 calibration are that it saturates at high metallicity, as well as being dependent on both the ionisation parameter and the ratio of N/O (Baldwin et al., 1981; Kewley & Dopita, 2002; Pérez-Montero & Contini, 2009). However, our galaxies are at significantly sub-solar metallicity, and the effect of the varying N/O ratio on the derived metallicities of these galaxies is negligible (V15). To further verify our N2-based metallicity values, we also use the O3N2 = $\log_{10}$(([OIII]5007/Hβ)/([NII]6583/Hα)) PP04 calibration to calculate metallicities of these galaxies, again using the MOIRCS data. Line fluxes for the MOIRCS-targeted lines, as well as the N2 and O3N2 metallicity estimates derived from these data, are given in Table 5.3. We find that the O3N2 indicator gives systematically lower metallicity than N2, as has also been seen at high-z by several other studies (e.g. Erb et al. 2006, Steidel et al. 2014, Zahid et al. 2014). Interestingly, the O3N2 metallicities are formally lower limits (except for the case of V422), due to the upper limits on [NII] and Hβ. We find a median metallicity offset between the metallicity limits inferred with N2 and O3N2 respectively of 0.09 dex, which is within the systematic uncertainties of the two estimators (0.18 dex and 0.14 dex for N2 and O3N2 respectively, PP04). We use N2 as our primary metallicity estimator, allowing us to make direct comparisons with the relevant literature (e.g. Magdis et al. 2011, 2012, V15).

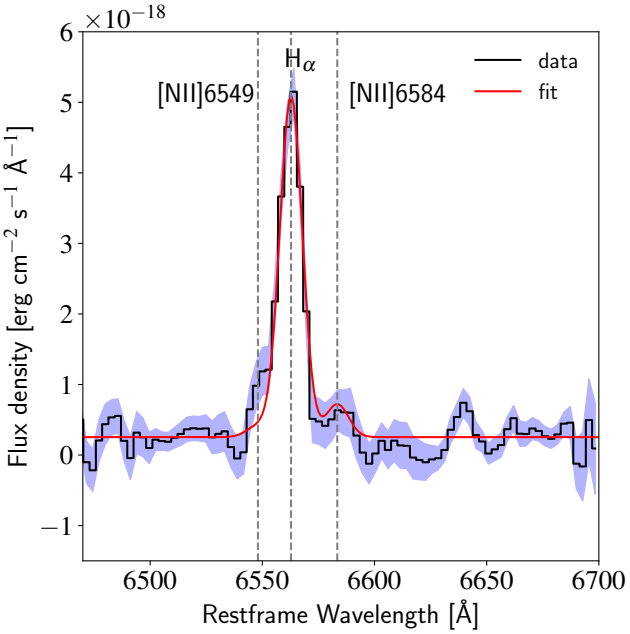

Figure 5.2: Stacked MOIRCS spectrum for our 5 low-metallicity galaxies. The weighted-average stacked spectrum is shown in black, with the 1σ errors given by the blue shading. The N[II]6549, [NII]6584 and Hα lines are indicated by dashed vertical lines. A fit, from Monte Carlo resampling of the data, is shown in red. Several standard constraints were placed on this fit, and are discussed in the text.

We report the metallicities of the individual galaxies used in this study in Table 5.1, as well as the offsets from the MZR at z$\sim$2. For the higher mass galaxies, with $M_\star > 10^{9.6} M_\odot$, their metallicity constraints place them $\sim$0.02 dex below the expected value (i.e. consistent, given the typical systematic error above), based on the mass-metallicity relation at z=2 (Zahid et al., 2014). For V105, the galaxy with the lowest SFR and stellar mass, the upper limit on the oxygen abundance places it $\sim$0.4 dex above the MZR[2]. The offsets $\delta_{\rm MZR}$ calculated with respect to the parametrisation of the MZR in Zahid et al. (2014) are consistent with those we derive for the MZR in both the N2 and O3N2 PP04 calibration, as reported by Steidel et al. (2014).

We derived a stacked metallicity estimate for all five galaxies combined. Following the same procedure as in V15, the continuum, Hα, [NII]6548 and [NII]6583 lines were modelled simultaneously in the stacked spectrum, using 1D Gaussian profiles. We imposed the positions of the [NII] lines to correspond to the redshift derived from the Hα line, as it has the highest SNR. We also imposed the standard constraint that the ratio of the line fluxes between the two [NII] lines must

[2]Note that 4/5 of our galaxies were reported as lying below the z=2 MZR in V15. It is the reduction of the stellar masses, discussed in Section 5.2.3, that brings these galaxies into agreement with the MZR (whilst metallicity values remain the same).

ID	I_{CO4-3} mJy kms^{-1}	I_{CO1-0} mJy kms^{-1}	F_{870GHz} µJy	F_{2mm} µJy
V568	<118	<39	<346	<32
V580	<74	<38	<203	<22
V422	<221	<79	-	<57
V510	<218	<58	-	<58
V105	<89	<31	<239	<30
Sample Ave.	<47	<20	-	<14

Table 5.4: Integrated line fluxes of the galaxies at the expected positions of the CO[4-3] and CO[1-0] lines, taken over the 90%-flux widths shown in Table 5.2, $W_{90\%}$. Continuum upper limits at 870µm and 2mm are also shown. 3σ upper limits are given. A dashed entry for a galaxy indicates that the galaxy was not covered by the 870µm mosaic. We do not give a sample average 870µm flux, as not all galaxies are present in the 870µm data.

be equal to 3.05 (Storey & Zeippen, 2000). The amplitude of a frequency-independent continuum contribution was left free to vary. We verified through a jackknifing analysis that our results are not heavily biased by individual galaxies, and that the method of stacking (optimal, median, average) does not significantly affect our results. The average metallicity and associated error we quote for the stacked galaxies is based on a Monte Carlo resampling, for which we created 1000 stacked spectra, each composed of a weighted average of individual, resampled galaxy spectra. An example of this fitting is shown in Fig. 5.2.

We find a weighted-average, stacked metallicity value Z=8.34±0.13. This error includes an additional factor derived from the spread of the metallicities from the jackknifing analysis, without the systematic uncertainty on the N2 PP04 calibration itself (0.18 dex). V15 used a sample of 6 low-metallicity cluster galaxies (4 of which are common to this study, with the exception of V105), to derive a mean metallicity value of Z=8.261±0.083, consistent with what we find for our sample. With an average mass $\log_{10}(M_\star/M_\odot)$ = 9.79±0.30, this stacked metallicity measurement implies an offset of ∼0.01 dex above the Zahid et al. (2014) MZR (the mean offset δ_{MZR} with respect to the Steidel et al. (2014) MZR at z=2.3 is -0.03 dex, consistent within 0.2σ).

5.3.2 Molecular line emission: CO[1-0] and CO[4-3]

As discussed in Section 5.2, by using the galaxy optical redshifts and the Hα linewidths, we can extract CO spectra and line fluxes for each galaxy over the expected velocity range. The CO[4-3] spectra for the individual galaxies are displayed in the top panel of Fig. 5.3 and show no significant

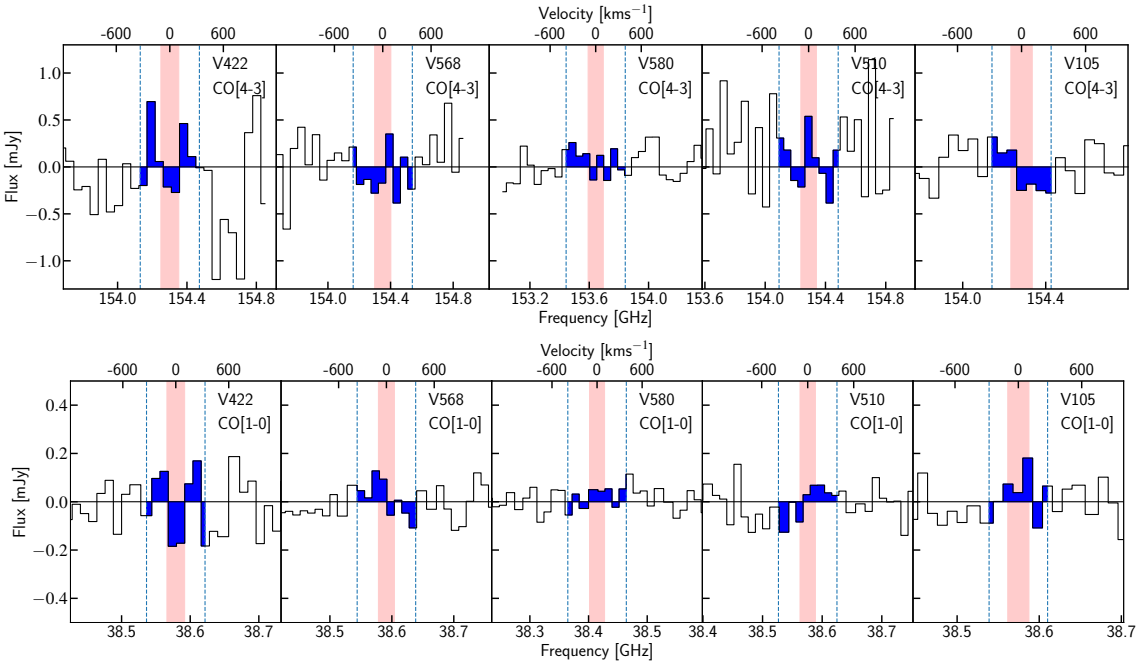

Figure 5.3: Top panel (lower panel): individual CO[4-3] (CO[1-0]) spectra binned into 90 km/s channels. The expected central position of the CO lines based on optical spectroscopic redshifts and associated errors are shown by the red vertical bands. The expected widths of the CO lines are shown by the blue shading of the spectra and the vertical dashed lines. The CO[4-3] and CO[1-0] transitions of all galaxies are individually undetected.

line detections. Similarly, the galaxies in our sample also remain individually undetected in the CO[1-0] transition (Fig. 5.3, lower panel). Upper limits for all line fluxes are presented in Table 5.4. We perform a weighted mean stack of all 5 galaxies (Fig. 5.4), and calculate the stacked line fluxes over the mean FWZI linewidth of the individual galaxies, Δv=753$\pm$22kms^{-1}. This corresponds to the weighted mean linewidth ($\langle\sigma_{H\alpha}\rangle$ = 231kms^{-1}), transformed to a FWZI containing 90% of the Hα flux. The error on this average linewidth reflects the error on the weighted mean. We perform Monte Carlo Markov Chain (MCMC) simulations to take into account the statistical errors on the redshifts of the individual spectra, displacing the individual spectra before stacking, according to the redshift sampled from a Gaussian distribution. The effect of this on the output stacked line fluxes is negligible. The flux uncertainties on the stacked spectra have been calculated using standard error propagation on the weighted mean of the individual channels. We verify that the error on the flux arising from the error on the linewidth is negligible, using a resampling approach over a Gaussian linewidth distribution. It should also be noted that the upper limits on these CO line fluxes are proportional to the square root of the linewidth. A factor of two difference in linewidth, for example, would therefore alter the derived (logarithmic) CO luminosities by $\pm$0.15 dex, and would not affect the conclusions of this work.

We find no detection of CO[4-3] emission, even in this stacked data, where the noise on the stacked spectrum is reduced by a factor $\sim\sqrt{5}$ compared to the individual spectra. We therefore place a 3σ upper limit on the stacked CO[4-3] line flux of $<$47mJy kms^{-1}, shown in Table 5.4. In the stacked CO[1-0] spectrum, we find a 3σ upper limit of $<$20mJy kms^{-1}. In both cases, we have scaled the errors on the spectra using the prescription that $\mathtt{Var}(S_\nu/\sigma_\nu)$ = 1 (where S_ν and σ_ν are the flux and associated error respectively in each line-free channel), thereby ensuring that they represent a true Gaussian distribution and are not underestimated. At the mean redshift of our targets, this corresponds to an upper limit log($L'_{\mathrm{CO1-0}}$ $<$9.58 (see Table 5.2). We discuss the potential implications of these low CO luminosities in Section 5.4.1.

5.3.3 Dust continuum emission

In order to estimate the dust mass of the cluster galaxies, we convert between submillimetre continuum flux and dust mass, M_d. This can be done separately for both the 870μm and 2mm continuum fluxes. As we cannot constrain the temperature of the dust with these data, we assume the shape of the z=2 IR-to-sub-mm MS SED from Magdis et al. (2012), the shape of which is consistent with the individual limits on our continuum fluxes. We then calculate dust mass using:

$$M_d = \frac{L_{IR}}{125\langle U\rangle} \propto \frac{4\pi d_L^2}{125\langle U\rangle} \times F_\lambda \tag{5.1}$$

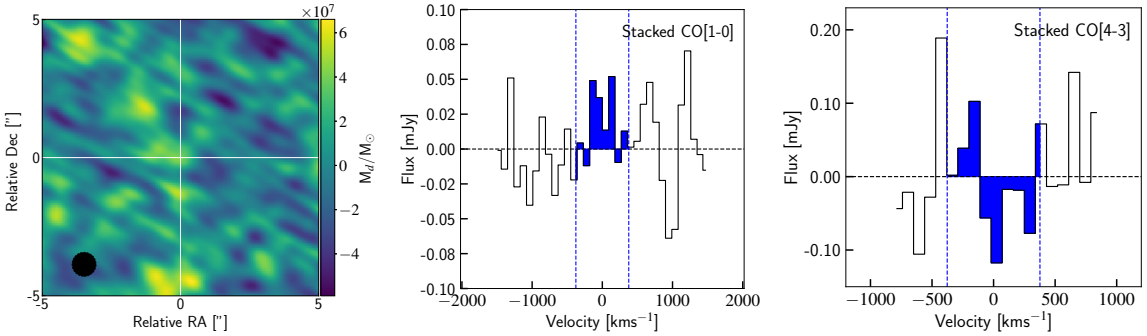

Figure 5.4: Left: stacked dust mass image for the five galaxies, created by combining the dust mass images from the 2mm data and 870µm data, as described in the text. The image is centered on the position of the stacked galaxies, and the white crosshair highlights the position of the peak pixel, used to derive the upper limit on dust mass. The average of the circularised beams for the two continuum datasets is shown in the bottom left corner. Center: weighted-average stacked CO[1-0] spectrum of the five galaxies, binned into 90 km/s channels and shown against velocity relative to the expected position of the CO[1-0] line. The blue shading illustrates the average linewidth (containing 90% of the flux) of the galaxies, $W_{90\%}$=753±22kms^{-1}, over which the stacked measurement was taken. Right: as for the center panel, but for the CO[4-3] spectral stack. The CO[4-3] spectrum covers a smaller velocity range than the CO[1-0] stack, as the spectral resolution was coarser in the sidebands used for continuum measurements.

where d_L is the luminosity distance of the galaxy, F_λ is either the 870µm or 2mm flux density and $\langle U \rangle$ is the mean, dust-weighted intensity of the stellar radiation field. The proportionality reflects the variable bolometric correction used to convert from sub-mm flux to L_{IR} for a given template shape (determined by our assumed value of $\langle U \rangle$=22, in accordance with the redshift-evolution of this parameter measured in Béthermin et al. 2015). 125 is the average scaling factor between L_{IR}/M_d from Magdis et al. (2012). If the dust temperatures in our galaxies were warmer than the template, as observed locally in low-mass and low-metallicity dwarf galaxies (e.g. Walter et al. 2007), this would in turn decrease the derived dust mass, and increase the G/D ratios. As we do not constrain the temperature, we allow a systematic error of 0.15 dex for these dust masses (Draine & Li, 2007). In this way, we first calculate separate dust mass estimates from the 870µm and 2mm measurements (for V105, V580 and V568, which we find to be consistent). The final dust mass of each galaxy is then calculated by combining the two dust mass estimates, weighted according to their errors. Where appropriate, the upper limit on the dust mass is calculated from this weighted average and associated error. For V422 and V510, the dust mass comes only from the 2mm measurements.

Similarly to the CO emission, we find no significant dust continuum detections for these

galaxies individually. The constraints on these dust masses are given in Table 5.2. We therefore created a stacked dust map for the five low-metallicity galaxies. To do this, we first made individual dust mass maps for each galaxy. We created 10"×10" cutouts centered on each galaxy, in both the 870µm and 2mm data. This was done using the dirty image maps, having removed all other sources and corresponding sidelobes by simultaneous flux modelling of the entire field in GALFIT, using the full known dirty beam pattern. Each flux emission map (2mm or 870µm) was then converted to a dust mass map, pixel by pixel, for each galaxy, by converting between flux and dust mass as described above. All of these individual dust maps were then stacked in the image plane, by performing a weighted average of the images at each pixel position. The weights were determined by the primary beam corrected RMS noise in the individual image cutouts. The stacked dust map is shown in Fig. 5.4.

As this image combines two datasets imaged with different synthesised beam shapes, PSF-fitting with GALFIT was not practical. If - as motivated in Section 5.2.2 based on their small optical sizes - the galaxies in the stack are unresolved, we can measure the dust mass associated with the stack by reading off the value of the central pixel in the stacked image and interpreting it as a peak flux measurement. We note that, as the circularised FWHM of the synthesized beams differ by only ∼10%, the two datasets sample similar spatial scales and have been imaged with the same pixel size. We find a 3σ upper limit on the stacked (weighted average) dust mass of $M_d < 7.4\times10^7$ $M_\odot$. This small amount of dust seems consistent with initial expectations for low-metallicity galaxies, and we discuss how the dust and gas in these galaxies scale with metallicity in Section 5.4.2.

5.3.4 Molecular gas masses

We have calculated the molecular gas content of the galaxies by taking the Hα SFR of each galaxy, and using the integrated Kennicutt-Schmidt (equation 5 of Sargent et al. 2014) law to convert between SFR and molecular gas mass M_{mol} as below:

$$M_{mol} = SFR \times \frac{1}{SFE} \tag{5.2}$$

As we do not know the star-formation efficiencies (SFEs) of the galaxies, we assume that SFE increases smoothly with distance above the MS (e.g. Sargent et al. 2014; Tacconi et al. 2018), for each individual galaxy, to obtain molecular gas masses from $SFR_{H\alpha}$. The assumption of these SFEs (corresponding to gas depletion times between ∼0.6-1.1 Gyr for our galaxies, with a sample median of 0.8 Gyr) is motivated by the position of our targets relative to the main-sequence of star-formation, and the consistency between the UV and Hα SFRs discussed below. We have no evidence that the galaxies have significantly increased SFEs or high gas excitation ratios. However,

we also indicate the effect of a strongly increased SFE in Fig. 5.6. The molecular gas masses derived assuming a MS SFE (i.e. the SFE increasing smoothly with distance above the MS) are shown in Table 5.2. It is these gas masses that are used in the remainder of the analysis.

5.4 The impact of a low gas-phase metallicity on ISM scaling relations at z∼2

A key outcome of this study is the notable lack of gas and dust detections in our star-forming galaxies. If we take the Hα SFRs of our galaxies, we would expect to detect the CO[4-3] and CO[1-0] emission at $\geq 3\sigma$ from 4/5 of our galaxies, assuming that the galaxies had BzK-like Spectral Line Energy Distributions (where BzK galaxies represent the 'normal', solar-enrichment population at this redshift). In the continuum data, we would expect to detect 3/5 of our galaxies at $\geq 3\sigma$ in the 2mm data (assuming a BzK-like SED), and to detect 2/3 of the galaxies covered by the 870μm mosaic. However, we see in Section 5.3 that we do not detect any of our galaxies in these datasets. We now discuss the implications of these low detection fractions.

5.4.1 SFR-L'_{CO} correlations for z=2, low-metallicity galaxies

Fig. 5.5 (a) shows the relation between SFR and L'_{CO1-0} for galaxies in our sample, together with literature data compiled by Sargent et al. (2014) and containing MS galaxies at $0<z<3$. With the exception of V105, we see that the 3σ L'_{CO1-0} limits for our galaxies lie on, or to the left of, the reference trend from Sargent et al. (2014). The stacked L'_{CO1-0} limit is offset by ∼0.5 dex from this relation. This suggests that on average the galaxies have high SFRs given their L'_{CO1-0}, and the stacked limit occupies the same part of parameter space as high-SFE starburst galaxies. However, the δMS values given in Table 5.1 indicate that our galaxies do not lie in the starburst regime in terms of their specific star-formation rates, with the exception of V422. An interpretation of this offset is then that the lack of L'_{CO1-0} in the galaxies is driven by their low gas-phase metallicities, consistent with an increased amount of photo-dissociation of CO molecules in diffuse clouds.

We also show in Fig. 5.5 (a) the predicted locus of 'typical' z∼0 and z∼2 galaxies in SFR-L'_{CO1-0} space. To trace this locus we start from the log-linear integrated Kennicutt-Schmidt relation - expressed in terms of SFR and M_{H2} - from Sargent et al. (2014). We then associate to a given SFR and M_{H2} a metallicity-dependent CO-to-H2 conversion factor α_{CO} via the following three steps. We assume that SFR and $M_\star$ are linked via the main-sequence relation, and $M_\star$ and metallicity via the MZR. We then consider α_{CO} vs. metallicity trends with a power-law form Z^γ, where $-2<\gamma<-1$ (e.g. Israel 1997; Glover & Mac Low 2011; Leroy et al. 2011; Narayanan

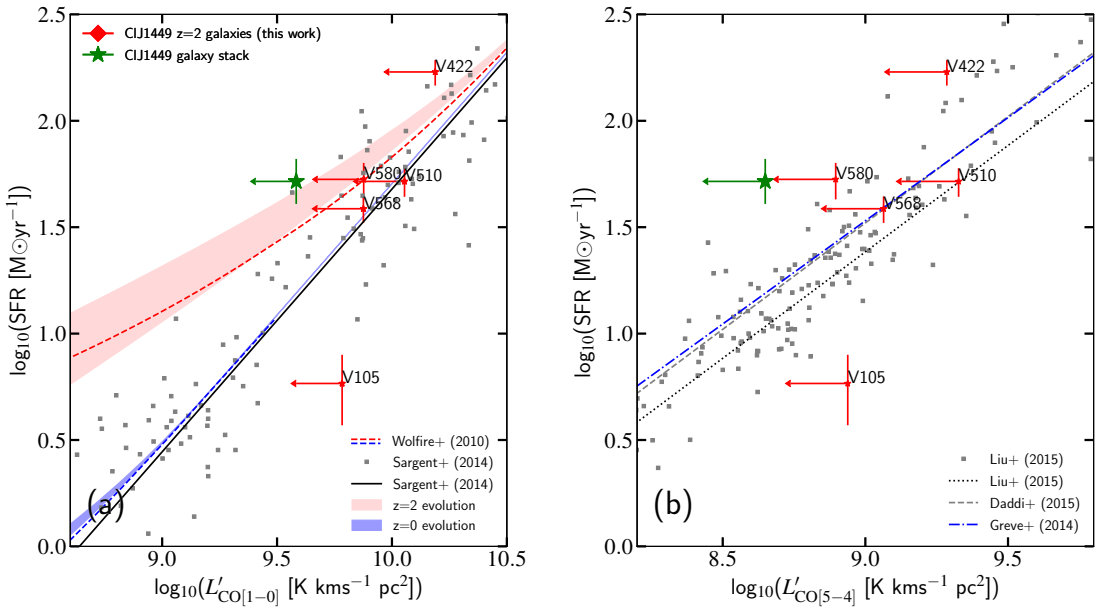

Figure 5.5: Left: SFR_{H_α} vs. L'_{CO1-0}, where upper limits are located at 3σ. Predicted evolutionary trends are shown for z=0.08 and z=2 by the blue and red shaded curves, assuming an α_{CO} vs. metallicity slope between -1 (lower edge) and -2 (upper edge), as well as evolutionary trends predicted by Wolfire et al. (2010) (dashed lines). Right: SFR_{H_α} as a function of L'_{CO5-4}. The green stars show the stacked upper limit on L'_{CO1-0} (left) and L'_{CO5-4} (right, from the stacked CO[4-3] data) respectively. The vertical green error bar on the stack shows the formal error on the median Hα SFR. Previous literature relations are indicated in the legend. We see evidence for metallicity-driven, systematically decreased line emission from the diffuse, extended (traced by CO[1-0]) and denser molecular gas phases (traced by CO[5-4]) in our targets.

et al. 2012; Schruba et al. 2012; Amorín et al. 2016), as well as the prescription from Wolfire et al. (2010) (see also our Fig. 5.6 (a)). We have normalised the relationship between α_{CO} and metallicity so that a galaxy with the stellar mass of the Milky Way ($M_\star$=5.7×10^{10}M$_\odot$, Licquia & Newman 2015) has α_{CO}=4.0[3]. The expected SFR-L'_{CO1-0} relation starts to curve away from a simple log-linear trend at low L'_{CO1-0}, with a 'detachment point' that shifts to higher luminosities with increasing redshift. While V422 and V580 are offset from the log-linear SFR-L'_{CO1-0} relation given by Sargent et al. (2014), the individual and stacked L'_{CO1-0} limits are more closely consistent with the expected locus for z∼2 galaxies. It should be noted here that the placement of starburst galaxies on this plane, offset from the SFR-L'_{CO1-0} relation, is driven by a high SFE compared with MS galaxies, rather than by low metallicity. The oxygen abundances of such high-z starbursts are typically higher than the galaxies discussed in this chapter, consistent with solar metallicity

[3]We omit the units of α_{CO} for brevity, but give α_{CO} in units of M$_\odot$(K kms^{-1} pc^2)$^{-1}$ throughout this chapter.

(e.g. Rigopoulou et al. 2018).

For further evidence that a CO-deficit rather than a SFE-enhancement is responsible for the position of our low-metallicity galaxies in SFR-L'_{CO} space, we can also look at the SFR - L'_{CO5-4} plane shown in Fig. 5.5 (b). L'_{CO5-4} was derived from the CO[4-3] data, assuming a MS, BzK-like excitation (I_{CO5-4} = 1.04×I_{CO4-3}, Daddi et al. 2015). The assumption of a BzK- or starburst-like excitation between CO[4-3] and CO[5-4] does not significantly affect the derivation of this quantity. The comparison dataset in this figure comprises local ULIRGs and spirals (Liu et al., 2015), BzK galaxies at z∼1.5 (Daddi et al., 2015) and high-z SMGs (Carilli & Walter, 2013). The individual limits on our galaxies again lie to the left of the literature relations, and the stacked L'_{CO5-4} constraint lies at ∼0.5-0.7 dex below the L'_{CO5-4} that would be expected from a galaxy with this SFR. This is particularly interesting, as Daddi et al. (2015) have shown that there is a tight, linear correlation between the CO[5-4] luminosity of a galaxy and its IR luminosity (and therefore SFR), regardless of whether the galaxy is MS or starbursting, with increased scatter only for the most extreme objects across cosmic time (Liu et al., 2015). The offset we see in Fig. 5.5 (b) must therefore be a consequence of another physical property of the galaxies.

To test whether this offset could be due to a SFR timescale effect, rather than low metallicity, we compare the Hα- and UV- SFRs in Table 5.1. Hα is a short timescale (<10 Myr) tracer of star-formation, whereas UV emission traces star-formation on timescales of ∼100 Myr (Calzetti, 2008; Kennicutt & Evans, 2012). The Hα- and UV- SFR estimates do not show large discrepancies, and are consistent to within $<2\sigma$, with the exception of very bright V422. The tension between these SFR indicators for V422 could indicate a recent increase in the SFR, but it should be noted that this comparison is dependent on the prescriptions of E(B-V) used for continuum and nebular extinction. This indicates that the SFRs of the galaxies have remained fairly constant for the last 100 Myr, i.e. show no indication of a rapidly declining SFR (which in turn would lead to low CO[5-4] emission compared to the SFR-L'_{CO5-4} trend, as CO[5-4] flux effectively represents an instantaneous SFR-tracer following Daddi et al. 2015). The clear offset of the stacked data in both panels of Fig. 5.5 is therefore unlikely to be driven by timescale effects, and reinforces the conclusion that it is the low gas-phase metallicity in these galaxies that is driving the lack of CO emission at J=1-0 and J=4-3.

It is not clear to what extent one would expect the high-J transitions of CO to suffer the same effects of low enrichment as the low-J transitions. Studies of dwarf galaxies in the local Universe have revealed CO[3-2]/CO[1-0] and CO[2-1]/CO[1-0] line ratios consistent with those observed in local spiral galaxies (e.g. Sage et al. 1992; Meier et al. 2001; Cormier et al. 2014), indicating that photo-dissociation impacts the CO Spectral Line Energy Distribution up to at least the J=3-2

transition in local low-metallicity galaxies. It is qualitatively understood that the effect of photo-dissociation is less prevalent in small regions of 'dense' CO gas (e.g. Bolatto et al. 2008), but it is not widely discussed to which CO excitation this extends to, and whether this is dependent on the individual galaxy. Aside from the destruction of CO by photo-dissociation, it is plausible that high-J excitation could be somewhat enhanced in low metallicity environments, due to the stronger radiation field. We see in our galaxies that, despite this possibly enhancing effect, the molecular ISM at densities of $\sim 10^5$ cm^{-3} ($\sim$40$\times$ the critical density of the CO[1-0] molecule) nevertheless displays a significant CO-deficit, compared to the tight SFR-L'_{CO5-4} relation observed by normal and starburst galaxies with approximately solar metallicity.

Although not well characterised to date, evidence that denser molecular gas phases in high-z galaxies can be affected by low metallicity has also been discussed by Tacconi et al. (2008) and Genzel et al. (2012), who find increasing numbers of galaxies at z$\sim$2 (e.g. ZC406690, Mancini et al. 2011) that lack CO[3-2] emission compared to expectations. Our results suggest that this effect is present to even higher-J CO transitions at z=2. We see evidence that the low metallicity in these galaxies may be either directly or indirectly influencing denser molecular gas reservoirs, implying that the linear correlation between CO[5-4] luminosity and SFR (which underpins SFR estimates based on CO emission) may not hold for low-metallicity galaxies at z=2. The deficit of CO emission in these galaxies is particularly relevant when considering high-J CO emission as an instantaneous star-formation tracer (e.g. Lu et al. 2014, Daddi et al. 2015, Liu et al. 2015, Yang et al. 2017).

5.4.2 Metallicity-dependence of α_{CO} and G/D for z$\sim$2 galaxies

The dependence of α_{CO} and G/D on metallicity at z$\sim$0 follows a strong inverse relation, observationally following a power-law Z^{γ} or broken power-law shape (e.g. Draine & Li 2007; Wolfire et al. 2010; Leroy et al. 2011; Rémy-Ruyer et al. 2014). However, as discussed extensively in the literature (e.g. Kewley & Ellison 2008), different metallicity calibrations lead to systematically different gas-phase metallicity derivations (by up to $\sim$0.6 dex). These offsets lead to different normalisations for G/D and α_{CO} vs. metallicity trends being reported in the literature (see, e.g., Sandstrom et al. 2013). For example, at a fixed oxygen abundance value and when assuming a power-law dependence on metallicity with exponent γ = -1, mean G/D ratios (and α_{CO} values) will differ by a factor 4.7 when using two of the metallicity scales with among the largest systematic offsets, namely the Pilyugin & Thuan (2005, PT05) and Kobulnicky & Kewley (2004, KK04) systems respectively. If we assume an even steeper slope with γ = -2, this discrepancy reaches a factor of 22 between the conversion factors derived using the PT05 and KK04 calibrations. It is therefore

imperative to correct for the offsets between metallicity scales to ensure meaningful results and comparisons, as these systematics complicate making robust statements about the evolution of scaling relations with redshift.

For this reason, in the following we consider a normalised metallicity scale (see Fig. 5.6) which minimises the systematic uncertainties introduced by different metallicity scales. We normalise all metallicities by the metallicity $Z_{M_\star MW,z=0}$ of a z∼0 Milky-Way-like galaxy of stellar mass $M_\star$=5.7×$10^{10}M_\odot$ (Licquia & Newman, 2015), using the relevant local MZR for each calibration (Kewley & Ellison, 2008). This is preferable to using a single, constant reference metallicity value, which has conflicting interpretations between different metallicity scales. For example, the canonical solar oxygen abundance 12+$\log_{10}$(O/H)$_\odot$ = 8.69 (Asplund et al., 2009) is ∼0.3 dex higher than the typical MW-like metallicity of Z=8.37 in the PT05 scale. Conversely, on the KK04 scale, the solar abundance value is ∼0.3 dex smaller than that of a MW-like galaxy. The advantage of our normalisation approach is thus that we can reconcile scaling relations expressed in different metallicity calibrations by means of our calibration-dependent normalisation factor $Z_{M_\star MW,z=0}$. If we were to instead convert the range of literature studies to one chosen metallicity system, we would find that straight-line, log-linear scaling relations in one system would map into curved loci in another. Converting to a normalised metallicity scale, as we have done, therefore preserves the shapes of the trend lines, and illustrates the full range of slopes reported in the literature. Additionally, conversions between certain metallicity calibrations are not available in Kewley & Ellison (2008), which would limit the relations available for comparison in this framework. Common calibrations used among literature relations are PT05, PP04, D02 and KK04, for which $Z_{M_\star MW,z=0}$ equals 8.37, 8.77, 8.85 and 9.05 respectively as outlined above.

$\alpha_{\rm CO}$ as a function of metallicity

Gas-phase metallicity is observed in the local Universe to have a direct effect on the $\alpha_{\rm CO}$ conversion factors of low-metallicity galaxies (e.g. Leroy et al. 2007; Amorín et al. 2016; Accurso et al. 2017, Hunt et al. 2017). The low gas-phase metallicity strongly increases $\alpha_{\rm CO}$, as the lower metal content of the ISM leads to lower dust shielding of the CO molecule, which can consequently be photo-dissociated by UV radiation from young stars. This leads to 'CO-dark' H_2 gas.

Fig. 5.6 (a) shows $\alpha_{\rm CO}$ as a function of metallicity. For all galaxies in our sample we have placed lower limits on $\alpha_{\rm CO}$ using the gas masses inferred in Section 5.3.4 and the upper limits on the CO[1-0] luminosity listed in Table 5.2:

$$\alpha_{\rm CO} = \frac{M_{mol}}{L'_{\rm CO1-0}} = \frac{SFR}{SFE}\frac{1}{L'_{\rm CO1-0}} \tag{5.3}$$

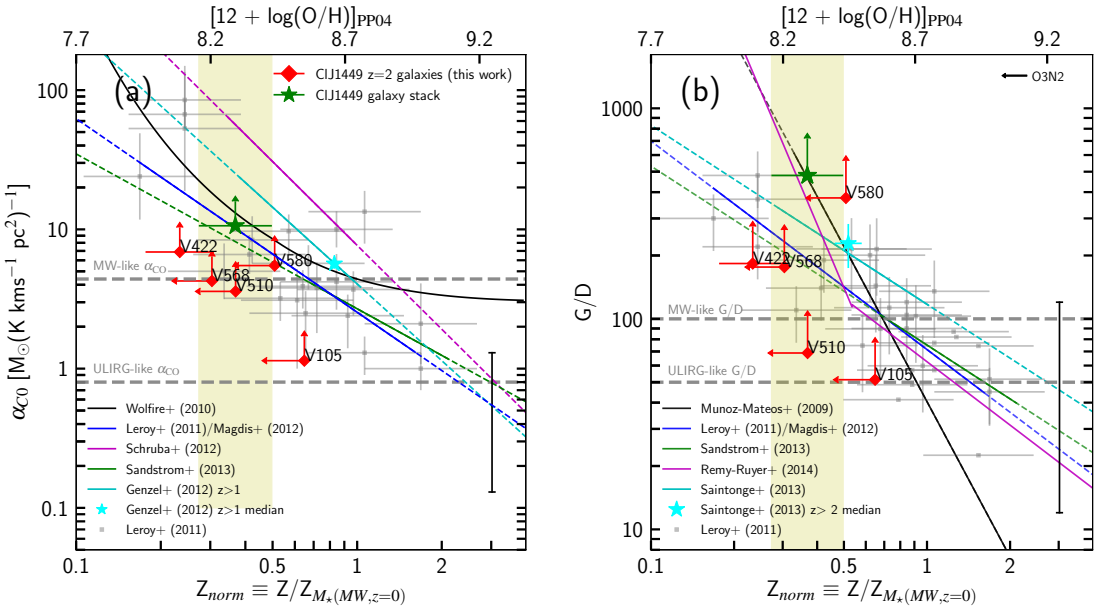

Figure 5.6: Left: CO-to-H_2 conversion factor α_{CO} as a function of metallicity. 3σ lower limits on α_{CO} are shown. Typical α_{CO} values for MW- and ULIRG-like galaxies are α_{CO}=4.4 and α_{CO}=0.8 respectively (Downes & Solomon, 1998), shown by the grey dashed lines. Right: Gas-to-dust ratio as a function of metallicity. 3σ lower limits on the G/D ratio are shown. Typical G/D ratios of 100 and 50 for MW- and ULIRG-like galaxies respectively are indicated by the grey dashed lines (Santini et al., 2014). In both panels, the comparison galaxy sample shown in grey comprises local galaxies, z$\sim$0.5-2.5 galaxies, local ULIRGS and submillimetre galaxies, taken from Leroy et al. (2011) and Magdis et al. (2012). The upper x-axis gives the equivalent PP04 metallicity, valid for the individual galaxy data points reported in this figure. The horizontal black arrow in the top right corner of panel (b) indicates the median offset in metallicity that would result if the O3N2, rather than the N2 diagnostic were used. Previous literature trends are indicated in the legends, where for observational studies solid lines indicate the metallicity range sampled by the corresponding data. (The dashed line segments illustrate the extrapolation of these trends to higher/lower metallicity). Each galaxy from our sample is shown by a red diamond. We show a representative error bar of 1 dex in the lower right corner, to illustrate by how much the quantity on the y-axis would decrease if the SFE was 10$\times$ higher, i.e. gas masses 10$\times$ lower. The stacked limit for the 5 galaxies is shown as a green star. The yellow shaded region shows the error on the mean (stacked) metallicity of the galaxies.

We plot in Fig. 5.6 (a) the relations observed by Genzel et al. (2012); Magdis et al. (2012), Schruba et al. (2012) and Sandstrom et al. (2013), and model predictions from Wolfire et al. (2010). The Genzel et al. (2012) sample comprises MS galaxies at z>1, and Magdis et al. (2012) fit local MS spiral galaxies from Leroy et al. (2011) with MS galaxies at 0.5<z<1.5. Schruba et al. (2012) use observations of HERACLES local dwarf galaxies to derive the relation shown, and Sandstrom et al. (2013) study local HERACLES star-forming galaxies, the majority of which (25/26) are spiral galaxies.

The 3σ lower limits on $\alpha_{\rm CO}$ shown for our sample in Fig. 5.6 (a) are consistent with the measured trends at low metallicity in the local Universe (e.g Leroy et al. 2011; Schruba et al. 2012; Sandstrom et al. 2013). Our deeper constraint on $\alpha_{\rm CO}$ from stacking (green star in Fig. 5.6 (a)) is also consistent with these low-z trends, as well as the model predictions from Wolfire et al. (2010).

We also show the result of a study at higher redshift, conducted by Genzel et al. (2012). Genzel et al. (2012) studied the effect of metallicity on $\alpha_{\rm CO}$ including MS galaxies up to z$\sim$2, tracing the molecular gas through the CO[3-2] and CO[2-1] transitions. In order to calculate these conversion factors, Genzel et al. (2012) take a near-unity KS slope of n=1.1. The inclusion of our data extends this work, allowing us to study this trend down to a lower median metallicity than the Genzel et al. (2012) sample, directly using the ground-state transition CO[1-0]. We find that both our individual and stacked limits are consistent with the z>1 Genzel et al. (2012) trend. We perform a linear fit between the median $\alpha_{\rm CO}$ and metallicity of the z>1 galaxies analysed by Genzel et al. (2012) (cyan star in Fig. 5.6 (a)) and our stacked limit. We find a lower limit on the dependence with metallicity of $Z^{-0.8}$, which is shallower than the low-redshift studies presented in Fig. 5.6 (a), but consistent with the range of slopes present in the literature (e.g. Wilson 1995; Arimoto et al. 1996; Bolatto et al. 2008). This value does not suggest a steeper slope between $\alpha_{\rm CO}$ and metallicity at high redshift than in the local Universe, as Genzel et al. (2012) report, but it is based on limited statistics and a low-S/N CO[1-0] flux constraint. It should also be noted that the Genzel et al. (2012) sample contains a larger number of galaxies in the range $1 \leq z \leq 1.5$ than at $2 \leq z \leq 2.4$, and therefore has a lower median redshift than our stacked sample.

To summarise, Fig. 5.6 (a) demonstrates that low-enrichment galaxies at z=2 have higher $\alpha_{\rm CO}$ values than their more enriched counterparts, consistent with what is found in the local Universe. We now look at the G/D ratios of these galaxies, to explore the impact of low metallicity at high redshift when deriving gas masses from dust continuum emission.

Gas-to-dust ratio as a function of metallicity

As ISM spectroscopy of galaxies is time-consuming and not always feasible, approaches to using the dust continuum emission of galaxies to estimate gas mass have also been developed (e.g. Guelin et al. 1993; Corbelli et al. 2012; Eales et al. 2012; Magdis et al. 2012; Bourne et al. 2013, Scoville et al. 2014; Groves et al. 2015). A typical value for the G/D ratio of a 'normal', solar-metallicity galaxy in the local Universe is ∼100 (Draine & Li, 2007). We show the G/D ratio as a function of metallicity in Fig. 5.6 (b). We have calculated the dust mass of the galaxies using their continuum emission at 2mm and 870µm where possible, as discussed in Section 5.3.3. The G/D ratio is calculated as below, where the gas mass derivation is described in Section 5.3.4:

$$GD = \frac{M_{mol} + M_{HI}}{M_d} \simeq \frac{M_{mol}}{M_d} = \frac{SFR}{SFE}\frac{1}{M_d} \tag{5.4}$$

We assume, following standard practice, that the gas phase in our galaxies at z=2 is dominated by molecular gas (Daddi et al., 2010b; Genzel et al., 2015; Lagos et al., 2015; Tacconi et al., 2018). In addition to the individual G/D ratios, we show in Fig. 5.6 (b) the stacked limit on the G/D ratio. It should be noted that Fig. 5.6 (b) shows total gas to dust ratios. In the case of local galaxies, where the molecular gas is not necessarily dominant, the total gas mass therefore also includes atomic hydrogen. The contribution of elements heavier than hydrogen is also accounted for at all redshifts[4].

We can use Fig. 5.6 (b) to evaluate whether low-metallicity galaxies at z=2 follow the same scaling relation between G/D and metallicity as local galaxies (e.g. Sandstrom et al. 2013; Rémy-Ruyer et al. 2014), and compare our sample with high-z studies such as those by Saintonge et al. (2013). Magdis et al. (2012) and Sandstrom et al. (2013) use the same galaxy samples described in Section 5.4.2. Muñoz-Mateos et al. (2009) use observations from the local SINGS galaxy sample, and Rémy-Ruyer et al. (2014) also study local galaxies, including dwarf galaxies from the Dwarf Galaxy Survey and KINGFISH. Saintonge et al. (2013) use observations of ∼7 lensed normal star-forming galaxies at z∼2. The best-fit relations derived from each of these works is shown in Fig. 5.6 (b).

With the exception of Muñoz-Mateos et al. (2009), the scaling relations from the literature display an approximately linear decrease of the G/D ratio with metallicity above $\sim 0.5 Z_{norm}$. Below $\sim 0.5 Z_{norm}$, a split occurs, where Magdis et al. (2012), Saintonge et al. (2013) and Sandstrom et al.

[4]We note that the prescriptions of Galliano et al. (2011), adopted by Rémy-Ruyer et al. (2014) to derive dust masses, and the one used by Sandstrom et al. (2013) and in our work (Draine & Li, 2007) are different. As Sandstrom et al. (2013) and Rémy-Ruyer et al. (2014) derive G/D ratios for a number of the same KINGFISH galaxies, we renormalise the G/D ratios in Rémy-Ruyer et al. (2014) by the mean G/D of the Sandstrom et al. (2013) sample, G/D=92.

(2013) predict a shallower dependance of G/D on Z than Muñoz-Mateos et al. (2009) and Rémy-Ruyer et al. (2014). Our stacked sample in particular probes this lower metallicity regime at z=2.

We find that the individual G/D ratios of our low-metallicity galaxies are consistent with all of the local relations shown (noting that all galaxies except V422 are also 2σ upper limits on metallicity), as well as the z>2 relation from Saintonge et al. (2013). Saintonge et al. (2013) report an increased normalisation at z>2 of a factor 1.7 compared with the local Leroy et al. (2011) relation. We show the median metallicity and G/D from Saintonge et al. (2013) in Fig. 5.6 (b), and find the difference between this value and the Leroy et al. (2011) relation to remain consistent with this factor 1.7 increase also after scaling of all studies to a common, renormalised metallicity scale. We do however note that the local relation of Muñoz-Mateos et al. (2009) shown in Fig. 5.6 (b) is also consistent with the Saintonge et al. (2013) median data point at z>2.

When we consider our stacked G/D limit, we see a clear elevation above the relations presented by Magdis et al. (2012), Saintonge et al. (2013) and Sandstrom et al. (2013) at this metallicity. We verify through jackknife analysis that this stacked G/D ratio is not strongly driven by the G/D of V580. We strongly favour the case of an increased G/D ratio at significantly sub-solar metallicities, as in seen in our sample. Our stacked limit is in good agreement with both the relations of Muñoz-Mateos et al. (2009) and Rémy-Ruyer et al. (2014) at this metallicity. Note also that Rémy-Ruyer et al. (2014) would derive higher G/D ratios if they were to assume MW-like dust grains, as discussed in Galliano et al. (2011), giving a steeper slope between G/D and metallicity. Fig. 5.6 (b) suggests that our galaxies at z=2 would be consistent with the Rémy-Ruyer et al. (2014) relation even for the steeper slope resulting as a consequence of adopting MW-like dust grains. We find a lower limit on the slope between our stacked G/D limit and the median Saintonge et al. (2013) value of -2.2, compared with the slopes of -2.45 and -3.10 found by Muñoz-Mateos et al. (2009) and Rémy-Ruyer et al. (2014) in this metallicity regime, respectively. The calculation of gas masses in our galaxies accounts for the increase in SFE for galaxies above the MS. In order for the lower limit on our G/D vs. Z slope to become consistent with the slope of local relations from Magdis et al. (2012) and Sandstrom et al. (2013), the average SFE would need to increase by at least an additional factor of 1.5. The depletion timescale fit given by Tacconi et al. (2018), which suggests a steeper evolution of SFE with offset from the MS than Sargent et al. (2014), as well as a dependence of SFE on stellar mass, is consistent with this order of decrease in G/D limit.

The constraints provided by our data are compatible with a G/D-metallicity relation at z$\sim$2 that does not evolve compared to low redshift. However, they strongly support a steep dependence on metallicity at low enrichment, as shown by Rémy-Ruyer et al. (2014). They are also in agreement

with the fudicial model predictions of Popping et al. (2017), which reproduces the double power-law shape observed by Rémy-Ruyer et al. (2014), and predicts only weak evolution of the G/D ratio with redshift (<0.3 dex increase in G/D at $<0.5Z_{\odot}$ from z=0 to z=9).

It is not trivial to assess how deviations of our galaxies from the star-forming MS (1.6σ above, on average) affect the position of these galaxies on scaling relations of G/D and $\alpha_{\rm CO}$ vs. metallicity (sections 5.4.2 and 5.4.2). It has been established that galaxies above the MS tend to have larger gas fractions than those galaxies below the MS (e.g. Magdis et al. 2012, Saintonge et al. 2012, Santini et al. 2014, Sargent et al. 2014, Scoville et al. 2017, Tacconi et al. 2018). However, gas-phase metallicity may also correlate with offset from the MS (as given by the Fundamental Metallicity Relation, FMR, Lara-López et al. 2010, Mannucci et al. 2010), where an increase in SFR at fixed stellar mass implies lower gas-phase metallicity (see e.g. Sanders et al. 2015, Onodera et al. 2016 and Cresci et al. 2018 for discussion on the existence of an FMR beyond the local Universe). Selection of galaxies with a systematic offset with respect to the MS may therefore not necessarily lead to shifts above and below the scaling relations we present here, but certainly have a component along the metallicity axis of these relations. However, the effect of main-sequence offset on ISM scaling relations cannot be dissected with the number of galaxies studied in this chapter.

5.4.3 Implications for gas mass derivations at z∼2

Figs 5.6 (a) and (b) demonstrate that the sub-solar metallicity of our galaxies at z=2 is impacting both the CO-to-H_2 conversion factor $\alpha_{\rm CO}$ and G/D ratio of the galaxies in our sample. Here we explore the implications of this for molecular gas mass calculations in the sub-M^* mass regime at the peak epoch of star-formation.

Gas content of individual sub-M^* galaxies

As discussed, the most simplistic approach to measuring gas masses is to assume that $\alpha_{\rm CO}$ or G/D do not vary with metallicity. In this case, MW-like conversion factors are often assumed regardless of a galaxy's properties. We find that our stacked $\alpha_{\rm CO}$ limit lies a factor >2.4 above the MW value $\alpha_{\rm CO}$=4.4. The deviation from a constant MW value will continue to increase at lower enrichment. Similarly, if we take a constant MW G/D=100, the G/D of our stack implies gas masses >4.8 times higher than would be inferred from the MW value.

Another approach one might take to calculate gas masses is to use conversion factors based on a well-studied population of galaxies at a given redshift (e.g., for z∼2, galaxies with stellar masses 10^{10}-$10^{11}M_{\odot}$). However, galaxies at the knee of the stellar mass function ($M_{\star}$ $\sim10^{10.4}M_{\odot}$; e.g. Davidzon et al. 2017) at z∼2 have metallicities approximately ∼0.47 dex higher than, e.g., $M_{\star}$

$\sim 10^9 M_\odot$ galaxies, depending on the metallicity calibration used (Kewley & Ellison, 2008; Zahid et al., 2014). Taking a slope of $\log_{10}(\alpha_{CO})$ vs. metallicity of -0.8 as suggested by our data would therefore give rise to an underestimation of the gas mass from CO by at least a factor 3, remembering that our data give a lower limit on this slope. Additionally, there is a steep dependence of G/D on metallicity in this regime ($<0.5 Z_{M_\star MW,z=0}$), where G/D $\propto Z^{-2.2}$ or even steeper according to our data. We see in Fig. 5.6 (b) that applying the G/D ratio of an $M_\star \sim 10^{10.4} M_\odot$ galaxy to an $M_\star \sim 10^9 M_\odot$ galaxy at z=2 would result in an underestimation of the gas mass by a factor >17 (Zahid et al., 2014).

These calculations highlight the importance of using physically motivated conversion factors when deriving gas masses for low enrichment or sub-M^* galaxies. Assuming MW-like conversion factors or factors appropriate for more massive galaxies would result in an underestimation of the molecular gas mass from both continuum and line emission.

Which galaxy population dominates the cosmic gas density at z$\sim$2?

Finally, it is interesting to consider the implications of these findings for measurements of the cold gas history of the universe (e.g. Lagos et al. 2011; Popping et al. 2014; Walter et al. 2014; Decarli et al. 2016; Scoville et al. 2017; Riechers et al. 2019), and in particular for the determination of which characteristic stellar mass scale contributes most to the comoving molecular gas density. Whether - given a set of observed dust masses or molecular line luminosities - we infer this to be, e.g., the M^* population or galaxies at lower masses partially depends on how strongly α_{CO} and G/D ratios depend on metallicity. The contribution of galaxies with stellar mass $M_\star$ to the comoving molecular gas density is:

$$\begin{aligned} \rho_{H_2} M_\star &\propto \Phi M_\star \langle M_{H_2} \rangle_{M_\star} \\ &\propto \Phi M_\star \langle \alpha_{CO} L'_{CO1-0} \rangle_{M_\star} \end{aligned} \tag{5.5}$$

(or $\rho_{H_2} M_\star \propto \Phi M_\star \langle GD \times M_d \rangle_{M_\star}$). Here $\langle M_{H_2} \rangle_{M_\star}$ is the characteristic H_2 mass of galaxies with stellar mass $M_\star$, and $\Phi M_\star$) is the comoving number density of galaxies with a given stellar mass, e.g. from the stellar mass function of actively star-forming galaxies in Davidzon et al. (2017). For $\log_{10}(M_\star)$ = 9 (10.4) at z$\sim$2, $\log_{10}(\Phi M_\star)$ = -2.26 (-2.86), corresponding to a 4-fold higher number density of $M_\star \sim 10^9 M_\odot$ systems, but a $\sim$6-fold higher contribution of $10^{10.4} M_\odot$ galaxies to the comoving stellar mass density $\rho M_\star$. By how much will the larger α_{CO} values for sub-M^* galaxies modify the relative contribution of these two stellar mass bins in terms of the z$\sim$2 cosmic gas mass density (compared to their contribution to the stellar mass density)?

Using our derived lower limits on the slopes of the $\log_{10}(\alpha_{CO})$ and $\log_{10}$(G/D) vs. Z relations,

we can derive a lower bound on the relative contribution to the cosmic gas mass density of galaxies at $M_\star$=$10^9 M_\odot$, and at the knee of the stellar mass function at M^*=$10^{10.4} M_\odot$. We find an increased ratio $\frac{\rho_{H_2} M_\star=10^9 M_\odot}{\rho_{H_2} M_\star=10^{10.4} M_\odot}$ >11× $\frac{L'_{CO1-0} M_\star=10^9 M_\odot}{L'_{CO1-0} M_\star=10^{10.4} M_\odot}$ of the comoving gas densities when using a metallicity dependent α_{CO}, compared with the considerably smaller increase of 4 times the L'_{CO1-0} ratio when a constant MW-like α_{CO} is assumed. When a metallicity dependent G/D is used, we find an increase in the comoving gas density of $\frac{\rho_{H_2} M_\star=10^9 M_\odot}{\rho_{H_2} M_\star=10^{10.4} M_\odot}$ >68× $\frac{M_d M_\star=10^9 M_\odot}{M_d M_\star=10^{10.4} M_\odot}$, compared to just 4 times the dust mass ratios when a constant G/D is assumed. For the contribution to the z∼2 cosmic gas mass density of sub-M^* galaxies, $\rho_{H_2} M_\star = 10^9 M_\odot$), to become at least as large as that of galaxies at the knee of the stellar mass function, the ratio of the typical L'_{CO1-0} (M_d) values in the low-mass bin over that in the high-mass bin would thus have to be ≥0.09 (≥0.015). If we follow the same formalism as in Section 5.4.1 to relate SFR, $M_\star$, M_{H_2} and Z for average galaxies in these mass bins (namely using the star-formation MS, the MZR and the integrated KS law to find SFR, metallicity and molecular gas mass, for a given $M_\star$), and take a power-law index γ=-0.8 of α_{CO} vs. metallicity from our data to derive α_{CO}, we can estimate average L'_{CO1-0} values for these stellar mass bins at z=2 (using L'_{CO1-0}=M_{H_2}/α_{CO}). We predict the average L'_{CO1-0} ratio to be 0.045, indicating that despite the increased α_{CO} in sub-M^* galaxies, the population at $M_\star$=$10^9 M_\odot$ has not overtaken that at M^*=$10^{10.4} M_\odot$ in terms of their contributions to the comoving gas mass density at z∼2. This also implies a much lower CO detection rate for low mass galaxies at z=2, compared with more massive, enriched galaxies.

Rising CO-to-H_2 conversion factors and G/D ratios at low mass/metallicity do, however, significantly shift the balance between different galaxy mass scales compared to the stellar mass density distribution. For example, in our example involving a metallicity-dependent α_{CO}, a more than 6-fold higher contribution of M^* galaxies to $\rho(M_\star)$ was reduced to an only 2× higher contribution to $\rho(M_{H_2})$, compared to the $M_\star$=$10^9 M_\odot$ population.

5.5 Conclusions

This chapter explores the relationship between molecular gas, dust, star-formation and metallicity in five sub-solar enrichment galaxies (average oxygen abundance ∼0.35 dex below solar) at z∼2. Studying the ISM of these sub-M^* galaxies gives us a greater understanding of how low-metallicity ISM scaling relations at z=2 compare with those calibrated in the local Universe, and on more massive and luminous z∼2 galaxies. Limits on the oxygen abundance of these galaxies were first constrained by Valentino et al. (2015), making use of the galaxies' bright Hα detections. Here we follow the same procedure to derive a sample average metallicity of Z=8.34±0.13 (PP04 N2 calibration).

Using deep ALMA and VLA data, we search for the CO[1-0] and CO[4-3] lines and 870μm and 2mm continuum emission from our targets, but find that they remain individually undetected. These non-detections highlight the low ISM enrichment of our galaxies, particularly when comparing with the expected detection percentage (60-80%) in our data, for solar enrichment galaxies with these Hα SFRs. We perform stacked analysis on the CO spectra and dust emission in order to place more stringent limits on the average ISM content of the five galaxies, and once again find these quantities undetected in the stacked data.

We place our galaxies on the L'_{CO1-0}-SFR plane, and see that our sample average has an offset of >0.5 dex below the expected L'_{CO1-0}, occupying the same parameter space as high-SFE starburst galaxies. We verify that this offset is not driven by a recent increase in star-formation, nor a high SFE in our galaxies. We therefore interpret this as evidence that the low metal enrichment of the ISM in our galaxies at z=2 is leading to dissociation of CO in the diffuse ISM phase, as seen in the local Universe.

This CO deficit also manifests itself for the denser ISM phases which are traced by CO[4-3]. We convert our stacked CO[4-3] constraint to CO[5-4] luminosity using a BzK excitation correction, in order to examine the position of our galaxies on the L'_{CO5-4}-SFR plane. We find an average luminosity of >0.5-0.7 dex less than the expected CO[5-4] luminosity. The position of galaxies on this relation is invariant to their star-formation efficiency, confirming that this CO deficit is most likely driven by the low gas-phase metallicity. This has important implications, as it could lead to systematic underestimation of the instantaneous SFRs of low-metallicity galaxies as traced through high-J CO transitions.

In order to investigate how the ISM properties of our galaxies scale with metallicity at z=2, we calculate molecular gas masses using the Hα SFRs, assuming a MS SFE. We then derive limits on the $\alpha_{\rm CO}$ conversion factors and G/D ratios of the galaxies. We find a power-law slope of $\alpha_{\rm CO}$ (G/D) vs. metallicity at z$\sim$2 of $\gamma < -0.8$ ($\gamma < -2.2$), consistent with dependencies observed at z=0. We stress the importance of comparing studies using different metallicity calibrations on a normalised metallicity scale, and place a compilation of literature scaling relations alongside our data. When systematic differences in metallicity are taken into account in this way, we find consistency between both the $\alpha_{\rm CO}$ and G/D vs. metallicity relations at z=2 compared with local relations. However, our stacked G/D limit strongly favours a steep G/D vs. Z slope at low metallicity ($\sim 0.5 Z_{M_\star MW,z=0}$), consistent with the double power-law relation given by Rémy-Ruyer et al. (2014).

Finally, we discuss the implications of these results on the calculation of molecular gas masses in low-metallicity, z=2 galaxies. We find that the assumption of G/D and $\alpha_{\rm CO}$ values based on the more routinely observed M* population at this redshift (or uniform application of the 'canonical'

MW-like conversion factors) would result in significant underestimation of the gas mass in these low-metallicity galaxies. We predict the average contribution of sub-M* galaxies with M$_\star$=10^{9}M$_\odot$ to the comoving molecular gas density at z=2, and find that their increased $\alpha_{\rm CO}$ values are not sufficient for this population to become dominant over M* galaxies in this respect. However, we see that increased $\alpha_{\rm CO}$ and G/D conversion factors at low enrichment significantly shift the balance between different galaxy mass scales compared to their relative contribution to stellar mass density distributions.

Our analysis has enabled us to place observational constraints on the ISM properties of low-enrichment galaxies at the peak epoch of star-formation. In combination with future, similar studies, this kind of work can inform the design of ISM surveys of sub-M* galaxies. Going forward, collating larger, statistical samples of galaxies spanning a large metallicity range will allow us to determine, e.g. the influence of starburstiness or MS-offset on the scatter of the ISM scaling relations studied here. To our knowledge, this has not yet been quantified at low or high redshift. In this way we will continue to explore the effect of low gas-phase metallicity on the interstellar medium, and characterise the evolution of the ISM outside of the local Universe.

Contributions

Veronica Strazzullo provided the stellar masses and reddening E(B-V)$_{neb}$ values given in Table 5.1, as well as un-reddened ultraviolet SFRs. Francesco Valentino performed the MOIRCS data reduction described in Section 5.2.1, and provided optical redshifts and gas-phase metallicity estimates for the individual (unstacked) galaxies in Table 5.1. Mark Sargent calculated the $\alpha_{\rm CO}$-Z trend based on the prescriptions of Wolfire et al. (2010) shown in Fig. 5.6. Raphael Gobat created the colour image that forms the basis of Fig. 5.1. All co-authors contributed comments and advice.

This chapter makes use of the following ALMA data: ADS/JAO.ALMA#2012.1.00885.S and ADS/JAO.ALMA#2015.1.01355.S. This chapter also makes use of VLA program 12A-188.

Chapter 6

The radio continuum sky as seen by the Square Kilometer Array

This chapter is being prepared for publication in Coogan et al. (2020), Monthly Notices of the Royal Astronomical Society.

Current co-authors are Mark T. Sargent, Anna Cibinel, Anna Bonaldi, Robert Braun and Roberto Scipioni.

Abstract

In preparation for the Square Kilometre Array, we are exploring the vast potential for galaxy evolution studies enabled by the planned SKA continuum surveys. We begin by characterising the detectable SFRs in each of the SKA band 2 ($\sim$1.4 GHz) surveys as a function of redshift, and find that SKA1-MID will detect MS-complete samples of star-forming galaxies down to $\log_{10}(M_\star)<10$, out to z$\sim$3. Having defined the parameter space that the tiered surveys will probe, we create mock images of an entire survey field, as observed by the wide, deep and ultradeep band 2 survey tiers.

In this chapter, we present our first set of analyses on these simulated data, focussed on recovering total flux, as well as morphological parameters of galaxies spanning a range of SFRs and stellar masses at $0<z<3$. With simulated images such as these, using the future instrumental response of the SKA, we can explore and quantify the power of the SKA to accurately measure such parameters. We find that both input fluxes and Gini parameters can be recovered from the simulated survey tiers, with decreasing scatter as a function of survey depth. We also show that fluxes are most accurately recovered for galaxies with concentrated regions of flux, rather than extended, low surface brightness sources. These types of study both inform future observational strategies, and provide solid grounding for future analysis of SKA survey data.

6.1 Introduction

One of the next observatories at the forefront to probe galaxy evolution across a range of environments is the Square Kilometer Array. Throughout this thesis, we have explored diverse populations of galaxies, from highly dust-obscured galaxies and AGN in the core of a cluster at z=1.99, to the population of significantly sub-solar enrichment galaxies at this redshift. Of significant interest for the study of cluster galaxies at z>1, it has been shown in recent years that radio continuum emission is a particularly good tracer of high-redshift structures such as proto(clusters). This is due to the large overdensity of star-formation and AGN activity that are present in these environments, giving rise to radio continuum emission in the frequency range of the SKA (e.g. Hatch et al. 2011; Daddi et al. 2017; Krishnan et al. 2017). Both the sensitivity and field of view of the SKA therefore make this observatory a highly effective tool for the detection of large numbers of galaxies and AGN, in the field and also in high-redshift (proto)clusters, leading to the compilation and characterisation of larger catalogues of these structures. In addition to the study of cluster galaxies themselves, there is also significant interest in using the SKA to observe the larger-scale emission from clusters, such as energy injection into the ICM from from radio-loud BCGs, or diffuse SZ emission (e.g. Ferrari et al. 2015; Gitti et al. 2015; Grainge et al. 2015, see Section. 2.2).

In this chapter, we therefore begin to explore the capabilities of the SKA for the study of galaxy evolution outside of the local Universe. The SKA will become the world's largest radio telescope when it is constructed over the next ∼5-10 years, with low-mid frequency instruments spread over sites in both South Africa and Australia. The observatory will provide world-class data to address a number of core research themes (see e.g. Carilli & Rawlings 2004; Taylor 2008; Braun et al. 2015). These will range from observations of the Milky Way and the Galactic core, to extragalactic science such as cosmology, lensing and the epoch of reionisation (through measurement of high-redshift 21cm emission, e.g. Blake et al. 2004; Carilli et al. 2004; Rawlings et al. 2004; McKean et al. 2015; Takahashi et al. 2015). Of most relevance to this chapter, a significant amount of SKA science will also focus on the history of galaxy evolution and AGN activity through continuum radio emission (e.g. Jarvis & Rawlings 2004; Afonso et al. 2015; Deane et al. 2015; Power et al. 2015; Smolčić et al. 2015; Wagg et al. 2015; Iqbal et al. 2017).

Here, we focus on the science of SKA1-MID, which is the mid-frequency component of phase 1 of the SKA. SKA1-MID will be comprised of 64×13.5 m dishes from its precursor telescope MeerKAT, combined with 133 SKA 15 m dishes, covering a frequency range ∼350 MHz -15 GHz. As discussed in Section 1.5.1, the use of interferometry enables high angular resolution to be achieved in submillimeter-radio arrays. In the case of SKA1-MID, the telescope array is planned to reach a maximum baseline of 150 km, giving an angular resolution between 0.04"-0.70" in

this frequency range. This high angular resolution science has a number of applications (e.g. Godfrey et al. 2012), in addition to allowing the identification of individual galaxies in crowded regions such as high-redshift overdensities. As detailed in the anticipated performance of the SKA[1], SKA1-MID is also expected to have sensitivities approximately an order of magnitude above that of the VLA at 1.4 GHz, which is expected to increase yet another order of magnitude on completion of phase 2. Even more strikingly, the survey speed of the SKA will be approximately $100\times$ that of facilities such as LOFAR and the VLA, due to the combination of the high sensitivity with the large 'noise-effective' field of view ($\sim$0.5 deg^2 at 1.4 GHz). The SKA's impact on the field of galaxy evolution will therefore be highly significant, providing observations tracing the star-formation history of the Universe with unprecedented statistics (see Section 6.2). Precursor telescopes in this frequency range are already operational, such as the Australian SKA Pathfinder (ASKAP) and MeerKAT, which will perform significant radio continuum and spectral surveys before SKA1-MID itself comes online (Duffy et al., 2012; Camilo et al., 2018; Reynolds et al., 2019; Leahy et al., 2019). Several 'pathfinder' facilities are also engaged in SKA-related activity, providing information about both the technology and science that SKA1-MID will pursue (Norris et al., 2013).

As the radio astronomy community builds up to the SKA, we need to gain a fuller understanding of what SKA1-MID will be able to observe, in terms of its ability to both detect galaxies and resolve their morphological properties. This will depend on the angular resolution and sensitivity of the observations, as well as factors such as the redshift and intrinsic radio brightness of a galaxy. Since the early years of planning the SKA, there has been considerable effort put into predicting observable properties the radio sky. One infrastructure for this is provided by the Square Kilometre Array Design Studies (SKADS) Simulated Skies (S^3), which creates mock radio skies using both Semi-Empirical and Semi-Analytical eXtragalactic simulations[2] (S-Cubed SEX and S-Cubed SAX respectively). This suite of simulations has provided catalogues describing the cosmological distribution of millions of radio sources, from star-forming and quiescent galaxies to both radio-quiet and radio-loud AGN (Wilman et al., 2008; Obreschkow et al., 2009). These types of catalogue, in addition to other models and extrapolations of current observations, can be used to predict properties such as radio luminosity functions and AGN/galaxy number counts in the sensitivity regime of the SKA (e.g. Hopkins et al. 2000; Windhorst 2003; Jackson 2004; Jarvis & Rawlings 2004; Whittam et al. 2017; Bonaldi et al. 2019; Zackrisson et al. 2019).

Interestingly, these catalogue predictions can also be used as model inputs into simulations

[1]https://astronomers.skatelescope.org/wp-content/uploads/2017/10/SKA-TEL-SKO-0000818-01_SKA1_Science_Perform.pdf

[2]http://s-cubed.physics.ox.ac.uk

that aim to produce realistic SKA images of the sky. In recent years, several teams have produced images of the sky as seen by either the SKA or its pathfinder instruments, ranging from cosmology to galaxy morphology and cluster studies (e.g. Willis 2008; Ferrari et al. 2015; Makhathini et al. 2015; Bonaldi et al. 2016; Loi et al. 2019). These simulations can be performed using a range of different software tools, such as Miriad (Sault et al., 1995), the `Faraday` package (Murgia et al., 2004), `MeqTrees` (Noordam & Smirnov, 2010) and OSKAR[3]. These software packages are not all specific to the SKA, but allow the user to input antenna and telescope configurations specific to the observatory that one wishes to simulate. This flexibility makes for a set of very powerful tools, which can be implemented in order to optimise factors such as array configuration, frequency, and observing times for specific observations. Similarly, image-type simulations like these can be used to explore the anticipated capabilities of telescopes such as the SKA to detect and characterise subsets of the galaxy population, for planned surveys such as those discussed in Section 6.2. Recently, the SKA Organisation (SKAO) themselves produced SKA-simulated images for the SKA Science Data Challenge #1[4]. These images were produced using a custom Miriad pipeline and the T-RECS model source catalog of Bonaldi et al. (2019), at several different exposure times and frequencies, for SKA1-MID. As one might expect, the recoverability of galaxy parameters may also depend on data analysis approaches, and these simulations allow the community to attempt to accurately characterise an unknown model SKA sky. However, the T-RECS catalogue is populated by sources with smoothly varying radio brightness profiles, and does not contain examples of the clumpy or irregular morphologies that can be observed in some galaxies. In this chapter, we expand on previous works building up to the SKA by: (i) exploring the parameter space (in terms of SFR and redshift) that will be probed by the planned SKA reference continuum surveys (Section 6.2); and (ii) complementing existing mock-catalogue SKA simulations by using resolved observations of real galaxies in the GOODS-North (GOODS-N) field, to create SKA1-MID simulated images of realistic star-formation distributions within galaxies across a range of redshifts (Section 6.3). We produce these simulated images at depths corresponding to the SKA reference continuum surveys discussed in Section 6.2, and start to explore the possibilities that these simulations open up, in terms of the physical properties that can be recovered from SKA observations.

The structure of this chapter is as follows. In Section 6.2, we present the tiered continuum surveys planned by the SKA Extragalactic Continuum Science Working Group (SWG), outline our methodology for relating observed radio fluxes and galaxy SFRs (Section 6.2.2), and present our results characterising the parameter space that these surveys will probe (Section 6.2.3). We introduce our SKA simulation in Section 6.3, and give our simulation results in Section 6.4.

[3]https://github.com/OxfordSKA/OSKAR

[4]https://astronomers.skatelescope.org/ska-science-data-challenge-1

Throughout this chapter we use a ΛCDM cosmology with H_0=70kms^{-1}Mpc^{-1}, Ω_M=0.3 and Ω_Λ=0.7. We adopt a Chabrier initial mass function (Chabrier, 2003).

6.2 Continuum galaxy and AGN co-evolution surveys with the SKA

6.2.1 Tiered continuum surveys

Three reference surveys have been planned for SKA1-MID by the Extragalactic Continuum SWG, for the purpose of galaxy evolution and AGN-galaxy co-evolution studies (Prandoni & Seymour, 2015). These have been planned for the SKA1-MID frequency ranges corresponding to band 1 (0.4-1.1 GHz), band 2 (0.9-1.75 GHz), and band 5b (8.3-15 GHz)[5]. Of these reference surveys, two have been planned as 'tiered' surveys, allowing for deep observations of the radio population, whilst also maintaining a large sky coverage. In bands 1/2, a tiered survey has been planned at 'wide', 'deep' and 'ultradeep' sensitivities. The band 2 ultradeep, deep and wide surveys have expected RMS sensitivities of 0.05μJy, 0.2μJy and 1.0μJy, over regions of size 1 deg^2, 10-30 deg^2 and 1000 deg^2 respectively. Compared to pre-SKA surveys, as outlined in Prandoni & Seymour (2015), the ultradeep tier will be 40$\times$ deeper than the Very Large Array Sky Survey (VLASS-3), but over a 10$\times$smaller area. The deep tier will be 10$\times$ deeper than VLASS-3 (over a similar area), and the wide tier will have a similar sensitivity to the MeerkAT International GHz Tiered Extragalactic Exploration (MIGHTEE-2) survey, but over a 30$\times$ larger area and at 8$\times$ higher resolution. Similarly, at 10 GHz (band 5b), a two-tiered survey at wide and deep depths has been planned. In this chapter, we explore the band 2 tiered reference surveys, the frequency of which correlates well with SFR (see Section 6.2.2). The band 2 SKA1-MID surveys will give us, for the first time, access to resolved radio imaging of a large number of galaxies out to high redshift at this frequency (1.4 GHz, L-band), with the exception of small area studies from e-Merlin such as the e-MERGE survey. This is one of the key motivations for these planned surveys, enabling resolved studies of the star-formation activity observed at 1.4 GHz for larger high-redshift samples than ever before. Although high angular resolution can currently be achieved at higher frequencies with the VLA, for example, the spectral slope of the radio SED means that flux densities at ν >1.4 GHz are intrinsically lower than at 1.4 GHz, and therefore become increasingly difficult to detect with increasing redshift.

Although the areas and radio continuum sensitivities of these surveys have been established, the physical properties of the galaxies that these tiered surveys will detect has not yet been quantified. A key property that we need to understand is the detectable SFRs that the SKA1-MID surveys will

[5]https://www.skatelescope.org/wp-content/uploads/2014/03/SKA-TEL-SKO-0000007_SKA1_Level_0_Science_RequirementsRev02-part-1-signed.pdf

probe as a function of galaxy redshift, and how this relates to the galaxy's position on the Main Sequence of star-formation. We therefore explore this for the band 2 SKA1-MID surveys in the following sections. We outline the different possible methods of deriving radio luminosity from SFR (and visa-versa) in Section 6.2.2. We implement these relations in Sections 6.2.3 and 6.3.4, in order to quantify detectable SFRs for each of the band 2 SKA continuum surveys, and to create simulated SKA images of star-forming galaxies, respectively.

6.2.2 Total radio luminosity and galaxy star-formation rate

As introduced in Section 1.2.2, there are two primary mechanisms by which radio continuum emission is emitted from star-forming galaxies: synchrotron emission and free-free emission. At low radio frequencies, $<$30 GHz rest-frame, the dominant emission mechanism is non-thermal synchrotron radiation (Condon, 1992). This is produced by electrons being accelerated within the galaxy as a result of passing through a magnetic field. In the case of a purely star-forming galaxy, supernova shocks of massive stars cause acceleration of charged particles within the magnetic field structure of the galaxy, such that synchrotron radiation is an effective indicator of the galaxy's star-formation rate (Berezhko & Völk, 2004; Longair, 2011). The contribution of synchrotron radiation to a star-forming galaxy's SED has been observed to have a spectral index α between approximately -0.7 and -0.8 (Lisenfeld & Völk 2000; Kimball & Ivezić 2008; Delhaize et al. 2017; Smolčić et al. 2017, Fig. 1.4). It should be noted however that in galaxies containing an AGN, electrons are also accelerated by the powerful magnetic fields around the jet of the AGN. In this situation, synchrotron emission is no longer directly linked to the galaxy's SFR. It can, on the other hand, be used to indicate that a galaxy contains an AGN, if its synchrotron emission is elevated above expectations (based on the SFR derived from other wavelengths, see discussion of the infrared-radio correlation below). Separating a galaxy's radio emission into purely star-forming and AGN components is an interesting topic, but here we consider star-forming galaxies that do not contain an AGN.

Radio emission in star-forming galaxies is also produced as so-called 'free-free' emission. This arises when an electron comes into close proximity to another ion, such as a positive ion in a star-forming HII region. The electron scatters off the ion but is not captured, and emits thermal bremsstrahlung radio emission in the interaction process. The contribution to the SED from free-free emission has a shallower spectral slope than synchrotron radiation, approximately β=-0.1. This emission is only significant in comparison to the synchrotron radiation at relatively high frequencies ($\sim$30-200 GHz rest-frame). Above these frequencies, the SED becomes dominated by thermal emission from dust, in the RJ tail of the SED. The radio continuum emission of a

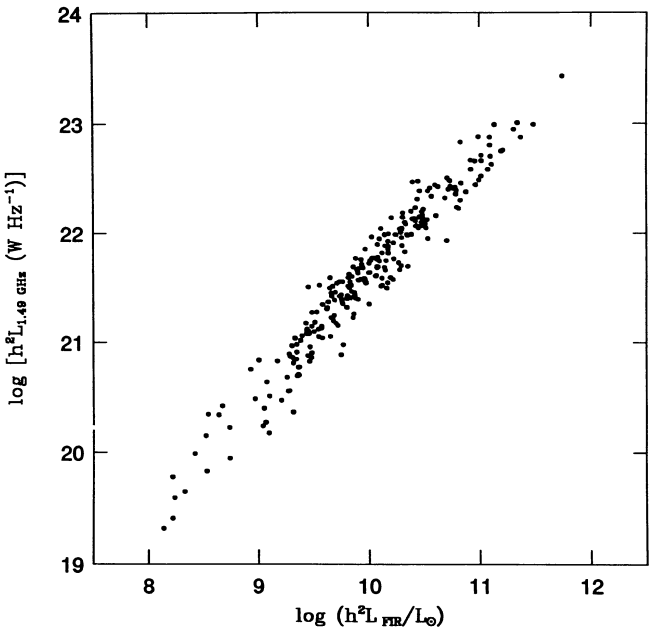

Figure 6.1: The Infrared-Radio Correlation. We see a tight relationship between synchrotron emission at radio frequencies (ordinate) and infrared luminosity (abscissa), in this case for local galaxies in the IRAS Bright Galaxy Sample (Soifer et al., 1989). Figure taken from Condon (1992).

galaxy that does not contain an AGN is therefore produced by two mechanisms related to the star-formation in the galaxy, and has been calibrated as an indicator of star-formation rate (see below). Where ultraviolet emission is heavily attenuated and re-emitted by a galaxy's dust (Section 1.2.2), radio emission allows us to trace the obscured star-formation in galaxies, as radio emission is not absorbed by dust grains in the ISM.

Following from this, there exists a tight correlation between the rest-frame 1.4 GHz luminosity and the total infrared luminosity of a galaxy. This correlation is known as the 'infrared-radio' correlation (IRRC, e.g. de Jong et al. 1985; Helou et al. 1985; Yun et al. 2001; Magnelli et al. 2015; Delhaize et al. 2017; Molnár et al. 2018), the radio contribution of which is dominated by synchrotron radiation at $\nu_{\rm rest}$=1.4 GHz. This relation therefore provides the framework in which radio continuum fluxes are related to the IR luminosities, and therefore star-formation rates of normal galaxies. The IRRC as compiled by Condon (1992) for local galaxies is shown in Fig. 6.1. Although single-dish telescopes such as the Herschel Space Observatory and the James Clerk Maxwell Telescope observe IR frequencies close to the peak of the RJ dust tail, their low angular resolution means that they are prone to suffering from significant source blending. However, the ability to measure and resolve star-formation on small angular scales is crucial to understanding galaxy evolution at high redshift, particularly across a wide range of galaxy morphologies and environments. Using radio observations rather than IR data can therefore be

particularly advantageous, as interferometers such as the VLA and SKA enable high angular resolution observations of star-formation to be achieved. Below, we outline how we can relate - in a quantitative way - synchrotron and free-free luminosities to a galaxy's SFR.

Synchrotron radiation

In order to relate L_{IR} and 1.4 GHz luminosity, we use the IRRC. The IRRC is governed by the logarithmic ratio, q_{TIR}, of the total infrared (8-1000μm; L_{TIR}) and 1.4 GHz radio ($L_{1.4}$) luminosities. We can convert between galaxy SFR and L_{TIR}, following standard practice for an assumed IMF. The relationship between synchrotron radio luminosity and SFR is therefore defined by the following equation:

$$L_{1.4\mathrm{GHz}} = \frac{SFR}{10^{-24} \times 10^{q_{\mathrm{TIR}}}} \tag{6.1}$$

where $L_{1.4GHz}$ is the derived synchrotron luminosity. Here, we are making the assumption that the IR-radio correlation sampled at high luminosities is a good proxy for how $L_{1.4GHz}$ relates to total SFR, as the dust-obscured SFR is dominant in this regime. As the IRRC is linear, we can extend this SFR-$L_{1.4GHz}$ calibration to lower luminosities, where the population has a more balanced mixture of obscured and unobscured star-formation. Although initially calibrated in the local Universe (e.g. de Jong et al. 1985; Helou et al. 1985; Bell 2003), advances in the sensitivity of IR-radio observatories have recently allowed the exploration of this parameter at higher redshifts (e.g. Delhaize et al. 2017; Molnár et al. 2018). However, these studies have not yet reached a clear consensus on the value of q_{TIR} outside of the local Universe. In agreement with studies such as Magnelli et al. (2015) and Calistro Rivera et al. (2017), Delhaize et al. (2017, D17) conclude that an evolution of q_{TIR} with redshift exists, based on a large sample of star-forming galaxies in the COSMOS field out to $z\sim6$. They find a smooth, decreasing trend of q_{TIR} with redshift. They also find that both the normalisation of the IRRC and the evolution of q_{TIR} with redshift are dependent on the assumed spectral index of the synchrotron radio emission, α. On the other hand, Molnár et al. (2018, M18) study the same population of galaxies, but limit the sample to $z<1.5$ in order to classify the galaxies based on a spheroidal or disk-like morphology. Molnár et al. (2018) find a decreasing value of q_{TIR} with redshift only in spheroidal-dominated galaxies. They find that for disk-like galaxies at $z<1.5$ (which are expected to have the most straightforward correlation between IR and radio luminosity, with both IR and radio emission being driven by star-formation alone), that q_{TIR} does not evolve with redshift, and is consistent with values measured in the local Universe (in agreement with e.g. Garrett 2002; Ibar et al. 2008; Jarvis et al. 2010; Sargent et al. 2010; Smith et al. 2014). Specifically, Molnár et al. (2018) find their derived value of q_{TIR} to be

consistent with the average value of Bell (2003), q_{TIR}=2.64.

We therefore consider two possibilities for the value of q_{TIR} in equation 6.1: (i) a constant q_{TIR}=2.64 (Bell 2003), and (ii) a redshift-dependent q_{TIR} (D17). For the redshift-dependent case, we take a synchrotron spectral slope of α=-0.8, and assume that q_{TIR} evolves as:

$$q_{\rm TIR} = 2.851 + z^{-0.22} \tag{6.2}$$

as derived by Delhaize et al. (2017). At a certain redshift, the q_{TIR} derived in the redshift -dependent and -independent regimes will 'crossover', with the crossover redshift depending on the assumed synchrotron spectral index. In practice, this means that at higher redshifts, synchrotron luminosities derived using equation 6.2 will be greater than synchrotron luminosities calculated assuming a constant q_{TIR}=2.64. In terms of assessing the signal-to-noise ratio of a detection, and thus the performance of the SKA, assuming a constant q_{TIR} at high redshift can therefore be regarded as the more conservative approach (z$\gtrsim$0.4, see Fig. 6.3).

Free-free radiation

In order to relate total radio luminosity with SFR, we must also consider the contribution from free-free emission, in addition to the synchrotron luminosity derived from the IRRC. We consider two approaches to this. The first is defining the free-free luminosity according to the star-formation rate of the galaxy (Murphy et al., 2012):

$$L_\nu = \frac{SFR}{4.6 \times 10^{-28} \times \frac{T_e}{10^4}^{-0.45} \times \nu^{0.1}} \tag{6.3}$$

where L_ν is the free-free luminosity in erg.s^{-1} at frequency ν (in GHz), and T_e is the electron temperature, T_e=10^4 K (Murphy et al., 2012). The second approach is to assume a fixed 1:1 ratio between synchrotron and free-free luminosity at rest-frame 30 GHz. This reflects the relative importance typically observed in local galaxies (Condon, 1992), as shown in Fig. 1.4.

Total radio luminosity

The total radio luminosity is the sum of the synchrotron and free-free emission. In order to assess the systematic differences arising from the different regimes of relating radio luminosity and star-formation, we define four possible combinations of the methods outlined above:

i. *Case 1*: constant q_{TIR} from Bell 2003 and M18; free-free derived from the SFR

ii. *Case 2*: constant q_{TIR} from Bell 2003 and M18; free-free luminosity equal to synchrotron luminosity at 30 GHz

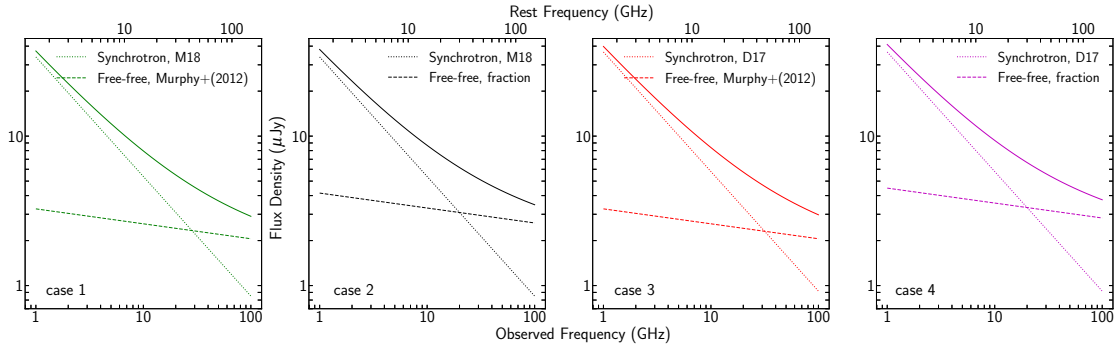

Figure 6.2: Decomposition of derived radio flux densities into synchrotron and free-free components, for the different methods outlined in the text. Cases 1-4 are shown from left to right. Both observed (lower axis) and rest-frame (upper axis) frequencies are displayed, for a galaxy at z=0.5 with SFR=10 $M_{\odot}yr^{-1}$.

iii. *Case 3*: q_{TIR} evolving with redshift (equation 6.2); free-free derived from the SFR

iv. *Case 4*: q_{TIR} evolving with redshift (equation 6.2); free-free luminosity equal to synchrotron luminosity at 30 GHz

Fig. 6.2 illustrates the radio SEDs derived in each of these four cases, for a galaxy with SFR=10 $M_{\odot}yr^{-1}$ at z=0.5. The differences between cases are predominantly driven by the derivation of synchrotron emission. For case 4, we see that synchrotron emission becomes more dominant over free-free emission compared to the other cases, due to the redshift evolution of q_{TIR}, combined with the fact that the free-free is derived independently of synchrotron luminosity. For cases 1 and 3, where free-free luminosity is derived from the SFR, we investigate the frequency at which the free-free emission reaches the same luminosity as the synchrotron luminosity. At z=0.5, we find a ratio of 1:1 at ν_{rest} $\sim$45 GHz for cases 1 and 3, compared with the expected value of 30 GHz. For case 3, this crossover rest-frequency increases with redshift as the derived synchrotron emission evolves.

We show in Fig. 6.3 the evolution of total observed radio flux from each method, for a galaxy with SFR=10 $M_{\odot}yr^{-1}$ at z=0.38 and z=3 respectively. We choose z=0.38 for the left panel as this is the redshift at which the fluxes derived from cases 1 and 4 (the most and least conservative in the right panel, respectively), are approximately equal near the central frequency of SKA1-MID band 2, 1.4 GHz. We see that at z=0.38, the four methods give very similar results. However, when we move to z=3, the radio fluxes derived using a redshift-dependent q_{TIR} are raised significantly above those derived using a constant q_{TIR}. At z=3 (the maximum redshift of our simulation galaxy sample, see Section 6.3.1), the greatest difference between derived radio fluxes (cases 1 and 4) reaches an average factor of $\sim$4 across these observed frequencies.

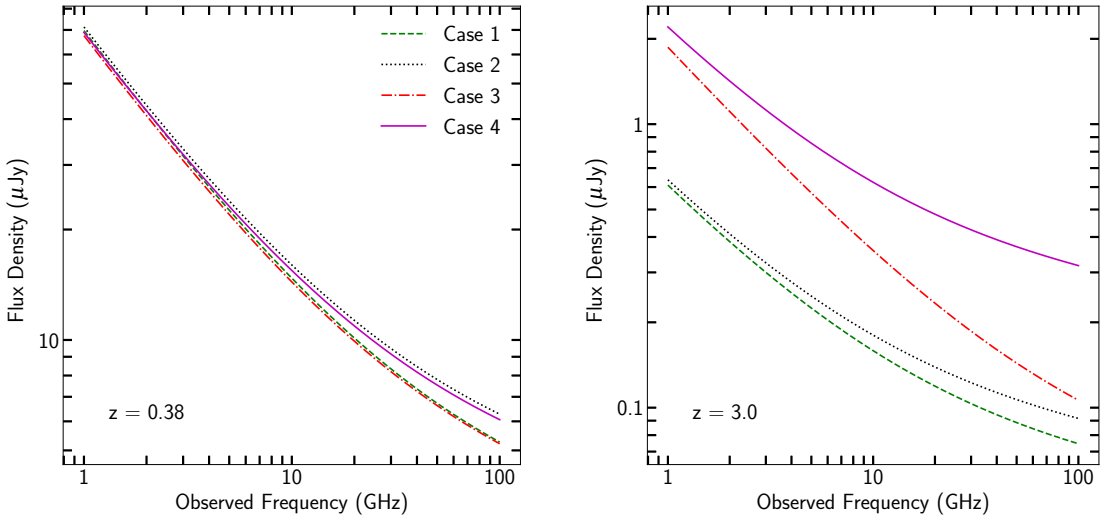

Figure 6.3: Total radio flux density derived from a SFR of 10 $M_{\odot}yr^{-1}$, using the methods outlined for cases 1-4 in the text. The left panel shows the derived flux for a galaxy at z=0.38, and the right panel shows the evolution with redshift of the different methods, for the same galaxy at z=3.

In order to be conservative in our predictions at high redshift, where we are probing the technical capabilities of the SKA, we use limiting cases 1 and 4 in order to derive our total radio fluxes. Above z=0.38, we see that case 4 gives higher fluxes than case 1, where the inverse is true at z<0.38. We also note that at z<0.38, case 4 is the most conservative method (gives the lowest flux), whereas case 2 gives the highest observed flux at these low redshifts.

6.2.3 Detectable star-formation rates of SKA reference surveys

As discussed in Section 6.2.1, several reference surveys have been planned for phase 1 of the SKA by the Extragalactic Continuum SWG. In order to understand the physical properties of the galaxies that will be detectable by these surveys, we must relate the anticipated depths of the surveys (Section 6.2.1) to galaxy star-formation rates. We take the survey sensitivity in terms of radio flux density, and then use the framework described in Section 6.2.2 to calculate the SFRs that would give rise to this level of flux. We show in the left panel of Fig. 6.4 the minimum SFRs that will be detectable by SKA1-MID at the $\geq 5\sigma$ level, for the three tiers of survey in band 2, using derivation cases 1 and 4 above. We see that the method used to relate SFR and radio flux makes a less significant difference at lower redshifts, and we see a crossover between the results using cases 1 and 4 at z$\sim$0.4.

At z=0.1 (the lowest redshift in the galaxy sample used for our SKA1-MID simulation, see Section 6.3.1), the SKA will be able to probe galaxies with SFRs down to small values, $\sim 10^{-1}$-$10^{-2} M_{\odot}yr^{-1}$ in all tiers of the survey. At z=3, the minimum detectable SFR is between $\sim$1-

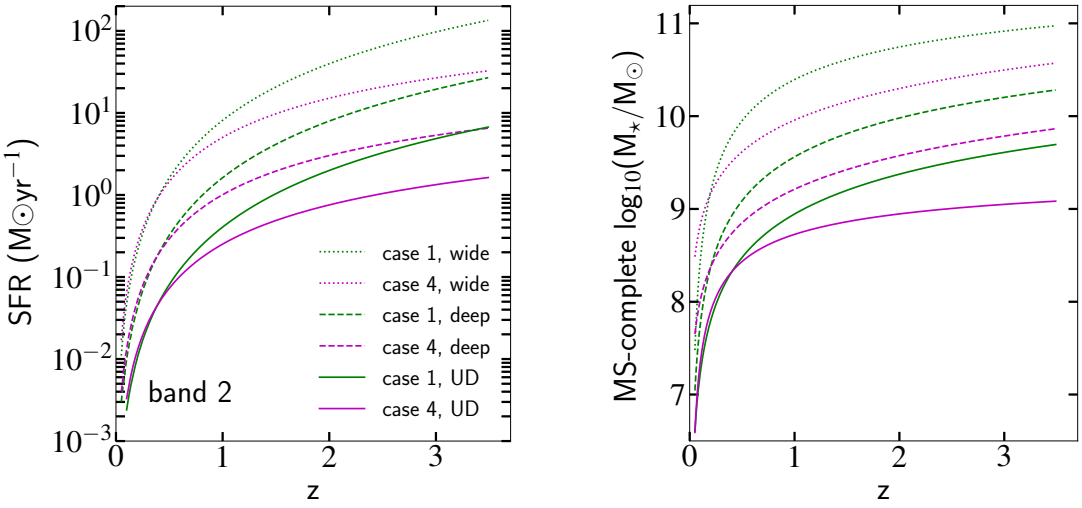

Figure 6.4: Left: Minimum detectable 5σ SFRs as a function of redshift, for the SKA1-MID reference surveys shown. Band 2 ultradeep (UD, solid lines), deep (dashed lines) and wide (dotted lines) tiered surveys are shown. Right: the minimum stellar mass to which the same surveys will be able to detect Main Sequence complete samples.

4 $M_\odot yr^{-1}$ in the ultradeep tier, 5-19$M_\odot yr^{-1}$ in the deep tier and $\sim$27-100 $M_\odot yr^{-1}$ in the wide tier (5σ) respectively. These figures highlight the factor $\sim$3-4 variation arising from the different derivations of radio flux at high redshift, but more importantly, they provide crucial information about the star-formation properties of the galaxies that will be detected. In the right panel of Fig. 6.4, we show the 'Main Sequence completeness' of these surveys. For each tier of the survey, we show the stellar masses down to which SKA1-MID will be able to detect galaxies on the MS. We see that, similarly to the SFR limits themselves, the MS mass limits increase with redshift, and that the different survey tiers will probe the MS population from $M_\star \sim 10^{7.2}$-$10^{8.8} M_\odot$ at z=0.1, to $M_\star \sim 10^{9.0}$-$10^{10.9} M_\odot$ at z=3.

In order to further quantify the regions of the MS that the surveys will characterise, we plot the survey SFR detection limits in relation to the locus of the MS in Fig. 6.5. We show redshifts spanning z=0.1 to z=3.0, with three different MS loci and their scatter displayed. In each panel, we colour the regions of the MS that will be detectable by the different tiers of the band 2 surveys. The horizontal boundaries correspond to the minimum detectable 5σ SFRs shown in Fig. 6.4, which then intersect with the MS at that redshift. We draw our survey boundaries reaching the lowest edge of the 1σ scatter from the three Main Sequence curves at that SFR. We are therefore calculating a conservative stellar mass for each SFR limit, in order to quantify to which mass the tiers will be Main Sequence complete.

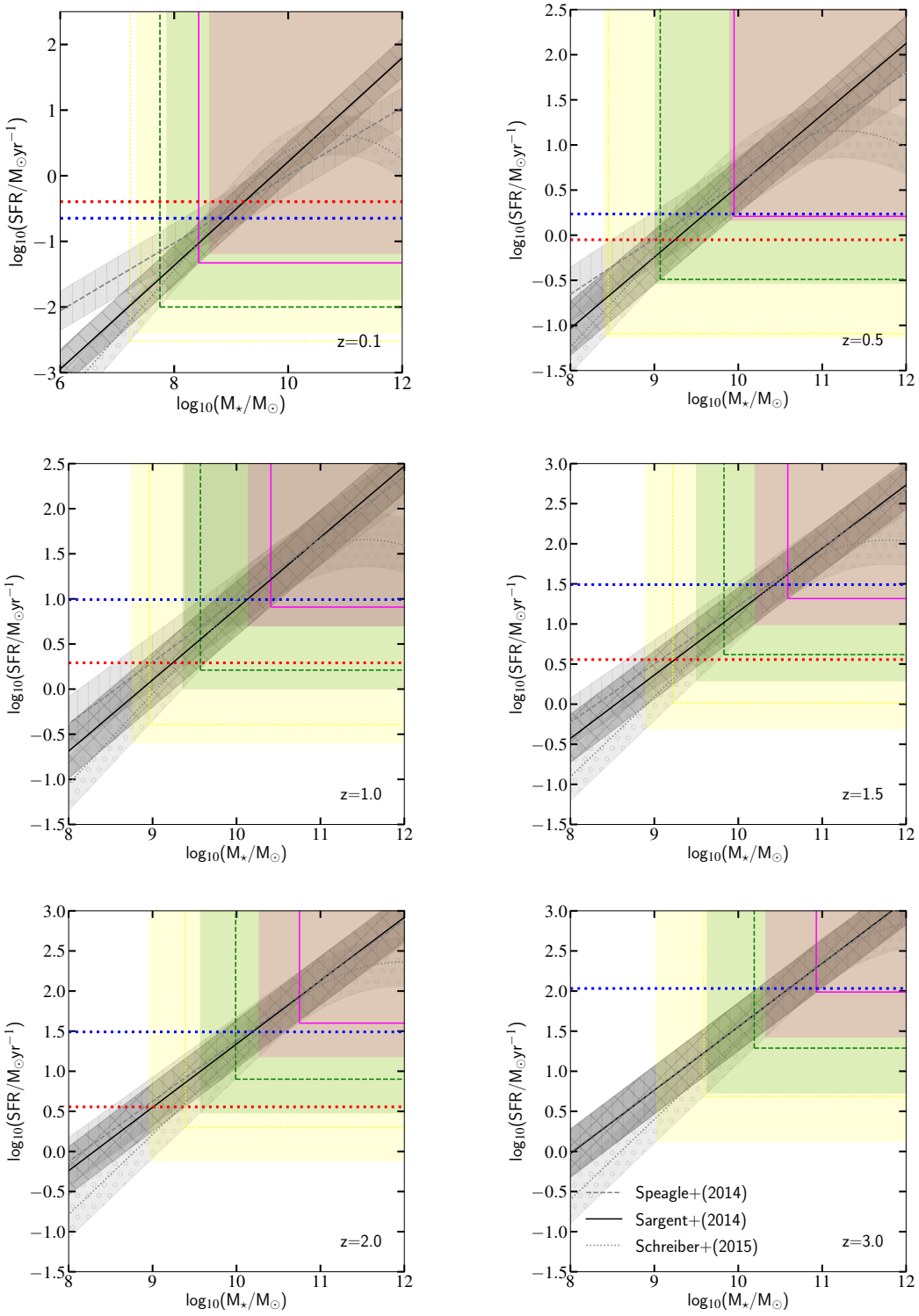

Figure 6.5: Regions on the MS accessible to the SKA band 2 continuum reference surveys, at the given redshifts. Three main sequence loci and their 0.3 dex scatter are shown. The coloured regions (yellow: ultradeep, green: deep, magenta: wide) and the corresponding coloured lines (dotted: ultradeep, dashed: deep, solid: wide) indicate the regions of the MS that will be detectable by different survey tiers for case 4 and case 1 respectively, according to the 5σ minimum SFRs shown in Fig. 6.4. The blue and red dotted lines show the minimum SFR probed by the galaxy sample used for our SKA simulations (Section 6.3).

Interestingly, looking across the wide redshift range shown in Fig. 6.5, we can see that between z=0.5 and z=3.0, the MS mass-completeness limit changes by less than an order of magnitude for case 4 ($\sim$an order of magnitude for case 1). At z=0.1, the band 2 wide tier will be MS complete to $M_{\star}\sim10^{8.5}$ $M_{\odot}$. The deep and ultradeep surveys will probe to even lower stellar masses at this redshift, detecting complete samples down to $M_{\star}\sim10^{7.8}$ $M_{\odot}$ and $M_{\star}\sim10^{7.3}$ $M_{\odot}$ respectively.

Looking considerably further into the star-formation history of the Universe, we can quantify the region of the MS probed by these surveys at z=3. The band 2 surveys will be complete for galaxies on the Main Sequence of star-formation down to $M_{\star}=10^{10.3-10.9}$ $M_{\odot}$, $M_{\star}=10^{9.6-10.2}$ $M_{\odot}$, and $M_{\star}=10^{9.0-9.6}$ $M_{\odot}$, for the wide, deep, and ultradeep surveys respectively, with the range reflecting the differences between cases 1 and 4. We also see in Fig. 6.5 that the SKA band 2 continuum surveys will be able to detect galaxies with SFRs significantly below the MS. For example, at $M_{\star}=10^{10-10.5}$ $M_{\odot}$, the SKA will be able to detect galaxies with SFRs up to an order of magnitude below the MS between $0.1 < z < 3$, over the ultradeep and deep survey regions covering 1-30 deg^2 respectively.

Fig. 6.5 demonstrates that the high sensitivity of SKA1-MID will allow for MS-complete samples (in addition to low-SFR, passive galaxies) to be detected over several orders of stellar mass, even beyond the peak epoch of star-formation (z$\sim$2). Measuring the SFRs of statistical samples of star-forming galaxies in this way is crucial for our understanding of galaxy evolution, enabling us to map the dust-obscured star-formation history of the Universe from these early times. Having quantified the SFRs that the reference continuum survey tiers will probe, the next step to understanding the science that the SKA will enable is to characterise how accurately SKA1-MID will recover galaxy parameters. We therefore explore this in Section 6.3, by creating SKA-simulated continuum images of real observed galaxies, to the depths of the three tiers of the band 2 continuum reference survey.

6.3 SKA simulations

As discussed in Section 6.1, it is essential to understand the future capabilities of the SKA, in order to most effectively plan observations and interpret large amounts of SKA survey data. In this section, we create simulated images of the SKA sky, using previous multiwavelength, resolved observations of galaxies in the GOODS-North field. We use these previous observations to calculate resolved radio flux densities of the galaxies, as well as galaxy morphological parameters relating to their concentration and flux distribution. Having simulated our galaxies with the anticipated observational response of SKA1-MID, we can quantify the ability of the SKA to accurately recover these parameters. In Sections 6.3.1 to 6.3.3, we describe our observed galaxy sample, and the

derivation of the resolved radio flux maps. We outline the simulation process in Section 6.3.4. In Section 6.4, we present the first results of our simulations.

6.3.1 Sample selection

As input into our simulated SKA images, we combine two samples of galaxies that have been selected from the GOODS-North field. The first is a mass-selected sample of galaxies ($\log(M_\star)>9.5$, derived from multiwavelength SED fitting with FAST), that have both HST F336W and F275W ultraviolet coverage from the Hubble Deep UV Legacy Survey (HDUV, Oesch et al. 2018). These galaxies have redshifts between $0<z<2.5$, derived either from EAZY spectral energy distribution modelling (Brammer et al., 2008) or 3DHST spectroscopy, where available. This selection results in 1174 sources taken from the GOODS-North field. These galaxies have SFRs spanning the Main Sequence of star-formation and also significantly below (see Fig. 6.7), with some galaxies falling into the region below the MS where they might be considered quiescent.

In order to also sample galaxies from the entire GOODS-N field (i.e. not limited to the HDUV), we take an additional 439 IR-selected (and therefore SFR-selected) galaxies in the GOODS-N field that did not satisfy all of the above criteria, but are present in the infrared catalogue published by Liu et al. (2018). These galaxies are taken from the IRAC GOODS-Spitzer survey (PI: M. Dickinson), have both MIPS 24 μm and VLA 20 cm detections, and H-band magnitudes $H<24$, as originally selected for study by Cibinel et al. (2019). The 3DHST sizes, $R_{\rm Kron}$, of these galaxies were required to be greater than $5\times$ the HST H-band PSF, in order to derive reliable morphological parameters. These galaxies lie in the redshift range $0<z<3$ (derived from 3DHST photometry or spectroscopy, where available), pushing to higher redshifts than found in the mass-selected sample. By combining the mass- and IR-selected samples, we are able to simulate galaxies spanning a range of stellar mass, SFR and redshift, over large regions of the GOODS-North field.

Finally, we note that AGN were not removed from our galaxy samples. However, the SED-fitting routines used to derive pixel-by-pixel SFRs (Section 6.3.2) account for the possibility of emission from AGN. Additionally, our simulation analysis is based on the assessment of input vs. output parameters, and are therefore not affected by the mechanism giving rise to the emission itself.

6.3.2 Star-formation rates of the GOODS-North sample

Construction of resolved star-formation maps

As our galaxies lie in a region of the sky that has previously been observed by many different instruments, large multiwavelength (MWL) auxiliary datasets exist for the derivation of resolved galaxy

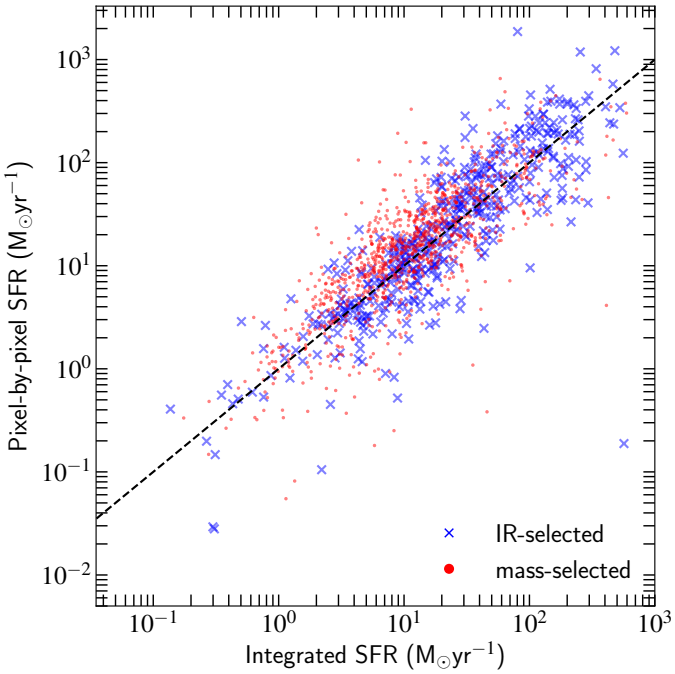

Figure 6.6: Integrated star-formation rates vs. pixel-by-pixel SFR sums, for our GOODS-North galaxy sample. The galaxies are coloured according to their selection technique, where red is mass-selected, and blue is IR-selected.

properties. As described in Cibinel et al. (2015), all HST WFC3 and ACS images were convolved to the same, HST H-band resolution before deriving resolved SFR maps. The adaptive smoothing routine `ADAPTSMOOTH` was applied to stacks of HST WFC/ACS images to ensure homogenisation of the SNR for SED fitting. Resolved star-formation rate maps were then constructed for each galaxy using pixel-by-pixel SED fitting of the available HST photometry (see Cibinel et al. 2015, 2019), using bands B_{435}, V_{606}, i_{775}, i_{814}, z_{850}, J_{125} and J_{140}, as well as H-band and Y_{105} images. For galaxies in the HDUV, F275W and F336W data were also available. Median SFRs were taken from the LePhare (Arnouts et al., 1999; Ilbert et al., 2006) outputs. If the adaptive smoothing required averaging over >5 pixels in order to reach SNR=5 (as may be the case towards the edges of a galaxy, for example), the resolved SFR derivations were truncated at this point. SFR cutouts were made for each galaxy out to a maximum of $1.5\times R_{\rm Kron}$, and assumed to be zero outside of this radius. For reference, the average Kron radius of our sample is 14.9 kpc (proper). The pixel scale of all resolved SFR maps is 0.06"/pixel.

Integrated star-formation rates

In order to discuss the global star-forming properties of our galaxies, we now demonstrate the consistency between our resolved SFRs and the integrated values present in the literature. For our

IR-selected sample, integrated UV+IR SFRs were derived in Liu et al. (2018), using SED fitting of super de-blended photometry from 2μm to radio wavelengths, in addition to UV observations or an appropriate SFR_{UV}/SFR_{IR} ratio. As discussed in Cibinel et al. (2019), the inclusion of this long-wavelength emission becomes particularly important for calculating SFRs in the highly star-forming, dust-obscured regime. For this reason, where galaxies from our mass-selected sample are also present in the catalogue of Liu et al. (2018, which is the case for 247 galaxies), we adopt these UV+IR SFRs for these mass-selected galaxies. For the majority of the remaining mass-selected galaxies (857 galaxies), UV+IR SFRs were derived as described in Whitaker et al. (2014, based on the work of Bell et al. 2005), taking advantage of Spitzer 24μm observations in order to derive the IR contribution to the SFR. There were only a small number of galaxies (70) for which integrated UV+IR SFRs were not available for comparison with our resolved SFRs. For these mass-selected galaxies ($\sim$6% of the sample), total SFRs have been derived by Whitaker et al. (2014) using MWL FAST SED fitting, without the benefit of observations at IR-radio wavelengths. We perform a search for all galaxies with FAST SFRs from Whitaker et al. (2014) that are also present in the catalogue of Liu et al. (2018), and find 693 matches between the two catalogues. This allows us to calculate a median systematic offset between the two SFR derivations. Therefore, for our small fraction of mass-selected galaxies where no integrated UV+IR SFR exists, we take the corrected FAST SFRs from the literature as the integrated SFRs (which we find to be consistent with our resolved SFRs, see Fig. 6.6).

In Fig. 6.6, we show the integrated SFRs of our galaxies, in comparison with the sum of their pixel-by-pixel LePhare SFRs, from which the resolved radio maps were created (Section 6.3.2). We show only those galaxies that lie no more than 1 dex below the MS of star-formation, as the pixel-by-pixel SFR sums of galaxies significantly below the MS are subject to significant uncertainty. We see that the two SFR estimates for the IR-selected sample (blue) are in good agreement (median $SFR_{int} = SFR_{pix} - 0.03$ dex, scatter of 0.39 dex around the 1:1 line). The integrated SFRs of the mass-selected sample (red) are also in agreement with their corresponding pixel sums (median $SFR_{int} = SFR_{pix} - 0.13$ dex, scatter of 0.38 dex around the 1:1 line).

In order to illustrate the star-formation parameter space sampled by our data, we now show the position of our galaxies on the MS of star-formation using their integrated SFRs, in Fig. 6.7. Here we have divided our sample into three redshift bins, with 519, 579 and 515 galaxies at $0.0 \leq z < 0.9$ (left), $0.9 \leq z < 1.6$ (center) and $1.6 \leq z < 3.0$ (right) respectively. In order to assess the position of all galaxies with respect to the MS, we have normalised their SFRs according to the MS displayed in the relevant panel, such that the galaxies are at their correct offset from the MS, ΔMS. Fig. 6.7 illustrates that our galaxy sample spans between 2-3 orders of magnitude in specific star-formation

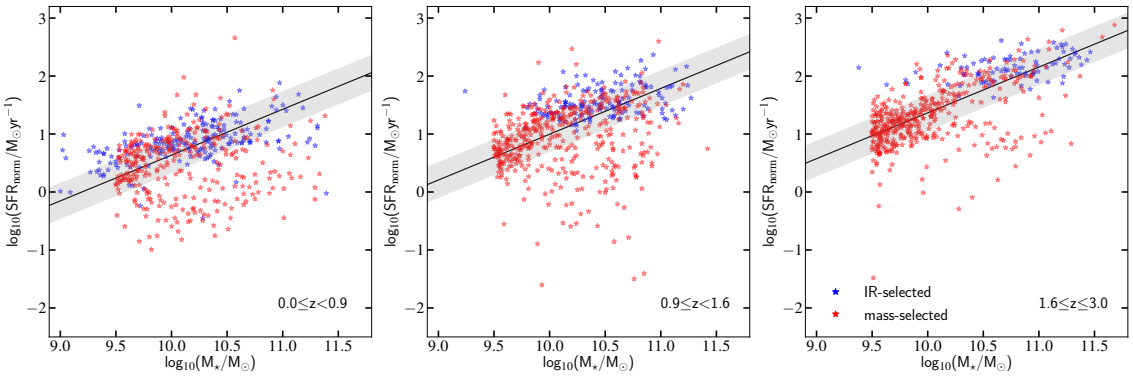

Figure 6.7: The position of our GOODS-North sample on the Main Sequence of star-formation. Three redshift bins are shown, as indicated in the lower right of each panel. The MS of Sargent et al. (2014) at the average redshift of each bin is shown by the solid black line, with the grey shaded area indicating a 0.3 dex scatter. The SFRs of the galaxies have been normalised in order to lie at their intrinsic ΔMS, with respect to the MS shown. The galaxies are coloured according to their selection technique, where red is mass-selected, and blue is IR-selected.

rate, with a range of sSFRs from starburst to quiescent, in all three redshift bins. We colour our galaxies by their selection technique, highlighting the regions of the MS occupied by the different samples.

In order to further quantify the SFR depths probed by our sample, we show in Fig. 6.8 the minimum SFRs of our galaxies as a function of redshift. We define the minimum SFR by dividing the sample into redshift bins of Δz=0.5, and taking the average SFR of the lowest (least star-forming) 20% of galaxies in each bin. In the case of our mass-selected galaxies, we consider only those galaxies that lie no more than 1 dex below the MS. Having done this for both the IR- and mass-selected samples, we fit an exponential curve defining the minimum SFR with redshift for each sample, which can be seen in Fig. 6.8.

We now relate these limits to the depths of the survey tiers that we are simulating for these galaxies, by overplotting the derived minimum SFR of each of our samples in Fig. 6.5. At z=0.1, we see from the blue and red horizontal lines that the minimum SFR of both of our samples is detectable by all three tiers of the band 2 survey, in the stellar mass range of our galaxies (log($M_\star$>9). As we move to higher redshifts, our IR-selected sample remains detectable by all three tiers of the survey, due to the relatively high SFRs. On the other hand, the faintest star-forming galaxies in our mass-selected sample probe different survey parameter space. At z$\geq$0.5, the minimum SFR of the mass-selected sample will not be detectable by the wide tier - only the deep and ultradeep tiers. This is a particularly relevant observation, as it allows us to explore the detectability of our galaxies as a function of survey depth, as we do not expect all of them to be present in the shallower tiers.

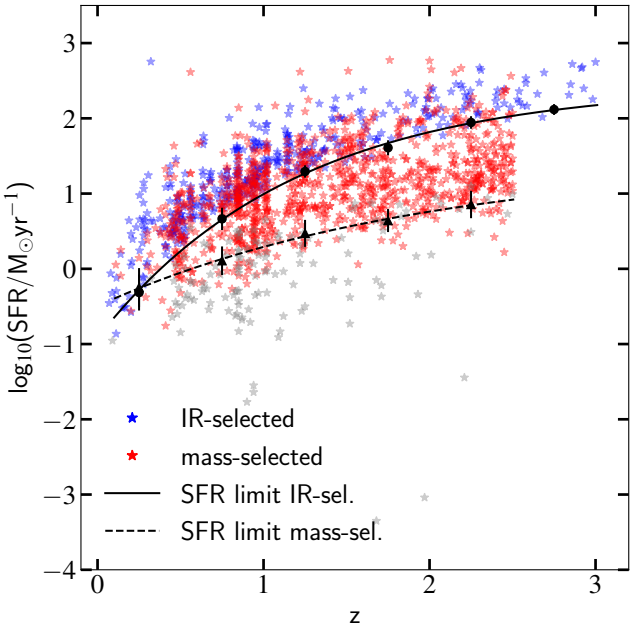

Figure 6.8: SFR-redshift distribution of our GOODS-North sample. The red and blue stars indicate the IR-selected and mass-selected samples respectively. The black solid line shows the minimum SFR for the IR-selected sample, fit to the average SFR of the bottom 20% in each Δz=0.5 bin (black circles). The black dashed line shows the minimum SFR for the mass-selected sample at $\log(\Delta_{\rm MS})$>-1, again from the average of the bottom 20% of the bin (black triangles). In both cases, the errorbars show the SFR standard deviation of the selected 20%. The grey stars show mass-selected galaxies $\geq$1 dex below the MS.

For comparison, we note that the area of the GOODS-North field is $\sim$0.02 deg^2, which is smaller than the planned 1 deg^2 coverage of the ultradeep tier. We also stress that due to the high angular resolution of SKA1-MID (sub-arcsecond at 1.4 GHz), it is not expected that source confusion will limit the sensitivity of surveys such as these, and hence should not affect the ability of SKA1-MID to probe MS parameter space as demonstrated in Fig. 6.5 (e.g. Condon et al. 2012).

To summarise, we are using two samples of galaxies as inputs into our SKA1-MID simulation. The first is mass-selected at $\log(M_\star)$>9.5, with redshifts 0<z<2.5. These galaxies are located in the central 56.5 arcmin^2 of the GOODS-North field, covered by the HDUV survey. The second is an IR-selected sample between 0<z<3, observed over the entire $\sim$0.02 deg^2 area of the GOODS-North field. We see in Fig. 6.8 that between 0<z<2.5, the mass-selected sample probes down to SFRs on average 5$\times$ lower than the IR-selected sample.

6.3.3 Intrinsic radio flux distributions

For each galaxy, we create resolved observed radio flux maps at the continuum frequency of SKA band 2, $\nu_{\rm obs}$ ~1.4 GHz. SFR values were converted to total radio luminosity, on a pixel-by-pixel basis, using the method described in Section 6.2.2. For our first set of simulations, presented in this chapter, we use radio derivation case 1. This is most conservative at higher redshift (z>0.4), as it gives rise to the lowest predicted radio fluxes. Having created individual radio cutouts of each galaxy, these cutouts were combined into a single image (using the observed positions of the galaxies on the sky), representing the GOODS-North field as seen at radio frequencies. Example regions of this 'intrinsic' or 'model' (meaning before the SKA simulation) band 2 continuum map, in addition to HST/WFC3 H-band images of the galaxies, are shown in the first two rows of Fig. 6.9. The angular resolution of the H-band images shown in the top row of Fig. 6.9 is FWHM=0.15", and it is from HST images of this resolution that the model SFR (and therefore radio) maps were produced. We note that the output resolution of our simulated images is coarser than this, FWHM=0.6" (see Section 6.4). Further examples demonstrating the range of galaxy morphologies in our sample can be found in Appendix C (Fig. C.1), along with a full continuum model image of the GOODS-North field, Fig. C.2. We will discuss the images output from our simulations (shown in the lower three rows of Fig. 6.9) in Section 6.4.3.

We show examples of model radio maps for four different galaxies in Fig. 6.9. As the original SFR cutouts were created to a maximum of $1.5\times R_{\rm Kron}$, with SFR=0 outside of this region, our intrinsic radio field can be considered as noise-free. This means that the pixels surrounding the galaxies are zero-valued in the model images, such that the limits of the radio continuum emission are clearly visible. In the first column, we show a galaxy at z=0.11 with clearly visible H-band spiral arms, oriented face-on towards the observer. Due to both the inclination of the disk, and the low redshift of the galaxy, the full extent of the radio map extends to almost 20"×20" on the sky. In next column (galaxy 20617), we see a disk at a much steeper angle, relatively edge-on to the observer, with a bright elongated core. The cutout in the third column is centred on a galaxy (ID 21683) whose morphology appears relatively spheroidal in the H-band image. However, we also see two neighbouring galaxies in the H-band image - one galaxy to the East, and a fainter galaxy to the West. The model radio continuum therefore shows the contribution from all three galaxies. What's particularly interesting about this cutout is that galaxy ID 21683 and its neighbour to the East are both at the same redshift, z=0.56. We can see from the radio image that although the cores of their stellar emission are separable in the H-band image, the limit between their star-formation emission regions is not visually distinct. Finally, in the fourth column of Fig. 6.9, we see a galaxy at much higher redshift, z=2.39. This galaxy is much fainter in the H-band image than the lower

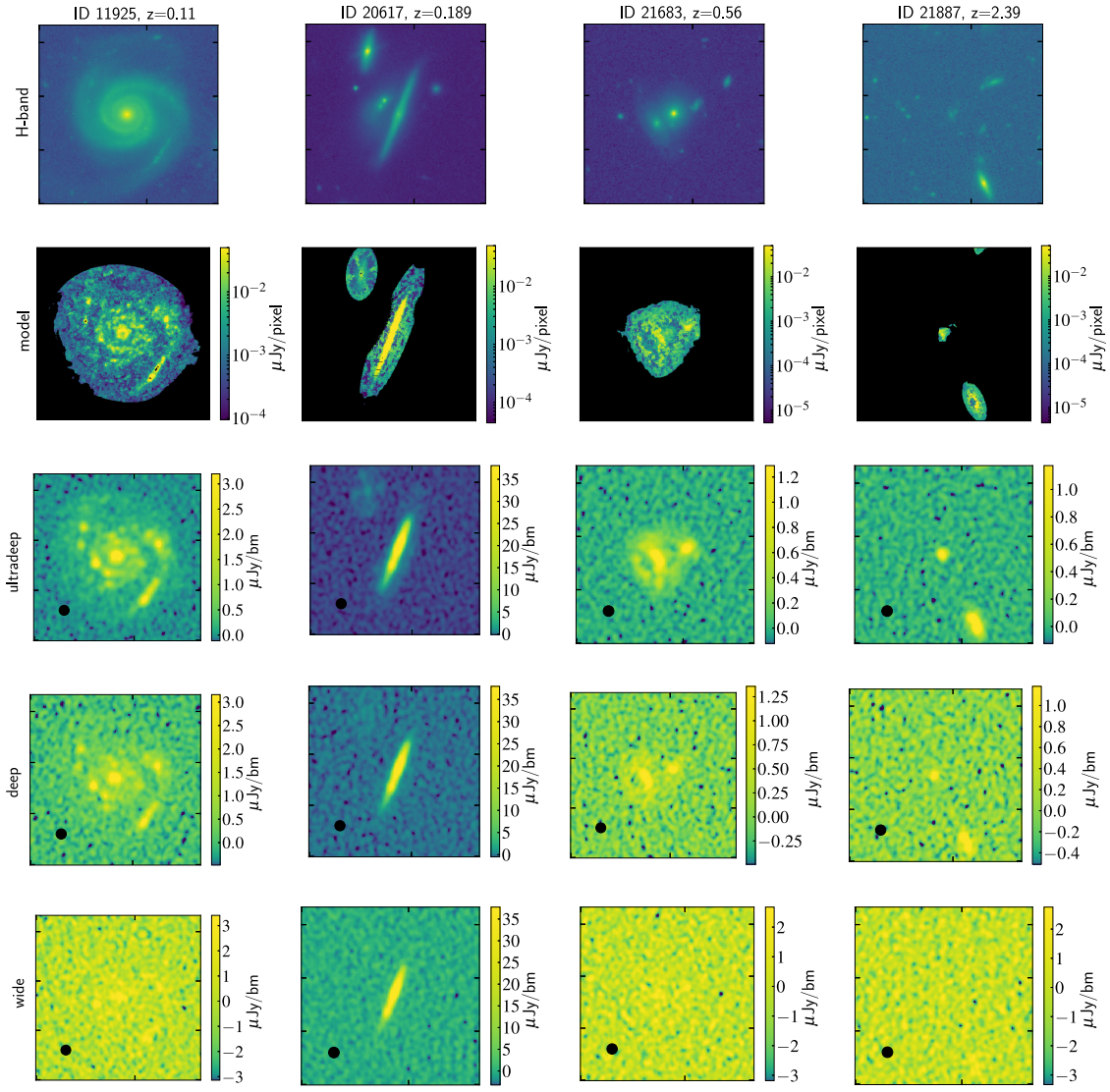

Figure 6.9: Examples of HST/WFC3 H-band, intrinsic/model radio, and SKA-simulated radio images for the ultradeep, deep and wide survey tiers, for our galaxy sample. The rows are labelled on the left side of the figure, and galaxy IDs and redshifts are shown above each column. All cutouts are 20"×20". The H-band and model images are at a scale of 0.06"/pixel, and the black regions in the model row indicate the zero-valued background. The simulated survey images are at a scale of 0.12"/pixel, and the FWHM=0.6" of the simulated synthesised beam is shown by the black circles.

redshift galaxies, but can still be seen through its star-formation in the intrinsic radio maps.

6.3.4 Simulation outline and setup

We perform our SKA1-MID simulation in band 2 (0.95-1.76 GHz), taking a central instantaneous bandwidth (IB) of 420 MHz. We limit ourselves to this conservative fractional bandwidth $\delta\nu\nu$=0.3, as it closely matches the anticipated fractional bandwidth that the science data processor will provide from the SKA pipeline. Additionally, we note that in practice the useable IB will be reduced from the full 0.85 GHz receiver width, as we can expect to lose $\sim$20% of the frequency coverage in band 2 to radio frequency interference. A 30% fractional bandwidth is also adopted for SKA Science Data Challenge #1, allowing a direct comparison with these data.

In preparation for putting our resolved radio image through the SKA simulation, we resample the image to a pixel scale that will appropriately sample an SKA1-MID synthesised beam. In our images, we will implement a circular Gaussian synthesised beam of FWHM=0.6", as this is the highest resolution (given the SKA1-MID baseline distribution), that can be achieved whilst also maximising the sensitivity. Additionally, this matches the resolution of the simulated images produced for SKA Science Data Challenge #1 (see Fig. 6.10). We therefore reduce our native pixel scale by a factor of two, from 0.06"/pixel to 0.12"/pixel. These resampled images are then input into the SKA simulation pipeline. The pipeline is based on the sequence of modified Miriad routines developed by the SKA Organisation (SKAO), and has been adapted for use with our data. The key steps of the simulation are as follows:

1. Take science image as input (observed radio flux intrinsic image).
2. Take SKA1-MID band 2 primary beam response as input.
3. Re-sample the primary beam image to match the pixel scale and world coordinate system (WCS) of the science image.
4. Convolve the science image with a Gaussian ('clean') beam, to give image units of Jy/beam.
5. Apply the primary beam attenuation to the science image.
6. Generate the SKA1-MID mock visibility coverage. This depends upon the SKA1-MID configuration of 197 dish antenna, correlator frequency setup (number of spectral windows, bandwidth, channel width), hour angle range on the sky, polarisation, source position, telescope latitude, and the Jy/K and system temperature of the telescope.
7. Create image of the dirty beam from these visibilities, as well as a dirty image containing only noise.
8. Adjust the absolute scale of the dirty noise image, so that the RMS corresponds to the desired depth of observation.

9. Clip the science image (in Jy/beam) at a certain flux level. This produces a 'residuals' image, containing only the data below the clip level. The clip level is taken to be the 3σ noise of the 8 hour RMS noise.
10. Subtract the residuals image from the science image, leaving an image containing only peaks above the 3σ noise.
11. Deconvolve the residuals from the clean beam. Then, convolve them with the dirty beam created in step 7.
12. Add the peak image to the dirty-beam-convolved residuals image.
13. Add the dirty noise image (at the desired RMS level) to the peak+residual image.

To those familiar with classic 'deconvolution' techniques, steps 9-12 are somewhat equivalent to `CLEAN`ing an interferometric image. When `CLEAN`ing an image, the dirty science image is inspected for peaks in flux above a given threshold. On finding these peaks, the flux above the threshold is subtracted from the image, and added to a 'model' image. This is done iteratively, leaving a residual image below the set threshold, and a model image. The peaks in the model image are convolved with the 'clean', or synthesised beam, and then added back to the residual image (which remains convolved only with the dirty beam). Steps 9-12 of our Miriad pipeline are therefore emulating this process, by convolving the SKA dirty and clean beams with the residual and peak images derived from the input science image, respectively. As with the SKA Science Data Challenge #1, a full end-to-end simulation was not performed due to the sheer volume of data that this would produce, and thus the high-performance computing requirements needed to perform the simulation. Although this approach makes producing meaningful simulations more efficient (and therefore more accessible), we should keep in mind the limitations. As we are not modelling our galaxies in the uv-plane (only the noise), our achievable RMS sensitivity is not affected by the dynamic range of our sources, for example, nor do we suffer from image artefacts from very bright sources. However, although our galaxy selection contains a wide range of star-formation rates, it does not contain emission from objects such as radio-loud AGN, which would typically increase the dynamic range of an image. Additionally, our simulations do not consider a frequency-dependent synthesised beam, which could become a non-negligible effect if we were to move to higher fractional bandwidths. Finally, we note that our simulation does not account for calibration errors that might be introduced in the raw data reduction.

The inputs to the Miriad pipeline are therefore: science image to be simulated, primary beam response for the desired frequency, technical setup to generate the visibility coverage (step 6), target RMS of the output image and FWHM of the desired synthesised beam. We note that we take all 197 SKA1-MID dishes to have a 15 m diameter, and have therefore not modelled the

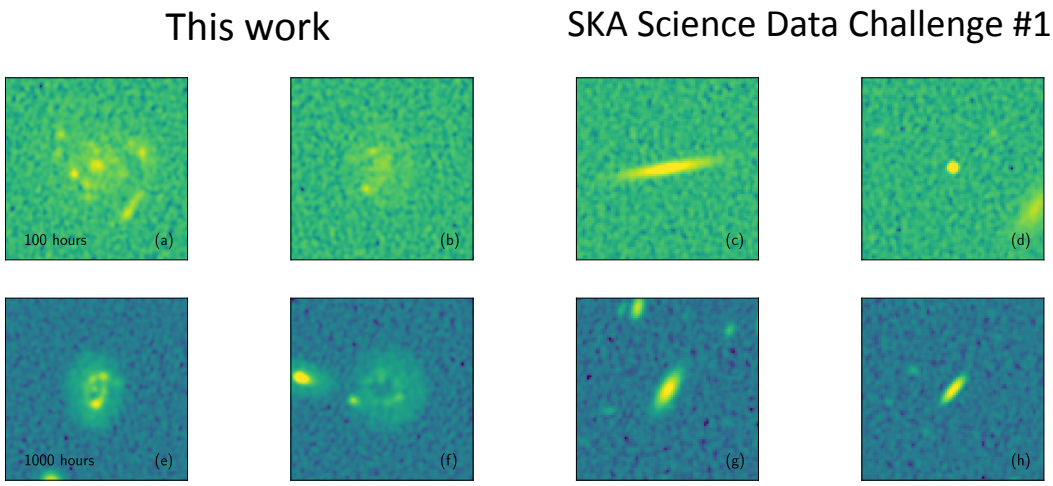

Figure 6.10: Comparison between our simulated sky and the SKA Science Data Challenge #1. Left: our simulated band 2 images of real star-forming galaxies. Right: simulated band 2 images of T-RECS galaxies from the SKA Science Data Challenge #1. The rows show 100 h and 1000 h observations as labelled. Each 100 hour (1000 hour) image has the same RMS noise, and the same image colour scaling. All cutouts are 20"×20".

smaller diameter of the 64 MeerKat dishes (13.5 m) that will be incorporated into SKA1-MID. This approach was also taken for the SKA Science Data Challenge #1. We provide the Miriad code for our SKA1-MID simulation in Appendix D. We also note here that the source position for our science image was given as zenith in the simulation, as the GOODS-North field itself is not well positioned to be observed by the SKA in the Southern hemisphere. However, the galaxies in the GOODS-North field are representative of the galaxies that the SKA will observe, and have the advantage of full ancillary datasets with which to create our resolved intrinsic maps.

6.4 Simulation results

6.4.1 Comparison with the SKA Science Data Challenge #1

In Fig. 6.10, we show 20"×20" example cutouts of our simulated images, alongside images from the SKA Science Data Challenge #1. For this comparison, we have produced images with RMS noise levels corresponding to observation times of 8 hours, 100 hours and 1000 hours, at 0.71 μJy/beam, 0.20 μJy/beam and 0.06 μJy/beam respectively. This allows for direct comparison with the SKAO images, which have also been produced for these observation times at a resolution of FWHM=0.6". Additionally, we have used the provided 'truth' catalogue of the SKA Science Data Challenge #1, to select sources at comparative flux levels in panels (a)+(c), and (b)+(d) respectively. The same is true for the corresponding 1000 h panels. All 100 h (1000 h) panels are scaled to the same

colourmap.

The primary difference between the two simulations is the input galaxy catalogue. As discussed in Section 6.1, the SKA science challenge images have been created not using observations of real galaxies, but using the simulated galaxy catalogue T-RECS (Bonaldi et al., 2019). This catalogue contains both AGN and star-forming galaxies, modelled as combinations of extended and compact radio sources. In all cases, the brightness distributions of the T-RECS star-forming galaxies are input as smooth functions, and do not therefore contain irregularities or off-center clumps. We see examples of this on the right side of Fig. 6.10. We show examples of three T-RECS star-forming galaxies, and one AGN (panel (d)). For the star-forming galaxies, the brightness profiles are modelled as either Gaussian (panels (c) and (g)) or Exponential profiles (panel (h)). Conversely, our input galaxies have radio flux distributions derived from high-resolution observations. Our simulated sky is however lacking in large, extended radio sources (such as the jets of AGN, which are present in the T-RECS catalogue). These differences are highlighted visually in Fig. 6.10. We see that the SKAO images do not contain irregular sub-structure within the galaxies, even in the 1000 hour image. The two sets of simulations are therefore highly complementary.

6.4.2 Galaxy parameter measurements

A key goal of this study is to quantify how well SKA1-MID will be able to accurately recover galaxy properties such as flux and morphology. As discussed in Section 6.2.1, the band 2 SKA1-MID tiered surveys will give us high-resolution observations at 1.4 GHz, for unprecedented numbers of high-redshift galaxies. In order to measure the success of the output parameter recovery, we must also create an 'intrinsic' catalogue of galaxy properties, for comparison with the outputs after convolution with the telescope response. It's important to state that the segmentation maps used to quantify intrinsic galaxy properties (before simulation) do not include the emission from neighbouring galaxies. For example, this means that the intrinsic segmentation map used for galaxy ID 21683 (third column in Fig. 6.9) will include only those pixels that were classified as belonging to ID 21683 in the original resolved SFR images (Cibinel et al., 2019). On the other hand, when we analyse the simulated SKA images in Section 6.4.1, we can no longer use these intrinsic segmentation maps. The extraction will therefore emulate the realistic data analysis of an SKA observation.

For our input-output recoverability tests, we take three key galaxy parameters: the flux, the moment of the brightest 20% of pixels (M_{20}), and the Gini parameter (G). The measured radio flux from the SKA images is of particular interest, as arguably the most important physical property that will be measured using SKA continuum observations is the star-formation rates of large samples

of galaxies, via their radio fluxes. Then, in addition to the flux itself, an important outcome of SKA1-MID will be the morphological studies of galaxies, through the distribution of their star-formation. In order to quantify this, we identify two considerations - the degree of concentration of the flux, and the distribution of the brightest regions of flux. Although the concentration parameter itself (C) is often used in morphological studies, C is measured at the core of a galaxy, and is therefore insensitive to potential off-center concentrations of flux. Concentration however has been shown to correlate with both M_{20} and G, in opposite senses (see Scarlata et al. (2007) for morphological studies in the COSMOS field, for example). Concentration is positively correlated with the Gini parameter, as G gives a measure of how equally distributed (i.e. concentrated vs. diffuse) the total flux of a galaxy is, taking into account all of the galaxy pixels. On the other hand, concentration is negatively correlated with M_{20}, as the second-order moment of the brightest 20% of the galaxy increases with distance from the core. When we combine M_{20} and G, we therefore gain an indication of whether the flux is relatively concentrated or extended throughout the galaxy, in addition to the spatial distribution of the most star-forming regions. Where both AGN activity and nuclear starbursts would have high C and G parameters (with low M_{20}), bright star-forming regions can also exist in the outskirts of a galaxy, for example in tidal tails of galaxies undergoing an interaction with their large-scale environment (low C, high G and M_{20}).

We first measure the total radio flux, M_{20} and Gini parameters for our galaxies using their intrinsic segmentation maps (at 0.06"/pixel, before resampling). The total radio flux was derived by summing the individual pixel values. The Gini parameter is defined as:

$$G = \frac{1}{\overline{X}nn-1} \sum_{i}^{n} 2i - n - 1X_i \tag{6.4}$$

(Glasser, 1962), where n is the total number of pixels, and X_i is the flux value in the *i*th pixel, having first sorted X_i into increasing order. This definition returns Gini values between 0 and 1, where a value of 0 would indicate that the flux is distributed equally over all pixels in the galaxy, and conversely G=1 implies that all of the galaxy flux is located in one pixel.

The second-order moment of the brightest 20% of pixels, M_{20}, is calculated according to Lotz et al. (2004). This is done by first calculating the total second order moment:

$$M_{\rm tot} = \sum_{i}^{n} M_i = \sum_{i}^{n} f_i \left[(x_i - x_c)^2 + (y_i - y_c)^2 \right]. \tag{6.5}$$

This total moment is the sum of the flux in each pixel (f_i) multiplied by the squared distance to the center of the galaxy. The center of the galaxy is given by coordinates (x_c, y_c), and the positions of each pixel in the galaxy segmentation map are the (x_i, y_i). We take the center coordinate of the galaxy to be the radio flux-weighted centroid position, both before and after simulation. M_{20} is

then calculated by rank-ordering the galaxy pixels by flux, and taking the sum of the *i*th brightest pixels until the sum reaches 20% of the total galaxy flux. M_{20} is then the sum of the moments of these brightest pixels, normalised by the total moment:

$$M_{20} \equiv \log_{10}\left(\frac{\sum_i M_i}{M_{\rm tot}}\right), \text{ while } \sum_i f_i < 0.2 f_{\rm tot}. \tag{6.6}$$

Here, the normalisation by $M_{\rm tot}$ removes the dependence on total galaxy flux or size. In equation 6.6, $f_{\rm tot}$ is the total flux contained within the segmentation map, and the f_i are the individual pixel fluxes, ordered such that i=1 is the brightest pixel. Combining equations 6.5 and 6.6, we see that M_{20} returns negative values, where a less negative M_{20} indicates a larger second-order moment, and therefore a distribution of the brightest flux further from the center of the galaxy (and visa-versa). Having been measured for the intrinsic maps, these fluxes and morphological parameters are compared to those measured in the SKA-simulated images for our entire sample in Section 6.4.4.

6.4.3 Detected sources in the simulated images

We will now discuss our simulated continuum survey tiers. In Fig. 6.11, we show 450"×150" regions of our simulated sky (a little less than one quarter of our total simulated area), for each of the three band 2 survey tiers (RMS levels 0.05 μJy/beam, 0.2 μJy/beam and 1 μJy/beam for the ultradeep to wide tiers respectively). We see that the brightest galaxies are already visible in the wide tier, distributed around the edges of the image, for this cutout. As we move to the deep and ultradeep tiers, we see that increasing numbers of galaxies become visible. In addition to this, increasing amounts of structure are revealed, in the distribution of the star-formation within the galaxies. The galaxy detection rates in these tiers, the measured output fluxes, and the morphological parameters that can be recovered in these tiers are quantified in the following sections.

In order to inspect these images in more detail, we also show simulated cutouts of our individual example galaxies alongside their model distributions in Fig. 6.9, in the ultradeep, deep, and wide tiers. We again see that the galaxies become more pronounced with increasing survey depth, as expected. The internal, sometimes clumpy distribution of the star-formation, in galaxy ID 11925 for example, is revealed most clearly in the deep and ultradeep tiers. Interestingly, although bright galaxy 20617 is evidently visible in the wide tier, increasing amounts of emission towards the outskirts of the galaxy are revealed with increasing survey depth. Further examples of galaxies seen in our simulated survey tiers, covering a variety of galaxy morphologies and flux densities, can be found in Fig. C.1.

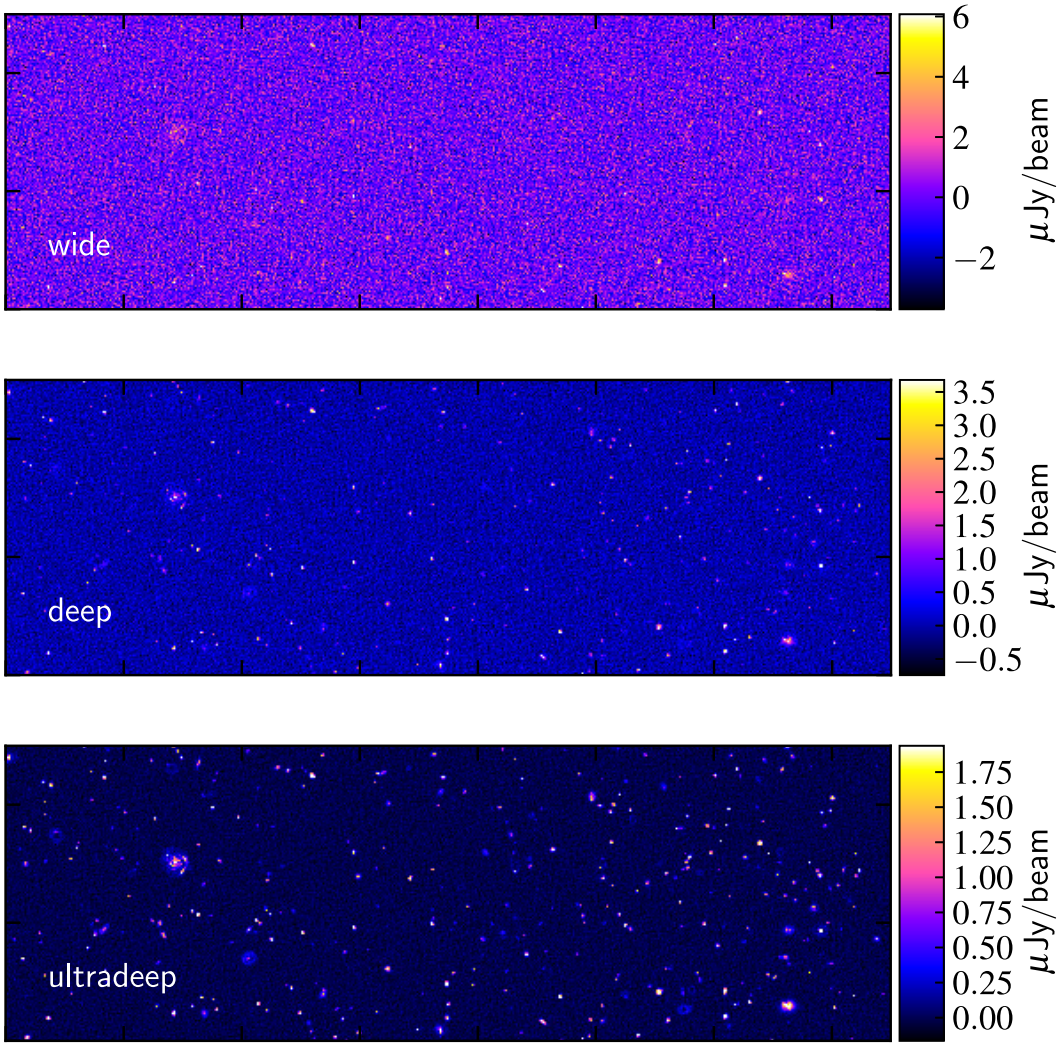

Figure 6.11: Comparison of different SKA survey tiers. The wide, deep and ultradeep tiers are shown in the top, center and lower panels respectively. The same 450"×150" position on the sky is shown for all three tiers.

In order to perform quantitative tests on our recoverable parameters, we need to create output segmentation maps over which to perform the analysis. To do this, we use 'SExtractor', a source extraction software (Bertin & Arnouts, 1996). The primary parameters that SExtractor requires in order to perform extraction (and therefore create segmentation maps) are the threshold SNR of the detection over a given number of pixels, the filtering to be applied (if any), and the flux contrast at which neighbouring sources/pixels should be considered as different sources. We vary the detection threshold between 2-4σ (σ being the RMS of the simulated image) over a minimum of 1-5 pixels, with a contrast threshold between 5-20%, whilst applying a resolution-matched (optimal) Gaussian filter of FWHM=0.6". We verify that the variation of these parameters does not significantly affect the number of our input sources that are detected, nor their recovered radio fluxes. We therefore adopt a detection threshold of 2σ, a minimum number of pixels at this threshold of 5, and a deblending contrast of 20%. This balance of parameters was chosen in order to extract the most representative segmentation maps (i.e. they do not truncate at very small distances from the centers of the galaxies), whilst maintaining conservative fragmenting of the segmentation maps (particularly relevant for our most irregular, low-redshift structures). Although we find that the number of detected input galaxies is not highly sensitive to these parameters, we do see that the overall number of (spurious) sources detected by SExtractor increases with decreasing SNR threshold, number of pixels, and deblending contrast, as expected.

Having performed source extraction on each of the tiers, we match the extracted SExtractor catalogues with our input catalog. We take the radio flux centroid position as the centers of the galaxies. For each of our input galaxies, we take the closest SExtracted source as a match, on the condition that the two central positions must lie within a matching radius of 0.6". We find that increasing this radius up to 1" does not significantly affect the number of matched galaxies. We also consider a matching radius of 0.6" as a reasonable limit, as the FWHM=0.6" synthesised beam used in imaging may have induced small shifts in the flux centroid position. We are therefore performing our output detection using the positional prior knowledge gained from large multiwavelength datasets, rather than a blind survey approach. Following this, our detection algorithm is not optimised towards minimising the number of spurious detections, as these are disregarded in our subsequent analysis. We find 691, 1257 and 1351 matches in the wide, deep and ultradeep tiers respectively, corresponding to detection percentages of 43%, 78% and 84%. As discussed in Section 6.3.2, we do not expect to detect our entire sample in each tier. Using the minimum detectable SFRs as a function of redshift for each tier, as shown in Fig. 6.9, we can compare our detection rate with the expected values for point-like sources with the same SFRs as our sample. Taking a detection SNR of 2σ in this case, we calculate expected detection fractions

of 75%, 97%, and 99% for the wide, deep and ultradeep tiers, respectively. However, we caution against a stringent comparison between these expected and recovered detection rates. The analysis shown in Fig. 6.9 is based on the total source SFR, as opposed to the surface brightness detection approach that SExtractor employs. The 2σ pixel threshold set in SExtractor therefore does not map directly to the SNR=2 in our minimum detectable SFR analysis. The galaxies that are missed in these tiers demonstrate the importance of performing a range of studies in preparation for the SKA, such as the optimisation of galaxy detection in large surveys. As a particularly large number of galaxies are missed in the wide tier, this may be highlighting the importance of survey depth, once the substructure of a galaxy starts being extended and resolved, rather than appearing point-like. This line of investigation would be a valuable study in itself, but we do not pursue this work in this chapter.

6.4.4 Survey tier parameter measurements

Finally, we discuss the recoverability of parameters in the SKA1-MID band 2 planned surveys, using our simulated maps. We calculate the output flux, M_{20} and Gini parameter for all detected galaxies in each tier, within the segmentation maps defined by the SExtractor output. We show the results of these calculations, compared to the intrinsic/input parameters, in Fig. 6.12.

We begin by looking at the flux recoverability in the top row of Fig. 6.12. We see that in all three tiers, there is a clear positive correlation between input flux and output flux. We have marked the location of total flux SNR_{out}=5 for reference, but we remind the reader that this definition of SNR (total output flux/image RMS) does not take into account the fact that the galaxies are not necessarily point sources within the SKA beam (a flux SNR=2 over a minimum of 5 pixels was the adopted SExtractor detection method). Despite the correlation between input and output fluxes, we do however see that the measured fluxes are being systematically underestimated in the simulated images, rather than scattering evenly around the 1:1 relation. In each tier, we divide the data into bins of equal galaxy number, and calculate the median value and standard deviation of each bin, shown by the black circles. To this data, we fit a curve of the form $y = ax^b + c$, with the constraint that the fit must asymptote towards the 1:1 relation at the high flux end. In the ultradeep tier, this trend confirms a tight, near-linear correlation between input and output flux, with good agreement between the two values even in the lowest flux bin. At 1.2μJy input flux (corresponding to the first flux bin), the output fluxes lie $\sim$0.1 dex below the input values, and this underestimation decreases with increasing flux. In the deep and wide tiers, we see a more pronounced departure from a linear slope towards low flux densities, and an increased scatter around the best-fitting trend. In the deep tier, the best-fitting trend lies 0.25 dex below the 1:1 relation at the flux of the lowest bin (input

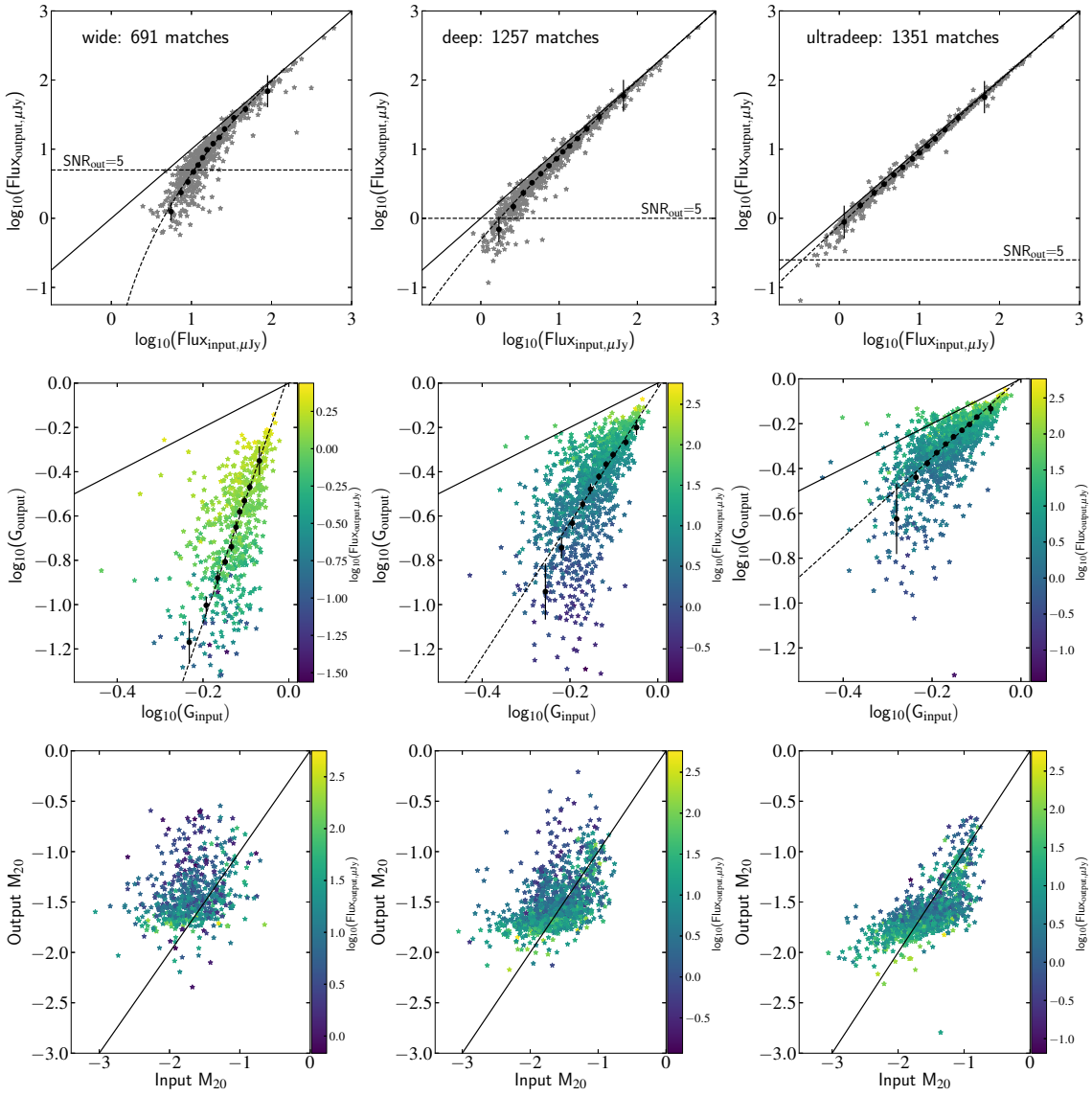

Figure 6.12: Comparison of input and output parameters for our SKA1-MID band 2 simulations. Fluxes are the pixel sums within the input/output segmentation maps, respectively. The survey tier and number of input galaxies successfully detected in the simulated image (from a total of 1613 galaxies), is indicated for each column in the first row. In the first two rows, the black circles show median binned values, where the errorbar shows the standard deviation within the bin. The dashed black lines show the fits to these data. We have marked the location of total flux SNR$_{\rm out}$=5 (for a point source) in the top panel, simply for reference. In the center and lower rows, the individual datapoints are coloured by recovered $\log_{10}(\mathrm{Flux}_{\rm output})$. The solid black lines show the 1:1 relation.

1.7μJy), whereas the wide tier is underestimating the input fluxes by 0.6 dex at the low flux end (input 5μJy). A possible explanation for the systematic underestimation in flux is that the output segmentation maps do not cover the full extent of the input SFR distribution, and may thus miss extended regions of low surface brightness. As several of our galaxies have lower star-formation rates in their outskirts than in their centers (see e.g. Fig. 6.9), it's plausible that the pixel values may fall below the SExtractor detection threshold in these regions.

We next examine the measured Gini parameters - an indication of the galaxy's brightness concentration - in the center row of Fig. 6.12. It's important to note here that although we show the 1:1 relationship for reference, we would not expect to recover the same values for parameters such as G in two images at different pixel scales and resolutions. Instead, we need to quantify how accurately an output Gini parameter can be mapped to an input or intrinsic G, in each of the survey tiers. Again, we see a positive correlation between input and output Gini parameters in each tier of the survey. This is an important observation, as it tells us that although the numerical values of G have changed, we have not lost the ability to assess the relative concentration of galaxies in the simulated/observed image. In order to quantify the recoverability of G, we once again bin the data into bins of equal galaxy number. Using the median bin values and standard deviations, we fit a linear relation to each of the three tiers, shown by the black dashed lines. We find that the slope of the fit becomes steeper with decreasing survey depth, namely 1.8, 3.0 and 5.6 in the ultradeep, deep and wide tiers respectively. This indicates that an increasingly large range of output Gini parameters are mapped to a narrow range of inputs, with decreasing depth. When we measure the 1σ scatter around these relations, we find that the scatter increases with decreasing survey depth, at 0.12 dex, 0.18 dex and 0.28 dex for the ultradeep, deep and wide tiers respectively. As an observer, these values indicate the accuracy to which one can assess the Gini parameters of observed galaxies as a function of the different SKA survey tiers, if one is carrying out a morphological study. We also see in Fig. 6.12 that the output measured values of G are systematically lower than the input values. This is most likely due to the 'smoothing' of the intrinsic maps, by the FWHM=0.6" of the synthesised beam. This convolution has the effect of distributing the flux more evenly over the pixels within the beam, and therefore lowering the output Gini parameter. It is this smoothing effect that leads to a deviation from the 1:1 slope, with the extent of the deviation changing as a function of survey depth. We also see additional effects in these panels when we examine the total output flux of the galaxies. The first is that the galaxies with the highest output fluxes are those with the highest Gini parameters (most concentrated flux), and it is these galaxies that also lie closest to the 1:1 Gini relation in all three tiers. The second observation is particularly visible in the deep and ultradeep tiers, where galaxies with the lowest output fluxes can be seen to fall

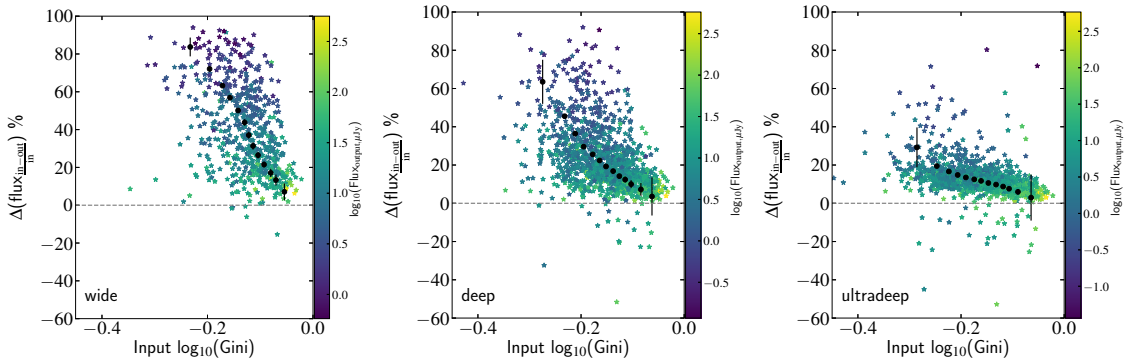

Figure 6.13: Δ(flux) vs. input Gini parameter for each of our simulated tiers. The data has been binned into bins of equal galaxy number, shown by the black circles, where the errorbars represent the standard deviation in each bin. The individual datapoints are coloured by their recovered $\log_{10}(\mathrm{Flux}_{\mathrm{output}})$. The grey dashed line is placed at Δ(flux)=0.

vertically below the best-fitting relations, towards lower Gini parameters.

Finally, we discuss the output M_{20} values from our simulated images. We find very different behaviour for M_{20} than the fluxes and Gini parameters. As can be seen in the bottom row of Fig. 6.12, the output M_{20} parameters are scattered around the 1:1 relation. However, we do not see a correlation between input and output M_{20} values. We see a somewhat flat relationship between input and recovered M_{20}, particularly for the most negative input values (where a more negative M_{20} indicates a distribution of flux closer the the centre of the galaxy). This flat relation means that unlike the Gini parameter, it is not possible to map an output M_{20} value to an intrinsic parameter using the simulated SKA data. For those studies interested in the distribution of the brightest star-forming regions of a galaxy, the measured M_{20} parameters for these observations therefore do not appear to be meaningful. Interestingly, we see that the galaxies with the highest output fluxes give rise to the lowest output M_{20} values, indicating more centrally distributed star-formation. In fact, the output M_{20} values appear to have a lower bound of approximately -1.8 in all tiers, which is not present in the input data. This lower limit on M_{20} most likely arises as a result of the lower image resolution, compared with the input image. This may be primarily driven by the smoothing effect of the synthesised beam, or as a result of the increase in pixel angular scale, or a combination of both. This degradation of the input resolution may therefore be imposing a limit on the minimum distance from the core that can be distinguished, which would give rise to a corresponding limit on M_{20}.

Moving beyond these input-output analyses, we finish this section by examining the cross-correlation between recovered flux and input Gini parameter. We see in Fig. 6.12 that the measured output fluxes approach the input fluxes with increasing output flux. We also see evidence that

the galaxies with the highest output fluxes have the highest input (and output) Gini parameters. We therefore investigate the connection between the percentage of total flux that is recovered and the intrinsic Gini parameter of a galaxy's flux distribution, in Fig. 6.13. When we bin the data to highlight this correlation, we see a decrease in Δflux (input-output) with increasing Gini parameter. This is visible in each tier of the survey. Fig. 6.13 therefore demonstrates that fluxes are more accurately recovered for galaxies with concentrated regions of flux, rather than diffuse, low surface brightness emission distributed more evenly over a galaxy. This is an important consideration for studies aiming to measure total star-formation rates using high-resolution SKA1-MID data, the accuracy of which may vary as a function of galaxy concentration (including bright off-center knots, to which G is also sensitive).

6.5 Summary

In preparation for the SKA, we are quantifying the avenues that will be explored by the SKA tiered continuum surveys, and performing simulations to characterise the ability of SKA1-MID to accurately measure physical parameters of its detected galaxies. We calculate the minimum SFRs that can be detected by each of the band 2 survey tiers, and relate these SFRs to the Main Sequence of star-formation as a function of redshift. We find that the ultradeep, deep and wide survey tiers will be MS complete between $\log_{10}(M_\star)<$7.3-8.5 at z=0.1, rising to $\log_{10}(M_\star)<$9.0-10.3 at z=3. Next, we create simulated continuum images of an entire survey field as seen by SKA1-MID, in each of the different tiers. To do this, we select previously observed galaxies at $0<z<3$ in the GOODS-North field, spanning a range of morphologies and SFRs. We create spatially resolved maps of continuum radio emission within the galaxies, using resolved images of their star-formation distributions that were constructed using previous MWL SED analysis. These images are input into our SKA simulation pipeline, representing the intrinsic distribution of star-formation over the GOODS-North field. Our pipeline convolves these images with the anticipated response of SKA1-MID, taking into account factors such as antenna configuration, correlator setup and survey depth. In this way, we create simulated images of resolved SFR distributions as observed in each of the band 2 reference surveys, on which to perform further analysis.

In this chapter, we begin investigations to quantify the recoverability of key galaxy parameters, namely the total radio flux, and morphological parameters M_{20} and Gini. We perform source extraction on our simulated images, in order to compare the output parameters with those intrinsic parameters measured before simulation. We find that the total flux is recovered with increasing accuracy as a function of survey depth, and define the degree of intrinsic flux underestimation as a function of input flux for each survey, reaching 0.1 dex and 0.6 dex in the ultradeep and

wide tiers respectively. We find a clear correlation between input and output Gini parameters, with the scatter on the output G increasing from 0.12 dex to 0.28 dex as we move from the ultradeep to the wide tier. On the other hand, we see that M_{20} (measuring the distribution of the brightest regions of the galaxies), is not well recovered in our output images, with a lower limit on the measurable M_{20} being introduced due to the degradation of the output angular resolution. Finally, we demonstrate that total fluxes are most accurately recovered for galaxies with relatively concentrated flux distributions, which are detected at the highest SNRs in our simulated survey tiers.

Building on these results, we can continue to explore further means of quantifying galaxy morphology, and the reliability of such properties as a function of survey depth. Producing simulated images, here for the first time using real resolved distributions of star-formation, is a tool that can be adopted for a range of applications within the SKA community. The work in this chapter lays the foundations for future research that moves beyond ranking galaxies by their morphological parameters, to measuring the reliability of full morphological classification using SKA continuum survey data. This topic will be pursued in a future work.

Contributions

Anna Cibinel provided catalogues, HST images and resolved SFR maps of galaxies in the GOODS-North field, as described in Sections 6.3.1 and 6.3.2. The catalogue included the galaxy RA and Dec positions, redshifts, and stellar masses. Robert Braun and Anna Bonaldi provided their framework for simulating the response of SKA1-MID (Appendix D).

Chapter 7

Conclusions and future work

In this chapter, I summarise the main findings of this thesis, and outline the future research that has arisen from this work.

7.1 The galaxy population of Cl J1449+0856 - a significant star-formation overdensity alongside a quenched population

In Chapter 2, I introduce a high-redshift, mature galaxy cluster, Cl J1449+0856. Cl J1449+0856 is a particularly good case for the study of the environmental effect on galaxy evolution, as it emits signatures of diffuse X-ray emission from the ICM, indicating a virialised cluster atmosphere at this early cosmic time. Recently, Gobat et al. (2019) used 92 GHz ALMA and ACA data to search for signatures of SZ emission from the cluster ICM, and find a significant detection, giving further evidence of a warm, energetic ICM. As highlighted by previous studies such as Gobat et al. (2013); Strazzullo et al. (2013), the galaxy population in the core of Cl J1449+0856 is extremely varied, containing both blue star-forming galaxies and dusty red star-forming galaxies, as well as a population of galaxies that is already massive and quenched. The work presented in Chapter 3, published in Strazzullo et al. (2018), goes on to study the galaxy population of Cl J1449+0856 using submillimeter ALMA 870μm and CO[4-3] observations to trace the star-formation density in the cluster core. We find a 10σ overdensity of 870μm emitters in the cluster core, compared to expected number counts from field studies such as Oteo et al. (2016). We calculate star-formation rates for the cluster members using both the 870μm and CO[4-3] data, and find that the two tracers give consistent results. We calculate a projected SFR density of $\sim(0.9\pm0.1)\times10^4$ $M_\odot yr^{-1}$, which corresponds to a SFR volume overdensity of five orders of magnitude compared to the field at z=2. Finally, we combine previous HST observations with the ALMA data, in order to explore in detail the Brightest Cluster Galaxy, which is still in the process of assembling. This reveals that the

forming BCG in Cl J1449+0856 is in a particularly interesting evolutionary stage, as a population of red passive, galaxies are interacting and merging with highly star-forming, dust-obscured galaxies, which are almost hidden in the HST imaging.

7.2 The environmental effect on galaxy evolution in Cl J1449+0856 at z=1.99

In Chapter 4 (Coogan et al., 2018), we use multiwavelength data, particularly at submillimeter-radio wavelengths, to study the environmental effect on the ISM of galaxies in cluster Cl J1449+0856 at z=1.99. We study the continuum at 870μm, 2mm, 3mm, 7mm and 10cm, as well as multiple transitions of CO, to study the molecular gas and dust content of galaxies in the core of the cluster. We find CO[4-3] detections in eight cluster members, which directly traces the denser, star-forming phase of the molecular gas. When we compare these CO[4-3] detections with rest-frame optical HST data, we see that a significant fraction of our sample (5/8 galaxies) are in merging or interacting systems, with a further galaxy hosting an AGN. We construct CO spectral line energy distributions, and find that 50% of the sample show evidence for highly-excited, starburst-like molecular gas - a significantly higher fraction than found in the field at z=2 (Rodighiero et al., 2011; Sargent et al., 2012). We derive star-formation rates using UV to radio wavelengths, and place our galaxies on the Kennicutt-Schmidt relation, in order to assess their SFEs. We find a significant ($\sim$0.4 dex) increase in the SFEs of our cluster galaxies compared to the MS locus, seen both via the observable L'_{CO1-0}, and also when a conversion factor is used to derive molecular gas mass. Interestingly, despite this, we find no evidence for an environmental effect on the sSFRs of the galaxies. We derive α_{CO} and G/D conversion factors for a subset of our galaxy sample, using dynamical constraints, and find that they have conversion factors in keeping with a starburst-like population, consistent with their merging activity. We calculate the dust masses of the sample through continuum SED fitting, and find that the cluster galaxies have low dust-to-stellar mass ratios compared to the coeval field population, in addition to low molecular gas fractions. We calculate molecular gas depletion timescales for our sample, and find that all galaxies will deplete their gas supply in $<$100-400 Myrs, consistent with their elevated SFEs. We conclude that there are clear environmental effects influencing the ISM and thus the evolution of these galaxies, and that these effects are most likely driven by the high fraction of mergers, interactions, and AGN in the cluster core.

Outlook

There are several further projects that have arisen as a result of the work presented in Chapter 4. In Chapter 4, we discuss two galaxies in the cluster field of view (A4 and A5) that are detected very brightly at 870μm (>0.5 mJy), but are not detected in CO[4-3], CO[3-2], or CO[1-0]. We have been unable to confirm their cluster membership, as they also do not present lines in rest-frame optical spectroscopy from previous work (Gobat et al., 2013), nor in any of the broadband submillimeter datasets outlined in Section 4.2. This excludes a wide range of possible redshifts. However, the probability of these bright galaxies being independently located so close to the core of the cluster is $<10^{-5}$ (see Section 4.3.8). There are then two possible theories for these galaxies: (i) that A4 and A5 are not cluster members, and lie in the narrow redshift ranges not probed by our current data; or (ii) A4 and A5 are cluster members that have very recently quenched their star-formation. As discussed in Chapter 4, the continuum at 870μm traces star-formation on longer timescales than CO. If these galaxies have quenched their star-formation within the last $\sim$100 Myrs, we would expect to detect them in the continuum, but not in CO. To distinguish between these two possibilities, I have been awarded observations of A4 and A5 on the NOEMA interferometer spanning a wide range of frequencies, which will fill in the small gaps of our current spectral coverage. This will be pursued as a next step of the study of Cl J1449+0856.

Secondly, the ISM content of early-type galaxies is a compelling subject to further our understanding of massive galaxy evolution (e.g. Sansom et al. 2015; O'Sullivan et al. 2018), but we are currently limited by our ability to detect the residual ISM in these gas-poor systems. In Chapter 4 we detect gas and dust in ETGs and colour-passive cluster galaxies at z=2 (such as IDs 2, 3 and 6) - an exciting indication of the physics revealed through overdense environments. The residual ISM content of recently quenched galaxies at high redshift gives direct insight into the mechanism that terminated star-formation, and few direct detections currently exist. Gobat et al. (2018) find a 'surprisingly' large amount of residual dust inside field galaxies at z>1.4, providing a high-redshift field comparison for this research. As a future work, we intend to analyse the properties of these cluster ETGs using multiwavelength SED analysis to probe deeper into the stellar populations comprising these galaxies, the residual gas content, and the driving mechanisms behind rapid quenching in dense environments.

Finally, I would like to obtain higher-resolution submillimeter data in the core of Cl J1449+0856, to put tighter constraints on the size of the ISM in the cluster galaxies studied in Chapter 4. In particular, I would like to study whether the observed mergers and interactions are compacting the molecular gas, which in turn may give rise to the high gas excitations and SFEs found in these galaxies.

7.3 The ISM in low-mass, low-metallicity galaxies outside of the local Universe

In Chapter 5 (Coogan et al., 2019), we shift our focus from the large-scale environment of galaxies, to the effect of low gas-phase metallicity on their observable properties. This was made possible by the diverse variety of galaxies hosted within cluster Cl J1449+0856, where we have uncovered a population of low mass, low-metallicity galaxies at z=2. Studies of the ISM in low mass galaxies at z=2 is a sparsely characterised area of research, due to the observational difficulties in detecting such a faint population. We use rest-frame optical MOIRCS spectroscopy to derive individual and stacked gas-phase metallicities for our five galaxies, finding that they lie on the mass-metallicity relation, and are thus representative of the numerous sub-M* population at z=2 (e.g. Davidzon et al. 2017). ALMA and VLA submillimeter data are used to measure CO[4-3] and CO[1-0] line fluxes at the galaxies' known optical redshifts, as well as their dust continuum emission. However, we find no detections in either the stacked or individual data, despite an expected detection fraction of $>$60%. This demonstrates that it is not only the diffuse molecular gas that is photodisocciated in this low-metallicity environment, but also the denser phases traced through CO[4-3]. We then use our continuum emission and CO line upper limits to put constraints on the galaxies' $\alpha_{\rm CO}$ and G/D conversion factors. We quantify the importance of comparing ISM scaling relations on a normalised metallicity scale, and place our galaxies on a compilation of ISM-metallicity relations calibrated in the local Universe. We find no evidence that the $\alpha_{\rm CO}$-metallicity relation evolves with redshift, but our lower limit on the sample-stacked G/D suggests an increase in G/D ratios for low-metallicity galaxies at z=2, compared with the local Universe. Finally, we quantify the relative contributions of sub-M* and M* galaxies to the comoving molecular gas density at z=2, and find that M* galaxies are the dominant population in this regard. However, we highlight that the relative contributions from sub-M* and M* galaxies are significantly shifted, compared to their contributions to the stellar mass density at z=2.

Outlook

In order to progress this research, by deepening the constraints on $\alpha_{\rm CO}$, G/D ratio and CO luminosity presented in Chapter 5, we require deeper data on this submillimeter-faint population at z=2, for which I have proposed. As shown in Chapter 5, accurate conversion factors are crucial in order to derive molecular gas masses for the sub-M* population at z=2. I believe that this will become an increasingly important area of research, as observational facilities continue to expand.

7.4 The power of the SKA to resolve star-formation activity in large surveys

In Chapter 6, we begin to explore the future capabilities of the Square Kilometer Array, specifically through the planned continuum reference surveys. The SKA will be a key instrument for studying a number of areas of galaxy evolution, but one topic it will particularly advance is the detection and resolution of high-redshift radio continuum emission, such as from star-forming galaxies and AGN in forming (proto)clusters. We investigate the SFR detection limits for the wide, deep and ultradeep SKA1-MID band 2 continuum surveys (RMS 1μJy/beam, 0.2μJy/beam and 0.05μJy/beam respectively), using the limiting cases of derived radio flux at high redshift. We find that the SKA band 2 ultradeep tier will probe down to 5σ SFRs of $\sim$1-4 $M_{\odot}yr^{-1}$ at z=3, with the deep and wide surveys detecting galaxies down to 5-100 $M_{\odot}yr^{-1}$ over larger areas. In terms of completeness, these surveys will detect MS-complete samples down to stellar masses of $\log_{10}(M_{\star})<$7.3-8.5 at z=0.1, rising to $\log_{10}(M_{\star})<$9.0-10.3 at z=3.

Starting from resolved maps of star-formation, we construct resolved radio frequency images for a diverse sample of galaxies at $0<z<3$ in the GOODS-North field. Intrinsic parameters (total radio flux, Gini coefficient and M_{20}) are derived for each of these galaxies, in order to assess the recoverability of such properties through SKA1-MID observations. We then use our radio images to create, for the first time, resolved simulated images of the continuum sky as seen by SKA1-MID, in each of the planned band 2 survey tiers. We compare our simulations with the SKA Science Data Challenge #1, and demonstrate that the two sets of simulations contain complementary samples of input galaxies, in terms of their SFR distributions. Having performed source extraction in each of the simulated tiers, output parameters were calculated for each galaxy within the SExtractor-defined segmentation maps. We quantify trends between input vs. output total radio flux and morphological parameters, in order to assess the correlations as a function of survey tier. We find that both flux and Gini parameter can be recovered from the SKA-simulated images, with increasing scatter in the shallower tiers. Additionally, examining the relationship between radio flux and Gini parameter reveals that the output fluxes are most reliable for galaxies with concentrated distributions of flux (and therefore star-formation), at all survey depths. However, we find that M_{20} is not well recovered at the resolution of our simulated observations, reinforcing the importance of carrying out such studies in preparation for the SKA.

Outlook

There is a wide variety of research that can be pursued using simulated SKA images, such as those we have produced in Chapter 6. In terms of the study of galaxy morphologies, our first results suggest that some parameters measured from SKA1-MID data give more physically meaningful results than others. We therefore plan to extend our current analysis to galaxy properties such as size, brightness profile, central concentration and ellipticity, in order to assess the ability of the SKA to carry out detailed morphological classification as a function of redshift, SFR and observation depth.

There is also significant scope to perform additional simulations, for example in different frequency bands. Moving to SKA band 5b ($\sim$10 GHz) would be accompanied by an increase in angular resolution, and it may be revealing to compare the results found in Chapter 6 with similar analyses at different parts of the radio SED. Lastly, our work looking at purely star-forming galaxies could be further extended by combining observations of real galaxies (as we have done in Chapter 6) with simulated components (see e.g. Bonaldi et al. 2019). This could involve the inclusion of an AGN component, for example, as it would be highly relevant to investigate whether nuclear AGN emission can be spatially resolved from star-forming regions with the SKA. We hope that simulations such as these will provide valuable information to the community, and demonstrate the merits of thorough preparation as we approach the era of the SKA.

Bibliography

Abadi M. G., Moore B., Bower R. G., 1999, MNRAS, 308, 947 22

Abramson L. E., Kelson D. D., Dressler A., Poggianti B., Gladders M. D., Oemler Jr. A., Vulcani B., 2014, ApJL, 785, L36 10

Accurso G., et al., 2017, MNRAS, 470, 4750 130

Adam R., et al., 2017, AAP, 598, A115 21

Afonso J., Casanellas J., Prandoni I., Jarvis M., Lorenzoni S., Magliocchetti M., Seymour N., 2015, Advancing Astrophysics with the Square Kilometre Array (AASKA14), p. 71 141

Aguilar L. A., White S. D. M., 1985, ApJ, 295, 374 56

Aird J., et al., 2010, MNRAS, 401, 2531 5

Alavi A., et al., 2016, ApJ, 832, 56 43

Alberts S., et al., 2014, MNRAS, 437, 437 44

Alberts S., et al., 2016, ApJ, 825, 72 19, 34, 44, 102

Allen D. A., 1976, MNRAS, 174, 29P 7

Allen S. W., Schmidt R. W., Fabian A. C., 2002, MNRAS, 334, L11 20

Allen S. W., Schmidt R. W., Ebeling H., Fabian A. C., van Speybroeck L., 2004, MNRAS, 353, 457 21

Allen S. W., Evrard A. E., Mantz A. B., 2011, ARAA, 49, 409 20

Amorín R., Muñoz-Tuñón C., Aguerri J. A. L., Planesas P., 2016, AAP, 588, A23 112, 127, 130

Andreon S., 2006, AAP, 448, 447 34

Andreon S., Puddu E., de Propris R., Cuillandre J.-C., 2008, MNRAS, 385, 979 21

Andreon S., Maughan B., Trinchieri G., Kurk J., 2009, AAP, 507, 147 34

Andreon S., Newman A. B., Trinchieri G., Raichoor A., Ellis R. S., Treu T., 2014, AAP, 565, A120 35

Andreon S., Dong H., Raichoor A., 2016, AAP, 593, A2 35

Ao Y., Weiß A., Downes D., Walter F., Henkel C., Menten K. M., 2008, AAP, 491, 747 12

Aravena M., et al., 2010, ApJ, 718, 177 12, 111

Aravena M., et al., 2012, MNRAS, 426, 258 19, 35

Aravena M., et al., 2016a, MNRAS, 457, 4406 11, 90

Aravena M., et al., 2016b, ApJ, 833, 68 5

Arimoto N., Sofue Y., Tsujimoto T., 1996, PASJ, 48, 275 132

Armus L., Heckman T., Miley G., 1987, AJ, 94, 831 9

Arnouts S., Cristiani S., Moscardini L., Matarrese S., Lucchin F., Fontana A., Giallongo E., 1999, MNRAS, 310, 540 155

Asplund M., Grevesse N., Sauval A. J., Scott P., 2009, ARAA, 47, 481 130

Baldry I. K., Glazebrook K., Brinkmann J., Ivezić Ž., Lupton R. H., Nichol R. C., Szalay A. S., 2004, ApJ, 600, 681 2

Baldry I. K., Balogh M. L., Bower R. G., Glazebrook K., Nichol R. C., Bamford S. P., Budavari T., 2006, MNRAS, 373, 469 2

Baldwin J. A., Phillips M. M., Terlevich R., 1981, PASP, 93, 5 119

Barnes D. J., et al., 2017, MNRAS, 471, 1088 25

Battye R. A., Weller J., 2003, PRD, 68, 083506 20

Bauer A., Springel V., Vogelsberger M., Genel S., Torrey P., Sijacki D., Nelson D., Hernquist L., 2015, MNRAS, 453, 3593 25

Bauermeister A., et al., 2013, ApJ, 768, 132 88, 101

Baugh C. M., Cole S., Frenk C. S., 1996, MNRAS, 283, 1361 19

Begelman M. C., Blandford R. D., Rees M. J., 1984, Reviews of Modern Physics, 56, 255 1

Behroozi P. S., Wechsler R. H., Conroy C., 2013, ApJ, 770, 57 4

Beifiori A., et al., 2017, ApJ, 846, 120 35

Belfiore F., et al., 2015, MNRAS, 449, 867 112

Bell E. F., 2003, ApJ, 586, 794 5, 147, 148

Bell E. F., McIntosh D. H., Katz N., Weinberg M. D., 2003, ApJS, 149, 289 4

Bell E. F., et al., 2004, ApJ, 608, 752 2

Bell E. F., et al., 2005, ApJ, 625, 23 156

Bellstedt S., et al., 2016, MNRAS, 460, 2862 19

Berezhko E. G., Völk H. J., 2004, AAP, 427, 525 145

Berta S., Lutz D., Genzel R., Förster-Schreiber N. M., Tacconi L. J., 2016, AAP, 587, A73 11

Bertin E., Arnouts S., 1996, AAPS, 117, 393 168

Béthermin M., et al., 2012, ApJL, 757, L23 40

Béthermin M., et al., 2015, AAP, 573, A113 6, 11, 15, 86, 87, 92, 93, 98, 105, 106, 124

Bhowmick A. K., Campbell D., Di Matteo T., Feng Y., 2018, MNRAS, 480, 3177 25

Blake C. A., Abdalla F. B., Bridle S. L., Rawlings S., 2004, New Astron. Rev., 48, 1063 11, 24, 141

Bleem L. E., et al., 2015, ApJS, 216, 27 34

Böhringer H., et al., 2000, ApJS, 129, 435 21

Böhringer H., et al., 2007, AAP, 469, 363 21

Bolatto A. D., Leroy A. K., Rosolowsky E., Walter F., Blitz L., 2008, ApJ, 686, 948 129, 132

Bolatto A. D., Wolfire M., Leroy A. K., 2013, ARAA, 51, 207 13, 15, 56

Bolzonella M., Miralles J.-M., Pelló R., 2000, AAP, 363, 476 3

Bonaldi A., Harrison I., Camera S., Brown M. L., 2016, MNRAS, 463, 3686 143

Bonaldi A., Bonato M., Galluzzi V., Harrison I., Massardi M., Kay S., De Zotti G., Brown M. L., 2019, MNRAS, 482, 2 142, 143, 164, 180

Bonaventura N. R., et al., 2017, MNRAS, 469, 1259 51

Borgani S., Rosati P., Tozzi P., Norman C., 1999, ApJ, 517, 40 20

Borgani S., et al., 2004, MNRAS, 348, 1078 21

Boselli A., Gavazzi G., 2006, PASP, 118, 517 22

Boselli A., Lequeux J., Gavazzi G., 2002, AAP, 384, 33 11, 12

Bothwell M. S., et al., 2013, MNRAS, 429, 3047 41

Bouché N., et al., 2007, ApJ, 671, 303 17

Bournaud F., Daddi E., Weiß A., Renaud F., Mastropietro C., Teyssier R., 2015, AAP, 575, A56 12, 15

Bourne N., et al., 2013, MNRAS, 436, 479 112, 133

Bouwens R. J., et al., 2012a, ApJL, 752, L5 4

Bouwens R. J., et al., 2012b, ApJ, 754, 83 8

Boyle B. J., Terlevich R. J., 1998, MNRAS, 293, L49 5

Brammer G. B., van Dokkum P. G., Coppi P., 2008, ApJ, 686, 1503 3, 154

Braun R., Bourke T., Green J. A., Keane E., Wagg J., 2015, Advancing Astrophysics with the Square Kilometre Array (AASKA14), p. 174 11, 24, 141

Bridge C. R., et al., 2007, ApJ, 659, 931 9

Brinchmann J., Charlot S., White S. D. M., Tremonti C., Kauffmann G., Heckman T., Brinkmann J., 2004, MNRAS, 351, 1151 8

Brodwin M., et al., 2011, ApJ, 732, 33 102

Brodwin M., et al., 2013, ApJ, 779, 138 34, 55

Bruzual G., Charlot S., 2003, MNRAS, 344, 1000 45

Bryant P. M., Scoville N. Z., 1999, AJ, 117, 2632 11, 13

Burgarella D., Buat V., Iglesias-Páramo J., 2005, MNRAS, 360, 1413 3

Burstein D., Heiles C., 1982, AJ, 87, 1165 112

Butcher H. R., Oemler Jr. A., 1984, Nature, 310, 31 19

Cai Z., et al., 2017, ApJ, 839, 131 20, 34

Calistro Rivera G., et al., 2017, MNRAS, 469, 3468 147

Calzetti D., 2008, in Knapen J. H., Mahoney T. J., Vazdekis A., eds, Astronomical Society of the Pacific Conference Series Vol. 390, Pathways Through an Eclectic Universe. p. 121 (arXiv:0707.0467) 5, 128

Calzetti D., Armus L., Bohlin R. C., Kinney A. L., Koornneef J., Storchi-Bergmann T., 2000, ApJ, 533, 682 6, 7, 45, 118

Camilo F., et al., 2018, ApJ, 856, 180 142

Cao C., et al., 2016, ApJS, 222, 16 9

Capasso R., et al., 2019, MNRAS, 482, 1043 21

Carilli C. L., Rawlings S., 2004, New Astronomy Reviews, 48, 979 141

Carilli C. L., Walter F., 2013, ARAA, 51, 105 11, 12, 15, 128

Carilli C. L., Gnedin N., Furlanetto S., Owen F., 2004, New Astron. Rev., 48, 1053 141

Carnall A. C., McLure R. J., Dunlop J. S., Davé R., 2018, MNRAS, 480, 4379 3

Casasola V., Magrini L., Combes F., Mignano A., Sani E., Paladino R., Fontani F., 2013, AAP, 558, A60 35

Casey C. M., 2012, MNRAS, 425, 3094 3, 6

Casey C. M., 2016, ApJ, 824, 36 35

Casey C. M., Narayanan D., Cooray A., 2014, Phys. Rep., 541, 45 98

Casey C. M., et al., 2015, ApJL, 808, L33 20, 34

Castignani G., Chiaberge M., Celotti A., Norman C., 2014, ApJ, 792, 113 20

Chabrier G., 2003, PASP, 115, 763 6, 16, 58, 113, 144

Chan J. C. C., et al., 2018, ApJ, 856, 8 35

Charlot S., Fall S. M., 2000, ApJ, 539, 718 6

Chiosi C., Carraro G., 2002, MNRAS, 335, 335 3

Cibinel A., et al., 2015, ApJ, 805, 181 155

Cibinel A., et al., 2019, MNRAS, 485, 5631 9, 154, 155, 156, 164

Ciesla L., Elbaz D., Fensch J., 2017, AAP, 608, A41 5

Ciesla L., Elbaz D., Schreiber C., Daddi E., Wang T., 2018, AAP, 615, A61 3

Clements D. L., et al., 2014, MNRAS, 439, 1193 20, 34, 43

Clerc N., et al., 2014, MNRAS, 444, 2723 21

Cole S., Lacey C. G., Baugh C. M., Frenk C. S., 2000, MNRAS, 319, 168 25

Collins C. A., et al., 2009, Nature, 458, 603 19

Combes F., et al., 2012, AAP, 538, L4 12

Compiègne M., et al., 2011, AAP, 525, A103 11

Condon J. J., 1992, ARAA, 30, 575 xii, 7, 86, 145, 146, 148

Condon J. J., 1997, PASP, 109, 166 78

Condon J. J., Anderson M. L., Helou G., 1991, ApJ, 376, 95 86

Condon J. J., et al., 2012, ApJ, 758, 23 158

Conselice C. J., Blackburne J. A., Papovich C., 2005, ApJ, 620, 564 4

Coogan R. T., et al., 2018, MNRAS ii, 19, 28, 29, 32, 36, 51, 53, 54, 113, 114, 115, 118, 176

Coogan R. T., et al., 2019, MNRAS, 485, 2092 ii, 29, 110, 178

Cooke E. A., Hatch N. A., Muldrew S. I., Rigby E. E., Kurk J. D., 2014, MNRAS, 440, 3262 35

Cooke E. A., et al., 2016, ApJ, 816, 83 35

Cooper M. C., et al., 2008, MNRAS, 383, 1058 19, 55

Coppin K. E. K., et al., 2012, MNRAS, 427, 520 12

Corbelli E., et al., 2012, AAP, 542, A32 6, 112, 133

Cormier D., et al., 2014, AAP, 564, A121 128

Cortese L., et al., 2012, AAP, 540, A52 6

Cortijo-Ferrero C., et al., 2017, MNRAS, 467, 3898 9

Cousin M., Buat V., Lagache G., Bethermin M., 2019, AAP, 627, A132 6

Cresci G., Mannucci F., Curti M., 2018, arXiv e-prints 135

Daddi E., Cimatti A., Renzini A., Fontana A., Mignoli M., Pozzetti L., Tozzi P., Zamorani G., 2004, ApJ, 617, 746 83

Daddi E., et al., 2009, ApJ, 694, 1517 4

Daddi E., et al., 2010a, ApJ, 713, 686 9, 11, 89, 90, 95, 111

Daddi E., et al., 2010b, ApJL, 714, L118 8, 11, 13, 16, 88, 92, 101, 104, 111, 133

Daddi E., et al., 2015, AAP, 577, A46 12, 14, 15, 40, 41, 67, 70, 82, 83, 86, 87, 128, 129

Daddi E., et al., 2017, ApJL, 846, L31 34, 93, 141

Dale D. A., Helou G., Contursi A., Silbermann N. A., Kolhatkar S., 2001, ApJ, 549, 215 11

Danielson A. L. R., et al., 2011, MNRAS, 410, 1687 12

Dannerbauer H., et al., 2014, AAP, 570, A55 34, 43

Dannerbauer H., et al., 2017, AAP, 608, A48 35, 57, 88

Dannerbauer H., Harrington K., Díaz-Sánchez A., Iglesias-Groth S., Rebolo R., Genova-Santos R. T., Krips M., 2019, AJ, 158, 34 15

Dasyra K. M., Yan L., Helou G., Surace J., Sajina A., Colbert J., 2008, ApJ, 680, 232 9

Davidzon I., et al., 2017, AAP, 605, A70 4, 113, 135, 136, 178

Davies J. I., et al., 2017, PASP, 129, 044102 6

Davies L. J. M., et al., 2019, MNRAS, 483, 5444 22

De Lucia G., Blaizot J., 2007, MNRAS, 375, 2 51

De Lucia G., Weinmann S., Poggianti B. M., Aragón-Salamanca A., Zaritsky D., 2012, MNRAS, 423, 1277 19

De Propris R., Stanford S. A., Eisenhardt P. R., Holden B. P., Rosati P., 2007, AJ, 133, 2209 34

Deane R., Paragi Z., Jarvis M., Coriat M., Bernardi G., Frey S., Heywood I., Kloeckner H. R., 2015, Advancing Astrophysics with the Square Kilometre Array (AASKA14), p. 151 141

Deason A. J., Belokurov V., Evans N. W., McCarthy I. G., 2012, ApJ, 748, 2 19

Decarli R., et al., 2016, ApJ, 833, 70 111, 136

Dekel A., Birnboim Y., 2006, MNRAS, 368, 2 2

Delaye L., et al., 2014, MNRAS, 441, 203 102

Delhaize J., et al., 2017, AAP, 602, A4 145, 146, 147, 148

Delvecchio I., et al., 2014, MNRAS, 439, 2736 5

Denicoló G., Terlevich R., Terlevich E., 2002, MNRAS, 330, 69 112

Di Matteo T., Springel V., Hernquist L., 2005, Nature, 433, 604 25

Dicke R. H., Peebles P. J. E., Roll P. G., Wilkinson D. T., 1965, ApJ, 142, 414 21

Domínguez Sánchez H., et al., 2012, MNRAS, 426, 330 5

Donas J., Deharveng J. M., 1984, AAP, 140, 325 5

Downes D., Solomon P. M., 1998, ApJ, 507, 615 9, 13, 131

Downes D., Solomon P. M., Radford S. J. E., 1993, ApJL, 414, L13 13

Draine B. T., 2003, ARAA, 41, 241 6

Draine B. T., Li A., 2007, ApJ, 657, 810 6, 11, 93, 124, 129, 133

Draine B. T., et al., 2007, ApJ, 663, 866 112

Dressler A., 1980, ApJ, 236, 351 xii, 18

Duffy A. R., Meyer M. J., Staveley-Smith L., Bernyk M., Croton D. J., Koribalski B. S., Gerstmann D., Westerlund S., 2012, MNRAS, 426, 3385 142

Dunlop J. S., et al., 2017, MNRAS, 466, 861 5

Eales S., et al., 2012, ApJ, 761, 168 112, 133

Eisenhardt P. R. M., et al., 2008, ApJ, 684, 905 20, 34

Elbaz D., et al., 2007, AAP, 468, 33 8, 9, 19, 28, 55

Elbaz D., et al., 2011, AAP, 533, A119 8, 83

Elbaz D., et al., 2018, AAP, 616, A110 17

Ellison S. L., Mendel J. T., Scudder J. M., Patton D. R., Palmer M. J. D., 2013, MNRAS, 430, 3128 9

Emonts B. H. C., et al., 2013, MNRAS, 430, 3465 35

Erb D. K., Shapley A. E., Pettini M., Steidel C. C., Reddy N. A., Adelberger K. L., 2006, ApJ, 644, 813 119

Farouki R. T., Hoffman G. L., Salpeter E. E., 1983, ApJ, 271, 11 20

Feng Y., Di-Matteo T., Croft R. A., Bird S., Battaglia N., Wilkins S., 2016, MNRAS, 455, 2778 25

Fensch J., et al., 2017, MNRAS, 465, 1934 9

Ferrarese L., Ford H., 2005, SSR, 116, 523 1

Ferrari C., et al., 2015, Advancing Astrophysics with the Square Kilometre Array (AASKA14), p. 75 141, 143

Ferrière K. M., 2001, Reviews of Modern Physics, 73, 1031 10

Fitzpatrick E. L., 1986, AJ, 92, 1068 7

Fixsen D. J., Bennett C. L., Mather J. C., 1999, ApJ, 526, 207 41

Flores-Cacho I., et al., 2016, AAP, 585, A54 20, 34

Förster Schreiber N. M., et al., 2004, ApJ, 616, 40 3

Franco M., et al., 2018, AAP, 620, A152 5

Freundlich J., et al., 2019, AAP, 622, A105 17

Galliano F., 2018, MNRAS, 476, 1445 11

Galliano F., et al., 2011, AAP, 536, A88 133, 134

Gargiulo A., Saracco P., Longhetti M., La Barbera F., Tamburri S., 2012, MNRAS, 425, 2698 2

Garrett M. A., 2002, AAP, 384, L19 147

Geach J. E., et al., 2006, ApJ, 649, 661 44

Geach J. E., Murphy D. N. A., Bower R. G., 2011, MNRAS, 413, 3059 88, 101

Genzel R., et al., 2010, MNRAS, 407, 2091 10, 17, 111

Genzel R., et al., 2012, ApJ, 746, 69 112, 129, 132

Genzel R., et al., 2015, ApJ, 800, 20 11, 14, 57, 104, 133

Genzel R., et al., 2017, Nature, 543, 397 90

Gitti M., et al., 2015, Advancing Astrophysics with the Square Kilometre Array (AASKA14), p. 76 141

Gladders M. D., Yee H. K. C., 2005, ApJS, 157, 1 19

Gladders M. D., López-Cruz O., Yee H. K. C., Kodama T., 1998, ApJ, 501, 571 21

Glasser G., 1962, Journal of the American Statistical Association, 57, 648 165

Glover S. C. O., Mac Low M.-M., 2011, MNRAS, 412, 337 126

Gobat R., Rosati P., Strazzullo V., Rettura A., Demarco R., Nonino M., 2008, AAP, 488, 853 56

Gobat R., et al., 2011, AAP, 526, A133 27, 28, 32, 34, 35, 36, 50, 51, 56, 68, 85, 99, 113

Gobat R., et al., 2013, ApJ, 776, 9 27, 30, 35, 36, 39, 48, 49, 50, 51, 56, 67, 74, 76, 113, 115, 175, 177

Gobat R., et al., 2018, Nature Astronomy, 2, 239 48, 102, 107, 177

Gobat R., et al., 2019, AAP, 629, A104 21, 24, 29, 31, 32, 175

Godfrey L. E. H., et al., 2012, PASA, 29, 42 142

Gonzalez-Perez V., Baugh C. M., Lacey C. G., Kim J. W., 2011, MNRAS, 417, 517 19

Goto T., Yamauchi C., Fujita Y., Okamura S., Sekiguchi M., Smail I., Bernardi M., Gomez P. L., 2003, MNRAS, 346, 601 xii, 18

Grainge K., Borgani S., Colafrancesco S., Ferrari C., Scaife A., Marchegiani P., Emritte S., Weller J., 2015, Advancing Astrophysics with the Square Kilometre Array (AASKA14), p. 170 141

Granato G. L., Ragone-Figueroa C., Domínguez-Tenreiro R., Obreja A., Borgani S., De Lucia G., Murante G., 2015, MNRAS, 450, 1320 35

Grenier I. A., Casandjian J.-M., Terrier R., 2005a, Science, 307, 1292 13

Grenier I. A., Casandjian J.-M., Terrier R., 2005b, Science, 307, 1292 112

Greve T. R., et al., 2005, MNRAS, 359, 1165 9, 11

Groves B. A., et al., 2015, ApJ, 799, 96 112, 133

Guelin M., Zylka R., Mezger P. G., Haslam C. G. T., Kreysa E., Lemke R., Sievers A. W., 1993, AAP, 279, L37 11, 112, 133

Gullberg B., et al., 2016, AAP, 591, A73 35

Gunn J. E., Gott III J. R., 1972, ApJ, 176, 1 56

Guo Q., White S., Li C., Boylan-Kolchin M., 2010, MNRAS, 404, 1111 4

Guo Y., et al., 2013, ApJS, 207, 24 45, 91

Gutcke T. A., Fanidakis N., Macciò A. V., Lacey C., 2015, MNRAS, 451, 3759 25

Hahn O., Martizzi D., Wu H.-Y., Evrard A. E., Teyssier R., Wechsler R. H., 2017, MNRAS, 470, 166 25

Hatch N. A., Overzier R. A., Kurk J. D., Miley G. K., Röttgering H. J. A., Zirm A. W., 2009, MNRAS, 395, 114 19

Hatch N. A., et al., 2011, MNRAS, 410, 1537 20, 35, 141

Hatch N. A., Muldrew S. I., Cooke E. A., Hartley W. G., Almaini O., Simpson C. J., Conselice C. J., 2016, MNRAS, 459, 387 35

Hayashi M., Kodama T., Koyama Y., Tanaka I., Shimasaku K., Okamura S., 2010, MNRAS, 402, 1980 19, 34

Hayashi M., Kodama T., Koyama Y., Tadaki K.-I., Tanaka I., 2011, MNRAS, 415, 2670 34, 35, 55

Hayashi M., Kodama T., Tanaka I., Shimakawa R., Koyama Y., Tadaki K.-i., Suzuki T. L., Yamamoto M., 2016, ApJL, 826, L28 19, 35

Hayashi M., et al., 2017, ApJL, 841, L21 35, 58, 104

Hayashi M., et al., 2018, ApJ, 856, 118 35

Heinis S., et al., 2014, MNRAS, 437, 1268 6

Helou G., Soifer B. T., Rowan-Robinson M., 1985, ApJL, 298, L7 146, 147

Henriques B. M. B., White S. D. M., Thomas P. A., Angulo R., Guo Q., Lemson G., Springel V., Overzier R., 2015, MNRAS, 451, 2663 25

Heyer M., Krawczyk C., Duval J., Jackson J. M., 2009, ApJ, 699, 1092 13

Hilton M., et al., 2010, ApJ, 718, 133 34, 55

Högbom J. A., 1974, AAPS, 15, 417 23

Hopkins A., Windhorst R., Cram L., Ekers R., 2000, Experimental Astronomy, 10, 419 142

Hopkins P. F., Hernquist L., Cox T. J., Di Matteo T., Martini P., Robertson B., Springel V., 2005, ApJ, 630, 705 25

Hubble E., 1929, Proceedings of the National Academy of Science, 15, 168 2

Hubble E. P., 1936, Realm of the Nebulae xii, 2

Hung C.-L., et al., 2016, ApJ, 826, 130 35

Hunt L. K., et al., 2017, preprint (arXiv:1704.05252) 130

Hurier G., Adam R., Keshet U., 2019, AAP, 622, A136 21

Husband K., Bremer M. N., Stott J. P., Murphy D. N. A., 2016, MNRAS, 462, 421 35

Huynh M., Lazio J., 2013, arXiv e-prints 24

Huynh M. T., et al., 2017, MNRAS, 467, 1222 56

Ibar E., et al., 2008, MNRAS, 386, 953 147

Ilbert O., et al., 2006, AAP, 457, 841 155

Ilbert O., et al., 2010, ApJ, 709, 644 4, 113

Ilbert O., et al., 2013, AAP, 556, A55 113

Inagaki T., Lin Y.-T., Huang H.-J., Hsieh B.-C., Sugiyama N., 2015, MNRAS, 446, 1107 19

Iqbal A., Kale R., Majumdar S., Nath B. B., Pandge M., Sharma P., Malik M. A., Raychaudhury S., 2017, Journal of Astrophysics and Astronomy, 38, 68 141

Israel F. P., 1997, AAP, 328, 471 112, 126

Issa M. R., MacLaren I., Wolfendale A. W., 1990, AAP, 236, 237 112

Itoh N., Kohyama Y., Nozawa S., 1998, ApJ, 502, 7 21

Ivison R. J., et al., 2010, AAP, 518, L35 12

Ivison R. J., Papadopoulos P. P., Smail I., Greve T. R., Thomson A. P., Xilouris E. M., Chapman S. C., 2011, MNRAS, 412, 1913 9, 14

Ivison R. J., et al., 2013, ApJ, 772, 137 35

Jackson C. A., 2004, New Astron. Rev., 48, 1187 142

Jarvis M. J., Rawlings S., 2004, New Astron. Rev., 48, 1173 11, 24, 141, 142

Jarvis M. J., et al., 2010, MNRAS, 409, 92 147

Jiang L., Cole S., Sawala T., Frenk C. S., 2015, MNRAS, 448, 1674 19

Jogee S., et al., 2009, ApJ, 697, 1971 9

Kacprzak G. G., et al., 2015, ApJL, 802, L26 35

Kajisawa M., et al., 2000, PASJ, 52, 61 21

Kamenetzky J., Rangwala N., Glenn J., 2017, MNRAS, 471, 2917 13

Karim A., et al., 2011, ApJ, 730, 61 8

Karim A., et al., 2013, MNRAS, 432, 2 5, 99

Kartaltepe J. S., et al., 2012, ApJ, 757, 23 9

Kashino D., et al., 2013, ApJL, 777, L8 118

Kauffmann G., Haehnelt M., 2000, MNRAS, 311, 576 25

Kauffmann G., White S. D. M., Guiderdoni B., 1993, MNRAS, 264, 201 19

Kauffmann G., Colberg J. M., Diaferio A., White S. D. M., 1999, MNRAS, 303, 188 19

Kaviraj S., et al., 2013, MNRAS, 429, L40 9

Kay S. T., Peel M. W., Short C. J., Thomas P. A., Young O. E., Battye R. A., Liddle A. R., Pearce F. R., 2012, MNRAS, 422, 1999 21

Kennicutt Jr. R. C., 1998a, ARAA, 36, 189 5, 43

Kennicutt Jr. R. C., 1998b, ApJ, 498, 541 16, 17

Kennicutt R. C., Evans N. J., 2012, ARAA, 50, 531 128

Kewley L. J., Dopita M. A., 2002, ApJS, 142, 35 119

Kewley L. J., Ellison S. L., 2008, ApJ, 681, 1183 129, 130, 136

Kewley L. J., Geller M. J., Jansen R. A., Dopita M. A., 2002, AJ, 124, 3135 5

Kewley L. J., Maier C., Yabe K., Ohta K., Akiyama M., Dopita M. A., Yuan T., 2013, ApJL, 774, L10 113

Kewley L. J., et al., 2016, ApJ, 819, 100 35

Kimball A. E., Ivezić Ž., 2008, AJ, 136, 684 145

Kinney A. L., Calzetti D., Bohlin R. C., McQuade K., Storchi-Bergmann T., Schmitt H. R., 1996, ApJ, 467, 38 3

Kirkpatrick A., et al., 2017, ApJ, 843, 71 11

Kobulnicky H. A., Kewley L. J., 2004, ApJ, 617, 240 129

Kodama T., Arimoto N., 1997, AAP, 320, 41 21

Kormendy J., Gebhardt K., 2001, in Wheeler J. C., Martel H., eds, American Institute of Physics Conference Series Vol. 586, 20th Texas Symposium on relativistic astrophysics. pp 363–381 (arXiv:astro-ph/0105230), doi:10.1063/1.1419581 1

Kormendy J., Richstone D., 1995, ARAA, 33, 581 1

Kormendy J., Fisher D. B., Cornell M. E., Bender R., 2009, ApJS, 182, 216 3

Koyama Y., et al., 2013, MNRAS, 434, 423 35

Koyama Y., Kodama T., Tadaki K.-i., Hayashi M., Tanaka I., Shimakawa R., 2014, ApJ, 789, 18 35

Kriek M., van Dokkum P. G., Labbé I., Franx M., Illingworth G. D., Marchesini D., Quadri R. F., 2009, ApJ, 700, 221 90, 118

Krishnan C., et al., 2017, MNRAS, 470, 2170 35, 55, 102, 141

Kroupa P., 2001, MNRAS, 322, 231 6

Krumholz M. R., McKee C. F., 2005, ApJ, 630, 250 17

Kubo M., et al., 2013, ApJ, 778, 170 35

Kubo M., Yamada T., Ichikawa T., Kajisawa M., Matsuda Y., Tanaka I., Umehata H., 2016, MNRAS, 455, 3333 51, 53

Kulas K. R., et al., 2013, ApJ, 774, 130 35

Kurk J. D., et al., 2000, AAP, 358, L1 20, 34

Kurk J., et al., 2009, AAP, 504, 331 35

Lacey C., Cole S., 1993, MNRAS, 262, 627 19

Lacey C. G., et al., 2016, MNRAS, 462, 3854 25

Lagos C. D. P., Baugh C. M., Lacey C. G., Benson A. J., Kim H.-S., Power C., 2011, MNRAS, 418, 1649 57, 136

Lagos C. d. P., Bayet E., Baugh C. M., Lacey C. G., Bell T. A., Fanidakis N., Geach J. E., 2012, MNRAS, 426, 2142 15

Lagos C. d. P., et al., 2015, MNRAS, 452, 3815 11, 57, 133

Lambas D. G., Tissera P. B., Alonso M. S., Coldwell G., 2003, MNRAS, 346, 1189 9

Lara-López M. A., et al., 2010, AAP, 521, L53 135

Larson R. B., 1981, MNRAS, 194, 809 13

Laureijs R., et al., 2011, preprint (arXiv:1110.3193) 108

Le Brun A. M. C., Arnaud M., Pratt G. W., Teyssier R., 2018, MNRAS, 473, L69 25

Leahy D. A., et al., 2019, arXiv e-prints 142

Lee-Brown D. B., et al., 2017, ApJ, 844, 43 35

Lee K.-S., et al., 2012, ApJ, 752, 66 8

Lee S.-K., Im M., Kim J.-W., Lotz J., McPartland C., Peth M., Koekemoer A., 2015, ApJ, 810, 90 10

Lee M. M., et al., 2017, ApJ, 842, 55 35, 57

Leroy A., Cannon J., Walter F., Bolatto A., Weiss A., 2007, ApJ, 663, 990 130

Leroy A. K., et al., 2011, ApJ, 737, 12 11, 112, 126, 129, 131, 132, 134

Leroy A. K., et al., 2013, AJ, 146, 19 104

Levin Y., Pakter R., Rizzato F. B., 2008, PRE, 78, 021130 20

Licquia T. C., Newman J. A., 2015, ApJ, 806, 96 127, 130

Lidman C., et al., 2008, AAP, 489, 981 21, 34

Lilly S. J., Carollo C. M., Pipino A., Renzini A., Peng Y., 2013, ApJ, 772, 119 4

Lin Y.-T., Brodwin M., Gonzalez A. H., Bode P., Eisenhardt P. R. M., Stanford S. A., Vikhlinin A., 2013, ApJ, 771, 61 19

Lindner R. R., et al., 2011, ApJ, 737, 83 5

Lisenfeld U., Völk H. J., 2000, AAP, 354, 423 145

Lisenfeld U., Isaak K. G., Hills R., 2000, MNRAS, 312, 433 11

Liu D., Gao Y., Isaak K., Daddi E., Yang C., Lu N., van der Werf P., 2015, ApJL, 810, L14 12, 15, 87, 128, 129

Liu C., Mutch S. J., Poole G. B., Angel P. W., Duffy A. R., Geil P. M., Mesinger A., Wyithe J. S. B., 2017, MNRAS, 465, 3134 25

Liu D., et al., 2018, ApJ, 853, 172 154, 156

Loi F., Murgia M., Govoni F., Vacca V., Prandoni I., Bonafede A., Feretti L., 2019, MNRAS, 485, 5285 143

Longair M. S., 2011, High Energy Astrophysics 145

Longhetti M., Bressan A., Rampazzo R., Chiosi C., 1999, in Carral P., Cepa J., eds, Astronomical Society of the Pacific Conference Series Vol. 163, Star Formation in Early Type Galaxies. p. 34 3

Lotz J. M., Primack J., Madau P., 2004, AJ, 128, 163 165

Lotz J. M., Jonsson P., Cox T. J., Croton D., Primack J. R., Somerville R. S., Stewart K., 2011, ApJ, 742, 103 52

Lotz J. M., et al., 2013, ApJ, 773, 154 34, 55, 102

Lu N., et al., 2014, ApJL, 787, L23 129

Lynden-Bell D., 1967, MNRAS, 136, 101 20

Lynden-Bell D., 1969, Nature, 223, 690 1

Ma C.-J., et al., 2015, ApJ, 806, 257 34, 44

Madau P., Dickinson M., 2014, ARAA, 52, 415 xii, 4, 43

Magdis G. E., et al., 2011, ApJL, 740, L15 14, 119

Magdis G. E., et al., 2012, ApJ, 760, 6 11, 15, 88, 93, 101, 105, 106, 111, 112, 119, 123, 124, 131, 132, 133, 134, 135

Magnelli B., et al., 2012, AAP, 548, A22 14

Magnelli B., et al., 2014, AAP, 561, A86 6

Magnelli B., et al., 2015, AAP, 573, A45 146, 147

Maiolino R., et al., 2015, MNRAS, 452, 54 4

Makhathini S., Jarvis M., Smirnov O., Heywood I., 2015, Advancing Astrophysics with the Square Kilometre Array (AASKA14), p. 81 143

Maltby D. T., Almaini O., Wild V., Hatch N. A., Hartley W. G., Simpson C., Rowlands K., Socolovsky M., 2018, MNRAS, 480, 381 3

Mancini C., et al., 2011, ApJ, 743, 86 129

Mancini C., et al., 2019, arXiv e-prints 10

Mancone C. L., Gonzalez A. H., Brodwin M., Stanford S. A., Eisenhardt P. R. M., Stern D., Jones C., 2010, ApJ, 720, 284 34, 56

Mannucci F., Cresci G., Maiolino R., Marconi A., Gnerucci A., 2010, MNRAS, 408, 2115 96, 135

Mantz A. B., Allen S. W., Morris R. G., 2016, MNRAS, 462, 681 20

Mantz A. B., et al., 2018, AAP, 620, A2 34

Marasco A., Crain R. A., Schaye J., Bahé Y. M., van der Hulst T., Theuns T., Bower R. G., 2016, MNRAS, 461, 2630 22

Marian V., Ziegler B., Kuchner U., Verdugo M., 2018, AAP, 617, A34 2

Marleau F. R., Clancy D., Habas R., Bianconi M., 2017, AAP, 602, A28 1

Mateus A., Sodré L., Cid Fernandes R., Stasińska G., Schoenell W., Gomes J. M., 2006, MNRAS, 370, 721 2

Mathis J. S., 1990, ARAA, 28, 37 6

McAlpine S., Bower R. G., Harrison C. M., Crain R. A., Schaller M., Schaye J., Theuns T., 2017, MNRAS, 468, 3395 25

McDonald M., et al., 2016, ApJ, 817, 86 51

McGee S. L., Bower R. G., Balogh M. L., 2014, MNRAS, 442, L105 22

McKean J., et al., 2015, Advancing Astrophysics with the Square Kilometre Array (AASKA14), p. 84 141

McLure R. J., Dunlop J. S., Cirasuolo M., Koekemoer A. M., Sabbi E., Stark D. P., Targett T. A., Ellis R. S., 2010, MNRAS, 403, 960 4

McMullin J. P., Waters B., Schiebel D., Young W., Golap K., 2007, in Shaw R. A., Hill F., Bell D. J., eds, Astronomical Society of the Pacific Conference Series Vol. 376, Astronomical Data Analysis Software and Systems XVI. p. 127 62, 118

Mei S., et al., 2009, ApJ, 690, 42 21, 34

Mei S., et al., 2015, ApJ, 804, 117 102

Meier D. S., Turner J. L., Crosthwaite L. P., Beck S. C., 2001, AJ, 121, 740 128

Meurer G. R., Heckman T. M., Calzetti D., 1999, ApJ, 521, 64 7

Mezger P. G., Mathis J. S., Panagia N., 1982, AAP, 105, 372 6

Miller T. B., et al., 2018, Nature, 556, 469 19

Mo H., van den Bosch F. C., White S., 2010, Galaxy Formation and Evolution 20

Molnár D. C., et al., 2018, MNRAS, 475, 827 146, 147

Moore B., Katz N., Lake G., Dressler A., Oemler A., 1996, Nature, 379, 613 22

Motl P. M., Hallman E. J., Burns J. O., Norman M. L., 2005, ApJ, 623, L63 21

Mroczkowski T., et al., 2019, arXiv e-prints 21

Muñoz-Mateos J. C., et al., 2009, ApJ, 701, 1965 133, 134

Mullaney J. R., et al., 2012a, MNRAS, 419, 95 87

Mullaney J. R., et al., 2012b, ApJL, 753, L30 5

Mullis C. R., Rosati P., Lamer G., Böhringer H., Schwope A., Schuecker P., Fassbender R., 2005, ApJL, 623, L85 34

Murgia M., Govoni F., Feretti L., Giovannini G., Dallacasa D., Fanti R., Taylor G. B., Dolag K., 2004, AAP, 424, 429 143

Murphy E. J., et al., 2011, ApJ, 737, 67 5

Murphy E. J., et al., 2012, ApJ, 761, 97 148

Muzzin A., Wilson G., Demarco R., Lidman C., Nantais J., Hoekstra H., Yee H. K. C., Rettura A., 2013, ApJ, 767, 39 34

Nantais J. B., et al., 2017, MNRAS, 465, L104 35

Narayanan D., Krumholz M. R., 2014, MNRAS, 442, 1411 15

Narayanan D., Cox T. J., Hayward C. C., Hernquist L., 2011, MNRAS, 412, 287 17

Narayanan D., Krumholz M. R., Ostriker E. C., Hernquist L., 2012, MNRAS, 421, 3127 14, 126

Navarro J. F., Frenk C. S., White S. D. M., 1996, ApJ, 462, 563 3

Nelson D., et al., 2018, MNRAS, 475, 624 2

Newman A. B., Ellis R. S., Andreon S., Treu T., Raichoor A., Trinchieri G., 2014, ApJ, 788, 51 35

Noble A. G., et al., 2017, ApJL, 842, L21 35, 57

Noeske K. G., et al., 2007, ApJL, 660, L43 8

Noirot G., et al., 2018, ApJ, 859, 38 20

Noordam J. E., Smirnov O. M., 2010, AAP, 524, A61 143

Norris R. P., et al., 2013, PASA, 30, e020 142

O'Sullivan E., et al., 2018, AAP, 618, A126 177

Obreschkow D., Klöckner H.-R., Heywood I., Levrier F., Rawlings S., 2009, ApJ, 703, 1890 142

Oesch P. A., et al., 2010, ApJL, 709, L16 4

Oesch P. A., et al., 2018, ApJS, 237, 12 154

Oke J. B., 1971, ApJ, 170, 193 3

Oke J. B., Postman M., Lubin L. M., 1998, AJ, 116, 549 20

Onodera M., et al., 2016, ApJ, 822, 42 96, 135

Oteo I., Zwaan M. A., Ivison R. J., Smail I., Biggs A. D., 2016, ApJ, 822, 36 39, 175

Overzier R. A., 2016, AAPR, 24, 14 xii, 20, 21, 34

Overzier R. A., et al., 2011, ApJL, 726, L7 7

Padmanabhan N., et al., 2004, New Astronomy, 9, 329 19

Pannella M., Elbaz D., Daddi E., 2013, in Wong T., Ott J., eds, IAU Symposium Vol. 292, Molecular Gas, Dust, and Star Formation in Galaxies. pp 289–289, doi:10.1017/S1743921313001439 118

Pannella M., et al., 2015, ApJ, 807, 141 6, 45, 91

Papadopoulos P. P., van der Werf P. P., Xilouris E. M., Isaak K. G., Gao Y., Mühle S., 2012a, MNRAS, 426, 2601 14, 16, 40, 41, 82, 86

Papadopoulos P. P., van der Werf P., Xilouris E., Isaak K. G., Gao Y., 2012b, ApJ, 751, 10 13

Papovich C., et al., 2010, ApJ, 716, 1503 34, 35

Parsa S., Dunlop J. S., McLure R. J., Mortlock A., 2016, MNRAS, 456, 3194 43

Peng C., 2010, in American Astronomical Society Meeting Abstracts #215. p. 578 65, 118

Peng Y., Maiolino R., Cochrane R., 2015, Nature, 521, 192 56

Pérez-Montero E., Contini T., 2009, MNRAS, 398, 949 119

Perley R., et al., 2009, IEEE Proceedings, 97, 1448 23

Perret V., Renaud F., Epinat B., Amram P., Bournaud F., Contini T., Teyssier R., Lambert J.-C., 2014, AAP, 562, A1 9

Pettini M., Pagel B. E. J., 2004, MNRAS, 348, L59 119

Pike S. R., Kay S. T., Newton R. D. A., Thomas P. A., Jenkins A., 2014, MNRAS, 445, 1774 25

Pillepich A., Porciani C., Reiprich T. H., 2012, MNRAS, 422, 44 21

Pilyugin L. S., Thuan T. X., 2005, ApJ, 631, 231 129

Pineda J. L., Goldsmith P. F., Chapman N., Snell R. L., Li D., Cambrésy L., Brunt C., 2010, ApJ, 721, 686 13

Planck Collaboration et al., 2011, AAP, 536, A19 13

Planck Collaboration et al., 2014, AAP, 571, A20 20

Poggianti B. M., et al., 2017, ApJ, 844, 48 22

Popesso P., et al., 2015a, AAP, 574, A105 43

Popesso P., et al., 2015b, AAP, 579, A132 34, 44

Popesso P., et al., 2019, MNRAS, 483, 3213 10

Popping G., Somerville R. S., Trager S. C., 2014, MNRAS, 442, 2398 15, 136

Popping G., Somerville R. S., Galametz M., 2017, MNRAS, 471, 3152 6, 135

Power C., et al., 2015, Advancing Astrophysics with the Square Kilometre Array (AASKA14), p. 133 141

Prandoni I., Seymour N., 2015, Advancing Astrophysics with the Square Kilometre Array (AASKA14), p. 67 144

Prichard L. J., et al., 2017, ApJ, 850, 203 35

Puglisi A., et al., 2017, ApJL, 838, L18 92

Quadri R. F., Williams R. J., Franx M., Hildebrandt H., 2012, ApJ, 744, 88 19

Quilis V., Moore B., Bower R., 2000, Science, 288, 1617 22

Ragone-Figueroa C., Granato G. L., Ferraro M. E., Murante G., Biffi V., Borgani S., Planelles S., Rasia E., 2018, MNRAS, 479, 1125 19

Rasia E., et al., 2015, ApJ, 813, L17 25

Rawlings S., Abdalla F. B., Bridle S. L., Blake C. A., Baugh C. M., Greenhill L. J., van der Hulst J. M., 2004, New Astron. Rev., 48, 1013 141

Rees M. J., Ostriker J. P., 1977, MNRAS, 179, 541 20

Reese E. D., Kawahara H., Kitayama T., Ota N., Sasaki S., Suto Y., 2010, ApJ, 721, 653 21

Reines A. E., Plotkin R. M., Russell T. D., Mezcua M., Condon J. J., Sivakoff G. R., Johnson K. E., 2014, ApJL, 787, L30 1

Rémy-Ruyer A., et al., 2014, AAP, 563, A31 96, 112, 129, 133, 134, 135, 138

Renzini A., Peng Y.-j., 2015, ApJL, 801, L29 10

Reynolds T. N., et al., 2019, MNRAS, 482, 3591 142

Riechers D. A., et al., 2019, ApJ, 872, 7 11, 136

Rigopoulou D., Pereira-Santaella M., Magdis G. E., Cooray A., Farrah D., Marques-Chaves R., Perez-Fournon I., Riechers D., 2018, MNRAS, 473, 20 128

Robaina A. R., et al., 2009, ApJ, 704, 324 9

Rodighiero G., et al., 2011, ApJL, 739, L40 8, 9, 103, 118, 176

Rosati P., Stanford S. A., Eisenhardt P. R., Elston R., Spinrad H., Stern D., Dey A., 1999, AJ, 118, 76 34

Rosati P., Borgani S., Norman C., 2002, ARAA, 40, 539 21

Rowlands K., et al., 2018, MNRAS, 473, 1168 3

Rudnick G. H., Tran K.-V., Papovich C., Momcheva I., Willmer C., 2012, ApJ, 755, 14 21

Rudnick G., et al., 2017, ApJ, 849, 27 35, 58

Sage L. J., Salzer J. J., Loose H.-H., Henkel C., 1992, AAP, 265, 19 128

Saintonge A., et al., 2011, MNRAS, 415, 32 4, 10, 11, 56

Saintonge A., et al., 2012, ApJ, 758, 73 17, 104, 135

Saintonge A., et al., 2013, ApJ, 778, 2 112, 133, 134

Saintonge A., et al., 2016, MNRAS, 462, 1749 17, 104

Salmi F., Daddi E., Elbaz D., Sargent M. T., Dickinson M., Renzini A., Bethermin M., Le Borgne D., 2012, ApJL, 754, L14 8

Salmon B., et al., 2015, ApJ, 799, 183 9

Salpeter E. E., 1955, ApJ, 121, 161 6, 37

Salpeter E. E., 1964, ApJ, 140, 796 1

Salvaterra R., Ferrara A., Dayal P., 2011, MNRAS, 414, 847 25

Sanders D. B., Mirabel I. F., 1996, ARAA, 34, 749 9

Sanders R. L., et al., 2015, ApJ, 799, 138 96, 135

Sandstrom K. M., et al., 2013, ApJ, 777, 5 13, 112, 129, 132, 133, 134

Sansom A. E., Thirlwall J. J., Deakin M. A., Väisänen P., Kniazev A. Y., van Loon J. T., 2015, MNRAS, 450, 1338 177

Santini P., et al., 2014, AAP, 562, A30 6, 11, 57, 111, 131, 135

Santos J. S., et al., 2011, AAP, 531, L15 34

Santos J. S., et al., 2015a, MNRAS, 447, L65 19, 34, 43, 44, 102

Santos J. S., et al., 2015b, MNRAS, 447, L65 19

Sargent M. T., et al., 2010, ApJL, 714, L190 147

Sargent M. T., Béthermin M., Daddi E., Elbaz D., 2012, ApJL, 747, L31 9, 103, 118, 176

Sargent M. T., et al., 2014, ApJ, 793, 19 xii, 10, 16, 17, 47, 57, 88, 91, 96, 102, 104, 111, 116, 117, 125, 126, 127, 134, 135, 157

Sargent M. T., et al., 2015, ApJL, 806, L20 102

Saro A., Borgani S., Tornatore L., De Lucia G., Dolag K., Murante G., 2009, MNRAS, 392, 795 58

Sault R. J., Teuben P. J., Wright M. C. H., 1995, in Shaw R. A., Payne H. E., Hayes J. J. E., eds, Astronomical Society of the Pacific Conference Series Vol. 77, Astronomical Data Analysis Software and Systems IV. p. 433 (arXiv:astro-ph/0612759) 143

Scarlata C., et al., 2007, ApJS, 172, 406 165

Schaye J., et al., 2015, MNRAS, 446, 521 25

Schinnerer E., et al., 2016, ApJ, 833, 112 10, 11, 17, 56

Schmidt M., 1959, ApJ, 129, 243 16, 17

Schmitt H. R., Calzetti D., Armus L., Giavalisco M., Heckman T. M., Kennicutt Jr. R. C., Leitherer C., Meurer G. R., 2006, ApJS, 164, 52 5

Schreiber C., et al., 2015, AAP, 575, A74 xii, 8, 9, 45, 91

Schreiber C., Elbaz D., Pannella M., Ciesla L., Wang T., Franco M., 2018, AAP, 609, A30 6, 11

Schruba A., et al., 2012, AJ, 143, 138 127, 132

Schultheis M., et al., 2014, AAP, 566, A120 13

Scoville N. Z., Yun M. S., Clemens D. P., Sanders D. B., Waller W. H., 1987, ApJS, 63, 821 13

Scoville N. Z., Yun M. S., Bryant P. M., 1997, ApJ, 484, 702 13

Scoville N., et al., 2014, ApJ, 783, 84 11, 111, 112, 133

Scoville N., et al., 2016, ApJ, 820, 83 14

Scoville N., et al., 2017, ApJ, 837, 150 10, 11, 57, 111, 135, 136

Shankar F., 2009, New Astron. Rev., 53, 57 5

Shapley A. E., Steidel C. C., Adelberger K. L., Dickinson M., Giavalisco M., Pettini M., 2001, ApJ, 562, 95 4

Shimakawa R., Kodama T., Tadaki K.-i., Hayashi M., Koyama Y., Tanaka I., 2015, MNRAS, 448, 666 35

Shimakawa R., et al., 2018, MNRAS, 473, 1977 35

Silk J., Mamon G. A., 2012, Research in Astronomy and Astrophysics, 12, 917 25

Silverman J. D., et al., 2008, ApJ, 679, 118 5

Silverman J. D., et al., 2015, ApJL, 812, L23 92

Silverman J. D., et al., 2018, ApJ, 868, 75 9

Simpson J. M., et al., 2015, ApJ, 807, 128 5

Sliwa K., Wilson C. D., Petitpas G. R., Armus L., Juvela M., Matsushita S., Peck A. B., Yun M. S., 2012, ApJ, 753, 46 13

Smail I., et al., 2014, ApJ, 782, 19 35, 44

Smith D. J. B., et al., 2014, MNRAS, 445, 2232 147

Smith C. M. A., Gear W. K., Smith M. W. L., Papageorgiou A., Eales S. A., 2019, MNRAS 19, 28

Smolčić V., et al., 2015, Advancing Astrophysics with the Square Kilometre Array (AASKA14), p. 69 141

Smolčić V., et al., 2017, AAP, 602, A1 145

Snyder G. F., et al., 2012a, ApJ, 756, 114 21

Snyder G. F., et al., 2012b, ApJ, 756, 114 35

Soifer B. T., Boehmer L., Neugebauer G., Sand ers D. B., 1989, AJ, 98, 766 146

Solomon P. M., Vanden Bout P. A., 2005, ARAA, 43, 677 9

Solomon P. M., Rivolo A. R., Barrett J., Yahil A., 1987, ApJ, 319, 730 11, 13

Solomon P. M., Downes D., Radford S. J. E., Barrett J. W., 1997, ApJ, 478, 144 9

Solomon P., Vanden Bout P., Carilli C., Guelin M., 2003, Nature, 426, 636 12

Somerville R. S., Hopkins P. F., Cox T. J., Robertson B. E., Hernquist L., 2008, MNRAS, 391, 481 25

Somerville R. S., Gilmore R. C., Primack J. R., Domínguez A., 2012, MNRAS, 423, 1992 19

Speagle J. S., Steinhardt C. L., Capak P. L., Silverman J. D., 2014, ApJS, 214, 15 8

Spilker J. S., et al., 2014, ApJ, 785, 149 98

Spitler L. R., et al., 2012, ApJL, 748, L21 34, 35, 56

Springel V., et al., 2005a, Nature, 435, 629 19

Springel V., Di Matteo T., Hernquist L., 2005b, ApJL, 620, L79 3

Stacey G. J., Hailey-Dunsheath S., Ferkinhoff C., Nikola T., Parshley S. C., Benford D. J., Staguhn J. G., Fiolet N., 2010, ApJ, 724, 957 12

Stach S. M., Swinbank A. M., Smail I., Hilton M., Simpson J. M., Cooke E. A., 2017, ApJ, 849, 154 19, 35, 58, 65, 104

Stanford S. A., et al., 2006, ApJL, 646, L13 34

Stanford S. A., et al., 2012, ApJ, 753, 164 34

Steidel C. C., Adelberger K. L., Giavalisco M., Dickinson M., Pettini M., 1999, ApJ, 519, 1 4

Steidel C. C., Adelberger K. L., Shapley A. E., Erb D. K., Reddy N. A., Pettini M., 2005, ApJ, 626, 44 35

Steidel C. C., et al., 2014, ApJ, 795, 165 15, 119, 120, 121

Steinhardt C. L., et al., 2014, ApJL, 791, L25 8

Storey P. J., Zeippen C. J., 2000, MNRAS, 312, 813 121

Strateva I., et al., 2001, AJ, 122, 1861 2

Strazzullo V., et al., 2010, AAP, 524, A17 34, 35

Strazzullo V., et al., 2013, ApJ, 772, 118 27, 35, 36, 39, 48, 50, 51, 56, 67, 98, 113, 175

Strazzullo V., et al., 2015, AAP, 576, L6 34, 102

Strazzullo V., et al., 2016, ApJL, 833, L20 21, 30, 35, 36, 50, 56, 67, 68, 71, 74, 75, 91, 102, 113, 118

Strazzullo V., et al., 2018, ApJ, 862, 64 ii, 19, 28, 29, 33, 53, 74, 86, 87, 113, 175

Strong A. W., Mattox J. R., 1996, AAP, 308, L21 13

Sunyaev R. A., Zeldovich I. B., 1980, ARAA, 18, 537 21

Tabatabaei F. S., et al., 2017, ApJ, 836, 185 5

Tacconi L. J., et al., 2008, ApJ, 680, 246 9, 14, 129

Tacconi L. J., et al., 2010, Nature, 463, 781 9

Tacconi L. J., et al., 2013, ApJ, 768, 74 4, 17, 88, 91, 101, 104, 111

Tacconi L. J., et al., 2018, ApJ, 853, 179 10, 11, 17, 56, 57, 104, 111, 125, 133, 134, 135

Tadaki K.-i., et al., 2014, ApJL, 788, L23 35

Takahashi K., et al., 2015, Advancing Astrophysics with the Square Kilometre Array (AASKA14), p. 159 141

Tan Q., et al., 2014, AAP, 569, A98 6, 95, 106, 111, 112

Tanaka M., Finoguenov A., Ueda Y., 2010, ApJL, 716, L152 35

Tanaka M., et al., 2013, ApJ, 772, 113 35

Taylor A. R., 2008, in Jin W. J., Platais I., Perryman M. A. C., eds, IAU Symposium Vol. 248, A Giant Step: from Milli- to Micro-arcsecond Astrometry. pp 164–169, doi:10.1017/S1743921308018954 141

Thacker R. J., MacMackin C., Wurster J., Hobbs A., 2014, MNRAS, 443, 1125 25

Thomas D., Maraston C., Bender R., Mendes de Oliveira C., 2005, ApJ, 621, 673 3, 19

Thompson A. R., Clark B. G., Wade C. M., Napier P. J., 1980, ApJS, 44, 151 23

Tomczak A. R., et al., 2014, ApJ, 783, 85 113

Tomczak A. R., et al., 2016, ApJ, 817, 118 8, 10

Tonini C., Bernyk M., Croton D., Maraston C., Thomas D., 2012, ApJ, 759, 43 51

Tonnesen S., Cen R., 2014, ApJ, 788, 133 19, 55

Tran K.-V. H., et al., 2010, ApJ, 719, L126 19

Tran K.-V. H., et al., 2015, ApJ, 811, 28 34, 35, 43, 55

Trayford J. W., Theuns T., Bower R. G., Crain R. A., Lagos C. d. P., Schaller M., Schaye J., 2016, MNRAS, 460, 3925 2

Trayford J. W., Frenk C. S., Theuns T., Schaye J., Correa C., 2019, MNRAS, 483, 744 8

Tremonti C. A., et al., 2004, ApJ, 613, 898 111

Truemper J., 1993, Science, 260, 1769 21

Valentino F., et al., 2015, ApJ, 801, 132 27, 28, 35, 36, 56, 60, 68, 73, 76, 85, 96, 113, 137

Valentino F., et al., 2016, ApJ, 829, 53 28, 32, 35, 36, 56, 87, 113

Venemans B. P., et al., 2007, AAP, 461, 823 34

Venemans B. P., et al., 2017, ApJL, 851, L8 4

Vogelsberger M., et al., 2014, MNRAS, 444, 1518 25

Voit G. M., 2005, Reviews of Modern Physics, 77, 207 20, 21

Vollmer B., Cayatte V., Balkowski C., Duschl W. J., 2001, ApJ, 561, 708 22

Volonteri M., Capelo P. R., Netzer H., Bellovary J., Dotti M., Governato F., 2015, MNRAS, 452, L6 25

Wagg J., et al., 2015, Advancing Astrophysics with the Square Kilometre Array (AASKA14), p. 161 141

Walter F., et al., 2007, ApJ, 661, 102 124

Walter F., Weiß A., Downes D., Decarli R., Henkel C., 2011, ApJ, 730, 18 12, 98

Walter F., et al., 2014, ApJ, 782, 79 136

Wang T.-G., Zhang X.-G., 2003, MNRAS, 340, 793 1

Wang T., et al., 2016, ApJ, 828, 56 19, 21, 34, 43, 44, 52, 57, 93, 104

Waters D., Wilkins S. M., Di Matteo T., Feng Y., Croft R., Nagai D., 2016, MNRAS, 461, L51 25

Webb T. M. A., et al., 2013, AJ, 146, 84 44

Webb T., et al., 2015a, ApJ, 809, 173 19, 51, 53

Webb T. M. A., et al., 2015b, ApJ, 814, 96 51

Weiß A., Downes D., Neri R., Walter F., Henkel C., Wilner D. J., Wagg J., Wiklind T., 2007, AAP, 467, 955 15

Whitaker K. E., van Dokkum P. G., Brammer G., Franx M., 2012, ApJL, 754, L29 8, 9

Whitaker K. E., et al., 2014, ApJ, 795, 104 6, 8, 156

Whitaker K. E., et al., 2015, ApJL, 811, L12 8, 10

Whittam I. H., Jarvis M. J., Green D. A., Heywood I., Riley J. M., 2017, MNRAS, 471, 908 142

Wild V., Walcher C. J., Johansson P. H., Tresse L., Charlot S., Pollo A., Le Fèvre O., de Ravel L., 2009, MNRAS, 395, 144 3

Wild V., et al., 2014, MNRAS, 440, 1880 3

Wilkins S. M., Bunker A. J., Stanway E., Lorenzoni S., Caruana J., 2011, MNRAS, 417, 717 4

Williams J. P., Blitz L., McKee C. F., 2000, Protostars and Planets IV, p. 97 11

Williams R. J., Quadri R. F., Franx M., van Dokkum P., Labbé I., 2009, ApJ, 691, 1879 45

Willis A. G., 2008, in Argyle R. W., Bunclark P. S., Lewis J. R., eds, Astronomical Society of the Pacific Conference Series Vol. 394, Astronomical Data Analysis Software and Systems XVII. p. 717 143

Wilman R. J., et al., 2008, MNRAS, 388, 1335 142

Wilson C. D., 1995, ApJL, 448, L97 132

Wilson T. L., Rohlfs K., Hüttemeister S., 2009a, Tools of Radio Astronomy. Springer-Verlag, doi:10.1007/978-3-540-85122-6 23

Wilson G., et al., 2009b, ApJ, 698, 1943 34

Windhorst R. A., 2003, New Astron. Rev., 47, 357 142

Wolfire M. G., Hollenbach D., McKee C. F., 2010, ApJ, 716, 1191 112, 127, 129, 132, 139

Wong K. C., et al., 2011, ApJ, 728, 119 9

Wootten A., Thompson A. R., 2009, IEEE Proceedings, 97, 1463 23

Wuyts S., et al., 2016, ApJ, 831, 149 90

Wylezalek D., et al., 2013, ApJ, 769, 79 34

Wylezalek D., et al., 2014, ApJ, 786, 17 34

Xu C. K., et al., 2012, ApJ, 760, 72 9

Xu W., Ramos-Ceja M. E., Pacaud F., Reiprich T. H., Erben T., 2018, AAP, 619, A162 21

Yan H., Windhorst R. A., 2004, ApJL, 612, L93 4

Yang C., et al., 2017, AAP, 608, A144 12, 129

Yao L., Seaquist E. R., Kuno N., Dunne L., 2003, ApJ, 588, 771 13

Yesuf H. M., Faber S. M., Trump J. R., Koo D. C., Fang J. J., Liu F. S., Wild V., Hayward C. C., 2014, ApJ, 792, 84 3

Yoshikawa T., et al., 2010, ApJ, 718, 112 114

Yun M. S., Reddy N. A., Condon J. J., 2001, ApJ, 554, 803 146

Zackrisson E., et al., 2019, arXiv e-prints 142

Zahid H. J., Dima G. I., Kudritzki R.-P., Kewley L. J., Geller M. J., Hwang H. S., Silverman J. D., Kashino D., 2014, ApJ, 791, 130 111, 116, 119, 120, 121, 136

Zanella A., et al., 2018, MNRAS, 481, 1976 12

Zeimann G. R., et al., 2012, ApJ, 756, 115 34

Ziparo F., et al., 2014, MNRAS, 437, 458 19

da Cunha E., Charlot S., Elbaz D., 2008, MNRAS, 388, 1595 xii, 5

da Cunha E., Charmandaris V., Díaz-Santos T., Armus L., Marshall J. A., Elbaz D., 2010, AAP, 523, A78 6

da Cunha E., et al., 2015, ApJ, 806, 110 3

de Jong T., Klein U., Wielebinski R., Wunderlich E., 1985, AAP, 147, L6 146, 147

van Dokkum P. G., Ellis R. S., 2003, ApJL, 592, L53 3

van den Bosch R. C. E., Gebhardt K., Gültekin K., van de Ven G., van der Wel A., Walsh J. L., 2012, Nature, 491, 729 1

van der Wel A., Bell E. F., Holden B. P., Skibba R. A., Rix H.-W., 2010, ApJ, 714, 1779 56

van der Wel A., et al., 2014, ApJL, 792, L6 8

Appendices

Appendix A

Image-plane vs. uv-plane flux extraction for cluster galaxies at z=2

This appendix relates to Chapter 4. Flux measurement simulations were performed for both `uvfit` and GALFIT. In both cases, the 2mm continuum data were used, having first removed all real continuum sources in the uv-plane. For GALFIT, the dirty data were then transported to the image plane. Three different simulated source sizes were used - a point source, a circular Gaussian with FWHM=1", and a circular Gaussian with FWHM=2". The size of the synthesised beam in the 2mm data is 1.19"$\times$0.96", so these Gaussian sizes correspond to approximately one and two times the synthesised beam size. Additionally, these simulated sizes span the range of measured sizes for the cluster galaxies (Table 4.2). One thousand sources of each size were injected, one by one. Having done this, the flux of the source was then re-measured using `uvfit` or GALFIT respectively, at fixed input position and over the fixed input size. Although this is a limited scenario, we perform our simulations under these conditions and we wish to primarily quantify the difference between the flux measurements in the image plane and the uv-plane. Additionally, the majority of the flux measurement in our analysis is performed at fixed position and size.

We then inspect the average measured flux of the 1000 sources, the average measurement error returned for the 1000 sources, and the dispersion of the returned flux distribution. These results are given in Tables A.1 and A.2. We find that the average returned flux is consistent with the input flux for both `uvfit` and GALFIT, although the formal flux error returned by GALFIT is underestimated. However, the dispersion of the flux distribution from GALFIT compares reasonably with the RMS noise of the input image. We find that `uvfit` performs marginally better for PSF sources than GALFIT, and that GALFIT returns a slightly smaller flux dispersion for 2" extended sources than `uvfit`.

Shape	Flux$_{in}$ (μJy)	Flux$_{ave,out}$ (μJy)	Error$_{ave,out}$ (μJy)	$\sigma_{flux,out}$ (μJy)
PSF	120.0	119.1	7.2	8.6
1" Gauss.	120.0	120.5	11.3	13.8
2" Gauss.	120.0	120.2	18.4	23.7

Table A.1: Flux measurement simulation results for `uvfit`. The shape, input flux, average output flux, average output flux error, and 1σ dispersion on the output fluxes are given. The RMS noise of the 2mm map is $\sim$8.5μJy/beam. The input flux therefore corresponds to a PSF SNR of $\sim$15σ. The 1σ dispersion of the output fluxes for the PSF closely reflects the RMS of the input map, as expected.

Shape	Flux$_{in}$ (μJy)	Flux$_{ave,out}$ (μJy)	Error$_{ave,out}$ (μJy)	$\sigma_{flux,out}$ (μJy)
PSF	120.0	119.8	0.7	9.3
1" Gauss.	120.0	120.5	1.1	13.7
2" Gauss.	120.0	120.7	1.1	21.9

Table A.2: Flux measurement simulation results for GALFIT. The shape, input flux, average output flux, average output flux error, and 1σ dispersion on the output fluxes are given. As above, the RMS noise of the 2mm map is $\sim$8.5μJy/beam. The input flux therefore corresponds to a PSF SNR of $\sim$15σ. The formal errors on the fluxes reported by GALFIT are strongly underestimated, as discussed in Section 4.2.6.

Appendix B

CO[3-2] and CO[1-0] 1D spectra of galaxies in the core of Cl J1449+0856

This appendix also relates to Chapter 4. The 1D spectra covering the CO[3-2] and CO[1-0] lines are shown in Figs B.1 and B.2 respectively, for the eight galaxies in Cl J1449+0856 with CO[4-3] line detections. We did not search for CO[3-2] or CO[1-0] lines in these spectra, but instead extracted line fluxes at fixed position for each galaxy, matching the position and shape of the CO[4-3] emission. This was done in the collapsed uv-data, over a fixed velocity range corresponding to that of the CO[4-3] line detection.

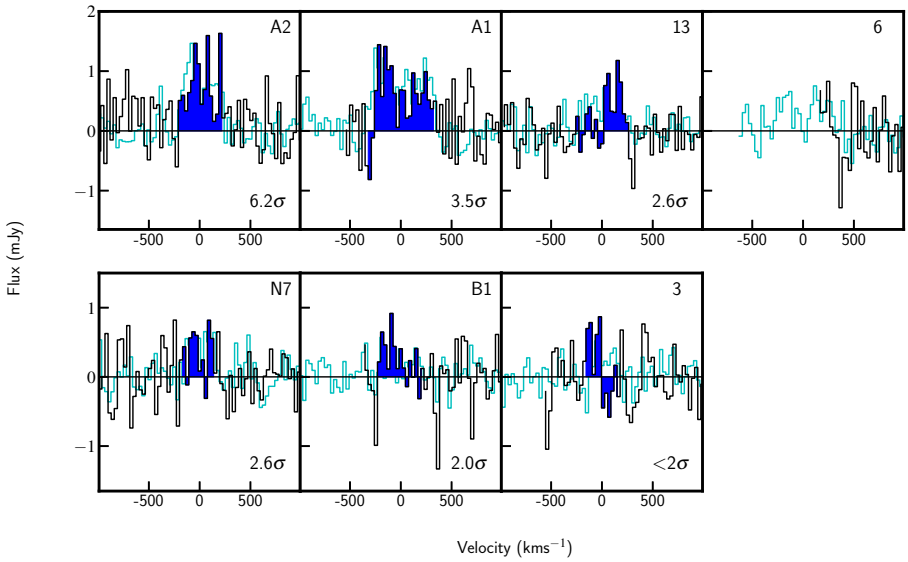

Figure B.1: CO[3-2] line spectra for seven galaxies in Cl J1449+0856, shown by the black line. Galaxy S7 has not been included, as the frequency coverage of the observations did not extend to the CO[3-2] position at the redshift of S7. Similarly, for galaxy 6 our band 3 data provides only partial coverage of the velocity range corresponding to the CO[4-3] line emission, shown in cyan. The blue shading indicates the velocity over which CO[3-2] emission was measured. The CO[3-2] line fluxes were extracted over this fixed velocity range, corresponding to the redshift and velocity range given by the CO[4-3] line detections. The CO[4-3] line spectra are shown in the background (cyan lines), at the same scale. The significances of the CO[3-2] line fluxes are shown are shown in the bottom-right corner of each panel, measured from the data collapsed over the linewidth shown in blue shading, over the same 2D shape as for the CO[4-3] emission of each galaxy.

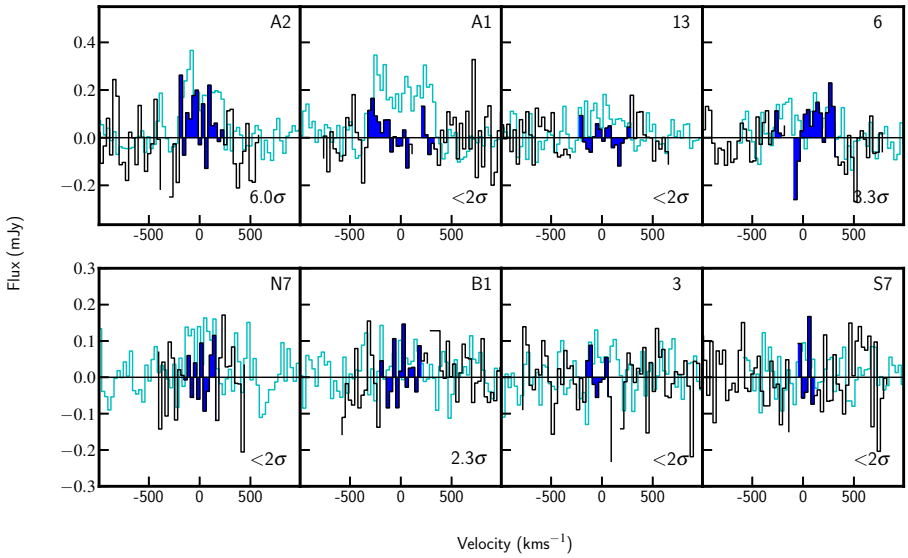

Figure B.2: CO[1-0] line spectra for eight galaxies in Cl J1449+0856, shown by the black line. The blue shading indicates the velocity over which CO[1-0] emission was measured. The line fluxes for the CO[1-0] line were extracted over this fixed velocity range, corresponding to the redshift and velocity range given by the CO[4-3] line detections. The CO[4-3] line spectra are shown in the background (cyan lines), with the magnitude of the flux scaled down by a factor of 4 for visualisation. The significances of the CO[1-0] line fluxes are shown are shown in the bottom-right corner of each panel, measured from the data collapsed over the linewidth indicated by the dashed lines, over the same 2D shape as for the CO[4-3] emission of each galaxy. Breaks in the CO[1-0] spectra along the velocity axis indicate the breaks between the VLA spectral windows, between which no data is available.

Appendix C

Radio continuum images for SKA simulations

C.1 Band 2 cutouts in the wide, deep and ultradeep SKA survey tiers

This appendix is related to Chapter 6. Additional examples of the radio continuum images that we have derived for our GOODS-North galaxies are shown in Fig. C.1. The cutouts are centered on the labelled galaxies, although in some cases we can see that there are nearby galaxies on the (projected) line of sight. The H-band image, intrinsic radio flux distribution, and SKA ultradeep, deep and wide tiers are shown for each galaxy.

C.2 GOODS-North band 2 model image

In Fig. C.2, I show the entire band 2 intrinsic (before simulation) image of the GOODS-North field. This contains all of the 1613 galaxies selected according to the criteria described in Section 6.3.1.

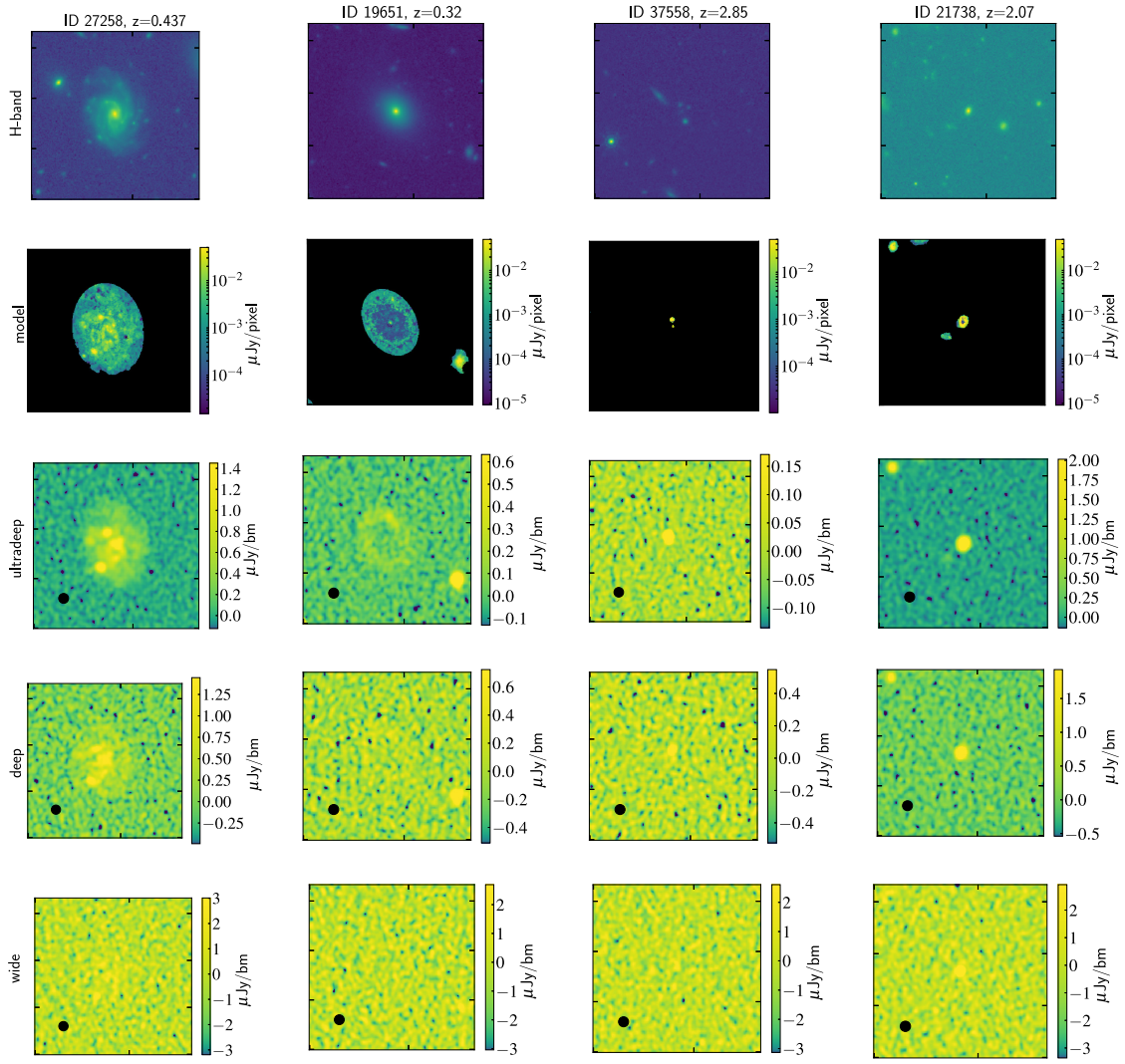

Figure C.1: Further examples of HST/WFC3 H-band, intrinsic/model radio, and SKA-simulated radio images for the ultradeep, deep and wide survey tiers, for our galaxy sample. The rows are labelled on the left side of the figure, and galaxy IDs and redshifts are shown above each column. All cutouts are 20"×20". The H-band and model images are at a scale of 0.06"/pixel, and the black regions in the model row indicate zero-valued background. The simulated survey images are at a scale of 0.12"/pixel, and the FWHM=0.6" of the simulated synthesised beam is shown by the black circles.

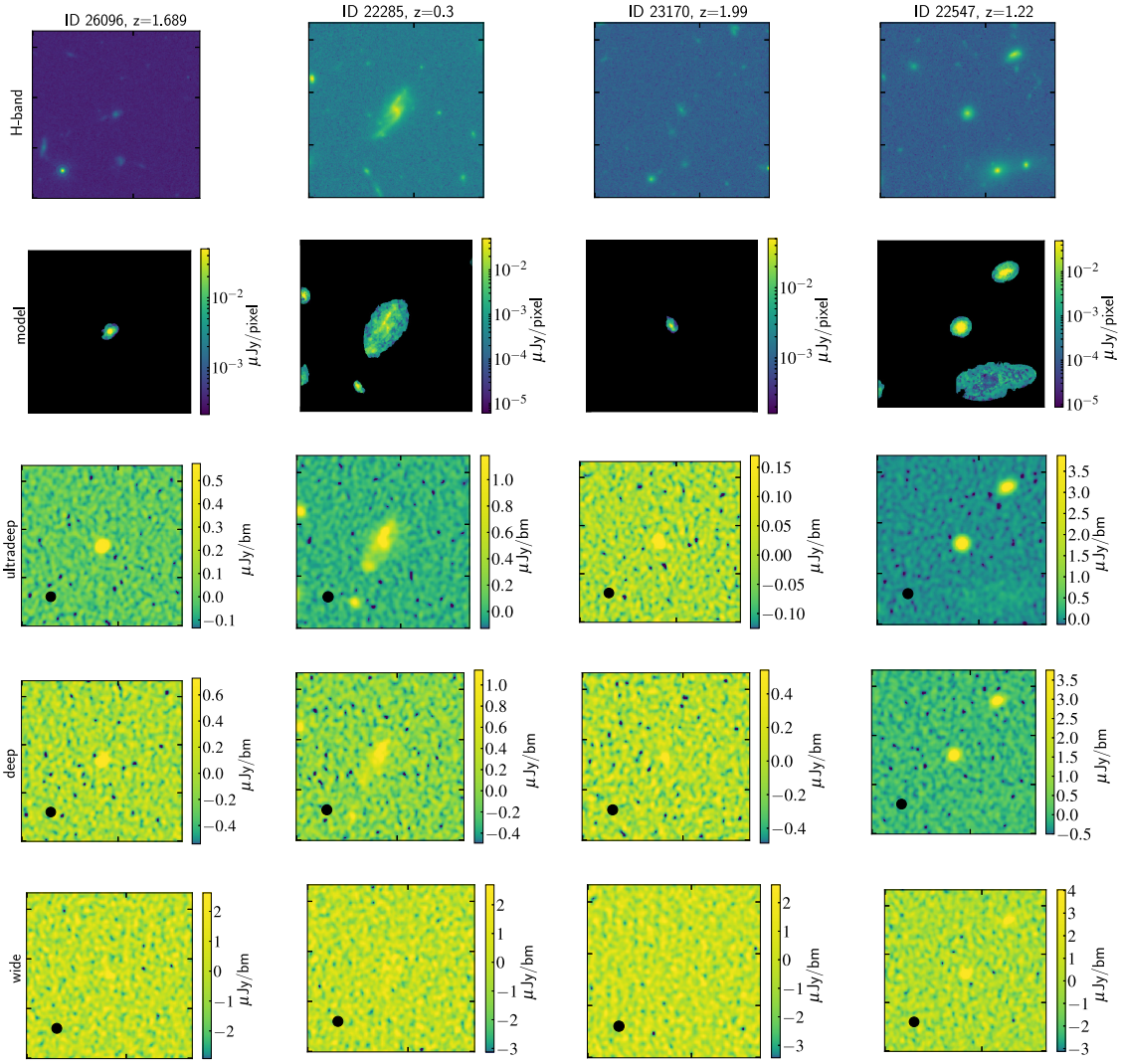

Figure C.1 (cont.)

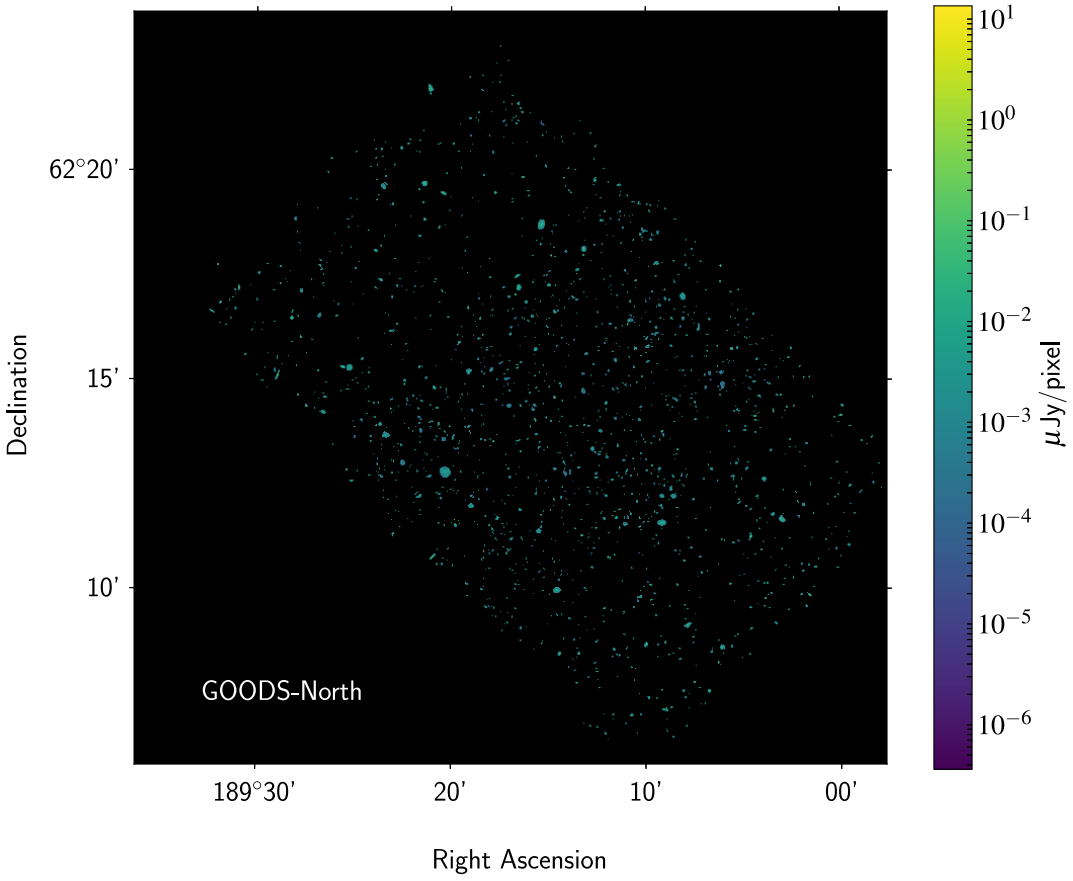

Figure C.2: Intrinsic, noise-free radio continuum image of the GOODS-North field, at 0.06"/pixel. SKA band 2 continuum fluxes ($\sim$1.4 GHz, derived using method case 1) are shown. We simulate this field of view with the SKA response in Chapter 6. The black background indicates zero values, outside of the modelled galaxies.

Appendix D

SKA Miriad simulation code

Here, I include the pipeline script used to create the SKA simulated maps in Miriad. The Miriad task names are shown in bold, with the parameters for each task shown alongside/below. Task names followed by a number (e.g. **imgen2**) are customised versions of the original Miriad task.

Read in the image of the SKA1-MID voltage beam (primary beam, PB, response) at 1.4 GHz. 'CDELT3' should match the continuum frequency bandwidth of the science image (below). The stokes parameters (if present in the image), should also match those of the science image.

```
fits op=xyin in=PB_b2.fits
out=PB_I_14_GN
```

Read in the input sky model image (i.e. intrinsic radio image of the GOODS-North field). This should be input with a 'BUNIT' of Jy/pixel in the header, and contain the continuum frequency bandwidth to be simulated as 'CDELT3'.

```
fits op=xyin in=GN_mosaic_band2_case1.fits
out=mosaic_band2_case1_GN
```

Prepare primary beam images of full size. This outputs a PB image the same pixel scale and pixel number as the sky image (the PB image RA and DEC should correspond to the observation pointing center).

```
regrid in=PB_I_14_GN
tin=mosaic_band2_case1_GN
axes="1,2"
out=PB_I_14_GN_skyb
```

As the input model has units of Jy/pixel, convolve it with the desired clean/restoring beam to give units of Jy/beam.

```
convol map=mosaic_band2_case1_GN
fwhm=0.6
out=mosaic_band2_case1_GNc
```

Apply the primary beam attenuation to the sky radio image, as a multiplication of the two images.

```
imcomb2 in="mosaic_band2_case1_GNc,PB_I_14_GN_skyb"
out=mosaic_band2_case1_GN_PB
options="multi,nonorm"
```

Generate the mock SKA1-MID visibility coverage at a frequency of 1.4 GHz, over a bandwidth of 420 MHz. For our simulation, the frequency sampling is 91 channels across the chosen continuum bandwidth every 30 seconds, over the course of 8 hours. This is done using the configuration of 197 SKA1-MID antennae (b2v1ska1mid.neu.197.ant), using an empty source list (fonaxis.src). The antennae are at the site of SKA1-MID, at a declination of 'lat'=-31 deg, and the pointing 'radec' is the center of the science image (zenith, in this case).

```
uvgen source="fonaxis.src"
ant="b2v1ska1mid.neu.197.ant"
baseunit=-3.33564
corr="91,1,0,420."
time="13JAN01.0"
freq="1.4,0"
radec="0.,-30."
harange="-4.,4.,0.008333"
stokes="rr"
lat=-31.
center="0,-0"
systemp=30.
jyperk=7.03
out=ska1-mid.b2.uv
telescop="altaz,0"
```

From this visibility coverage, make a dirty beam and a dirty noise image. As described in the SKA Science Data Challenge #1 document, the parameters below subject the visibility density grid to a fast-Fourier-transform-based convolution using a Gaussian convolving function, with FWHM of 215" in the image plane. The convolved density distribution was used to form 'uniform' weights for the visibilities, after which a Gaussian taper was applied to achieve the near-Gaussian dirty beam with a target FWHM = 0.6 arcsec.

```
invert vis=ska1-mid.b2.uv
map=ska1-mid.b2.map
beam=ska1-mid.8hb2z0.bm
imsize=9000
cell=0.12
options="radfft, mfs"
fwhm=0.6
sup=215.
```

Put CRPIX1, CRPIX2, CRPIX3 and CDELT3 into the header of the dirty noise image, to match the sky data. Here, CRVAL3 and CDELT3 are input in GHz.

```
puthd in=ska1-mid.8hb2z0.map/crpix1 value=4500.5

puthd in=ska1-mid.8hb2z0.map/crpix2 value=4500.5

puthd in=ska1-mid.8hb2z0.map/crpix3 value=1.

puthd in=ska1-mid.8hb2z0.map/crval3 value=1.4

puthd in=ska1-mid.8hb2z0.map/cdelt3 value=420.E-3
```

From the dirty noise image created by **invert**, generate noise images with RMS levels that correspond to the desired observation depth. In this case, we want to scale the noise to match the wide, deep and ultradeep tiers of the planned SKA continuum reference surveys.

First the noise for the wide tier (1μJy/bm). The noise image is scaled by the required factor.

```
imgen in=ska1-mid.b2.map
factor=1.45
out=ska1-mid.wide.b2c.map
object="point"
spar="1.e-20,0,0"
```

The noise for the deep tier (0.2μJy/bm). In addition to the scaling factor, the 'mode' parameter within **regrid** also allows the axes to be reordered, in order to vary the noise distribution with respect to the input image.

```
imgen in=ska1-mid.b2.map
factor=0.29 out=ska1-mid.deep.b2.map
object="point"
spar="1.e-20,0,0"

reorder in=ska1-mid.deep.b2.map
out=ska1-mid.deep.b2c.map
mode="-12"
```

The noise for the ultradeep tier (0.05μJy/bm). The noise is again re-ordered.

```
imgen in=ska1-mid.b2.map
factor=0.07
out=ska1-mid.UD.b2.map
object="point"
spar="1.e-20,0,0"

reorder in=ska1-mid.UD.b2.map
out=ska1-mid.UD.b2c.map
mode="1-2"
```

Generate a residual sky image, in units of Jy/beam. The clip level is set at the 3σ RMS of an 8 hour observation at this setup (2.1μJy/bm in this case, the noise map made by **invert** before rescaling), to reflect the SKA expected observing procedure. This residuals map contains the values of the science image that are less than 3σ.

```
imgen2 in=mosaic_band2_case1_GN_PB
factor=1.
object="clip"
spar=2.1e-6
out=mosaic_band2_case1_GN_PBrd
```

Subtract the residuals (created above) from the science image. This resulting clipped, or 'peak' image, is therefore the science image at $> 3\sigma$.

```
imcomb2 in="mosaic_band2_case1_GN_PB,mosaic_band2_case1_GN_PBrd"
options="subt,nonorm"
out=mosaic_band2_case1_GN_PB_1b2pd
```

Deconvolve out the clean/restoring beam from the residuals, to put them back into Jy/pixel. Put a zero beam size and the image units into the header of this deconvolved image.

```
convol map=mosaic_band2_case1_GN_PBrd
fwhm=0.6
options="divide"
sigma=1.e-1
out=mosaic_band2_case1_GN_PBrdd

puthd in=mosaic_band2_case1_GN_PBrdd/bmaj value=0.
puthd in=mosaic_band2_case1_GN_PBrdd/bmin value=0.
puthd in=mosaic_band2_case1_GN_PBrdd/bpa value=0.
puthd in=mosaic_band2_case1_GN_PBrdd/bunit value="JY/PIXEL"
```

Now convolve these residuals with the dirty beam. This is done as these low fluxes would not be CLEANed or deconvolved from the dirty beam in the true deconvolution process, at a threshold of 3σ.

```
convol map=mosaic_band2_case1_GN_PBrdd
beam=ska1-mid.8hb2z0.bm
out=mosaic_band2_case1_GN_PBrdcb
```

Add the residuals to the peak science image.

```
imcomb in="mosaic_band2_case1_GN_PB_1b2pd,mosaic_band2_case1_GN_PBrdcb"
options="nonorm"
out=mosaic_band2_case1_GN_cd
```

Finally, add the dirty noise images that were created for each tier of the continuum survey, to the combined science image. We use a 'relaxed' tolerance on matching the sky positions.

```
imcomb in="mosaic_band2_case1_GN_cd,ska1-mid.wide.b2c.map"
options="nonormalise,relax"
out=mosaic_band2_case1_GN_cdn_wide
```

```
imcomb in="mosaic_band2_case1_GN_cd,ska1-mid.deep.b2c.map"
options="nonormalise,relax"
out=mosaic_band2_case1_GN_cdn_deep

imcomb in="mosaic_band2_case1_GN_cd,ska1-mid.UD.b2c.map"
options="nonormalise,relax"
out=mosaic_band2_case1_GN_cdn_UD
```

Generate the output fits images for analysis.

```
fits op=xyout in=mosaic_band2_case1_GN_cdn_wide
out=mosaic_band2_case1_GN_cdn_wide_final.fits

fits op=xyout in=mosaic_band2_case1_GN_cdn_deep
out=mosaic_band2_case1_GN_cdn_deep_final.fits

fits op=xyout in=mosaic_band2_case1_GN_cdn_UD
out=mosaic_band2_case1_GN_cdn_UD_final.fits

fits op=xyout in=ska1-mid.8hb2z0.bm
out=ska1-mid.8hb2z0.bm_final.fits
```

Publications List

An. F.; [...]; Coogan, R. T. et al., 2019, “Multi-wavelength properties of radio and machine-learning identified counterparts to submillimeter sources in S2COSMOS”, Astrophysical Journal submitted, arXiv:1910.03596

Gobat, R.; Daddi, E.; Coogan, R. T. et al., 2019, “Sunyaev-Zel’dovich detection of Cl J1449+0856 at z = 1:99: the pressure profile in uv space", Astronomy & Astrophysics, 629, A104

Coogan, R. T. et al., 2019, “Suppressed CO emission and high G/D ratios in z=2 galaxies with sub-solar gas-phase metallicity”, Monthly Notices of the Royal Astronomical Society, 485, 2092

Simpson, J.; [...]; Coogan, R. T. et al., 2019, “The East Asian Observatory SCUBA2 survey of the COSMOS field: Unveiling 1147 bright submillimeter sources across 2.6 square degrees”, Astrophysical Journal, 880, 43

Coogan, R. T. et al., 2018, “Merger driven star-formation activity in Cl J1449+0856 at z=1.99 as seen by ALMA and JVLA”, Monthly Notices of the Royal Astronomical Society, 479, 703

Strazzullo, V.; Coogan, R. T. et al., 2018, “Deciphering the Activity and Quiescence of High-redshift Cluster Environments: ALMA Observations of Cl J1449+0856 at z = 2”, Astrophysical Journal, 862, 64S

Perna, M.; [...]; Coogan, R. T. et al., 2018, “The molecular gas content in obscured AGN at z $>$1”, Astronomy & Astrophysics, 619, 90

Zanella, A.; [...]; Coogan, R. T., 2018, “The [C II] emission as a molecular gas mass tracer in galaxies at low and high redshifts”, Monthly Notices of the Royal Astronomical Society, 481, 2

Daddi, E.; [...]; Coogan, R. et al., 2017, “Radio Selection of the Most Distant Galaxy Clusters”, Astrophysical Journal, 846L, 31

Coogan, R. T.; Brown, A. M. & Chadwick, P. M., 2016, “Localizing the gamma-ray emission region during the 2014 June outburst of 3C 454.3”, Monthly Notices of the Royal Astronomical Society, 458, 354

Publications library: ***ui.adsabs.harvard.edu/#/public-libraries/zMEyCBvNT4ym98uARlPPgg***